

**ACQUISITION, 3-D DISPLAY AND INTERPRETATION OF GPR DATA  
IN FLUVIAL SEDIMENTOLOGY**

**Master of Philosophy Thesis**

**University of Birmingham  
School of Geography, Earth and Environmental Sciences**

**Tomasz Żuk  
June 2011**

UNIVERSITY OF  
BIRMINGHAM

**University of Birmingham Research Archive**

**e-theses repository**

This unpublished thesis/dissertation is copyright of the author and/or third parties. The intellectual property rights of the author or third parties in respect of this work are as defined by The Copyright Designs and Patents Act 1988 or as modified by any successor legislation.

Any use made of information contained in this thesis/dissertation must be in accordance with that legislation and must be properly acknowledged. Further distribution or reproduction in any format is prohibited without the permission of the copyright holder.

## ABSTRACT

Alluvial architecture has an inherently three-dimensional character; however, standard methods used within fluvial sedimentology, including ground penetrating radar (GPR) surveys, generally provide only 1-D or 2-D information. Thus data on paleoflow directions, for example, have to be inferred from 2-D profiles. However, full-resolution 3-D GPR data collection and processing is both time consuming and technically challenging and thus has been rarely applied to study fluvial deposits. The primary aim of this thesis is thus to try and bridge this gap and demonstrate that improvements to the processing and visualization of 2-D GPR data, with readily available seismic software, can provide high-resolution 3-D images of fluvial deposits without the need for the application of more technically difficult full-resolution 3-D acquisition and processing. It also tries to find out the extent to which such a method can be used as a standard tool of fluvial sedimentology.

Three grids of very closely spaced GPR lines collected from a meandering and a braided river were processed in 2-D and compiled into 3-D datasets with open-source Seismic Unix. AGC, 'dewow' and band-pass filtering were replaced with gain functions and time-variable filtering, which by addressing the fast-alternating GPR signal added up to 40% penetration to the interpretable parts of profiles. Two sets of filter gate values produced lower and higher resolution data. The first one recovers otherwise lost information from the lower parts of the profiles, while the second datasets provides better resolution in the upper parts of the profiles.

The volume display, offered by Kingdom seismic interpretation software, helped to establish the internal organization of sedimentary facies and their bounding surfaces. Time slicing and horizon tracing were used to establish the orientation of the sedimentary structures, to infer changes of the paleocurrent directions and to build 3-D models of the fluvial sedimentary

architecture. This enabled features such as bartop hollows, crossbar channels, slipfaces and bar margin reactivation surfaces to be visualized that were not always apparent from 2-D sections alone. Quantitative comparison of interpretations carried out on 2-D profiles and 3-D volumes revealed that the accuracy of 2-D interpretation in relation to the facies recognised in 3-D was 76.0 to 99.9%. The last value does not take into account recognition of less than 20 degree changes of orientation of sedimentary structures which could only be revealed by 3-D volumes. On this basis it is concluded that 2-D data collection and analysis coupled with 3-D visualization may represent a useful compromise between quick 2-D surveys and more challenging fully 3-D methods. The approach outlined in this thesis may thus be especially useful for more complex areas of alluvial architecture. This final point is highlighted with illustrative examples of point bar, recirculation pool, deep scour fill and migrating unit bar deposits.

## AKNOWLEDGEMENTS

I would like to thank Dr. Greg Sambrook Smith for his excellent guidance, enthusiasm, advice and patience as well as for making available to me the South Saskatchewan River GPR data for this research project.

I also would like to thank to Prof. Tim Reston who recommended the subject of the project and Dr. Russell Exley for his help with SU script and guidance on using SMT Kingdom software. Many thanks to Dr. Dan Parsons for recommending the Macclesfield site and to Dr. Arjan Reesink who helped to collect the Macclesfield data.

I would like to acknowledge the helpful comments of the examiners,  
Prof. John Tellam and Dr. John Woodward.

Finally, I would like to thank my wife, Ziqian Chan, for her understanding, encouragement and support during this project.

## TABLE OF CONTENTS

	PAGE
LIST OF TABLES	
LIST OF FIGURES	
CHAPTER 1	
1.0 INTRODUCTION	1
1.1 BACKGROUND	2
1.2 OBJECTIVES AND STRUCTURE OF THESIS	3
CHAPTER 2	
2.0 LITERATURE REVIEW	6
2.1 HISTORICAL BACKGROUND	6
2.2 APPLICATION OF GPR OUTSIDE FLUVIAL SEDIMENTOLOGY	8
2.3 APPLICATION OF 2-D GPR DATA IN FLUVIAL SEDIMENTOLOGY	13
2.4 APPLICATION OF PSEUDO 3-D GPR DATA IN FLUVIAL SEDIMENTOLOGY	24
2.5 TRUE 3-D GPR SURVEYS IN FLUVIAL SEDIMENTOLOGY	26
2.6 SUMMARY	26
CHAPTER 3	
3.0 METHODOLOGY	35
3.1 DATA PROCESSING	41
3.2 THREE-DIMENSIONAL DATA DISPLAY	57
CHAPTER 4	
4.0 TWO-DIMENSIONAL INTERPRETATION OF GPR PROFILES	73
4.1 CLASSIFICATION AND INTERPRETATION OF RADAR FACIES REVEALED BY 2-D MACCLESFIELD DATA	78
4.2 CLASSIFICATION AND INTERPRETATION OF RADAR FACIES REVEALED BY 2-D SOUTH SASKATCHEWAN RIVER 120 X 40 M GRID DATA	92
4.3 CLASSIFICATION AND INTERPRETATION OF RADAR FACIES REVEALED BY 2-D SOUTH SASKATCHEWAN RIVER 10 X 10 M GRID DATA	100

## CHAPTER 5

5.0	INTERPRETATION OF 3-D DATASETS	109
5.1	CLASSIFICATION AND INTERPRETATION OF THE MACCLESFIELD RADAR FACIES BASED ON 3-D VISUALISATION	111
5.2	CLASSIFICATION AND INTERPRETATION OF RADAR FACIES REVEALED BY 3-D SOUTH SASKATCHEWAN RIVER 120 X 40 M GRID DATA	120
5.3	CLASSIFICATION AND INTERPRETATION OF RADAR FACIES REVEALED BY 3-D SOUTH SASKATCHEWAN RIVER 10 X 10 M GRID DATA	124

## CHAPTER 6

DISCUSSION	130
------------	-----

## CHAPTER 7

CONCLUSION	146
RECOMMENDATIONS FOR FURTHER WORK	147

## REFERENCES

APPENDIX 1	Glossary of term used in the thesis
APPENDIX 2A	Seismic Unix scripts for data processing
APPENDIX 2B	Seismic Unix scripts for compilation of 3-D data
APPENDIX 3	Animations

## LIST OF TABLES

Table 3.1 Summary of the processing steps used for the three datasets presented in this thesis.

Table 4.1 Summary of five identified radar facies with their variability on orthogonally oriented profiles.

Table 4.2 Summary of three identified radar facies with their variability on orthogonally oriented profiles.

Table 4.3 Summary of four identified radar facies with their variability on orthogonally oriented profiles.

Table 5.1 Summary of five 3-D radar facies identified in Macclesfield site.

Table 5.2 Summary of radar facies identified in the South Saskatchewan River 120 x 40 m pseudo 3-D grid.

Table 5.3 Summary of identified radar facies in the South Saskatchewan River 10 x 10 m true 3-D volume.

## LIST OF FIGURES

Fig. 2.2.1 Image of the radar surface representing paleosurface of 'basal till' underlying sequence of aeolian deposits by Pedersen and Clemmensen (2005).

Fig. 2.2.2 Time slices of pseudo 3-D volume collected by Whiting *et al.* (2001) to investigate structures left by Amerindian settlement on Barbados, West Indies.

Fig. 2.2.3 Pseudo 3-D dataset collected with 400 MHz antenna, 2-D processed and displayed with 3D QuickDraw for RADAN by Munroe *et al.* (2007) to investigate cryogenic features in Alaska.

Fig. 2.2.4 Pseudo 3-D dataset collected with 100 MHz antenna, 2-D processed and displayed with Slicer from Spyglass by Sigurdsson and Overgaard (1998) to carbonate formation in a limestone quarry on the island of Zealand, Denmark.

Fig. 2.3.1 Classification of the reflection facies, which were correlated with lithology known from exposures, adopted from seismic interpretation by Beres and Heani (1991).

Fig. 2.3.2 Classification of radar facies and interpretation of the lithology/depositional environments given by Huggenberger (1993).

Fig. 2.3.3 Images of the radar sequence boundary presented by Gawthorpe *et al.* (1993).

Fig. 2.3.4 Presentation of the sedimentary architecture combined with an interpretation of the depositional styles of a sandy unit bar in the Jamuna River (Best *et al.* 2003).

Fig. 2.3.5 Distribution of radar facies within a compound bar in the South Saskatchewan River based on 200 MHz GPR data by Sambrook Smith *et al.* (2006b).

Fig. 2.3.6 Correlation of sedimentary facies recorded on individual GPR profiles collected in the Sagavanirktok River presented by Lunt *et al.* (2004).

Fig. 2.3.7 Three-dimensional model of the sedimentary architecture of the Niobrara River by Skelly *et al.*(2003).

Fig. 2.3.8 The 3-D model of sedimentary facies by Bowling *et al.* (2005).

Fig. 2.3.9 Table presenting reflection patterns on 2-D GPR profiles (200 MHz) with sedimentological and hydrogeological interpretation of deposits from the Neckar Valley by Kostic and Aigner (2007).

Fig. 2.4.1 3-D GPR volume showing glaciofluvial river deposits in the Rhine valley, presented by Beres *et al.* (1995).

Fig. 2.4.2 Pseudo 3-D volume of 200 MHz data with time slices at 113 ns and chair diagram showing shallow alluvial deposits in the Boise River valley, Idaho by Peretti *et al.* (1999).

Fig. 2.4.3 Chair diagram of pseudo 3-D data presented by Heinz and Aigner (2003).

Fig. 2.4.4 Chair diagrams presenting pseudo 3-D data volumes of glaciolacustrine delta and glaciofluvial sediments in the Singen Basin in SW Germany by Asprion and Aigner (1999).

Fig. 2.4.5 Classification of radar facies based on their appearance on vertical profiles and time slices by Beres *et al.* (1999).

Fig. 2.5.1 True 3-D volume collected from the Ferron Sandstone Formation, Utah, USA by McMechan *et al.* (1997).

Fig. 2.5.2 Chair diagram and section from the Ferron Sandstone Formation, Utah, USA by Szerbiak *et al.* (2001)

Fig. 3.0.1 Photographs of the Macclesfield site.

Fig. 3.0.2 Grid of lines at the Macclesfield site with topographical survey information.

Fig. 3.0.3 Location of the true 3-D 10 x 10 m grid of data collected in the South Saskatchewan River in relation to other morphological forms.

Fig. 3.0.4 Location of the 120 x 40 m grid collected in the South Saskatchewan.

Fig. 3.1.1 Fragments of line 00 EW and 40 SN from the Macclesfield site with examples of amplitude spectrum in frequency domain.

Fig. 3.1.2 Examples of amplitude spectrum in frequency domain for selected traces from line 20 EW and line 01 SN from the Macclesfield site.

Fig. 3.1.3 Fragment of unprocessed line 21 EW from the Macclesfield site with the corresponding amplitude spectrum in frequency domain.

Fig. 3.1.4 Schematic representation of bandpass filters.

Fig. 3.1.5 Comparison results of 2-D processing applied to line 02 SN from Macclesfield dataset

Fig. 3.1.6 Comparison of lower resolution line 97 NS from the South Saskatchewan River 10 x 10 m grid before and after Wiener filtering.

Fig. 3.1.7 Comparison of higher resolution line 50 WE from the Macclesfield site before and after Wiener filtering.

Fig. 3.1.8 Comparison of lower resolution line 04 South Saskatchewan from the South Saskatchewan River 120 x 40 m grid before and after Wiener filtering.

Fig. 3.1.9 CMP profiles collected from the recirculation zone at the Macclesfield site.

Fig. 3.1.10 Velocity estimation based on the shape of parabolic reflections for the recirculation zone deposits at the Macclesfield site.

Fig. 3.1.11 Comparison of higher resolution line 97 NS from the South Saskatchewan River 10 x 10 m grid before and after Stolt migration.

Fig. 3.1.12 Lower resolution line 02 SN without NMO and DMO compared with profiles which were processed with NMO and DMO.

Fig. 3.1.13 Screen shot of the SMT Kingdom window during loading of the coordinates for the higher resolution W-E oriented lines of the South Saskatchewan River 10 x 10 m grid.

Fig. 3.1.14 Comparison of processing results of lower resolution line 80 WE from the South Saskatchewan River 10 x 10 m grid.

Fig. 3.2.1 Inversion to velocity volume presenting recirculation pool deposits from the River Dene, Macclesfield, site.

Fig. 3.2.2 Amplitude volumes presenting the deep scour fill in the South Saskatchewan River 10 x 10 m grid volume with trace and line spacing of 0.10 x 0.10 m (A), 0.30 x 0.30 m (B), and 0.50 x 0.50 m (C).

Fig. 3.2.3 Modified from Brown (2004): normal distribution of amplitude values of samples in seismic data volumes.

Fig. 3.2.4A The South Saskatchewan River 120 x 40 m dataset: transparency applied to the low and moderate signal amplitudes.

Fig. 3.2.4B The Macclesfield dataset: transparency applied to low and lower-moderate signal amplitudes.

Fig. 3.2.5A The South Saskatchewan River 120 x 40 m dataset: transparency applied to low and high signal values.

Fig. 3.2.5B The South Saskatchewan River 10 x 10 m dataset: transparency applied to low and high signal values.

Fig. 3.2.6A Transparency applied to high and moderate amplitudes in the South Saskatchewan River 120 x 40 m volume.

Fig. 3.2.6B Transparency applied to high and moderate amplitudes in the South Saskatchewan River 10 x 10 m volume.

Fig. 3.2.7 Example of applying horizon slices to display geomorphological features presented by Chopra and Marfurt (2007).

Fig. 3.2.8 Manual tracing of the erosional surface scoured by a recirculation pool was completed on an inverted velocity profile.

Fig. 3.2.9 The final result of horizon tracing: erosional surfaces of recirculation zone and older channel with the ground surface above.

Fig. 3.2.10 The South Saskatchewan River 10 x 10 m grid volume with time slice at 163.2 ns.

Fig. 3.2.11 Fragment of the South Saskatchewan River 10 x 10 m grid volume.

Fig. 3.2.12 Section of volume representing the recirculation zone on Macclesfield site is used to investigate details of sedimentary structures.

Fig. 3.2.13 Application of opacity/transparency technique to display in detail the sedimentary structures within the South Saskatchewan River 120 x 40 m grid dataset.

Fig. 4.0.1 Description followed in the thesis regarding the polarity of recorded wavelets and examples of relative electric permittivity of sediments taken from Neal (2004).

Fig. 4.0.2 Examples of radar facies described in terms of shape, configuration and relations between reflection lines modified from Neal (2004).

Fig. 4.0.3 Examples of the main types of termination of reflection lines determining classification of reflection surfaces, modified from Neal (2004) and Catuneanu (2002).

Fig. 4.0.4 Distribution of radar sequences within aeolian dune by Bristow (2009) with a chronostratigraphic chart based on radar sequences recognised in GPR profiles.

Fig. 4.1.1 Lower resolution line 24 EW from the Macclesfield site. Horizontal parallel reflections extend over the whole area of the site but are more distinct outside the former channel.

Fig. 4.1.2 Lower resolution line 02 SN from the Macclesfield site which is immediately adjacent to the east of the river bank.

Fig. 4.1.3 Higher resolution line 06 SN from the Macclesfield site.

Fig. 4.1.4 Fragments of higher resolution line 43 EW from the Macclesfield site and of higher resolution line 19 SN which show the concave upwards reflections to the north of the recently filled pool area at the Macclesfield site.

Fig. 4.1.5 Higher resolution line 37 SN from the Macclesfield site with examples of concave upwards shapes located to the north of the recirculation pool area.

Fig. 4.1.6 Lower resolution line 03 EW from the Macclesfield site which shows radar facies (4) located to the south of the recirculation pool.

Fig. 4.1.7 Lower resolution line 39 SN from the Macclesfield site which shows chaotic and parabolic reflections

Fig. 4.1.8 Lower resolution line 23 EW from the Macclesfield site which shows concave upwards, slightly inclined reflection pattern.

Fig. 4.1.9 Lower resolution line 26 WE from the Macclesfield site which shows convex pattern which separates two concave upwards zones within the recirculation pool.

Fig. 4.1.10 Lower resolution line 37 SN from the Macclesfield site which shows hyperbolic reflection with discontinuous undulating reflections of radar facies (5).

Fig. 4.1.11 Image of the Macclesfield site with the location of the ground-truth control GPR profile from the cut-bank of the River Dene.

Fig. 4.1.12 Section of the ground-truth control profile collected with 200 MHz antenna and correlated with cut-bank observations.

Fig. 4.1.13 Lower resolution line 20 SN from the Macclesfield site which shows spatial relations between the four main radar facies.

Fig. 4.2.1 Lower resolution line 12 from the South Saskatchewan River 120 x 40 m grid which shows radar facies (1).

Fig. 4.2.2 Lower resolution line 39 from the South Saskatchewan River 120 x 40 m grid which shows radar facies (1).

Fig. 4.2.3 Lower resolution line 100 from the South Saskatchewan River 120 x 40 m grid which shows radar facies (1).

Fig. 4.2.4 Higher resolution line 20 from the South Saskatchewan River 120 x 40 m grid which shows radar facies (2).

Fig. 4.2.5 Higher resolution line 09 from the South Saskatchewan River 120 x 40 m grid which shows radar facies (2).

Fig. 4.2.6 Lower resolution line 39 from the South Saskatchewan River 120 x 40 m grid which shows radar facies (2).

Fig. 4.2.7 Lower resolution line 47 from the South Saskatchewan River 120 x 40 m grid which shows lower group of radar facies (2).

Fig. 4.2.8 Lower resolution line 69 from the South Saskatchewan River 120 x 40 m grid which shows examples of reflections classified as radar facies (4).

Fig. 4.2.9 Higher resolution line 95 from the South Saskatchewan River 120 x 40 m grid which shows examples of reflections classified as radar facies (4).

Fig. 4.2.10 Lower resolution line 93 from the South Saskatchewan River 120 x 40 m grid which shows radar facies (4).

Fig. 4.2.11 Lower resolution line 05 from the South Saskatchewan River 120 x 40 m grid which shows radar surface, which separates facies (4) and (2).

Fig. 4.2.12 Lower resolution line 18 from the South Saskatchewan River 120 x 40 m grid which shows radar surface, which separates facies (4) and (2).

Fig. 4.2.13 Lower resolution line 73 from the South Saskatchewan River 120 x 40 m grid.

Fig. 4.2.14 Higher resolution line 14 from the South Saskatchewan River 120 x 40 m grid which shows distribution of the radar facies (1), (2) and (4).

Fig. 4.3.1 The upper part of higher resolution line 45 WE and line 45 NS from the South Saskatchewan River 10 x 10 m.

Fig. 4.3.2 The upper part of higher resolution line 10 WE line from the South Saskatchewan River 10 x 10 m which shows the concave upwards reflection pattern.

Fig. 4.3.3 Lower resolution line 79 WE from the South Saskatchewan River 10 x 10 m.

Fig. 4.3.4 Lower resolution line 60 NS from the South Saskatchewan River 10 x 10 m.

Fig. 4.3.5 Lower resolution line 83 WE from the South Saskatchewan River 10 x 10 m which shows radar surface between radar facies (5) and (6).

Fig. 4.3.6 Lower resolution line 93 NS from the South Saskatchewan River 10 x 10 m which shows hyperbolic reflections underlying the zone of the horizontal lines.

Fig. 4.3.7 Lower resolution line 45 WE from the South Saskatchewan River 10 x 10 m which shows main radar facies.

Fig. 5.0.1 Radar packages used in radar stratigraphy identified for general use in sedimentology proposed by Neal (2004).

Fig. 5.0.2 Examples of description of geometries of radar facies in 3-D. Top two are modified from Beres *et al.* (1999), bottom two modified from Neal (2004).

Fig. 5.1.1 Section of the lower resolution S-N amplitude volume with the elongated trough-shaped horizon bounding concave reflections of radar facies (4).

Fig. 5.1.2 Eastern section of the lower resolution 3-D Macclesfield amplitude volume.

Fig. 5.1.3 Section of the lower resolution S-N volume inverted to velocity seen from the south west also showing radar facies (4) within the elongated half trough-shaped horizon.

Fig. 5.1.4 Section of the lower resolution S-N amplitude volume which shows the elongated half trough-shaped horizon, which bounds radar facies (3).

Fig. 5.1.5 Upper elongated half-trough horizon which forms a boundary of the continuous concave concordant reflections.

Fig. 5.1.6 Upper and lower half-trough horizons from the Macclesfield site.

Fig. 5.1.7 Upper and lower half-trough horizons from the Macclesfield site.

Fig. 5.1.8 The recirculation pool horizon with concave reflection surfaces which dominate the N-S oriented profiles and edges of the pool on the E-W profiles.

Fig. 5.1.9 The recirculation pool horizon with a small section of the lower resolution amplitude volume.

Fig. 5.1.10 Part of the higher resolution amplitude volume and the horizon which represents the erosional surface associated with the recirculation pool.

Fig. 5.1.11 The Macclesfield volume with time slice at 30.2 ns reveals shape of recirculation pool and the edge of point bar.

Fig. 5.1.12 Lower resolution amplitude volume with all four distinguished horizons.

Fig. 5.2.1 Lower resolution amplitude volume showing 62.0 ns time slice which shows reflections of radar facies (1) inclined to the east and radar facies (4).

Fig. 5.2.2 Southern section of lower resolution amplitude volume showing 62.0 ns time slice.

Fig. 5.2.3 Section of lower resolution amplitude volume with transparency technique applied which revealed the upper group of radar facies (1) and (4).

Fig. 5.2.4 The South Saskatchewan River 120 x 40 m grid volume with time slice at 57.5 ns reveals the orientation of foresets.

Fig. 5.3.1 Lower resolution volume created from the South Saskatchewan River 10 x 10 m grid which shows the large-scale inclined horizon interpreted as fragment of a deep scour.

Fig. 5.3.2 Low resolution volume with time slice at 216 ns and which shows both of the horizons and radar facies (5).

Fig. 5.3.3 Section of the amplitude volume created from the South Saskatchewan River 10 x 10 m grid with time slice at 163 ns.

Fig. 5.3.4 Comparison of sections of the higher with lower resolution South Saskatchewan River 10 x 10 m volume.

Fig. 5.3.5 Upper part of the high resolution South Saskatchewan River 10 x 10 m amplitude volume with small-scale elongated trough-shaped horizon with its axis oriented along the N-S direction.

Fig. 5.3.6 Part of the volume inverted to velocity created from the South Saskatchewan River true 3-D dataset with the elongated trough-shaped horizon.

Fig. 5.3.7 Both of the identified horizons which helped in interpreting the 3-D volume.

Fig. 5.3.8 Part of a 2-D GPR profile collected in the South Saskatchewan River and which runs through the centre of the 10 x 10 m GPR grid.

Fig. 6.1 Comparison of 2-D profiles of inclined bedding related to the downstream accretion on the margin of a braid bar and of lateral accretion of point bar deposits in a meandering river.

Fig. 6.2 Comparison of 2-D profile (line 02) from the South Saskatchewan River 120 x 40 m grid with a section of 3-D volume (line 02 and time slice at 47 ns).

Fig. 6.3 The South Saskatchewan River 120 x 40 m dataset comparing the appearance of radar facies (4).

Fig. 6.4 Simplified decision flow chart for choosing optimal GPR survey method.

Fig. 6.5 Required maximum distance between survey points (stations and lines) in relation to dimensions of structures.

Fig. 6.6 Decision flow chart for basic data processing.

Fig. 6.7 Comparison of interpretation of 2-D profile with a section of the low resolution 3-D volume of the South Saskatchewan 10 x 10 m grid.

Fig. 6.8 Model of the recirculation pool deposits at the Macclesfield site.

Fig. 6.9 Model of point bar deposits based on the 3-D data from the Macclesfield site

Fig. 6.10 Model of scour fill deposits based on the South Saskatchewan River 10 x 10 m grid.

Fig. 6.11 Model of unit bar deposits based on 3-D data from the South Saskatchewan River.

## CHAPTER 1

### 1.0 INTRODUCTION

Ground-penetrating radar (GPR) was initially used in sedimentary studies at the beginning of the 1990s and quickly became one of the major tools of fluvial sedimentology. GPR is a high-resolution geophysical method providing continuous images of the subsurface which in the case of clastic deposits are presented as reflection patterns parallel to sedimentary structures (Neal 2004). The architecture of sedimentary bodies is defined by Middleton (2003, p. 54) as the “*spatial arrangement of individual bodies within component bodies*” and the “*internal organisation of an individual body showing a hierarchy of volumes and surfaces*”. Both definitions emphasise the three-dimensional aspect of sedimentary architecture. However, as data has traditionally been confined either to cores or restricted 2-D exposures, direct investigation of the spatial arrangement of fluvial sedimentary facies, their scale and the relations between structures within them is often problematic.

Combining GPR surveys with traditional sedimentological methods of investigation partly addresses this problem. As discussed in Chapter 2, 2-D GPR surveys (*e.g.* Best *et al.* 1995, 2003; Bridge *et al.* 1998; Wooldridge and Hickin 2005; Sambrook Smith *et al.* 2005, 2006b) have led to significant advances in the understanding of fluvial sedimentary architecture and the formative processes responsible for its character. However, interpretation of 2-D GPR profiles can sometimes be misleading. Over the last two decades many authors (*e.g.* Bridge 2009) have emphasised this point; for example, the orientation of survey lines (see Glossary) in relation to interpreted sedimentary structures is not always parallel. As was stressed by Beres *et al.* (1995, p. 1090), application of 2-D GPR surveys may be sufficient “*where the dominant trend of the near-surface geology is well known and relatively two-dimensional*”. This, however, is rarely the case with fluvial sedimentary architecture. Both in meandering

and braided rivers the direction of the flow may alter significantly over time, in some circumstances changing by more than 90 degrees. The common assumption that the lines are parallel or perpendicular to the investigated sedimentary structures leads to obvious misinterpretation of reflection patterns. Even if the direction of the flow does not change significantly, orientation of the 2-D survey lines is usually based on the morphological features seen on the ground surface which may lead to inaccuracies.

A potential solution to this issue is the application of three-dimensional geophysical imaging. 3-D GPR surveys involve collecting closely spaced grids of parallel individual lines, which according to the classification by Neal (2004) true 3-D surveys have equal distances between the lines and survey points. Pseudo 3-D surveys involve greater distances between survey lines than between survey points. Despite the potential of the 3-D GPR method, data collection and processing can be time consuming and technically difficult. Probably for this reason, it has not been widely adopted as one of the tools of fluvial sedimentology. The approach adopted in this thesis aims to explore the utility of adopting a compromise approach that takes advantage of 3-D imaging but avoids the technically difficult and time consuming aspects of the full 3-D GPR method.

## 1.1 BACKGROUND

The need for more reliable predictive models in fluvial sedimentology and therefore improved investigation techniques, which would help to build such models, was recently emphasised by Sambrook Smith *et al.* (2006). Predictive models aim to minimise the need for data in building effective models of depositional architecture which are essential in the geosciences, *i.e.* they help to minimise risks and maximise benefits associated with the distribution of properties in the subsurface, such as permeability in aquifers and hydrocarbon reservoirs or

even mechanical properties of deposits under stress conditions.

Fluvial deposits form important aquifers and therefore the study of alluvial sedimentary architecture is particularly relevant to the modelling of groundwater flow within aquifers and to the assessment of potential migration pathways of pollutants (Huggenberger 1993). Such modelling can be very difficult when only limited data from wells and outcrops is available. In hydrocarbon exploration, geologic modelling of channelised reservoirs requires a good understanding of fluvial sedimentary patterns. Because the resolution of conventional seismic data is limited to tens of metres, sedimentary structures below that scale have to be predicted using models and geostatistical methods (Wen 2005). As soft sediments and sedimentary rocks cover approximately 80 percent of the Earth (Folk 1965) and a large part of the deposits are associated with fluvial environments, an ability to predict heterogeneities associated with fluvial sedimentary architecture has application in many fields of mining and engineering. Finally, reliable predictive models and understanding of the fluvial formative processes would improve interpretation of the ancient sedimentary record and contribute to our understanding of the Earth's history.

## 1.2 OBJECTIVES AND STRUCTURE OF THESIS

This thesis presents three GPR datasets. Two of them image the sedimentary architecture of unit bars (see Glossary) in the South Saskatchewan River and were collected in 2005 (by Sambrook Smith & Lunt) and 2007 (by Sambrook Smith & Parker). The third dataset was collected during the summer of 2008 (by Zuk) to investigate recirculation pool deposits in the meandering River Dean near Macclesfield which was first described by Parsons (2002). Further description of the data in terms of the survey location, distances between lines and traces, equipment used are presented in Chapter 4.

This project aims to demonstrate that closely spaced grids of 2-D GPR data displayed with seismic interpretation software can provide high-resolution 3-D images of fluvial deposits without need for the technically challenging and time consuming full-resolution 3-D processing. Such 3-D display of individually processed 2-D profiles should provide an easy to use and powerful tool for displaying and analysing fluvial sedimentary architecture. This is accomplished by fulfilling the following objectives:

The first objective of this thesis is to provide a historical background of the subject discussed. A brief review of publications, which presents the GPR datasets applied to investigate fluvial sedimentary architecture and highlights the application of GPR in other fields of science and engineering, can be found in Chapter 2. This review also looks at the circumstances in which GPR has been introduced as a tool within fluvial sedimentology. It also addresses such aspects as distance between survey lines, methods of displaying and interpreting the data and the scope of data processing applied by previous studies.

The second objective is to undertake a comparison of interpretations resulting from just 2-D profiles versus those derived from 3-D data volumes. This is done to show the benefits and limitations of collecting closely spaced grids of 2-D GPR profiles, displaying them with seismic interpretation software in 3-D, and interpreting in accordance with the principles of radar stratigraphy. As stated by Neal (2004), sedimentary interpretation of GPR datasets should be done in a systematic and commonly agreed way. He emphasised that although there were commonly agreed principles of radar stratigraphy, which are highlighted in Section 4.0, these principles were not fully applied in the majority of fluvial sedimentary works. Interpretation of 2-D profiles is presented in Sections 4.1–4.2, while principles of 3-D interpretation are highlighted in Section 5.0, and interpretation of the datasets displayed in 3-

D with seismic interpretation software can be found in Sections 5.1–5.3. The Discussion in Chapter 6 compares the results of the 2-D and 3-D GPR data interpretation and tries to quantify the accuracy of both of the methods. This is done in order to demonstrate the sedimentological context in which it is beneficial to collect grids of 2-D data, process it individually, compile into 3-D datasets and display them as data volumes with seismic software.

The final objective is to try to establish best practices for the acquisition, displaying and interpreting GPR data. This is presented in the Discussion section to answer to the question about the extent to which 3-D display of closely spaced grids of 2-D data can be used as a standard tool of fluvial sedimentology. Some aspects of collecting GPR data in the context of sedimentary forms, such as choosing the survey mode and optimal distances between survey stations (see Glossary), and the benefits and limitations of some 2-D processing steps are highlighted in that section. The methodology relating to the processing and display of data is highlighted in Chapter 3 and summarised in the Discussion (Chapter 6). Thus the thesis aims to provide a detailed description of the method as a tool for investigating fluvial architecture.

The Discussion is followed by the Conclusion (Chapter 7) which summarises the findings of this thesis and highlights the fields of research which may require further investigation. Some of the geophysical and sedimentological terms which are used in this thesis are explained in the Glossary included in Appendix 1. Appendix 2 presents Seismic Unix scripts which have been used for 2-D processing and compilation of individual 2-D profiles into 3-D datasets. Appendix 3 presents 3-D animations of the volumes used in this thesis to illustrate the potential of the method.

## CHAPTER 2

### 2.0 LITERATURE REVIEW

There have been a great number of publications on the application of GPR in nearly all earth-related fields of science and engineering. Due to its non-invasive character, high resolution and continuous sampling, GPR has been successfully applied in archaeology, civil engineering, mining, glaciology, hydrogeology and sedimentology. As is shown in this chapter, despite the fact that fluvial sedimentary architecture has a 3-D character the application of 3-D datasets in fluvial sedimentology has been very limited, and its full potential has not been fully recognised. This relates not only to the 3-D display of data, but also that interpretation of datasets did not always take into account the 3-D nature of sedimentary facies. The following sections will briefly highlight the sedimentological context in which GPR was adopted as a tool of fluvial sedimentology, its application in other fields, and how it has been used to investigate fluvial sedimentary architecture.

### 2.1 HISTORICAL BACKGROUND

The concept of facies was first introduced by Gressely in 1838 and was defined as all of the properties which distinguished a sedimentary rock formation from its surrounding formations. When sedimentary models were gradually introduced in the 1960s, facies analysis became a tool for investigating depositional environments responsible for the character of sedimentary rocks and – based on data from boreholes and exposures – predicting the spatial distribution of facies which were associated with mineral resources (Reading 2001). Fluvial sedimentary facies were analysed and compared to qualitative sedimentary models which synthesised the spatial distribution of sedimentary facies, such as the ones introduced by Allen (1963) and Visher (1965). As fluvial sedimentary data predominantly originated from surface observations, drilling, wire-logs, shallow excavations and exposures, the facies models

comprised mainly vertical sequences of characteristic sedimentary structures (Miall 1985), such as the classic fining-up succession for point bars (see Glossary). Thus these models assumed that 3-D sedimentary architecture can be diagnosed from vertical sequences of sedimentary facies.

With time, however, due to the large variety of publications on contemporary and ancient fluvial sedimentary facies and because of the complex and variable character of the fluvial depositional environment, a great number of fluvial sedimentary models were introduced (*e.g.* Miall 1977). However, these simplified sedimentary models that were based on vertical sequences were not unique (Brierly 1989, Bristow and Best 1993), leading to inaccurate interpretation of ancient sedimentary records. This brought about the need for a more unified methodology, and in response to this, ‘hierarchical attributes’ were introduced by Jackson (1975). The theory classified bed forms as superposing micro-, meso- and macroforms with corresponding formative processes and time scales. Shortly after that Allen (1983) described the hierarchy of ‘bedding contacts’ as a way of analysing ancient depositional records, with the highest rank associated with major erosional surfaces. The ‘architectural elements’ defined by the shape of surfaces bounding the main sedimentary forms, their internal geometrical patterns, scale and orientation in relation to the paleoflow were also introduced by Miall (1985). Later, the hierarchy of bounding surfaces in fluvial environments was further developed into six orders, linked to the classification of bed forms introduced by Jackson, and even compared with submarine environments (Miall 1988, 1989).

The unified methodology of facies analysis required very accurate field observations. Description and interpretation of exposures could, however, be very difficult as the orientation of the exposure in relation to the direction of the paleocurrent had to be inferred

from it, while excavations could only penetrate to the level of the water table. Such descriptions were also not fully reliable as the patterns of sedimentary structures were affected by the angle at which they were observed and recorded. The GPR method was seen as a tool which could address the requirement for quantitative data for building the fluvial sedimentary models.

## 2.2 APPLICATION OF GPR OUTSIDE FLUVIAL SEDIMENTOLOGY

GPR was initially designed in the 1920s for detecting buried drums containing toxic substances. Equipment which was able to collect continuous 2-D profiles, however, was introduced in the 1970s (Leatherman 1987), and its wider application started at the beginning of the 1990s due to technological development and availability of the equipment. The method has been widely adopted in such applications as detection of buried services, road and railway engineering (Sarenkato 1992, 2009), locating underground voids and landmines (Daniels 1992). It has also been used by hydrogeologists as a tool for detecting groundwater table changes, moisture content and migration of the contaminants (van Overmeeren 1995, 1997). Pseudo 3-D GPR surveys combined with volume visualisation, and particularly time slicing, also became a conventional tool of archaeology (Grasmueck 2008).

In sedimentology one of the earliest applications was used to image coastal deposits by Leatherman (1987) and Beres and Heani (1991). At the beginning of the 1990s Jol and Smith (1992, p. 15), however, wrote: *“The application of GPR to subsurface sedimentology has been very limited. ... The objective of our work is to show and discuss how GPR can be used to better understand modern and ancient deltaic, fluvial and coastal processes and patterns, so that reconstruction of depositional environments can be made.”* Their work was followed

by numerous other publications on nearly all depositional environments. Due to the low signal attenuation within unsaturated sand, aeolian deposits belong to the most often studied with GPR. Examples include work by Bristow *et al.* (2000) who applied principles of sequence stratigraphy to interpret 2-D profiles collected from dune deposits or that by Pedersen and Clemmensen (2005) who used an extensive grid of widely spaced 2-D GPR profiles to map changes of paleotopography due to aeolian deposition associated with Holocene (see Glossary) climatic changes (Figure 2.2.1). Fluvial deposits have been also often investigated with GPR due to “*the widespread distribution of river deposits, their ease of access and their importance as shallow aquifers*” (Bristow *et al.* 2000, p. 2). The application of GPR in fluvial sedimentology is highlighted Section 2.3.

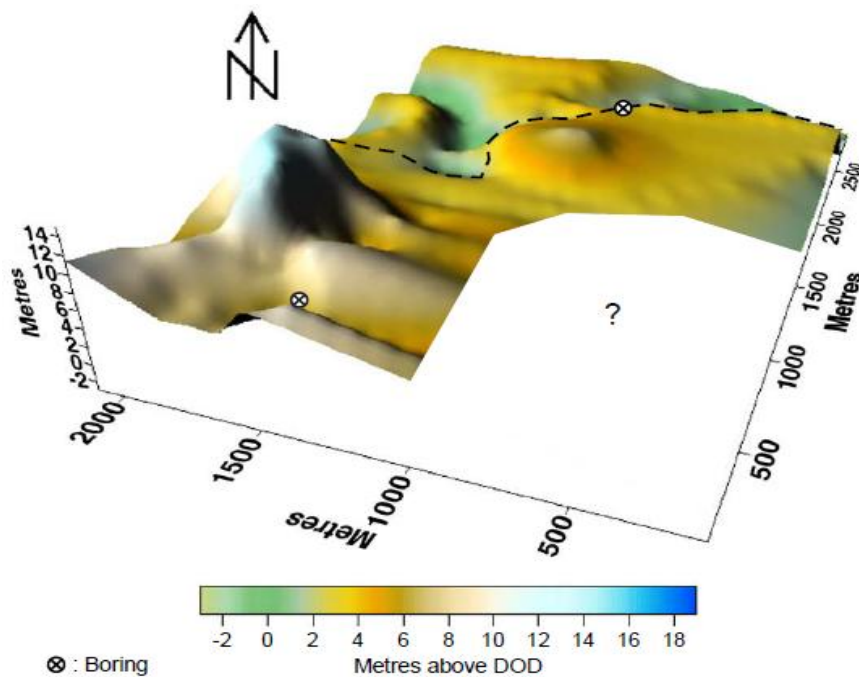


Fig. 2.2.1 Image of the radar surface representing paleosurface of ‘basal till’ underlying sequence of aeolian deposits. Image by Pedersen and Clemmensen (2005) based on widely spaced 2-D GPR lines (software not specified). Note the series of elongated ‘ridges’ probably a result of correlation of adjacent GPR profiles.

Shortly after the 2-D GPR method became widespread, 3-D GPR surveys were also introduced in many areas of research. The first 3-D GPR dataset was used by Hu in 1992 to locate buried pipelines (Grasmueck 1996), although the application of 3-D GPR datasets only became common in the second half of the 1990s. These surveys were used to detect buried

services (Bradford *et al.* 1996), to image fractures within quarried rock formations (Grasmueck 1996, Grandjean and Gourry 1996), to characterise archaeological sites (Pipan *et al.* 1996, Novo *et al.* 2008) and to investigate hydraulic properties of aquifers (Beres *et al.* 1995, 1999).

The technique was particularly successful in archaeological applications. Such works typically used pseudo 3-D surveys followed by 2-D processing, compilation of the individual lines into 3-D datasets and display as a series of time slices (*e.g.* Whiting *et al.* 2001; shown in Figure 2.2.2).

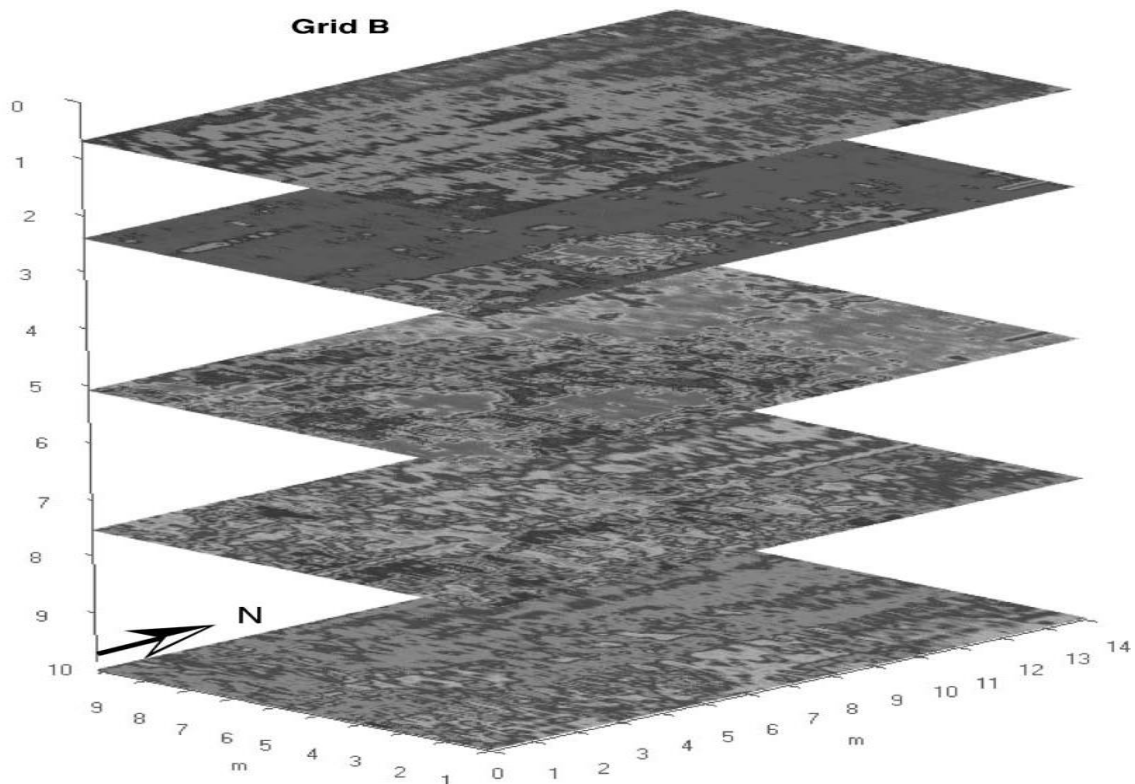


Fig. 2.2.2 Time slices of pseudo 3-D volume collected with 900 MHz antenna (2-D processing, display software not specified) used by Whiting *et al.* (2001) to investigate structures left by Amerindian settlement on Barbados, West Indies. The structures are represented by circular anomalies in the middle time slice (at 5 ns). Vertical scale displayed in TWTT and 5 ns corresponds to about 0.35 m, thus the bottom time slice represents ~0.7 m depth.

Full-resolution 3-D processing (see Glossary) which included 3-D migration (see Glossary) was, however, demonstrated by Novo *et al.* (2008) who attempted to enhance the resolution of their time slices by collecting lines every 5 cm and traces every 2.5 cm, and processing it in

3-D. The method was also applied by Böniger and Tronicke (2010) to a dataset collected in difficult ground conditions, *i.e.* an uneven ground surface which was densely overgrown with trees.

3-D GPR data was also applied to analyse structural properties of quarried rocks. Examples of such works include that by Grandjean and Gourry (1996) who used 300 and 900 MHz antennae to collect 1.0 and 2.0 m spaced 2-D lines, respectively, to map fractures within a marble quarry. 2-D profiles were processed with Seismic Unix, displayed together as 2-D profiles in CAD software which also was used for interpolation and tracing of the distribution of the fractures. A pseudo 3-D GPR data (100 MHz antenna, 0.1 x 0.2 m distances between stations and lines) collected to investigate the geometrical patterns of fractures within a limestone quarry by Grasmueck *et al.* (2005) was, however, processed in 3-D. The authors focused on application of time slices and reported that 2-D migration combined with half wavelength distance between survey points did not display some of the fractures. McClymont *et al.* (2010) used very extensive pseudo 3-D GPR datasets to image Alpine fault zones in New Zealand. The fault surfaces were displayed with time slices, fence diagrams and horizon surfaces (explained in Section 4.2).

Plan views available from time slices also provided an opportunity to study cryogenic structures (Munroe *et al.* 2007, shown in Figure 2.2.3; and Doolittle and Nelson 2009). 2-D processing and GPR specific software was here sufficient to display the structures in 3-D.

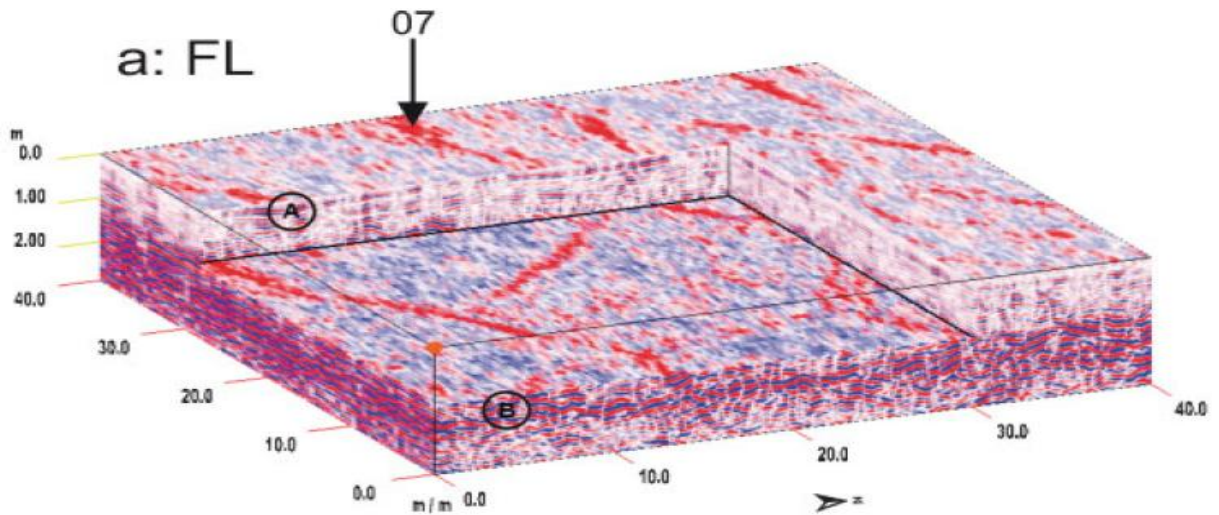


Fig. 2.2.3 Pseudo 3-D dataset (0.50 m line spacing, step not specified) collected with 400 MHz antenna, 2-D processed and displayed with 3D QuickDraw for RADAN by Munroe *et al.* (2007) to investigate cryogenic features in Alaska.

The first 3-D survey in sedimentology was presented by Beres *et al.* (1995, 1999) who applied it to study fluvial depositional architecture for aquifer characterisation (further described in Section 2.4). Shortly after that, Sigurdsson and Overgaard (1998) used true 3-D datasets to investigate marine carbonate deposits for planning selective mining in a limestone quarry on Zealand island, Denmark (presented in Figure 2.2.4). Another pseudo 3-D grid of GPR lines was applied by Pringle *et al.* (2004) to investigate the Carboniferous turbidity channels in the the Peak District National Park, UK as a hydrocarbon reservoir analogue. While both Sigurdsson and Overgaard (1998) and Pringle *et al.* (2004) processed individual profiles and displayed them with seismic interpretation software, Beres *et al.* (1995, 1999) used 3-D processing. The GPR images were also correlated with information known from outcrops or boreholes.

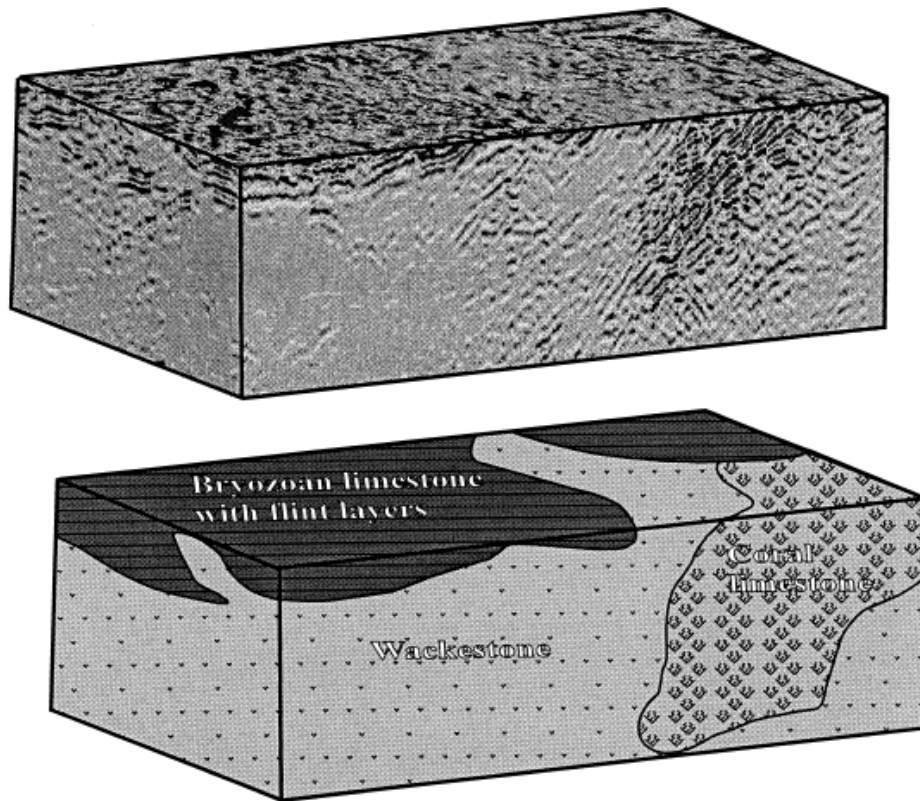


Fig. 2.2.4 Pseudo 3-D dataset (1.0 m line spacing, 0.20 m step) collected with 100 MHz antenna, 2-D processed and displayed with Slicer from Spyglass by Sigurdsson and Overgaard (1998) to carbonate formation in a limestone quarry on the island of Zealand, Denmark (vertical scale not included, the width of the volume is ~45 m and length ~70 m).

### 2.3 APPLICATION OF 2-D GPR DATA IN FLUVIAL SEDIMENTOLOGY

As the old qualitative fluvial sedimentary models which were based on 1-D and limited 2-D information were criticised for being unreliable, a new methodology was required for the quantitative characterisation of the distribution of sedimentary facies. Such detailed information could not be provided by borehole data, shallow trenches or spatially limited outcrops, although it could be provided by GPR data as was first demonstrated by Beres and Heani (1991) who applied it to investigate hydrogeological properties of glaciofluvial and glaciolacustrine deposit. Based on the geometry of reflection lines, they adapted principles of seismic interpretation to identify radar facies on 2-D GPR profiles which they referred as reflection facies. These patterns were compared with similar seismic facies from the literature in order to interpret them as lithological units. Their classification of geometrical patterns

(Figure 2.3.1) was based on the arrangement of reflections as viewed on individual 2-D profiles without any reference to information about their character when displayed on perpendicularly oriented lines.

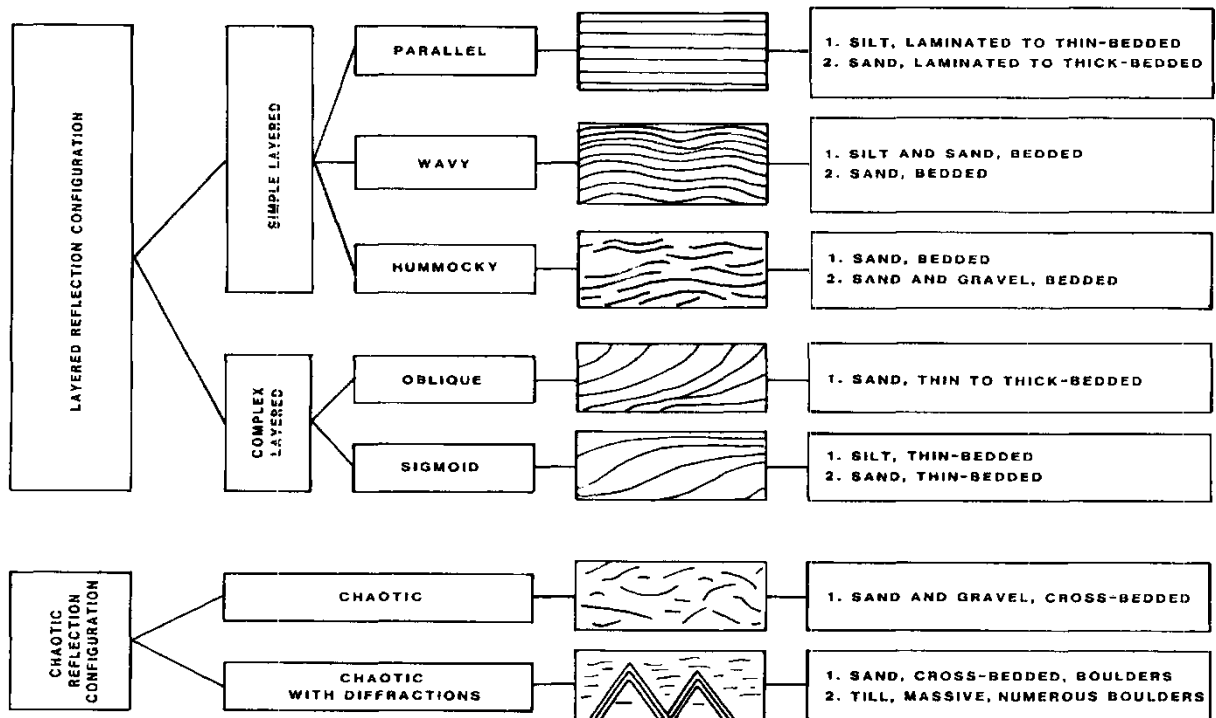


Fig. 2.3.1 Classification of the reflection facies, which were correlated with lithology known from exposures, adopted from seismic interpretation by Beres and Heani (1991).

A very similar classification of radar facies was later adopted by Gawthorpe *et al.* (1993) and Huggenburger (1993, Figure 2.3.2). The latter defined radar facies as three-dimensional units and the interpretation was based on patterns known from two orthogonal 2-D GPR profiles, *i.e.* lines parallel to and perpendicular to the paleoflow. However, the different appearance of the same facies when viewed on orthogonal profiles was not taken into account. The radar facies were compared with observations of lithology carried out in gravel pit exposures in order to establish the distribution of hydraulic properties within the glaciofluvial deposits. Correlation of lithology was, however, mixed with environmental interpretation.

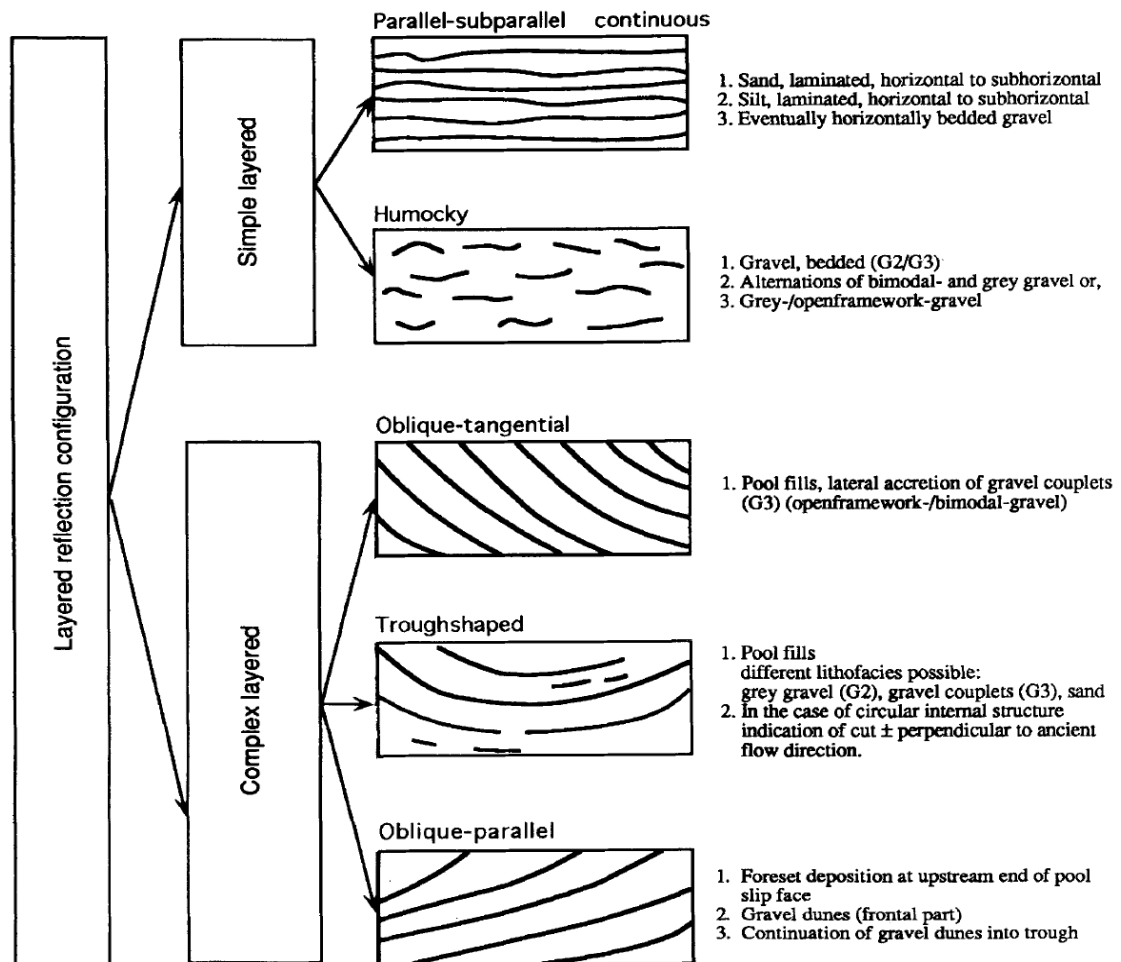


Fig. 2.3.2 Classification of radar facies and interpretation of the lithology/depositional environments given by Huggenberger (1993).

Gawthorpe *et al.* (1993) collected an irregular grid of GPR lines from a point bar (see Glossary) of the Madison River, Montana USA to investigate it as a hydrocarbon reservoir analogue. Interpretation of the reflection profiles was carried out on individual 2-D GPR lines, although the radar sequence boundary was displayed as a 3-D diagram (Figure 2.3.3). The work emphasised the importance of the character of termination of individual reflections for identifying radar sequence boundaries; and the principles of seismic interpretation were explained in the context of the GPR method (further explained in Chapter 4).

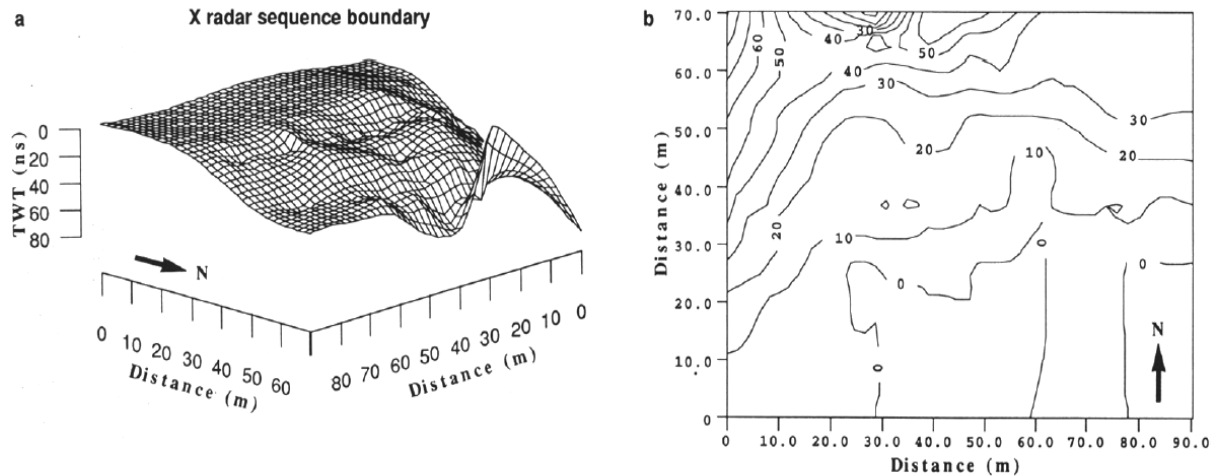


Figure 2.3.3 Left image presents 3-D display of the radar sequence boundary presented by Gawthorpe *et al.* (1993). The right image presents the radar sequence boundary displayed as a contour map.

The methodology established at the beginning of the 1990s by Beres and Heani (1991), Huggenberger (1993) and Gawthorpe *et al.* (1993) was followed by numerous studies which used 2-D GPR surveys. Some authors (*e.g.* Fisher *et al.* 1992a, b) focused more on technical aspects of GPR data acquisition and processing, while other works demonstrated that the 2-D GPR method could address the requirement for the accurate description of architectural elements. Individual GPR profiles could image both internal and external geometrical patterns associated with depositional forms. Such information could be correlated with the textural character of deposits known from boreholes and excavations. As was presented by Gawthorpe (1993) the boundaries of the facies could be interpolated between profiles in order to determine their 3-D character.

The second half of the 1990s witnessed a growth in GPR use, as demonstrated by the studies of Stephens (1994), Bridge *et al.* (1995, 1998), Wyatt and Temples (1996), Roberts *et al.* (1997), Leclerc (1997), Bristow (1999), Vandenberghe and van Overmeeren (1999) or Augustinus and Nichol (1999). For hydrogeological purposes, similar work was carried out by Naegeli *et al.* (1996), Birkhead *et al.* (1996), Poole *et al.* (1997), Asprien and Aigner (1997) and van Overmeeren (1997). Studies of hydrocarbon reservoir analogues were carried out on

sedimentary rocks by Aigner *et al.* (1996) and investigation of sedimentary facies to evaluate aggregate resources was completed by Fisher *et al.* (1996).

Later fluvial sedimentary works generally applied two different approaches to collecting, displaying and interpreting 2-D GPR data. The first one, represented by works of Bridge *et al.* (1998), Bristow *et al.* (2000), Best *et al.* (2003), Sambrook Smith *et al.* (2006, 2009) or Mumpy *et al.* (2007) used long individual lines collected over extensive contemporary depositional forms, most often braid bars. 2-D GPR profiles were very often displayed as fence diagrams presenting the distribution of sedimentary facies within the depositional forms. The second group, which include works by Skelly *et al.* (2003), Bowling *et al.* (2005) or Kostic and Aigner (2007) aimed to create 3-D models based on grids of closer spaced GPR profiles, and focused on internal patterns within sedimentary facies and spatial relations between them. Interpretation was still carried out on individual 2-D profiles, however, the 3-D appearances of facies was often emphasised and presented as 3-D models. This method was most often applied to smaller sites and aimed to investigate the distribution of hydraulic properties of aquifers and hydrocarbon reservoirs.

The first group mentioned above collected increasingly large datasets, with survey lines perpendicular and parallel to the flow from braided rivers, and correlated them with trench observations and vibro-cores. Examples of such works include the one by Best *et al.* (2003) who investigated a 3 km long and 1 km wide sandy mid-channel bar in the Brahmaputra River, Bangladesh. The interpreted sedimentary facies were displayed on fence diagrams and shown in reference to their location within the braid bar. Vertical profiles presenting vertical sequences of sedimentary facies within certain parts of the braid bar were also included (see Figure 2.3.4).

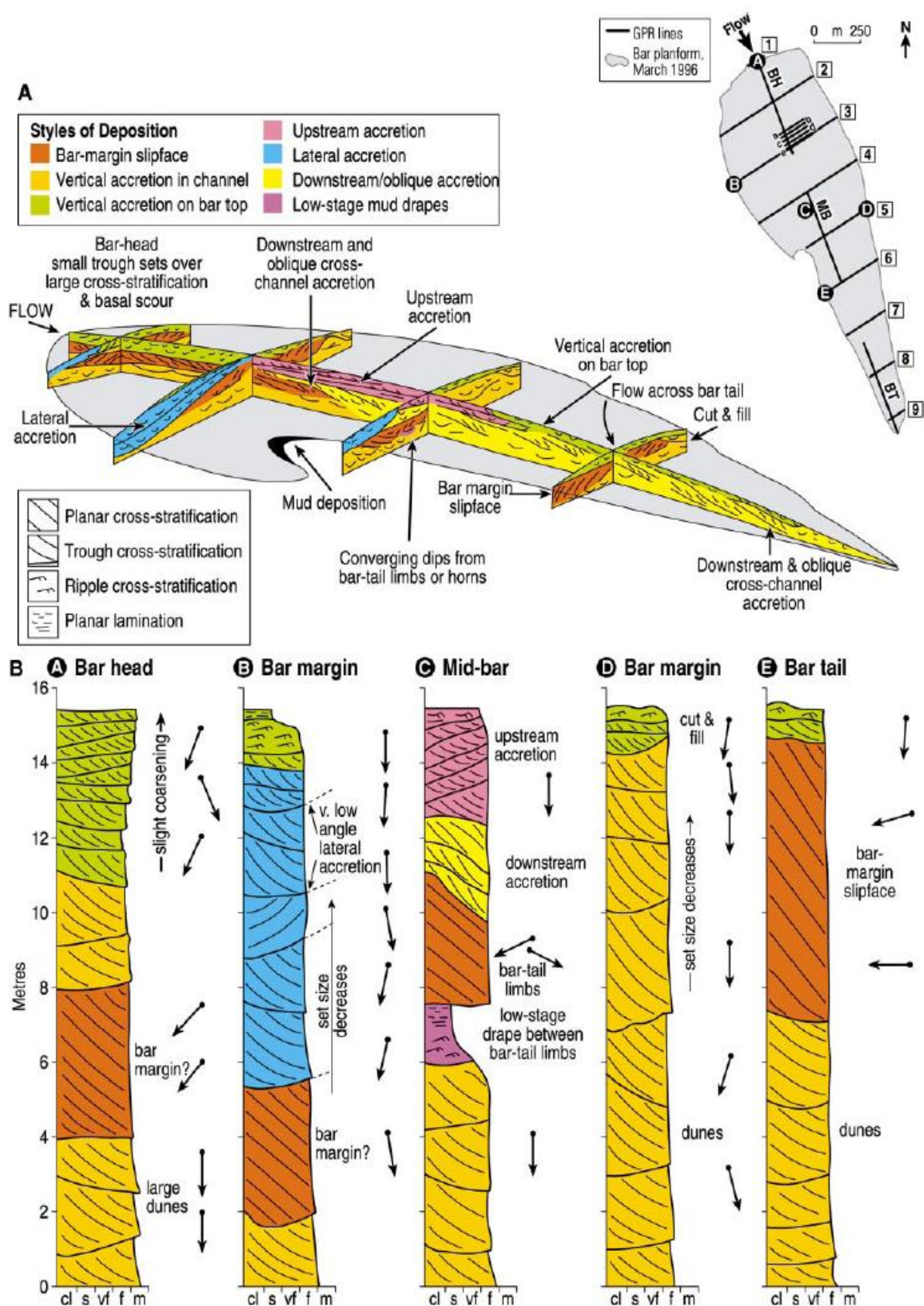


Fig. 2.3.4 Presentation of the sedimentary architecture combined with an interpretation of the depositional styles of a sandy unit bar in the Jamuna River (Best *et al.* 2003). The environmental interpretation of the structures was indicated with colours.

Another example is the work presented by Sambrook Smith *et al.* (2006b), who reviewed the earlier qualitative model for sandy braided rivers by Cant and Walker (1978) and collected ~3.5 km of GPR profiles in the same area of the South Saskatchewan River where the Cant and Walker model was originally derived. These profiles were correlated with trench observations, vibro-coring, topographical survey and aerial photographs. This led to identification of the following four radar facies linked with depositional facies: (1) high-angle inclined reflections associated with migration of bar margins, (2) discontinued undular or trough-shaped reflections associated with sinuous-crested dunes, (3) low-angle reflections associated with migration of low-amplitude dunes or unit bars, (4) concave reflections with inclined reflections of variable dip associated with channel fills. The facies distribution across compound bars was again displayed in fence diagrams (Figure 2.3.5) and their relative proportion was assessed quantitatively. Two of the 3-D datasets presented in this thesis were collected from this river, thus the radar facies classification presented in this thesis is consistent with that described above.

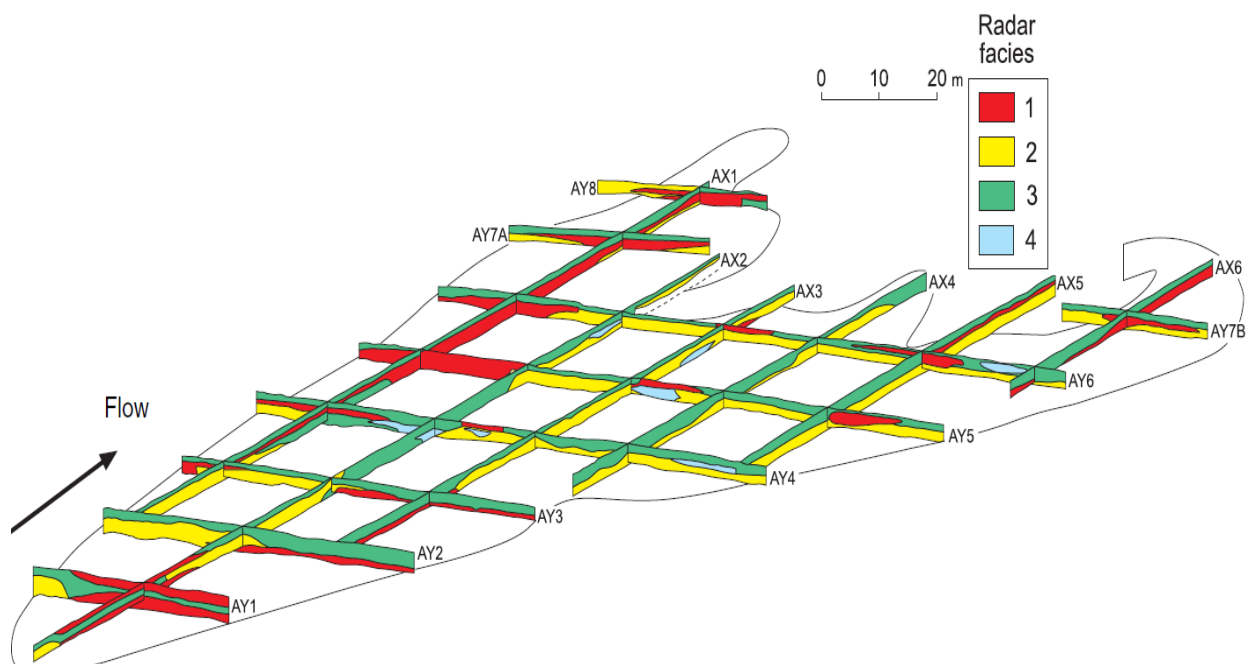


Fig. 2.3.5 Distribution of radar facies within a compound bar in the South Saskatchewan River based on 200 MHz GPR data by Sambrook Smith *et al.* (2006b). Numbers indicate radar facies (1) high-angle inclined reflections associated with migration of bar margins, (2) discontinued undular or trough-shaped reflections associated with sinuous-crested dunes, (3) low-angle reflections associated with migration of low-amplitude dunes or unit bars, (4) concave reflections with inclined reflections of variable dip associated with channel fills.

Results of the work by Mumpy *et al.* (2007) from the sandy braided Wisconsin River, Sambrook Smith *et al.* (2009) from the Rio Parana and Hickin *et al.* (2009) from the wandering gravel-bed Halfway River were presented in a very similar way. Sambrook Smith *et al.* (2009) noted that interpretation of radar facies (4) (consistent with radar facies (4) described in Chapters 4 and 5 in this thesis), represented by inclined reflections enclosed by concave upwards surface, was uncertain due to only 2-D information available from GPR profiles. The authors concluded that they could be interpreted as bartop hollows, cross-bar channels fills or scour holes (see Glossary) around logs.

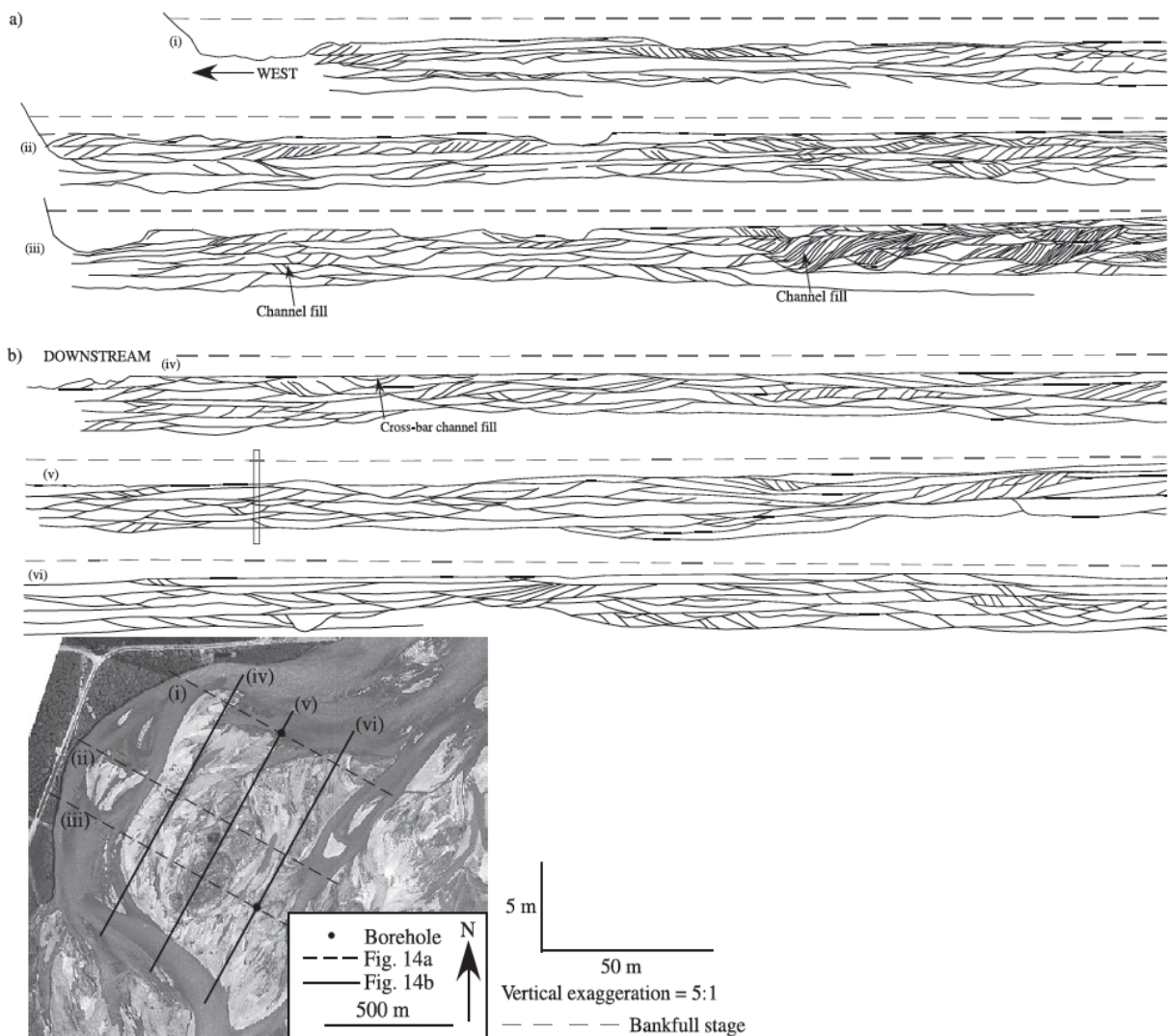


Fig. 2.3.6 Correlation of sedimentary facies recorded on individual GPR profiles collected in the Sagavanirktok River presented by Lunt *et al.* (2004). Location of the profiles is presented in the aerial photo (bottom image).

Although fence diagrams proved to be useful for presenting spatial distribution of

sedimentary facies, some authors such as Bridge *et al.* (1998) or Lunt *et al.* (2004) still preferred to display individually adjacent cross-sections, which were based on GPR profiles. Here due to the large distances between the individual lines, correlation was sometimes difficult. Lunt *et al.* (2004) used a widely spaced (50 and 100 m distances between lines) grid of 2-D GPR profiles (100, 250 and 450 MHz antennae) to investigate coarse-grained deposits of the braided Sagavanirktok River in northern Alaska (Figure 2.3.6). The GPR data were correlated with information from trenches, boreholes, wire-logging, common mid-point (CMP) surveys (explained in Section 3.1) and permeability tests.

The second group of fluvial sedimentary works which used GPR data collected grids of relatively closely spaced lines. This approach was applied both to modern and ancient, braided and meandering river deposits possibly because it could address the alternating nature of meandering river flow and smaller sizes of depositional forms. The only purely sedimentological work in this group was the one by Skelly *et al.* (2003) who documented the three-dimensional sedimentary architecture of the sandy braided Niobrara River which aggraded in response to base level change. In this work, a grid of vibro-cores was used together with a GPR grid of lines with 2.0 m distance between them. The lines were located approximately perpendicular and parallel to the direction of the river flow and the 2-D surveys were used to create a 3-D model of sedimentary facies. The authors identified common large scale high-angle clinoforms which filled topographic depressions. As the orientation to the paleoflow responsible for their deposition was assumed to be the same as during the survey, this facies was interpreted as 'cross-channel accretion' (see Figure 2.3.7). Similar facies in later works (*e.g.* Sambrook Smith 2006) were typically interpreted as downstream accretion on bar margins.

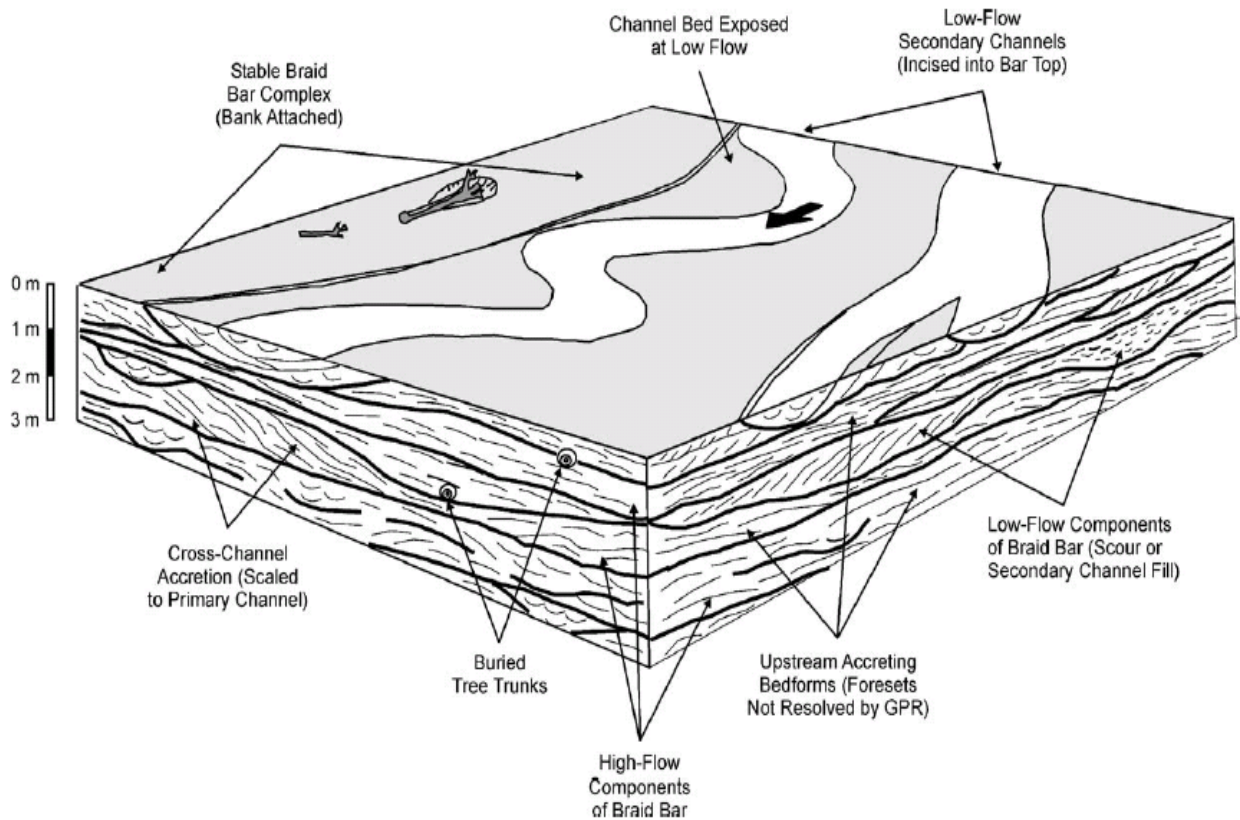


Fig. 2.3.7 Three-dimensional model of the sedimentary architecture of the Niobrara River. The continuous black lines indicate radar sequence boundaries, which separate radar sequences corresponding with macroform units. The model is based on 2-D GPR lines approximately perpendicular and parallel to the flow direction (from Skelly *et al.* 2003). Note that the interpretation of facies is uncertain due to unknown paleoflow (*e.g.* cross-channel accretion) responsible for their deposition. Lateral scale not available, although based on the profiles included in the article, the width of both of the orthogonal profiles is approximately 100 m.

The data was again interpreted according to the principles of sequence stratigraphy. Radar facies were identified based on reflection patterns, and radar sequence boundaries were based on the types of termination of reflection lines, *e.g.* toplap, onlap, downlap. Radar sequence boundaries indicated periods when there had been a break in deposition. A similar 3-D model of sedimentary facies, which was based on a grid of 2-D GPR profiles, was presented by Bowling *et al.* (2005) to predict the heterogeneity of an aquifer at the research site at Columbus Air Force Base in Mississippi. The GPR profiles were collected with 50 MHz antenna and 2.0 m distance between lines, and combined with resistivity surveys.

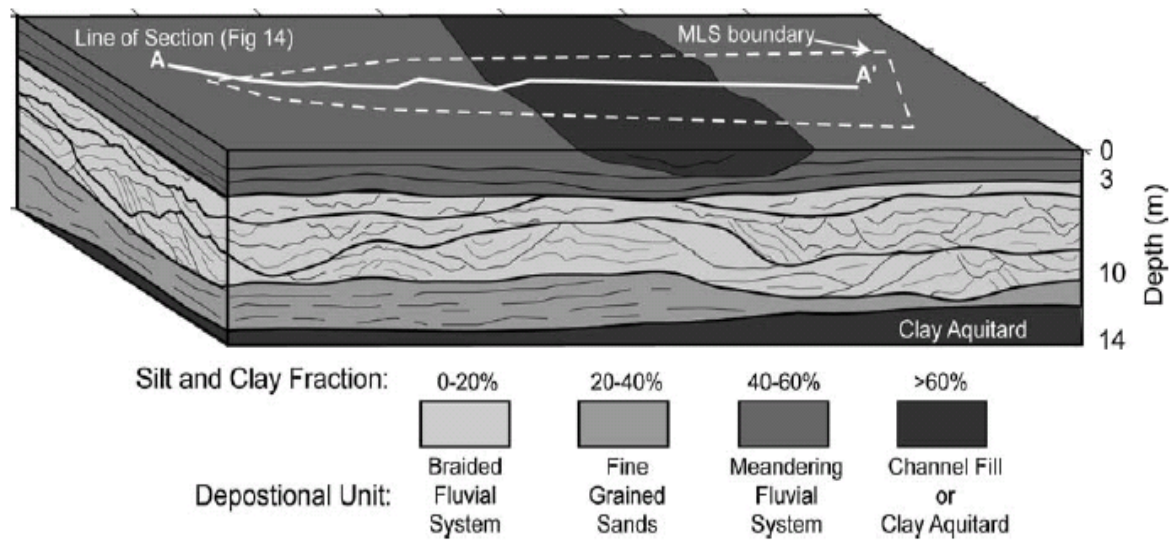


Fig. 2.3.8 The 3-D model of sedimentary facies by Bowling *et al.* (2005) was based on closely spaced grid of 2-D GPR data, resistivity survey and core information. The continuous black lines indicate radar sequence boundaries (horizontal scale not included).

The surfaces were also shown in 3-D diagrams (Figure 2.3.8). Individual profiles were interpreted in terms of radar bounding surfaces of four orders and identified two main depositional styles: meandering underlain by braided. The clay and silt content was estimated based on resistivity surveys and related to hydraulic properties of the sedimentary facies. 3-D presentation of radar facies of meandering and braided river deposits by Kostic and Aigner (2007) covered a larger area with 100 to 250 m long 2-D GPR profiles collected with 5 or 10 m distances between lines. Although the interpretation was carried out on 2-D profiles, some of the reflections were interpolated between lines and displayed in a table as the main 3-D surfaces (Figure 2.3.9). The geometrical patterns were correlated with information from exposures, interpreted as depositional forms together with their hydrogeological properties.

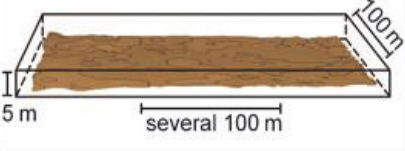
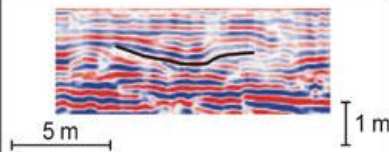
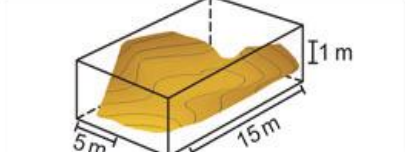
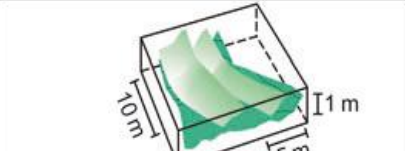
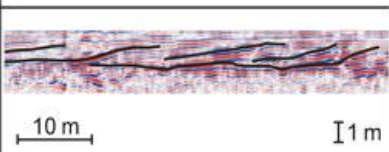
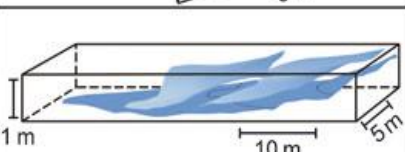
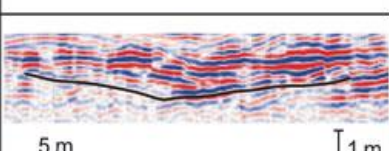
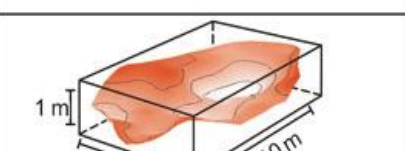
2D GPR pattern	3D GPR elements	Sedimentological GPR interpretation → hydrogeological implication
		<b>Floodplain element</b> Massive F-m with local fGcm channel fills → Highly extensive (100 s m-km), sheets of very low permeability
		<b>Chute channel</b> Massive or steeply inclined, often deformed fGcm-fGmm layers → Elongated channels of low permeability
		<b>Gravel dune</b> Steeply inclined Gcg,a cross-beds (dominated by Gcg,o) → Small-scale (dm) alteration of moderately and highly permeable sheets
		<b>Lateral accretion element</b> Low-inclined sheets of Gcm,(i), Gcg,o, S-x; basal gravel lag (cGcm) common → Extensive (m-10 's m), Highly permeable sheets embedded in moderately permeable sheets
		<b>Confluence scour fill</b> Trough-shaped cross-beds of Gcg,a and Gcm (rich in fine matrix) → Small-scale (dm-m) variation of low and high permeability trough-shaped units

Fig. 2.3.9 Table presenting reflection patterns on 2-D GPR profiles (200 MHz) with sedimentological and hydrogeological interpretation of deposits from the Neckar Valley by Kostic and Aigner (2007). The 3-D display of surfaces was done with GOCAD software.

## 2.4 APPLICATION OF PSEUDO 3-D GPR DATA IN FLUVIAL SEDIMENTOLOGY

The previous section identified the two main approaches to collecting and analysing 2-D GPR data in fluvial sedimentology. The first group attempted to present the spatial distribution of sedimentary facies from contemporary, most often braided, river deposits. The second group imaged both meandering and braided river deposits. With an exception for the work by Skelly (2003), all of these publications applied grids of closely spaced GPR profiles to study the distribution of hydraulic properties. These works were very similar to another approach which used datasets displayed in 3-D to investigate the hydraulic properties of gravelly deposits.

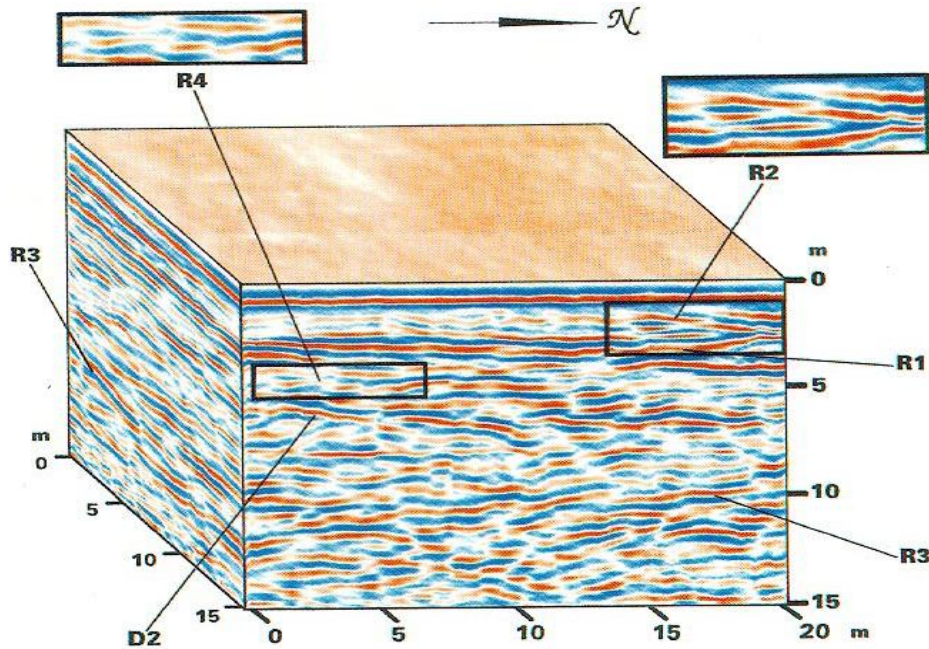


Fig. 2.4.1 The first published pseudo 3-D GPR volume (100 MHz with 0.50 m line spacing), 3-D processed and display with seismic software, showing glaciofluvial river deposits in the Rhine valley, presented by Beres *et al.* (1995): R1 – subhorizontal reflections from base of scour pool (see Glossary), R2 – reflections from pool-fill sediments inclined to the north, R3 – groundwater table, R4 – sand lens, D2 – diffraction hyperbola.

There were only several such works, and they involved collecting datasets with distances between the survey lines ranging from 0.20 m (Peretti *et al.* 1999) to 1.00 m (Asprion and Aigner 1999, Aigner 2003) with a step of between 0.10 m to 0.25 m. These surveys typically covered areas of a few hundreds of m<sup>2</sup> and the individual GPR profiles were also usually correlated with information about sedimentary texture and structure known from exposures.

Only Beres *et al.* (1995, 1999) applied full 3-D processing although in some cases 3-D migration was not used as it resulted in unclear images and only unmigrated data was presented (Figure 2.4.1). Other authors (Asprion and Aigner 1999, Aigner 2003) used limited 2-D processing, while Peretti *et al.* (1999) stated that 2-D migration distorted the images and presented unmigrated data (Figure 2.4.2). The display with seismic interpretation software allowed viewing spatial arrangement of the surfaces; however, the radar facies and radar surfaces were displayed separately. Beres *et al.* (1995, 1999) used Landmark/ITA seismic processing and interpretation software for displaying the 3-D volumes. The main radar facies

were interpreted as depositional forms, although radar surfaces were not shown. Heinz and Aigner (2003) displayed pseudo 3-D volumes with Slicer Dicer 3-D display software, while the radar surfaces were created and displayed with the GOCAD seismic interpretation package (Figure 2.4.3). Asprion and Aigner (1999) and Peretti *et al.* (1999) did not specify which 3-D display software they used. These works used time slices to present sedimentary structures associated with depositional element such as scour fills or foresets (Figure 2.4.4). All of the datasets displayed in 3-D were applied to gravelly deposits thus due to the scale of depositional forms these 3-D images had a limited size and resolution (see Figures 4.2.1 to 4.2.4).

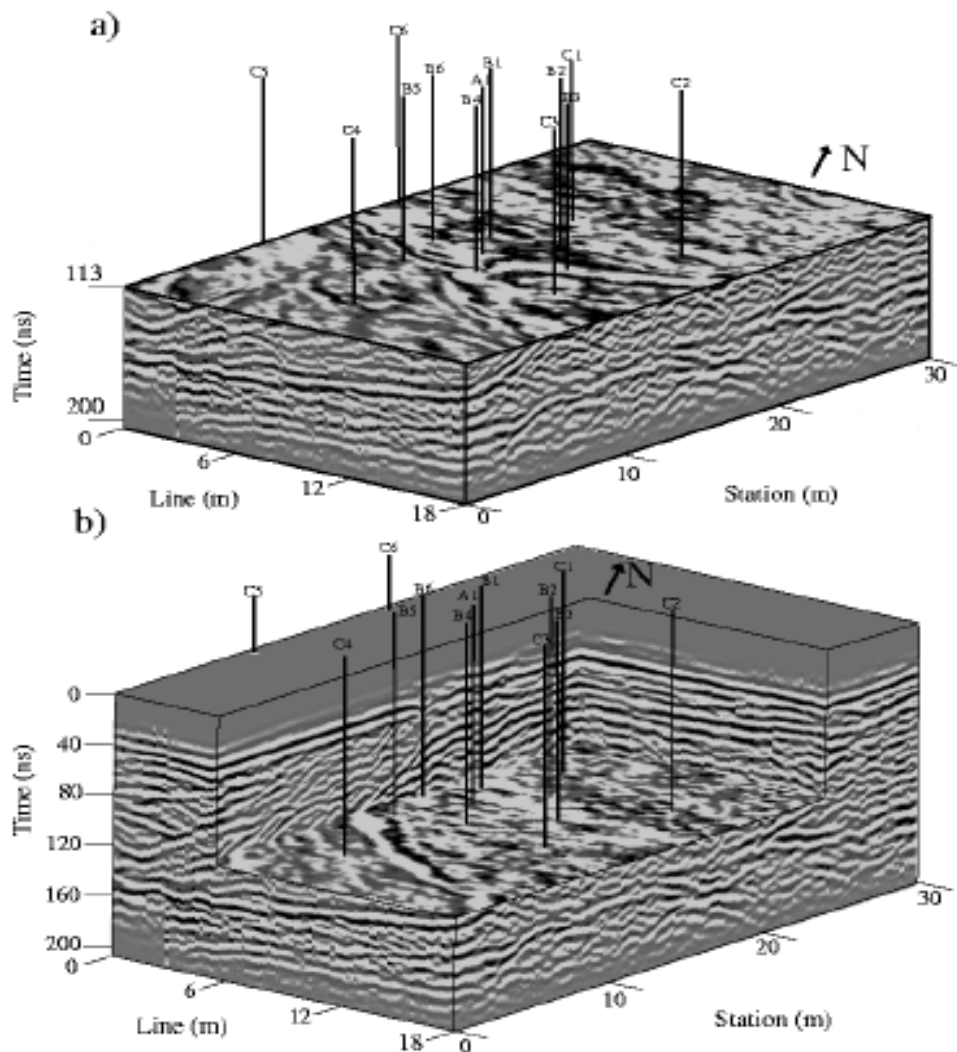


Fig. 2.4.2 Pseudo 3-D volume (0.10 x 0.20 m cell dimensions) of 200 MHz data with time slices at 113 ns (above) and chair diagram (display software not specified) showing shallow alluvial deposits in the Boise River valley, Idaho, by Peretti *et al.* (1999). Borehole data was used to predict the hydraulic properties of facies identified with GPR 3-D volumes.

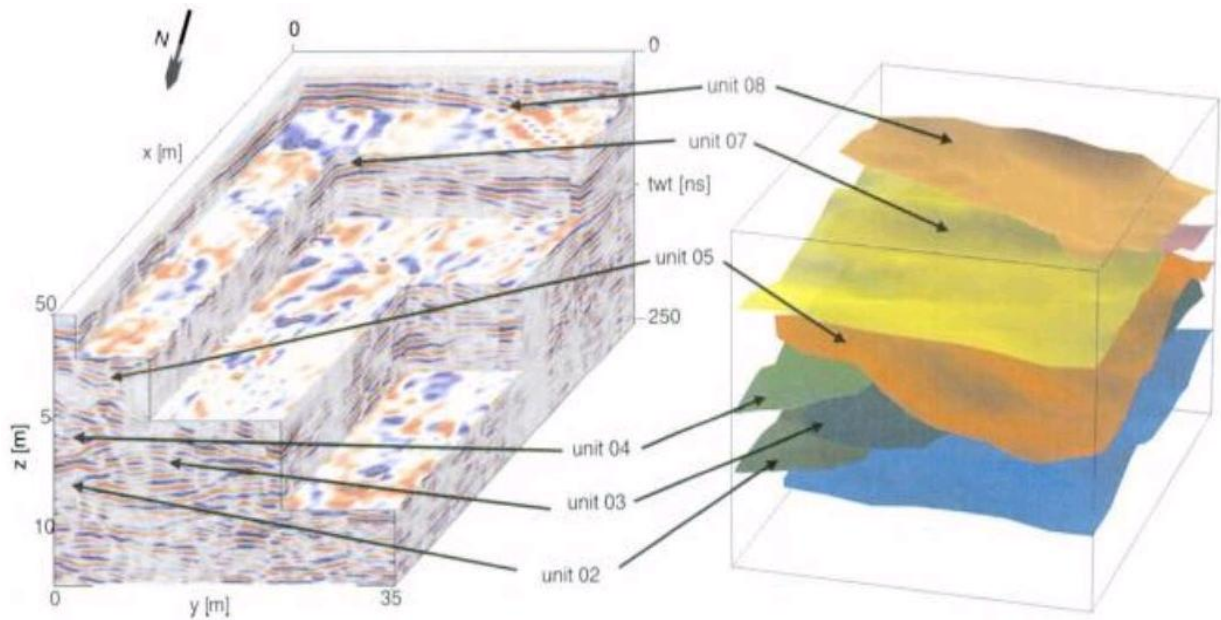


Fig. 2.4.3 Chair diagram of pseudo 3-D data (300 MHz) with 1.0 m line spacing presented with Slicer Dicer software (left) by Heinz and Aigner (2003) with a 3-D GOCAD display of lower boundaries of depositional elements, *i.e.* gravel bodies (right). Despite its 3-D character it is difficult to interpret the sedimentary architecture of imaged deposits.

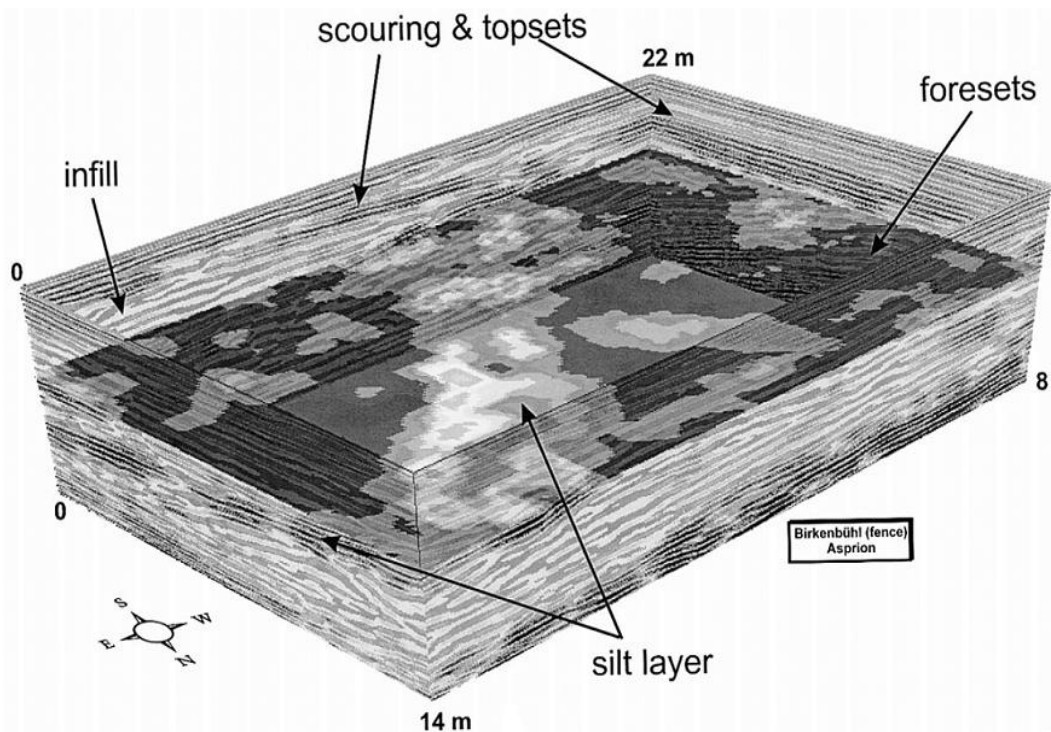


Fig. 2.4.4 Chair diagrams presenting pseudo 3-D data volumes (300 MHz) of glaciolacustrine delta and glaciofluvial sediments in the Singen Basin in SW Germany by Asprion and Aigner (1999).

Beres *et al.* (1995) emphasised that use of the 3-D datasets should significantly improve understanding of the sedimentary architecture and recommended adapting concepts of radar facies to include their 3-D nature. In their publication (Beres *et al.* 1999, see Figure 2.4.5)

time slices and vertical profiles were used for classification of radar facies, although it followed the one by Huggenberger (1993). Thus the classification did not take into account different appearance of facies on orthogonal profiles. The author stated that trends of changes of paleoflow directions, which were revealed by time-slices, could not be resolved by individual 2-D profiles.

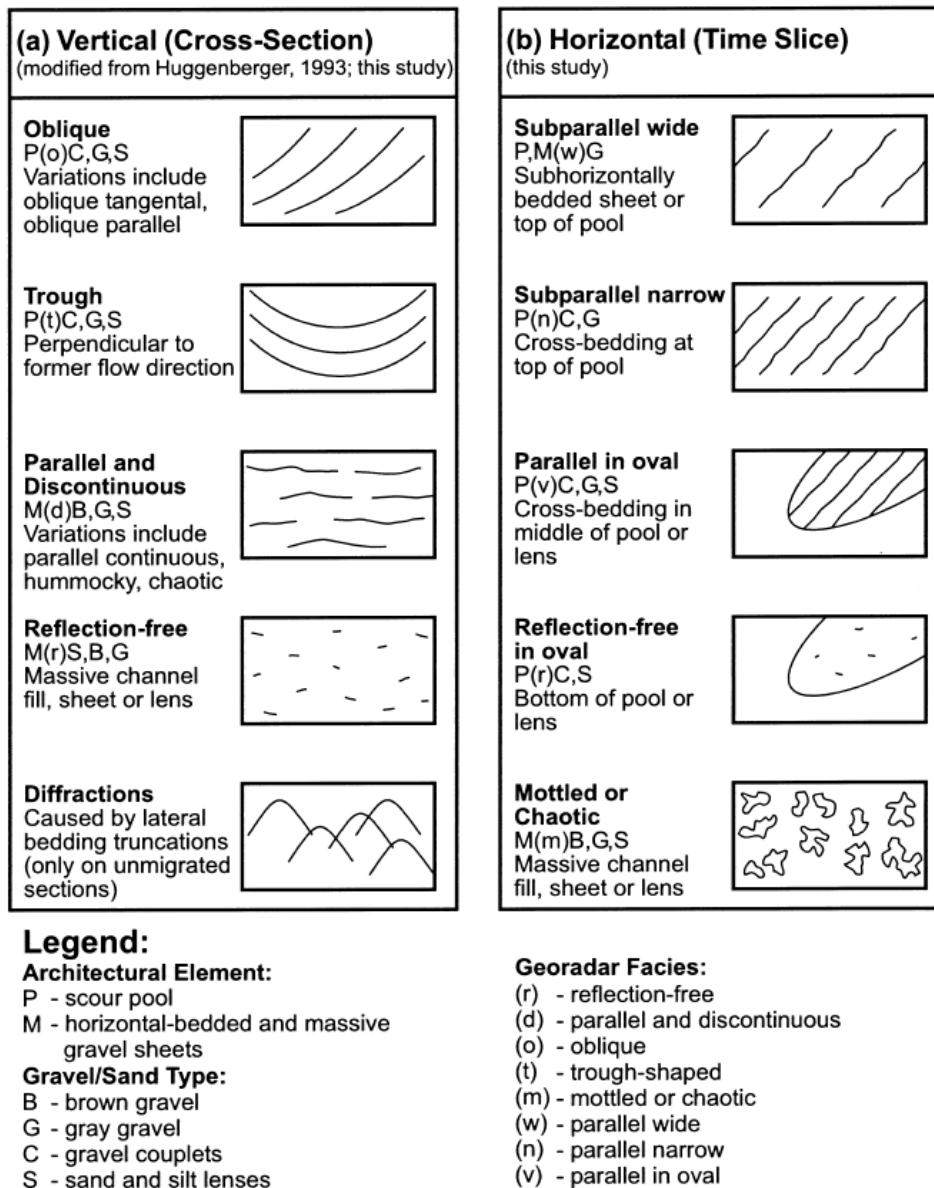


Fig. 2.4.5 Classification of radar facies based on their appearance on vertical profiles and time slices by Beres *et al.* (1999). Classification of patterns on vertical profiles was modified from Huggenberger (1993).

Work by Beres *et al.* (1997, 1999) was later criticised for inaccurate environmental interpretation (Bridge 2009) as identified radar patterns were not considered in relation to

their true appearance in 3-D and the same radar facies was interpreted as a number of facies due to the changing orientation of the paleoflow and viewing the same structure but differently oriented.

## 2.5 TRUE 3-D GPR SURVEYS IN FLUVIAL SEDIMENTOLOGY

Three publications, which presented the application of true 3-D GPR datasets to investigate the sedimentary architecture of fluvial deposits, were all applied to study the hydraulic properties of the Ferron Sandstone Formation, Utah, as an analogue of a clastic fluvial and deltaic sandstone hydrocarbon reservoir. The first one was published by McMechan *et al.* (1997) who undertook two 100 MHz surveys, 15 x 15 m and 25 x 25 m grids, with equal line and station spacings of 0.25 and 0.50 m respectively (Figure 2.5.1). The study correlated geophysical and outcrop data. Processing was done on individual 2-D profiles which were later compiled into 3-D volumes.

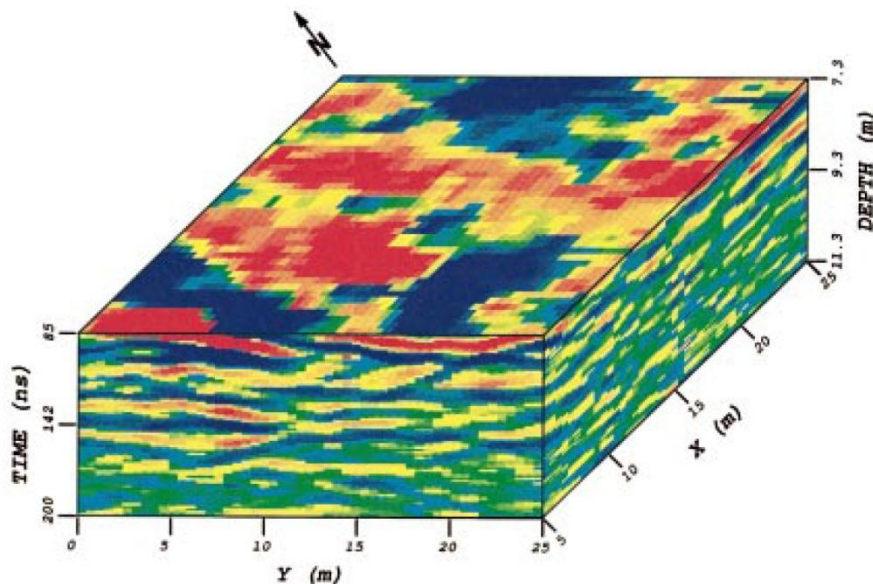


Fig. 2.5.1 True 3-D volume (0.50 x 0.50 m cell dimensions) of 100 MHz GPR data collected from the Ferron Sandstone Formation, Utah, with time slices presenting the distributary channel to the mouth bar (McMechan *et al.* 1997).

The study of the distribution of fluid permeability and fluid flow within the fluvial Ferron

Sandstone in east-central Utah was continued by Szerbiak *et al.* (2001) and Corbeanu *et al.* (2002). True 3-D GPR data of dimensions 40.0 x 16.5 m consisted of lines collected with 50, 100 and 200 MHz antennae and with 0.50 m spacing between lines and stations. The 3-D GPR data were correlated with borehole logs and permeability measurements undertaken *in situ* and on core samples. Full 3-D processing of data included 3-D Kirchhoff migration and 3-D velocity analysis. The results enabled presentation of the volume of the 3-D distribution of permeability (Figure 2.5.2). Due to the size of antenna used the resolution of the volumes is also low and their sedimentary interpretation appears to be difficult.

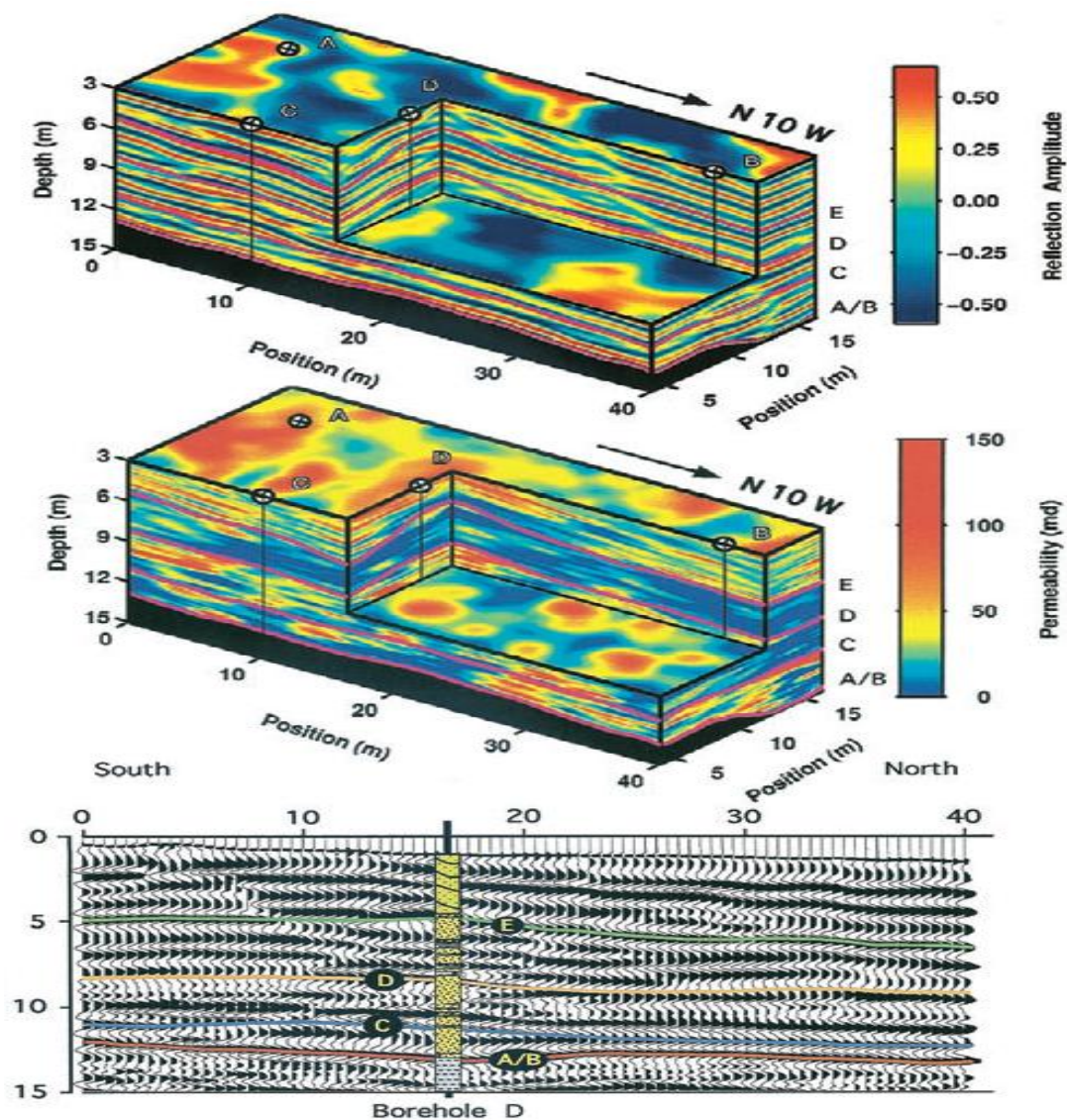


Fig. 2.5.2 Top: chair diagram of true 3-D amplitude volume (100 MHz, 0.5 x 0.5 m trace spacing) from the Ferron Sandstone Formation, Utah, presented by Szerbiak *et al.* (2001). Middle: 3-D display of fluid permeability based on correlation of GPR data with borehole data. Bottom: 2-D profile correlated with a borehole log.

## 2.6 SUMMARY

As in other fields of science and engineering, there have also been many GPR-based works in fluvial sedimentology. The early GPR users (*e.g.* Gawthorpe *et al.* 1993) emphasised that the GPR technique finally enabled interpretation of profiles in accordance with sequence stratigraphy and managed to overcome the limitations of traditional methods. This led to the development of radar stratigraphy, strengthened the methodology of analysis of sedimentary architecture introduced in the 1980s, and improved the understanding of fluvial formative processes. GPR based research revealed that fluvial architecture has a far more complex character than previously thought. Such conclusions about the architecture of meandering river deposits were made by Bridge *et al.* (1995), whose work revealed the presence of unit bars and different characters of the lower and upper point bar deposits. As concluded by Sambrook Smith *et al.* (2006b), sedimentary architecture of braid bars is also more complex than described by the earlier researchers. Planform shape of channel bars is common to rivers of different scales, however, the arrangement of facies in analysed rivers and even in braid bars within the same river were unique (Sambrook Smith *et al.* 2005). Bridge and Lunt (2006) stated that there is still not enough information to create reliable predictive models for braided rivers. Analysing such complex architecture still requires better tools with which to capture its character without the need for interpolation and inferring spatial relations from 2-D information.

The majority of authors (*e.g.* Gawthorpe *et al.* 1993, Lunt *et al.* 2004, Bridge 2009) have emphasised that fluvial sedimentary architecture has a strongly three-dimensional character. Despite that, radar facies were classified according to their appearance on individual profiles, and even 3-D classification of radar facies by Beres *et al.* (1999) did not take into account the different appearance of the same radar facies when viewed on orthogonally oriented profiles.

As has been shown in this chapter, research which applied GPR data to fluvial deposits could be divided into studies which used widely spaced hundreds of meters long GPR lines to investigate sedimentary architecture of extensive depositional forms and those which focused on smaller areas by applying closely spaced grids of lines sometimes displayed in 3-D. The first group mainly aimed to build quantitative sedimentary models of braided river deposits, while the second tried to investigate the spatial distribution of hydraulic properties associated with deposits of both meandering and braided rivers. Although grids of data were collected in this group, the lack of 3-D display and particularly time-slices resulted in uncertain estimates of the direction of paleoflow responsible for depositional forms leading to uncertain conclusions about depositional processes. The authors who used seismic visualisation techniques (*e.g.* Beres *et al.* 1999) emphasised that only time slices could accurately resolve the paleocurrent directions and help to accurately image sedimentary architecture. In fluvial sedimentology, there have only been several of such studies, and they were applied to investigate the architecture of coarse grained deposits. There have also been few works which used 3-D GPR datasets to investigate architecture associated with other sedimentary environments. Such works include the study of a turbidity channel presented by Pringle *et al.* (2004) and that of deltaic deposits by Lee *et al.* (2007); and these studies were also undertaken to investigate the hydraulic properties of the clastic reservoir analogues.

3-D GPR data has been widely used in archaeology and engineering, *i.e.* fields where detailed investigation of a limited size area is sufficient. This would suggest that one of the reasons for the rare application of 3-D methods in fluvial sedimentology is that collecting and displaying 3-D GPR datasets is time consuming and technically challenging. Thus collecting high resolution 3-D data over large depositional forms could not provide sufficient spatial coverage. Conversely, collecting 2-D GPR data is rapid and useful when large areas, such as

for compound bars in large braided rivers, where it is easier to predict the paleocurrent direction.

The discussion above provides the context and rationale for the work presented in this thesis. Thus while fully 3-D methods are available and have been used in a wide range of disciplines they are not well suited to the larger spatial dimensions of fluvial studies and typically require greater levels of expertise than most users possess. Hence despite a wide acknowledgement that alluvial architecture is inherently 3-D, fluvial sedimentologists have been relatively slow to adopt 3-D methods within radar studies. To bridge this gap the following chapters of this thesis will present a hybrid method where 2-D data is visualised in 3-D, so providing a technique that is easy to use and more suited to larger survey areas.

Although several workers (*e.g.* Peretti *et al.* 1999, Heinz and Aigner 2003) have used a similar approach to that which is demonstrated in this thesis they do have a number of limitations; 1) they were illustrated with only limited examples of 3-D interpretation, 2) they were all applied to large scale sedimentary structures formed by coarse grained glaciofluvial deposits, thus there are no studies from sand-bed fluvial settings, 3) the procedure for systematic analysis of radar facies in 3-D volumes was not fully documented hence the methods they used would be difficult to replicate by other sedimentologists, 4) an evaluation of the benefits of the method in contrast to using 2-D data was not undertaken, thus it is not clear under which circumstances a 2-D survey may be adequate and when additional visualisation in 3-D would be required. Thus in this thesis these issues will be addressed with examples used here to demonstrate how this method can be used in a simple and efficient way to provide improved interpretation over solely 2-D approaches. In such a way it is hoped to provide much more practical detail on methods than is typically reported in the literature such

that the techniques can be more widely adopted within the fluvial sedimentological community by users of GPR who may not necessarily be technical specialists.

## CHAPTER 3

### 3.0 METHODOLOGY

#### 3.0.1 Basic background of the method

GPR is a high resolution geophysical method. Its principle is based on the detection and recording of changes in dielectric properties in the shallow subsurface. The transmission antenna sends the signal of radio frequency and the receiving antenna records any signal reflected from the subsurface. Thus, the basic principles of the conventional GPR method are often compared to seismic reflection. This subsection highlights basic aspects of GPR method, and briefly explains the mechanisms which are responsible for the reflection of GPR signal, govern the signal velocity and attenuation. Main differences between GPR and seismic reflection method are also explained in the context of this project.

**Reflection of the signal.** The interfaces which reflect the signal are located between zones of different dielectric properties (Yelf 2006). Thus, vertical changes in dielectric properties result in diffraction of the signal. The wavelets diffracted on adjacent points interfere with each other. Thus part of the energy is sent back to the surface and part of it transmitted further into the subsurface (Fisher *et al.* 1992). The rate of reflected to transmitted energy as well as changes in the phase of the reflected signal are governed by the Fresnel reflection coefficient (see Glossary) which describes the contrast in velocity ( $V$ ) or relative electric permittivity ( $\epsilon_0$ ) between zones. When the signal passes between zones of lower to higher relative electric permittivity, *e.g.* at the interface between air and soil or between dry and saturated sediments, the reflection coefficient has a negative value and therefore the phase of the reflected waves changes to negative which is typically marked in white on greyscale profiles (Sensors & Software 2007). The transmitted signal initially consists of electromagnetic mono-cycles and is immediately transformed into Ricker-type (W-shaped or Mexican-hat-shaped) wavelets.

The shape of the wavelets results in a characteristic way that the reflection patterns appear on GPR profiles, *i.e.* typically negative phase amplitude surrounded by two weaker positive phase amplitude or positive phase surrounded by two weaker negative phase amplitudes (further explained in Section 4.0.1).

**The velocity** of the electromagnetic impulses depends mainly on the relative electric permittivity ( $\epsilon_0$ ) of the stratum, *i.e.* the capacity of the sediments to store and transmit an electric field. In low energy loss materials characterised by very low electric conductivity, such as sediments, the signal velocity is generally independent of the frequency of the electromagnetic waves (Reynolds 1997) and depends on the properties of the environment which it travels through. An environment where  $\epsilon_0$  is constant will be characterised by a generally constant velocity.

**Signal attenuation** of the electric field is related to the electric conductivity of sediments. Strong signal attenuation may be related to a high clay or ferromagnetic mineral content. The attenuation also depends on the frequency of the antenna used. When the time of one cycle of change of the electric field is shorter than the time required for the dipole, ion or electron orbit polarisation, part of the energy will be lost due to the cycle of polarisation not being completed (Neal 2004).

**Differences between GPR and seismic reflection** may be important when processing and interpreting GPR data with seismic software. They are related to differences between the properties of the electromagnetic and acoustic waves. The signal velocity and frequency range are much higher for electromagnetic waves. Additionally, the trends of mean velocity changes are different; the electromagnetic signal generally decreases with depth, particularly when crossing the groundwater table, while an acoustic signal will accelerate with depth. Rogers *et*

*al.* (2009) emphasise that electrical properties of the subsurface can change by over 100% within the first metre below ground level and this produces strong changes in ‘vertical exaggeration’, distortion of the subsurface image and fast signal attenuation. When compared to the seismic method, the generally decreasing velocity profile leads to less complex relations between the first registered waves (Claerbout 2000), which makes the method particularly suitable for investigation of shallow sediments.

### 3.0.2 Relation between radar reflections and sedimentary structures

Dielectric properties may be found in any material which is characterised by a low amount of free electrons with a vacuum being the perfect insulator. Relative electric permittivity is the ability of a material to become polarised in an electromagnetic field compared to the permittivity of a vacuum. Sedimentary structures are constituted by spatial changes in sedimentary texture, *i.e.* grain size, shape, orientation and compaction. These changes are always associated with changes in porosity of sediments. The largest contrasts in the dielectric properties of sediments are associated with changes in water content and therefore also the porosity of sediments. Changes in porosity of about 5% may distinctly affect the dielectric properties of sediments and create clear reflection patterns visible on GPR profiles (Neal 2004).

Van Dam (2001) argues, however, that this is true only when vertical distances between the main reflection surfaces are greater than the wavelength of the signal. His experiments enabled comparison of reflection patterns which were collected with different frequency antennas. The patterns differ between datasets and the majority of the reflection lines resulted from interference of the signal reflected from much more closely spaced interfaces. Detection of individual changes in electrical properties is therefore limited by the vertical resolution

which depends on the wavelength of the signal which is related to the velocity and frequency of the recorded signal. The distance of  $\frac{1}{4}$  of the wavelength is the oft-quoted critical detectable vertical dimension of an object. Any signal reflected from interfaces which are separated by a vertical distance less than  $\frac{1}{4}$  of the wavelength usually overlaps and produces interference. This phenomenon is known as the ‘tuning effect’ (Brown 2004). Due to the frequency range of radio waves, the vertical resolution of GPR data is high. For example, the peak frequency response of the 200 MHz antenna used on the Macclesfield site ranged between 120 and 180 MHz with an average velocity of between 0.055 and 0.120 m/ns. The minimum vertical resolution of the data is therefore estimated to be between 0.08 (saturated silty sand) and 0.25 m (unsaturated silty cobbly sand and gravel).

### 3.0.3 Study areas and equipment used

The first site was located on the southern bank of the meandering River Dene near Macclesfield and comprised a 20 x 25 m grid collected in June 2008 (see Figures 3.0.1 and 3.0.2). The survey was concentrated around a recirculation zone (see Glossary) which was filled by a flood in December 2007. This site is an example of deposition in a meandering river with flow separation on a sharp meander bend, as described by Parsons (2002). Such conditions result in a circular reverse current and erosion of channel banks. The recent fluvial deposits of the River Dean are surrounded and underlain by glacial outwash deposits. The exact extent of the fluvial deposits is not certain. GPR lines were collected along south-north and east-west directions with 0.50 m distance between lines and a 0.10 m step length forming pseudo 3-D datasets. Data was collected using a pulseEKKO PRO with 200 MHz horizontally polarised (EH) antennas separated by 0.50 m and with a 250 V pulser. In order to image point bar structures, some of the south-north running lines were extended by up to 9.3 m towards the north.



Fig. 3.0.1 Photographs of the Macclesfield site. The tape in the photo marks edges of the GPR grid. The yellow line indicates a break in topography related to the edges of the recirculation pool filled in November 2007.

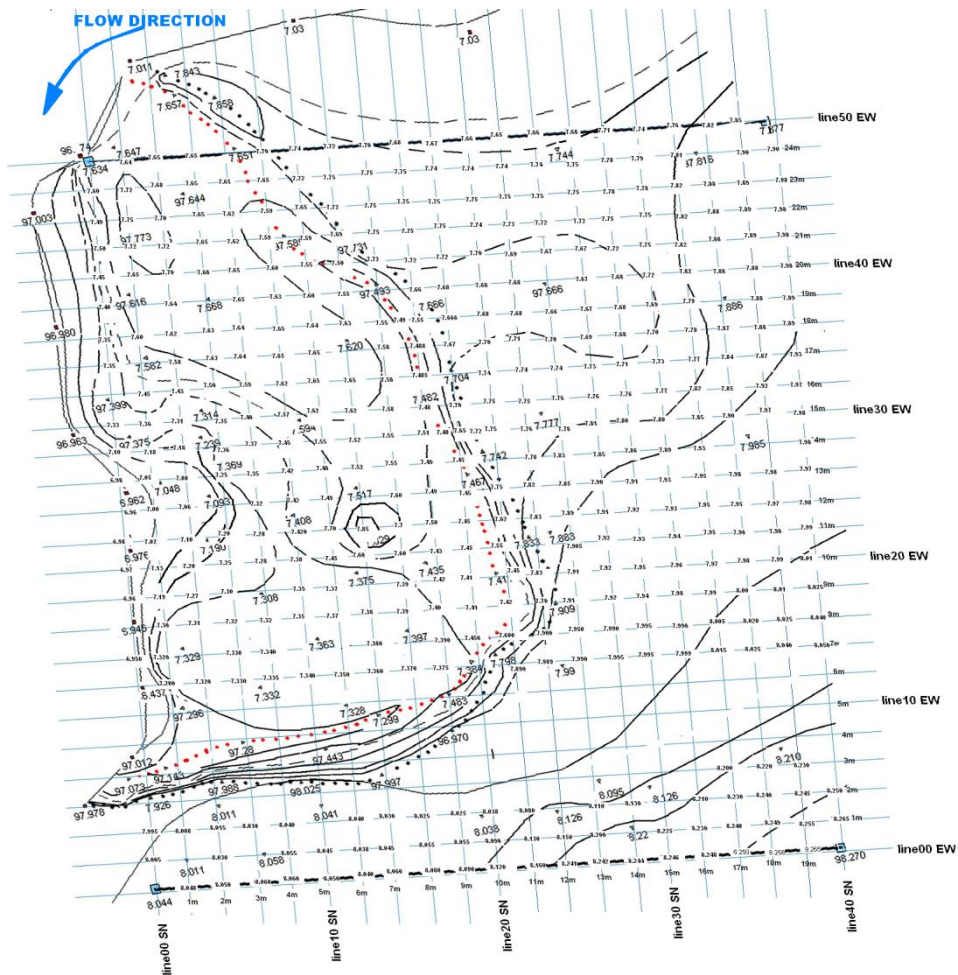


Fig. 3.0.2 Grid of lines at the Macclesfield site with topographical survey information. Red and black dotted lines on the map mark the top and bottom break in topography which are associated with the edges of the pool.

The datasets from the sandy braided South Saskatchewan River were made available for this

project by Dr. Greg Sambrook Smith. The study area lies in the proximity of the town of Outlook located about 25 km north from the Gardiner Dam on Lake Diefenbaker. The datasets document migrating unit bars within the sandy braided river with the recent deposits underlain by glacial till and Cretaceous shales and sandstones.

The first dataset was collected in 2005 (by Sambrook Smith & Lunt) and comprised lines arranged in a 10 x 10 m grid with 0.10 m spacing between lines and a 0.10 m step length forming true 3-D data. Lines were collected in both west-east and north-south orientations. This survey was done with a Sensors & Software PE100 GPR system using 200 MHz antennas separated by 0.75 m and a 1000 V pulser. Location of the grid in relation to the geomorphological forms is presented in Figure 3.0.3.

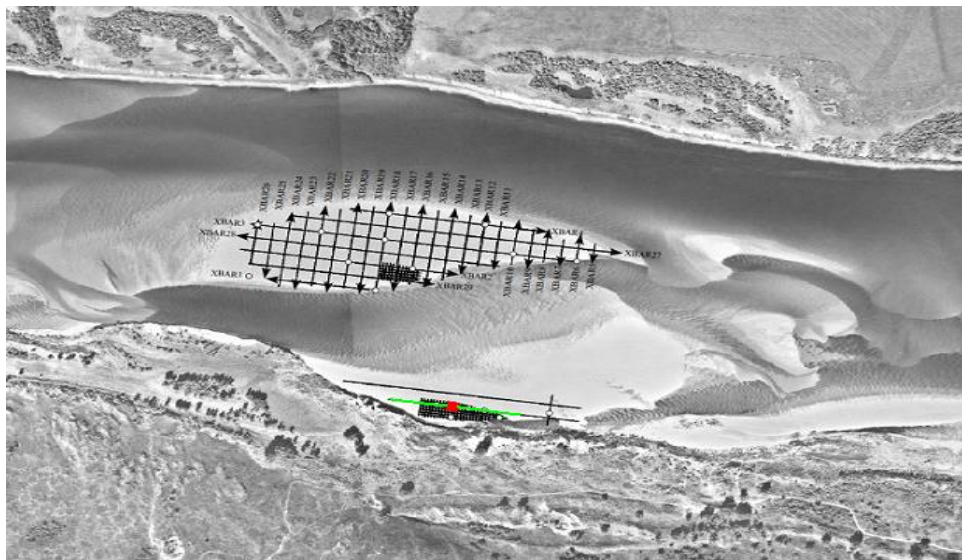


Fig. 3.0.3 Location of the true 3-D 10 x 10 m grid of data collected in the South Saskatchewan River in relation to other morphological forms (north to the right). Red square represents the grid location. Green line represents the 2-D GPR line, part of which is presented in Figure 5.2.8.

The second set was collected in 2007 (by Sambrook Smith & Parker) and comprised a larger 40 x 120 m grid with lines collected in west-east orientation. The distance between lines was 0.50 m and a 0.10 m step length to give a pseudo 3-D dataset. Data was collected using a pulseEKKO PRO with 200 MHz antenna. Location of the grid in relation to the geomorphological forms is presented in Figure 3.0.4.

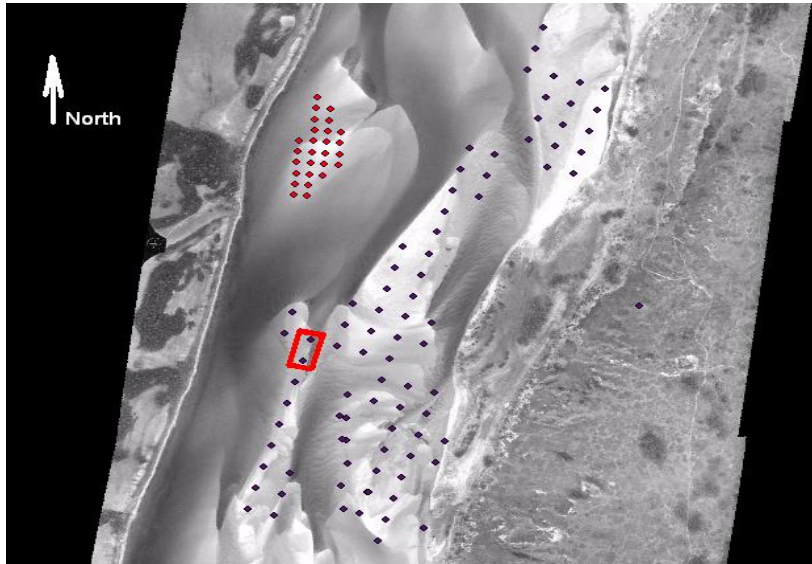


Fig. 3.0.4 Location of the 120 x 40 m grid collected in the South Saskatchewan River indicated by the red rectangle (direction of the river flow to the north). Lines were collected from the east to the north, starting from the northern edge of the grid.

Initial processing utilised Sensors & Software EKKO View Enhanced, followed by processing done with open source Seismic Unix software. 3-D SEG-Y format (see Glossary) volumes were uploaded and interpreted in Seismic Micro-Technology Kingdom software. Some field observations, mainly in cutbanks of the River Dene, were also included to aid the interpretation.

### 3.1 DATA PROCESSING

This section briefly explains the processing steps, which have been successfully applied to the datasets. Other processing steps, particularly those which were used but did not improve the quality of data, are mentioned in the Glossary included in Appendix 1.

The aim of processing is to increase the signal-to-noise ratio and reduce any potential image distortions. As Cassidy (2009) stated, “*How far a user should go beyond the basic processing steps ... is a matter of personal opinion, experience, and, ultimately, the nature of individual datasets.*” Annan (1999) emphasised that, most importantly, the post-fieldwork processing

must be cost-effective. Many processing techniques are directly borrowed from the seismic reflection methods, although as already has been stated, some may be less applicable when used for processing GPR datasets. Out of a large variety of available post-fieldwork processing techniques, a limited range was applied to improve the quality of the datasets presented in this project. The processing steps are highlighted below. Basic 2-D processing steps included data editing, filtering, gain recovery and compilation into 3-D datasets. Additionally, velocity analysis was carried out for topographical correction and conversion of time to depth scale. Knowledge of the signal velocity in the subsurface was also important for the application of other signal processing algorithms such as migration, normal move-out dip and move-out corrections and analysis of wavelet attributes.

Despite some recommended sequences for some of the processing steps, *e.g.* deconvolution (see Glossary) should be followed by application of gain recovery (Stockwell and Cohen 2008), and some published processing flow diagrams (*e.g.* Fisher *et al.* 1992, Annan 1999, Neal 2004, Cassidy 2009), the majority of authors have emphasised the iterative character of GPR signal processing. The sequence of applied steps may vary depending on the purpose of the survey, technical limitations of the software, character of the data and complexity of architecture of the subsurface. Unnecessary and excessive processing may introduce patterns which are not related to the investigated fluvial sedimentary architecture.

### 3.1.1 2-D vs 3-D processing

The 3-D method is particularly suitable for archaeological applications which require detailed display of plan views. Such surveys typically comprise pseudo 3-D surveys followed by 2-D processing and compilation of individual lines into 3-D datasets (Grasmueck 1996, Whiting *et al.* 2001, Munroe *et al.* 2007). Full-resolution 3-D processing including 3-D migration was,

however, demonstrated by Grasmueck *et al.* (2005) and Novo *et al.* (2008) and were applied to dataset collected in difficult ground conditions, *i.e.* uneven and densely overgrown with trees ground surface by Böniger and Tronicke (2010). Full resolution 3-D GPR migration, focuses not only distorted reflections along the survey lines, as is the case with 2-D migration, but also removes effects of any off-line reflections. This thesis presents data processed as individual 2-D profiles and compiled into 3-D datasets.

### 3.1.2 Editing, data compilation and topographical correction

One of the first processing steps required was editing the files which represented individual survey lines. There are three files for every GPR survey line: the header file, which includes basic information about the survey (such as the equipment used, length of the survey line, number of the survey points, time window), data file and the file including topographical information. Editing of the Macclesfield data utilised EKKO View Enhanced, whilst topographical correction was incorporated within the Seismic Unix processing script (Appendix 2). Topographic correction eliminates any potential deformation of the subsurface image which occurred due to an uneven ground surface. The site was surveyed and the information about the relative elevation of every survey point was included in topographic information files. The Seismic Unix script used for processing of individual GPR lines (Appendix 2) for displaying the processed profiles and include the elevation of every survey point. As data is displayed in TWTT scale, displaying the relative topography required knowledge of the mean signal velocity to convert elevation information from the depth to time format (see Section 3.1.4). Due to the uneven surface the length of each survey line was greater than the horizontal distance between the first and the last survey points (measured during the data collection). The differences between the lengths of survey lines recorded by the GPR and the horizontal distances did not exceed 10% of the horizontal distances. Thus the

topographic correction required adjusting the recorded length of the majority of lines which is often described as ‘rubber band’ interpolation (Jol 2009). As the length of the survey lines was shortened, the distance between survey points were shortened too and the data had to be re-sampled to restore the original distance between the traces. These two steps were done with EKKO View Enhanced.

### 3.1.3 Frequency analysis and filtering

Separation and effective removal of various types of noise is essential in any signal processing. Recorded traces are considered a result of the convolution of a number of time functions (Daniels 1996). The main aim of filtering is the removal or suppression of elements unrelated to the sedimentary architecture or which obscure the subsurface image. Among the many methods of signal filtering, discrete Fourier transform (DFT), restricted to defined ranges of frequencies, is the most commonly used (Smith 1999). DFT is carried out in 1-D, *i.e.*, it is applied to individual traces by decomposing the recorded signal into a series of different frequency functions. In this way, the function converts real time traces into complex frequency traces (Stockwell and Cohen 2008). The algorithm can be used to display amplitude spectrum, enabling frequency analysis (see below). When used as a filter, however, certain frequency ranges are limited or completely removed. There are a number of possible options for DFT frequency filtering: low-pass, high-pass, band-pass filter (a combination of the previous two) and notch filter which rejects a single frequency value (Cassidy 2009). In general, low-pass filtering enhances flat-lying reflectors, while high-pass filtering makes dipping reflections more distinct (Annan 1999). High-pass filtering is commonly used for the removal of a low frequency signal which saturates the GPR receiver antenna and masks near-surface reflection surfaces. This step is often referred to as ‘dewow’. The transmitting antenna typically produces a signal above 10 MHz, thus any recorded signal below that value should

be considered as noise. Application of the ‘dewow’ filtering may, however, also lead to the unnecessary removal of recorded signal and limit the maximum penetration depth on the GPR profile.

The frequency analysis applied in this study used the 1-D DFT approach described above. Examples of amplitude spectrum for individual traces for the Macclesfield data are shown in Figures 3.1.1 and 3.1.3. Frequency response was noted to be different in the case of coarse-grained deposits which surrounded the recirculation pool as compared with the silty sands which have recently been deposited in the recirculation zone. The separate low frequency component, potentially associated with antenna signal saturation, was not apparent on the profiles and therefore ‘dewow’ filtering was not applied.

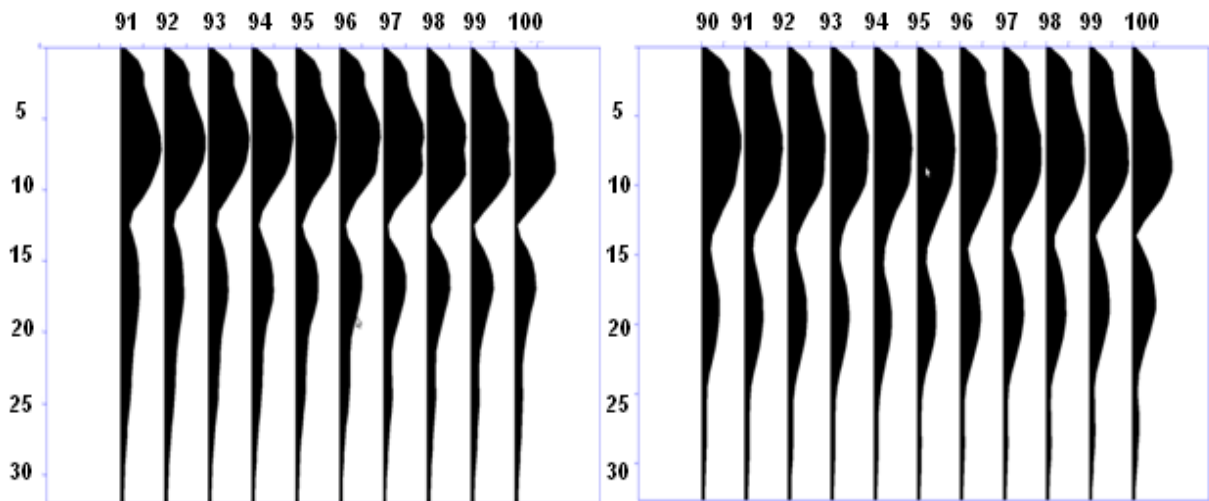


Fig. 3.1.1 Fragment of line 00 EW (left) and 40 SN (right) from the Macclesfield site. Examples of amplitude spectrum in frequency domain (before filtering) for traces collected from gravelly sandy with cobbles outside recirculation pool. Peak frequency response is between 70 and 100 MHz, although dominating frequencies range between 40 and 250 MHz (vertical scale in tens of MHz).

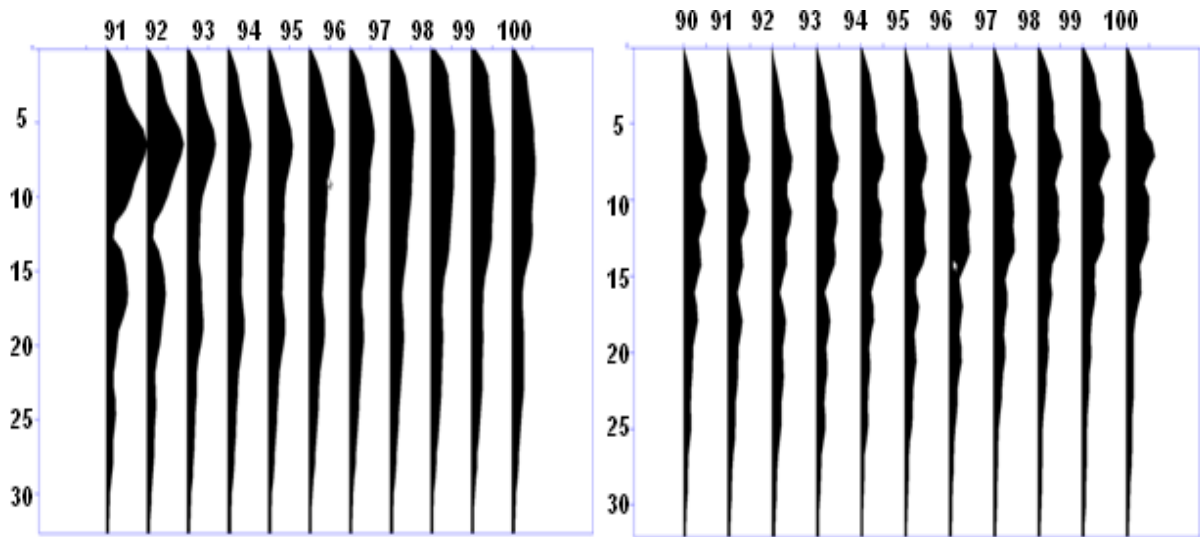


Fig. 3.1.2 Examples of amplitude spectrum in frequency domain (before filtering) for selected traces from line 20 EW (left) and line 01 SN (right) from the Macclesfield site. The fragment was collected from silty sand within recirculation pool. Peak frequency response is between 60 and 90 MHz (vertical scale in tens of MHz).

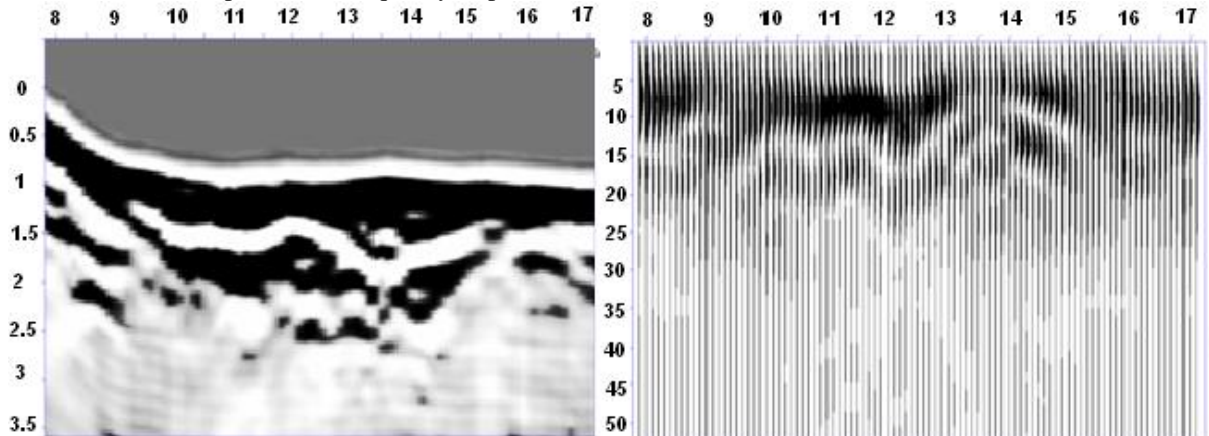


Fig. 3.1.3 Fragment of unprocessed line 21 EW (left) from the Macclesfield site (vertical scale in hundreds of ns) with the corresponding amplitude spectrum in frequency domain (right: vertical scale in tens of MHz). Changes in peak frequency response across traces towards lower values, *i.e.* creating a convex shape in the left image, correspond to the concave character of the reflectors.

Application of band-pass filtering is based on the assumption that random and repetitive noise must be associated with the frequencies above and below a certain range. There are four gate values required for bandpass filtering, with two middle values representing the pass-region, *i.e.* the frequency range which remains unaffected after filtering (Figure 3.1.4). The first value represents the upper boundary of a frequency range which is completely removed from datasets, while the last value represents a frequency above which the signal is also removed. Frequency response information was used to pick the band-pass values. Time-variable filtering is a series of band-pass filters with different gate values defined for specific depth

ranges expressed in two-way travel time (TWTT). This approach was followed here with various band-pass ranges used, which ultimately led to an improved resolution of profiles and better preservation of signal at greater depths. Cassidy (2009) recommends that the pass region is set around the peak frequency. A higher frequency band-pass resulted in higher resolution of the top part of the profiles as well as faster signal attenuation. Conversely, application of a lower frequency band-pass led to lower resolution, more flat-lying reflection patterns and greater depth of the interpretable profile.

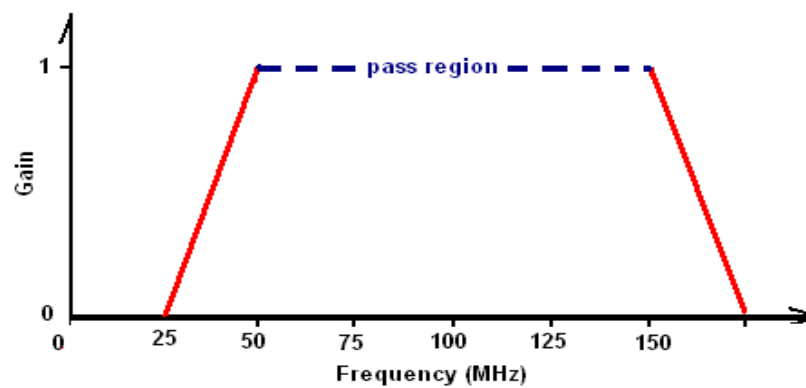


Fig. 3.1.4 Schematic representation of bandpass filters. The values of the bandpass filter gates are: 25, 50, 150, 175. Values between 0 and 25 MHz and above 175 MHz are completely removed. Signal of frequencies between 25 and 50 and 150 and 175 MHz is gradually introduced while frequencies between 50 and 150 are fully represented, *i.e.* they represent pass region.

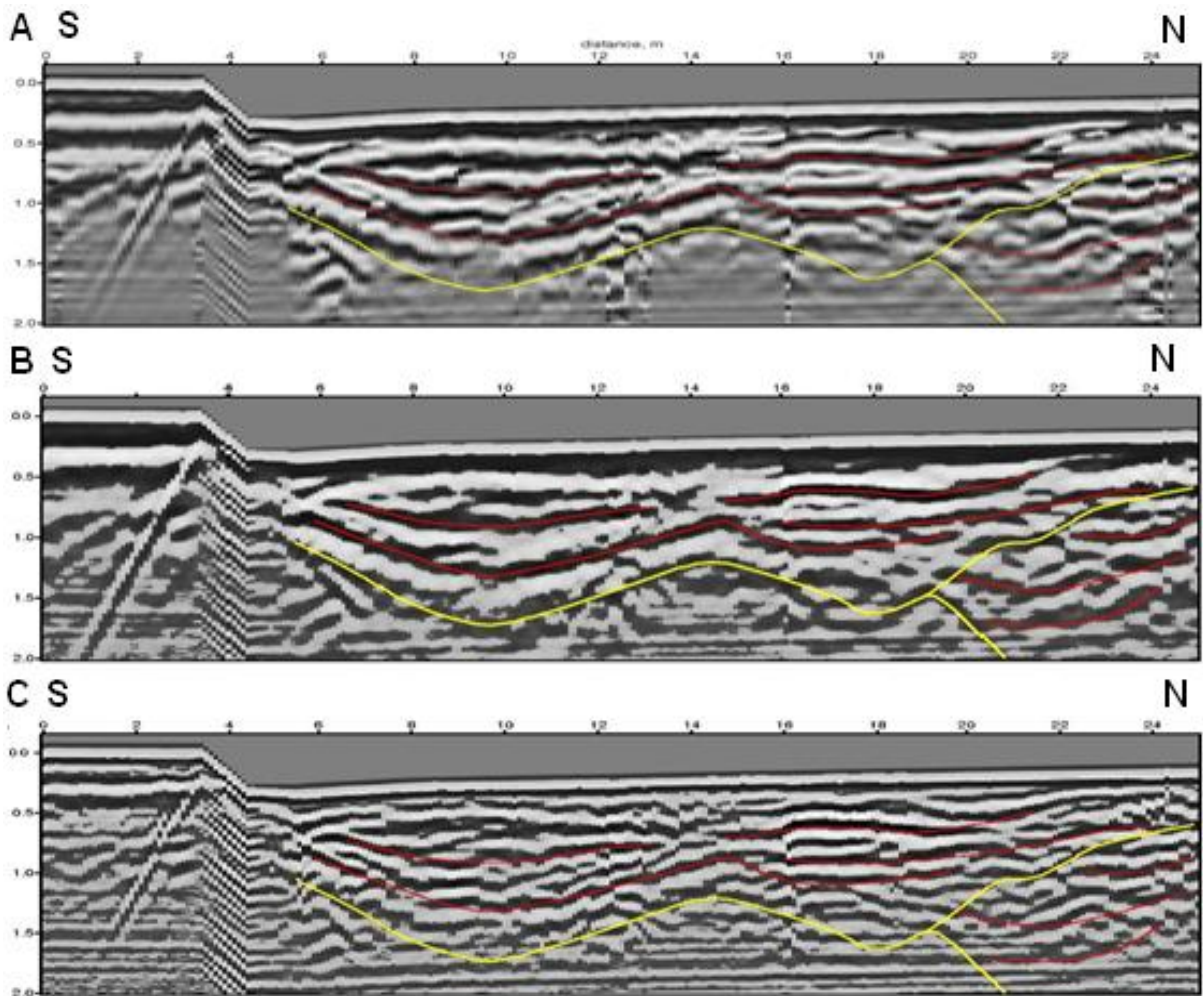


Fig. 3.1.5 A. Line 02 SN from Macclesfield dataset after ‘standard’ processing steps which included: AGC (time window of 10 ns); ‘dewow’ filter, band-pass filters: 20, 40, 150, 400 MHz. Two middle values represent pass-region. Image appears unclear which may be related to Gibbs effect (see Glossary). B. Lower resolution image of Macclesfield line 02 SN gives clearer picture of major reflection lines. Processing steps included Gain: time power of 1.5 and Gaussian time power of 0.3; time variable filters above 0.5 m: 5, 40, 250, 500 MHz; above 1.2 m: 5, 30, 300, 500 MHz; above 2.8 m: 5, 20, 400, 500 MHz. Note better preservation of amplitude in lower section of the profile. C. Higher resolution image of Macclesfield line 02 SN reveals better internal architecture of radar facies. Processing steps included Gain: time power of 1.2, Gaussian power of 0.4; time variable filters above 0.5 m: 20, 100, 400, 500 MHz; above 1.2 m: 20, 80, 350, 500 MHz; above 2.8 m: 20, 50, 300, 400 MHz. Note improved resolution of upper section of the profile (vertical scale in m).

A comparison of the results of frequency filtering as well as gain recovery modes is shown in

Figures 3.1.5A to C. The first image presents optimal band-pass filtering with AGC applied, while the following two figures are examples of time-variable filtering and time power gain recovery.

Systematic and repetitive noise, such as multiples and ghost reflections as well as random white noise, can be removed by the application of predictive noise filtering which is known as deconvolution. Predictive filtering was done with Seismic Unix software and required

maximum and minimum ‘time-lag’ parameters to be known. This could be assessed by application of ‘autocorrelation’ (represented in Seismic Unix processing script as ‘suacor’) which provides a measure of the time lag of periodical events, *i.e.* the period of the repetition of wavelets.

An attempt to apply Wiener predictive filtering was undertaken as part of this project. Resolution of the upper part of the profiles in many instances was improved; however, data from the lower sections were often completely removed. Figures 3.1.6 and 3.1.8 compare images before and after predictive filtering. Many authors (*e.g.* Annan 1999, Daniels 1996, Cassidy 2009) emphasised that a compressed, high frequency signal characterised by fast attenuation often results in a limited application of deconvolution to GPR data which aim to image sedimentary architecture.

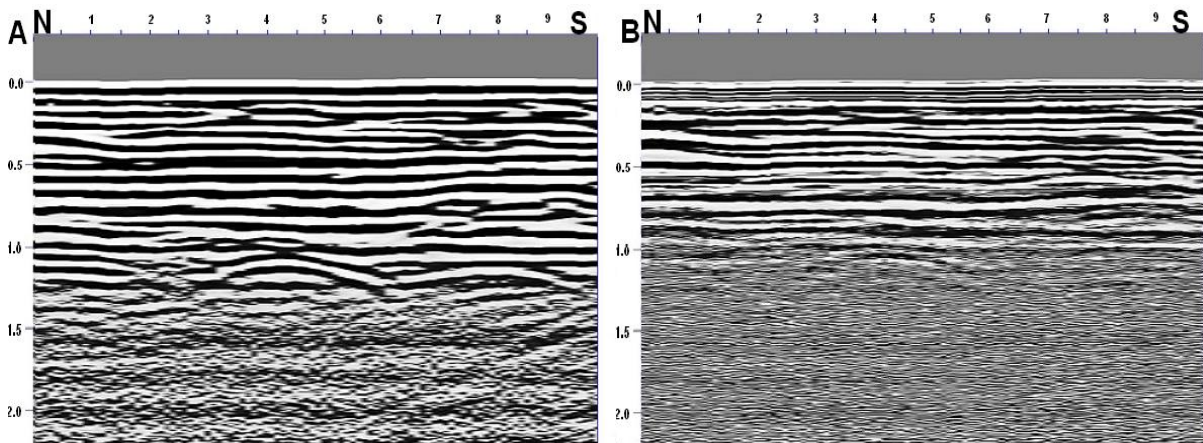


Fig. 3.1.6 Lower resolution line 97 NS from the South Saskatchewan River 10 x 10 m grid before (A) and after (B) Wiener filtering. Note improved resolution in the upper part of the profile.

K-x filtering is a combined temporal and spatial filter useful when a particular unwanted feature is to be removed from profiles (Annan 1999). Although useful in certain datasets this technique was not undertaken during the processing of data used in this project.

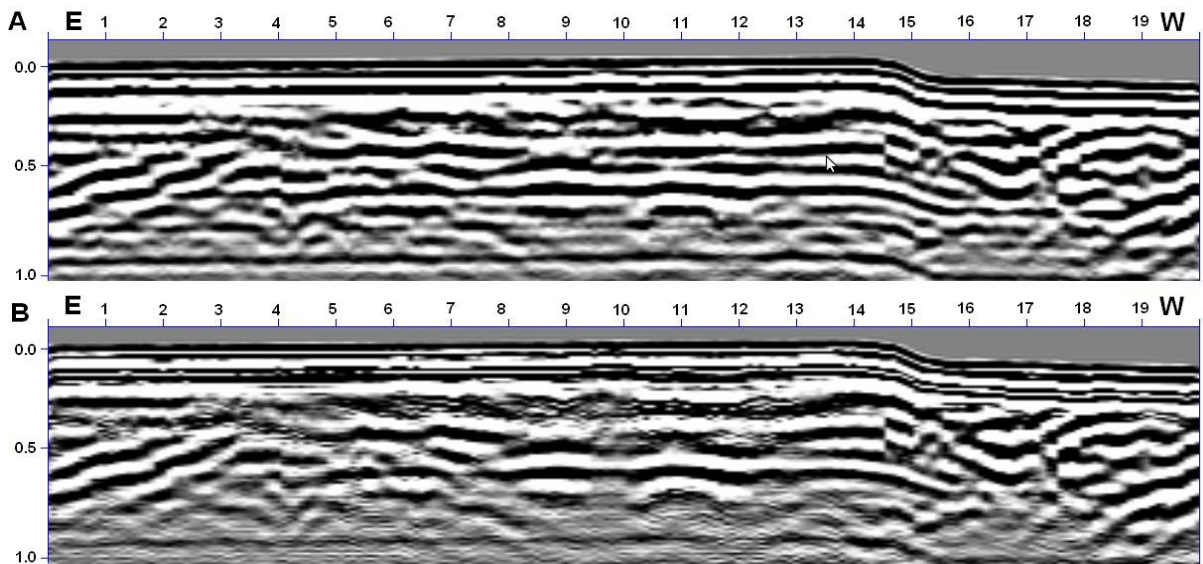


Fig. 3.1.7 Higher resolution line 50 WE from the Macclesfield site before (above) and after (below) Wiener filtering (vertical scale in hundreds of ns).

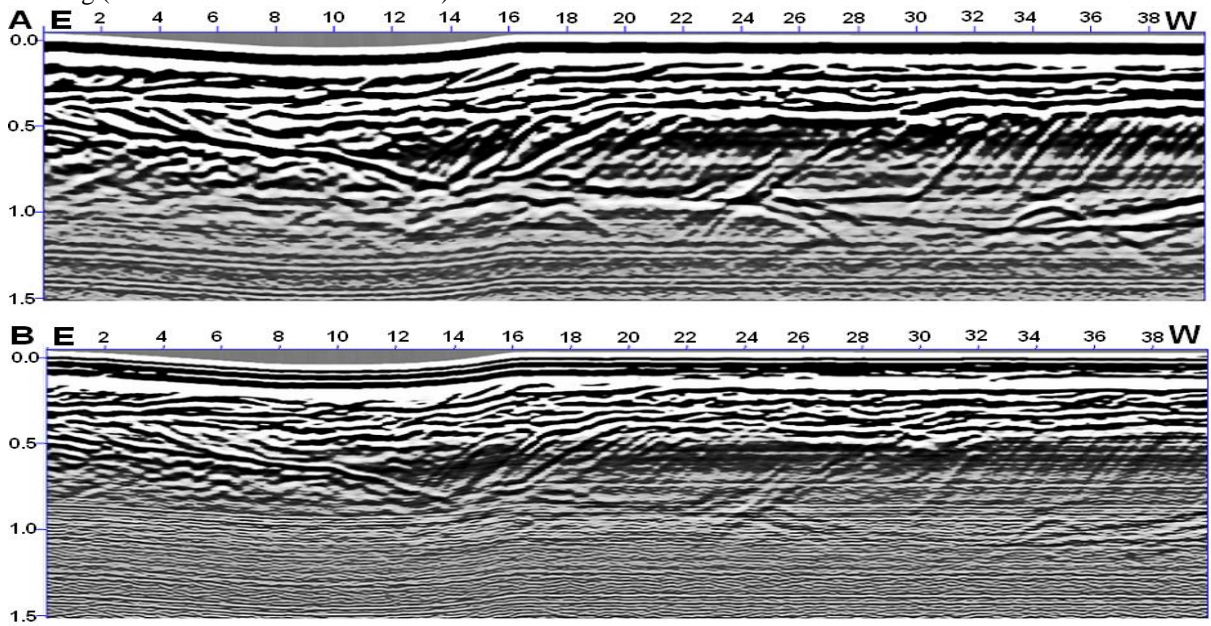


Fig. 3.1.8 Lower resolution line 04 South Saskatchewan from the South Saskatchewan River 120 x 40 m grid before (A) and after (B) Wiener filtering, which resulted in a general signal loss at greater depths and insignificant improvement of the signal-to-noise ratio (vertical scale in hundreds of ns).

### 3.1.3 Amplitude loss and gain recovery

Gain signal recovery is another basic processing technique which aims to minimise the effects of signal attenuation and its geometrical spreading in the subsurface (Fisher *et al.* 1992). There are many techniques which can be applied, such as linear and exponential gain functions, automatic gain control (AGC), programmed gain control (PGC) or spherical exponential compensation (SEC). AGC is an adaptive gain function which aims to adjust loss

of amplitude strength with increasing depth to a constant level. It corrects the amplitude in each individual trace with the difference between its mean in a set time window and its value at the centre of this window (Annan 1999). It has the potential to amplify noise and remove relative amplitude information. PGC is similar to AGC but it applies the same function to all traces. SEC requires knowledge of the mean velocity and attenuation. Many authors (e.g. Cassidy 2009) have emphasised that, in practice, application of SEC often requires an iterative approach. Other gain recovery techniques include time functions such as time power, Gaussian power and exponential power. AGC was initially applied during this project (Figure 3.1.5A); however, time power and Gaussian power functions were generally found to be more useful (Figures 3.1.5B and 3.1.5C). Amplitude loss analysis was attempted on time-amplitude sections to select an appropriate gain, although an iterative approach was also used.

#### 3.1.4 Velocity analysis

Mean velocities, which describe vertical propagation of acoustic or electromagnetic waves within particular zones in the subsurface, can be treated as a scalar value, *i.e.* they describe the character of the zone rather than a vector (Sheriff 1973). In sediments, however, due to their anisotropic character, mean velocity may vary in certain directions. Vertical exaggeration is a result of changes in the wave velocity (Claerbout 1993). In contrast to the velocity of acoustic waves, the velocity of electromagnetic waves rapidly decreases with depth, particularly in the shallow subsurface, with a major decrease associated with the groundwater table. Such a model of wave transmission results in a vertical exaggeration which increases with depth, and sections displayed in a time-scale are deformed, *i.e.* as depth increases dipping lines appear steeper than they really are and apparent strata thicknesses also become greater with increasing depth.

Mean velocity changes may be estimated based on a variety of methods and this knowledge enables the transformation of time-scale into depth. One of the methods is the common mid-point survey (CMP) which uses the measurement of TWTT to points of reflection lying on horizontal interfaces.

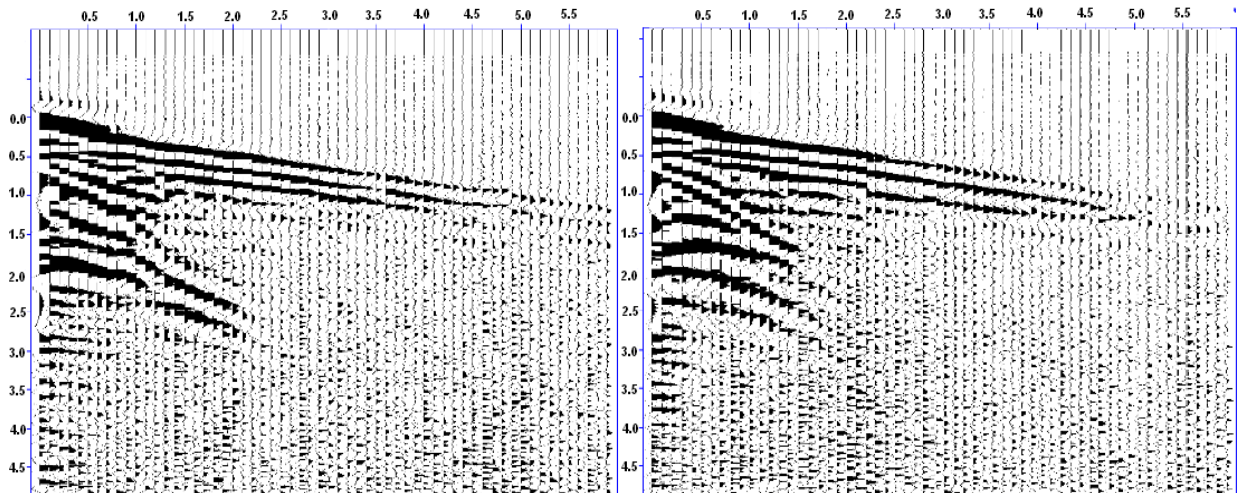


Fig. 3.1.9 CMP profiles collected from the recirculation zone at the Macclesfield site (left SN, right EW oriented). Velocity was estimated to range between 0.12 m/ns (above groundwater table) and 0.052 m/ns (below groundwater table). Vertical scale in hundreds of ns.

Other methods which can be used include measurement of the TWTT to a surface or object of known depth such as the groundwater table, estimation of velocity based on laboratory measured dielectric constant of sampled materials or iterative migration (Fisher *et al.* 1992a). The velocity of electromagnetic waves may vary between the speed of light in a vacuum and about 0.01 m/ns in seawater. Unsaturated and saturated coarser-grained clastic sediments typically have values of between 0.15 and 0.09 m/ns, and 0.09 and 0.04 m/ns respectively (Fisher *et al.* 1992a, van Heteren 1998). Mean signal velocities for the Macclesfield site deposits were estimated based on a CMP survey carried out within the recirculation zone.

The survey consisted of two perpendicular CMP profiles of 0.10 m step with a final distance of about 12 m between transmitter and receiver (Fig. 3.1.9). The acquired data were interpreted by picking reflection events manually and then applying the standard formula for the CMP estimation of mean velocity cited by Neal (2004):

$$v_1 = \sqrt{(x_2^2 - x_1^2) / (t_2^2 - t_1^2)}$$

where  $v_1$  is mean wave velocity within layer 1,  $t_1$  and  $t_2$  are TWTT to specific reflection events at antenna separations  $x_1$  and  $x_2$ . Unsaturated silty sand deposits were characterized by a velocity of about 0.13 m/ns, whilst below the groundwater table it decreased to 0.064 m/ns and below 150 ns to 0.052 m/ns. The mean velocity which was used for scale conversion was estimated as 0.09m/ns. The mean velocity assessed based on TWTT to the known depth which was the groundwater table along the cut-bank (see Section 4.1) outside the recirculation zone indicated velocity of about 0.90 m/ns. This material was characterised by a higher compaction and higher variability ranging from fine silty sand to sandy gravelly cobbles. Analysis of velocity carried out in EKKO\_View software, which involved adjustment of the shape of diffraction hyperbolas (Fig. 3.1.10), indicated mean velocity ranging between 0.70 and 0.90 m/ns at depths between 1.4 and 2.0 m in deposits outside the recirculation zone.

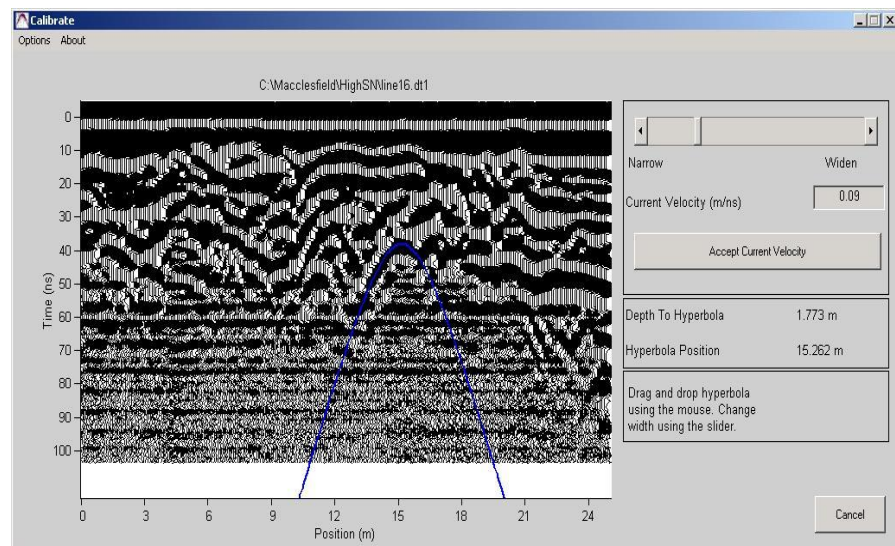


Fig. 3.1.10 Velocity estimation based on the shape of parabolic reflections for the recirculation zone deposits at the Macclesfield site.

### 3.1.5 Migration

An attempt to migrate reflection events of the potentially distorted images of the subsurface to their original location was also made as part of the post-fieldwork processing. The example

shown below utilised Stolt migration (Figure 3.1.11) which, unlike the majority of other migration algorithms, can be applied to common-offset data without prior application of dip move-out (DMO) transformation (explained below). Migration carried out on the data presented in this thesis did not improve the image quality and so was not applied.

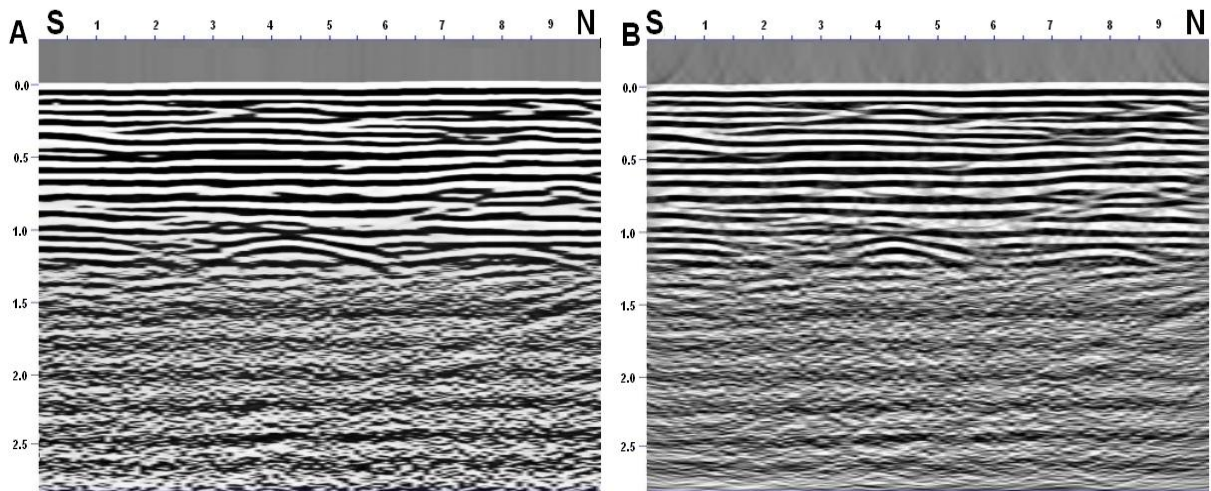


Fig. 3.1.11 Higher resolution line 97 NS from the South Saskatchewan River 10 x 10 m grid before (left) and after (right) Stolt migration. Part of the diffraction hyperbola was achieved; however, new image distortion was also introduced. Note the concave upwards features (vertical scale in hundreds of ns).

Due to the distance between the transmitter and receiver antennas, common-offset data also required the application of ‘normal move-out’ (NMO). The normal move-out step eliminates distortions of the near-surface reflection surfaces which are produced by the separation of transmitter and receiver antennas. As distance between the transmitter and the receiver is added to the distance to reflector, features appear to be deeper than they really are. Application of NMO changed the profiles only insignificantly, while ‘dip move-out’ (DMO), which is a similar technique applied to reduce the distortion of inclined reflectors, was found to improve the quality of the images. Comparison of profiles where NMO and DMO have been applied is presented in Figure 3.1.12. As DMO operates on several adjacent traces, this may, however, be just a result of ‘averaging’ between adjacent traces. Ground truth control would be necessary to assess the influence of DMO.

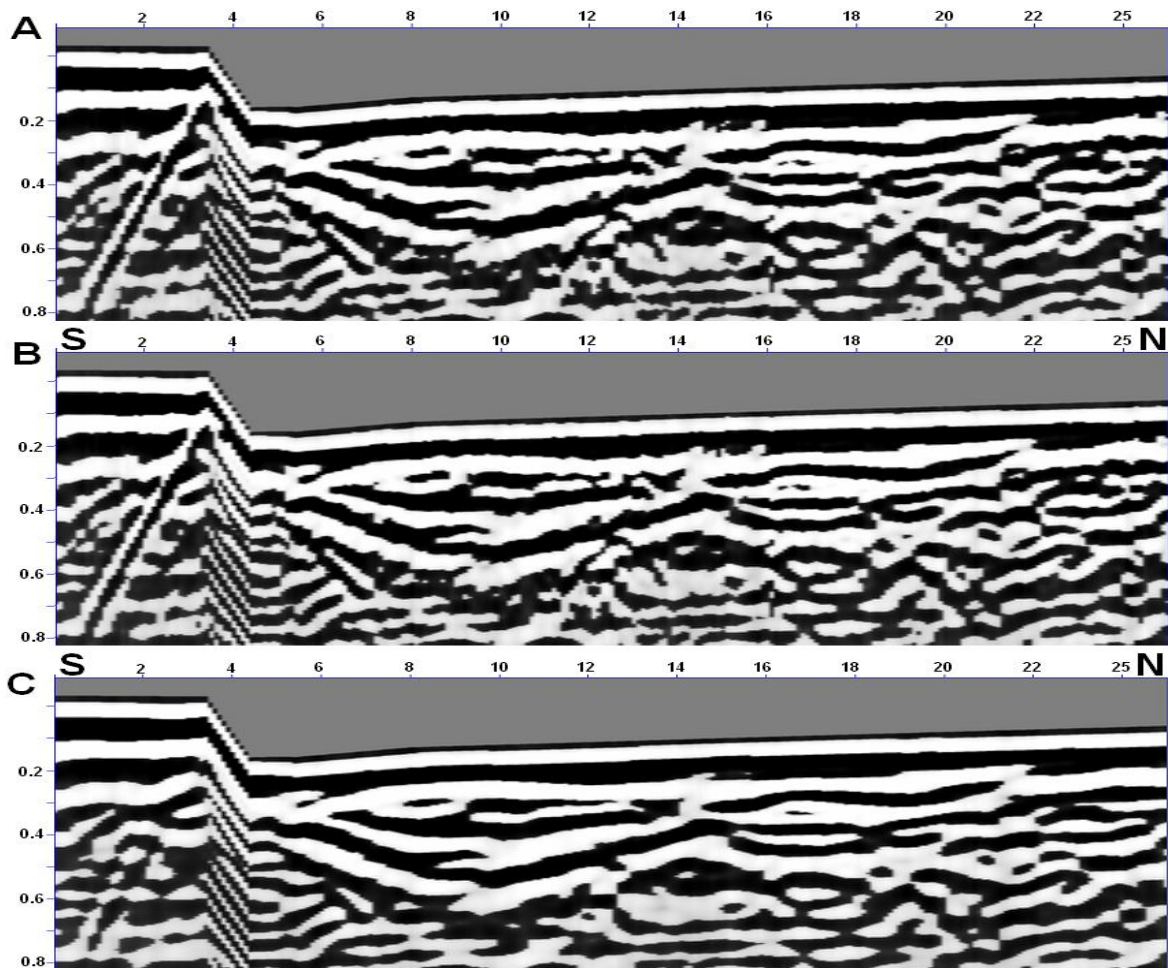


Figure 3.1.12 Lower resolution line 02 SN without NMO and DMO (image A) compared with profiles which were processed with NMO (image B) and DMO (image C). There is an insignificant difference between image A and B on which the structures are insignificantly slightly shallower. The reflectors in image C appear smoother and easier to interpret.

### 3.1.6 SEG Y format data and compilation of 3-D datasets

The final post-fieldwork processing step was creation of SEG Y format data, followed by compilation of the individual GPR lines into 3-D volumes, which was done using Seismic Unix software. The script used to compile individual files into 3-D datasets is presented in Appendix 2. Two SEG Y format files – lower and higher resolution – were also created for each of the datasets. These two sets of profiles were created by using two sets of filters. Lower frequency profiles are a result of applying low frequency filters and recover otherwise lost information from greater parts of the profiles, while higher frequency data improve the resolution of the upper parts of the profiles.

These files were uploaded into SMT Kingdom seismic interpretation software which also required coordinates for the corners of the grid, line and trace spacing (Figure 3.1.13). Traces were loaded sequentially. More information about loading SEGY datasets can be found in the Kingdom manual.

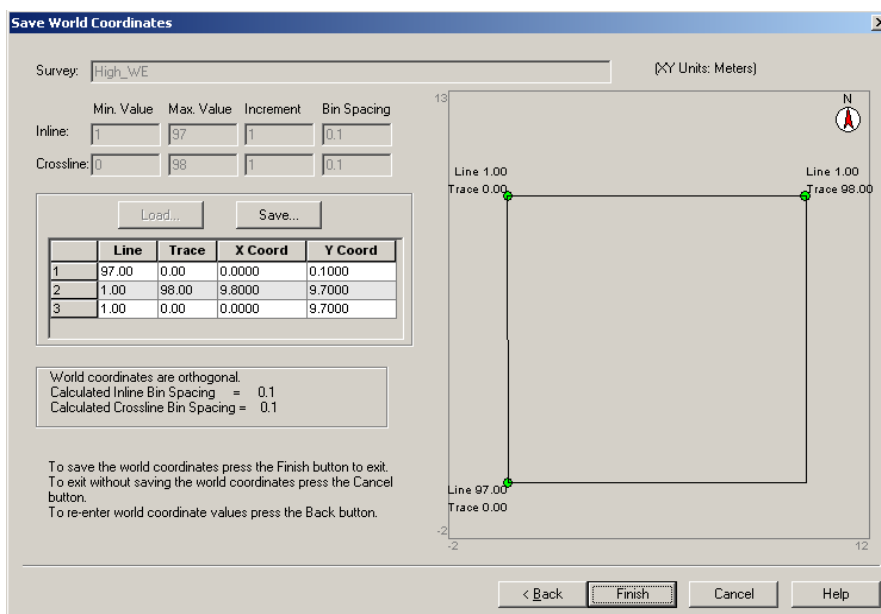


Fig. 3.1.13 Screen shot of the SMT Kingdom window during loading of the coordinates for the higher resolution W-E oriented lines of the South Saskatchewan River 10 x 10 m grid.

### 3.1.7 Summary of processing

Differences between parameters used for filtering and gain recovery are thought to be related to multiple factors including equipment used, lithology and also operator's bias. The final processing included only the most essential steps. A summary of the processing steps used for the datasets is shown in Table 3.1. As is shown in Figure 3.1.14, application of time-variable filtering and gain recovery together with creation of the low and high resolution datasets provides images which included much more information about sedimentary architecture than images which utilised 'standard' processing, *i.e.* 'dewow', band-pass filtering and AGC.

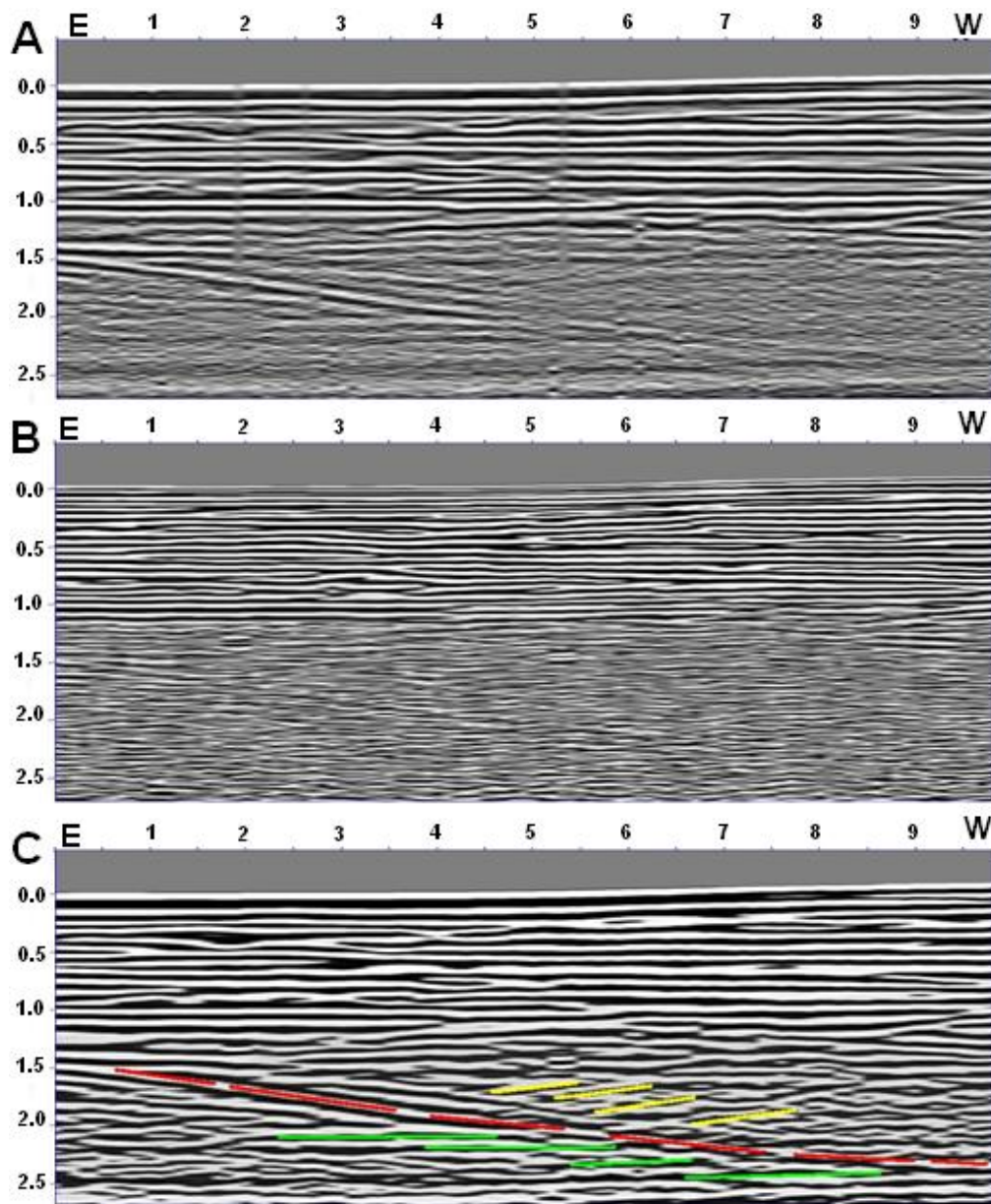


Fig. 3.1.14 Comparison of processing results of lower resolution line 80 WE from the South Saskatchewan River 10 x 10 m grid. Top image after applying 'standard' processing: band-pass filter 20, 40, 100, 500 MHz; and AGC. Two middle values represent pass-region. Middle image is a result of time-variable filter above 2.5 m: 80, 180, 640, 1280 MHz; above 6.9 m: 60, 180, 360, 640 MHz; Gains: time power of 3.5 and Gaussian power of 0.1; DMO. Bottom image is a result of time-variable filter above 2.5 m: 10, 80, 160, 240 MHz; above 6.9 m: 20, 40, 160, 240 MHz; Gains: time power of 3.5 and Gaussian power of 0.1; DMO. Note that some features are not resolved with 'standard' processing, *i.e.* truncation below the scour (red line) and the architecture of fill within the scour (green line) which forms an onlap relation with the scour surface.

Time-variable filtering and gain recovery address the changes in the character of the transmitted GPR signal with depth. These techniques were found to be very useful in contrast with techniques such as migration and deconvolution which generally require the signal to be relatively stable. These algorithms were found to limit the interpretability of lower parts of GPR profiles and to introduce features not related to fluvial sedimentary architecture.

Table 3.1 Summary of the processing steps used for the three datasets presented in this thesis.

<b>River Dene (Macclesfield)</b>	<b>South Saskatchewan River 10 x 10 m</b>	<b>South Saskatchewan River 120 x 40 m</b>
Editing, velocity analysis and static correction	Editing and static correction	Editing and static correction
Dewow (tried but not used)	Dewow (tried but not used)	Dewow (tried but not used)
Analysis of amplitude in frequency domain – 1-D discrete Fourier transform  Time-variable filtering Low resolution above 1.2 m: 10, 80, 160, 240 MHz above 2.8 m: 20, 40, 160, 240 MHz High resolution above 1.2 m: 80, 180, 640, 1280 MHz above 2.8 m: 60, 180, 360, 640 MHz	Analysis of amplitude in frequency domain – 1-D discrete Fourier transform  Time-variable filtering Low resolution above 2.5 m: 10, 80, 160, 240 MHz above 6.9 m: 20, 40, 160, 240 MHz High resolution above 2.5 m: 80, 180, 640, 1280 MHz above 6.9 m: 60, 180, 360, 640 MHz	Analysis of amplitude in frequency domain – 1-D discrete Fourier transform  Time-variable filtering Low resolution above 1.3 m: 10, 40, 360, 480 MHz above 4.0 m: 10, 60, 480, 640 MHz High resolution above 1.3 m: 30, 160, 480, 960 MHz above 4.0 m: 50, 160, 320, 400 MHz
Analysis of amplitude in frequency domain – 1-D discrete Fourier transform and iterative modification of filtering parameters	Analysis of amplitude in frequency domain – 1-D discrete Fourier transform and iterative modification of filtering parameters	Analysis of amplitude in frequency domain – 1-D discrete Fourier transform and iterative modification of filtering parameters
Normal move-out	Dip move-out	Dip move-out
Deconvolution – Wiener predictive filtering preceded by autocorrection time-lag analysis (tried but not used)	Deconvolution – Wiener predictive filtering preceded by autocorrection time-lag analysis (tried but not used)	Deconvolution – Wiener predictive filtering preceded by autocorrection time-lag analysis (tried but not used)
Gain recovery: AGC (tried but not used for 3-D) Lower resolution: Time power = 1.5 Gaussian power = 0.3 Higher resolution: Time power = 2 Gaussian power = 0.3	Gain recovery: AGC (tried but not used for 3-D) Lower resolution: Time power = 3.5 Gaussian power = 0.1 Higher resolution: Time power = 3 Gaussian power = 0.1	Gain recovery: AGC (tried but not used for 3-D) Lower resolution: Time power = 1.5 Gaussian power = 0.3 Higher resolution: Time power = 2 Gaussian power = 0.4
Stolt migration (tried but not used)	Stolt migration (tried but not used)	Stolt migration (tried but not used)
Conversion to SEG Y and compilation to 3-D datasets (lower and higher resolution)	Conversion to SEG Y and compilation to 3-D datasets (lower and higher resolution)	Conversion to SEG Y and compilation to 3-D datasets (lower and higher resolution)

### 3.2 THREE-DIMENSIONAL DATA DISPLAY

This section describes visualisation techniques which were applied to the processed data.

Detailed interpretation of the datasets carried out in 3-D are presented in Sections 5.1 to 5.3.

Three-dimensional data volumes were compiled using Seismic Unix. This required each of the GPR lines to have equal length, step and number of traces. Empty traces were added if required (note the white corner in Figure 3.2.1). The script which was used to compile the individual lines into the 3-D volumes was made available by Dr. Russell Exley (University of Birmingham) and is presented in Appendix 2. Stacking of two volumes comprising of lines

collected in perpendicular directions over the same area at the Macclesfield site was also attempted. However, the shape and phase of wavelets in the respective traces differed significantly and the newly created volume resulted in an unclear image of the subsurface. The differences in wavelet shapes of respective traces in the volumes may have resulted from differences in location of the traces, the polarized character of the GPR signal and the geometry of propagation of the signal reflected from dipping interfaces. Both of the volumes in the South Saskatchewan River 10 x 10 m datasets, however, presented a very similar image with only minor differences such as the shape of diffraction parabolas. The better quality of this dataset might have been the result of a more uniform environment, *i.e.* sandy deposits with relatively flat-lying reflectors, in comparison with the Macclesfield site where both the lithology and architecture were more heterogeneous. Application of GPS together with the GPR equipment during collection of the South Saskatchewan River datasets may also have significantly improved the quality of the datasets when compared with the Macclesfield data.

### 3.2.1 Line spacing, sampling and lateral resolution

The Macclesfield data was collected as a pseudo 3-D grid with 0.50 m spacing between lines and a 0.10 m step length. The 0.50 m spacing between lines was chosen to address the expected size of the sedimentary features, particularly within the recirculation pool. Similarly, the South Saskatchewan River 120 x 40 m grid comprised W-E running lines collected with 0.50 m distance between them and 0.10 m step. The South Saskatchewan River 10 x 10 m grid comprised lines with 0.10 m distance between lines and stations, collected along S-N and W-E directions, forming two true 3-D datasets. Given that collecting data for 3-D analysis is time-consuming, there is a clear trade-off between how close survey lines are spaced and the resulting resolution of the 3-D volume. In order to investigate the impact that line spacing would have on the resultant volume, a comparison was made with the same data that was

resampled at a coarser resolution. The effect of distance between lines and traces was analysed as part of the post-acquisition data analysis and aimed to establish the optimum spacing between lines and traces which would not compromise the quality of data and accurately image fluvial sedimentary architecture (Figures 3.2.1 and 3.2.2).

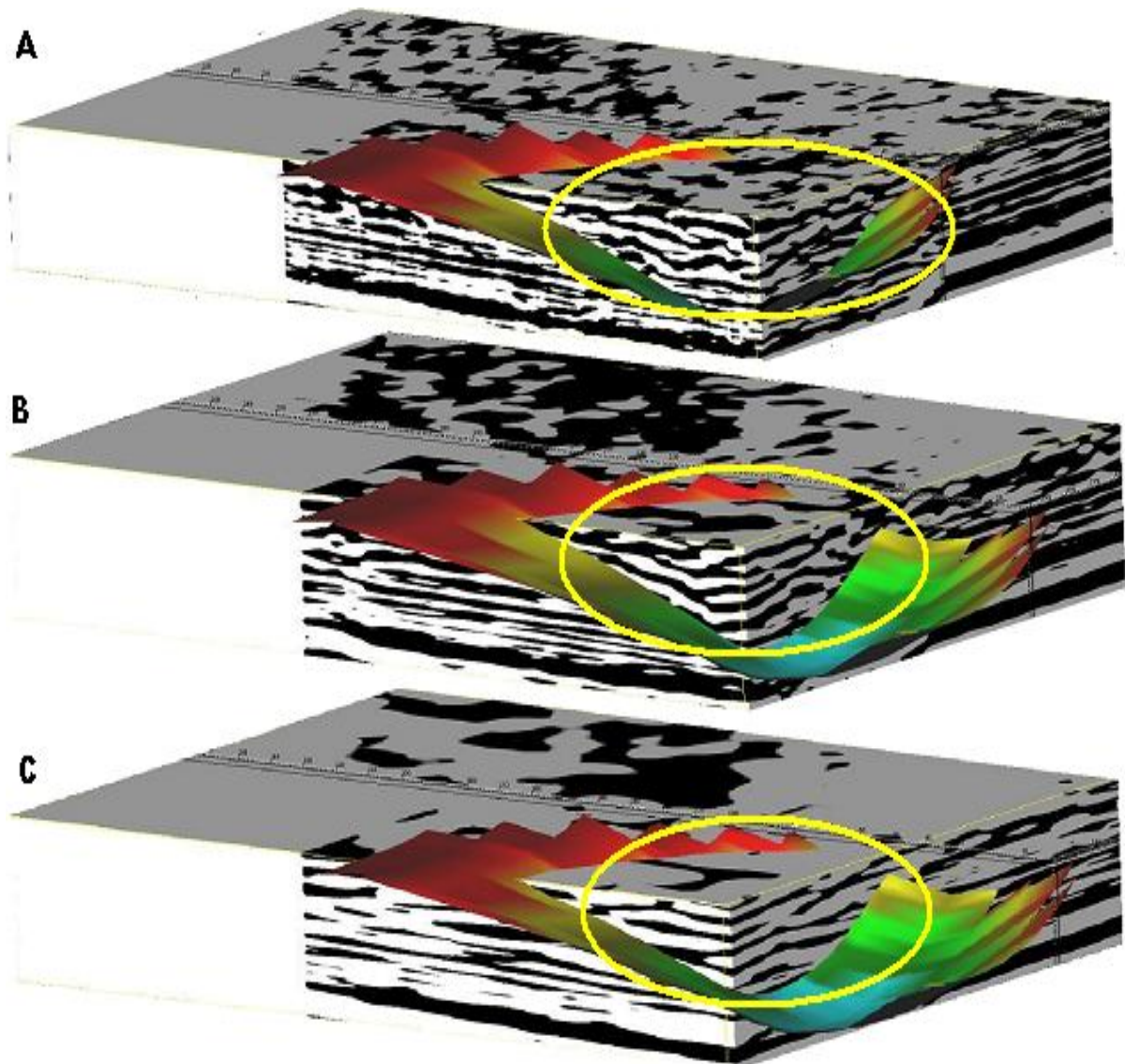


Fig. 3.2.1 Inversion to velocity volume presenting recirculation pool deposits from the River Dene, Macclesfield, site. Vertical extent of the volumes is 110 ns with the width of approximately 20 m and length of 50 m. Image A presents a volume with 0.5 m between lines and trace spacing of 0.10 m. The middle image (B) presents a volume with 0.50 m spacing between the lines and traces. Despite simplification of the image, when compared to the 0.50 x 0.10 m grid volume, the resolution is relatively good and the sedimentary information is still preserved. The bottom image (C) presents a true 3-D volume with 1.00 m between the lines and traces. The resolution is much poorer in comparison with the 0.50 x 0.50 m grid volume and the information related to sedimentary architecture is lost. The yellow circle indicates the recirculation pool deposits. The colour surface represent radar surface as explained in Chapter 4 and the colour represents relative TWTT.

A true 3-D data volume created from the pseudo 3-D Macclesfield data is shown as image B in Figure 3.2.1. This was done by including only 0.50 m spaced traces and therefore creating a 3-D volume with cell dimensions of 0.50 x 0.50 m. It should be noted that the resolution of the new volume was limited although the image remained interpretable. The bottom image (C) in Figure 3.2.1 presents the true 3-D data volume with cell dimensions of 1.0 x 1.0 m. Despite the interpolation between traces, the information included in this volume is oversimplified and the information on sedimentary architecture is lost, *e.g.* the concave reflection lines within the recently filled pool, indicated with a yellow circle, appear here to be flat-lying and the edge of the point bar behind the pool is not clear. The lateral distance between reflections from different interfaces recorded at the same depth (TWTT) or visible on time slices is between 0.3 and 0.5 m. The experiment would suggest that the cell dimensions of a 3-D grid should not be below distances between interfaces on time slices. The estimate does not account for loss of resolution due to signal attenuation and depth of the imaged structures.

Figure 3.2.2 presents a similar experiment for structures found in the South Saskatchewan River 10 x 10 m grid between depths of about 3.50 and 6.50 m (see facies classification in Section 4.3). The recorded signal which was reflected from interfaces at this depth has a much lower quality than the signal reflected from shallow interfaces in this dataset. The images show a deep scour fill with cell dimensions of 0.10 x 0.10 m (top), 0.30 x 0.30 m (middle) and 0.50 x 0.50 m (bottom). The lateral distance between inclined reflections in the volume with 0.10 x 0.10 m cell dimension is between 0.3 and 1.0 m. These structures were poorly imaged in the 0.50 x 0.50 m volume. These images show that the distances between parallel lines and traces not only depend on the scale and complexity of the imaged sedimentary structures but also the desired depth of penetration and quality of the recorded signal.

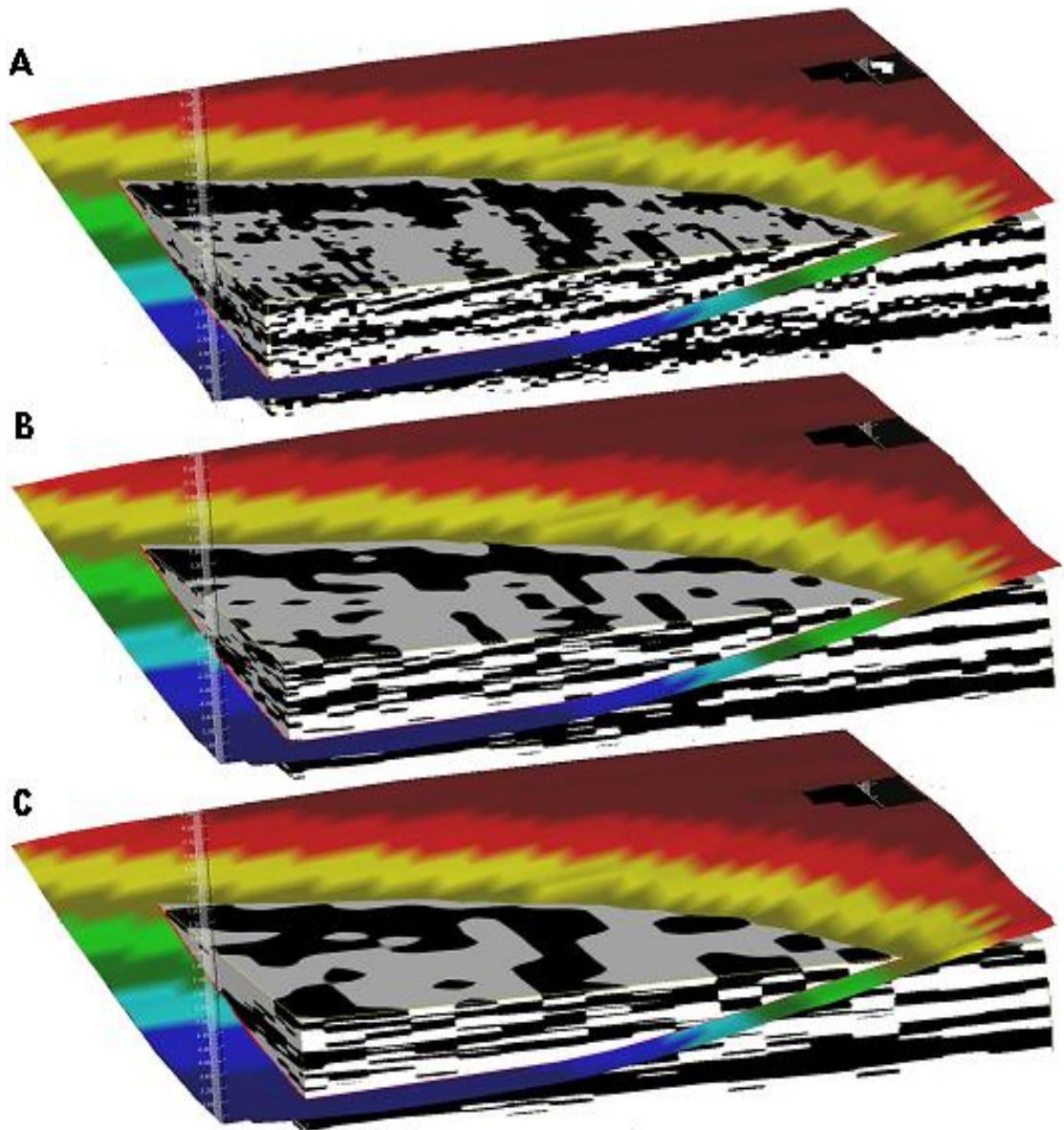


Fig. 3.2.2 Amplitude volumes presenting the deep scour fill in the South Saskatchewan River 10 x 10 m grid volume with trace and line spacing of 0.10 x 0.10 m (A), 0.30 x 0.30 m (B), and 0.50 x 0.50 m (C). Volume with cell dimensions of 0.10 x 0.10 m is presented at the top. Image of volume with cell dimensions of 0.30 x 0.30 m in presented in the middle. Resolution is significantly lost although some of the information can still be interpreted. Image of the volume with cell dimensions of 0.50 x 0.50 m is presented at the bottom. Resolution is very poor and very little can be interpreted from the volume.

This would again suggest that lateral resolution is directly related to the distance between stations and lines. Distances between survey points, *i.e.* traces and survey lines, will correspond with lateral resolution. Signal dispersion and attenuation will naturally lower the resolution with greater depth (Neal 2004, Annan 2009). Spherically shaped front of the propagating wave results in the dispersion of signal and gradually decreasing with depth lateral resolution.

Due to complex character of electromagnetic wave sent by bipolar antenna, it is difficult to establish a simple mathematical relation between line spacing and the size of the investigated sedimentary structure, particularly if they are characterised by a complex inclined pattern. Such a relation would be affected by the antenna frequency, attenuation of the materials in the subsurface and the character of the surface. However, it should be possible to establish simple empirical relations such as the one by Woodward *et al.* (2003) who reported that 10 survey stations above a certain feature was a minimum to be able to resolve it. As was shown on the examples in Figures 3.2.1 (Macclesfield dataset) and Figure and 3.2.2 (the South Saskatchewan River 10 x 10 m dataset), a distance of 0.50 m between lines was still able to provide sufficient lateral resolution to image structures of a lateral extent of a few to several metres. The subject of distances between survey points is further discussed in Chapter 6.

### 3.2.2 Amplitude volume visualisation

Three-dimensional data may be displayed as *surface visualisation*, which enables time slicing and the tracing of horizons across adjacent lines, or as *volume visualisation*, which allows display of the data as a cube (Kidd 1999). For volume visualisation, trace samples are converted into voxels, defined as three-dimensional pixel images. The pixel information (in colour or greyscale) corresponds to the original amplitude values. This technique enables the display of voxels in a defined colour scale and opacity known as the *zone system*. Application of scale and opacity has a trial-and-error character and aims to show only those ranges of amplitude values which are associated with the desired, interpretable information about the subsurface.

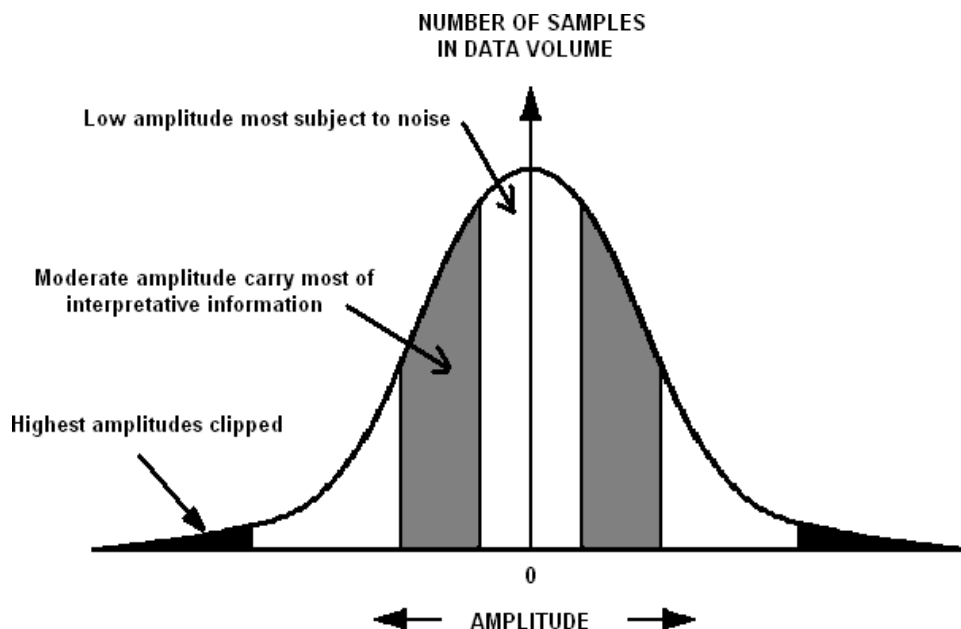


Fig. 3.2.3 Modified from Brown (2004): normal distribution of amplitude values of samples in seismic data volumes.

The model of the range of amplitude values for seismic datasets has a normal (Gaussian) distribution, and has been presented by Brown (2004) as shown in Figure 3.2.3. Moderate amplitudes are most often associated with structural information, whilst low amplitude samples are associated with random and systematic noise. The highest values are considered as anomalies and are usually removed from datasets. Distribution of the signal amplitude in GPR datasets is shown in the histograms included in Figures 3.2.4 to 3.2.6. The opacity/transparency technique enables the display of certain ranges of amplitude values in a user-defined colour scale. The datasets presented in this thesis are displayed in grey scale with high contrast applied. This was done to increase the contrast of the image. Although transparency may not always be useful for displaying reflection surfaces related to small-scale fluvial sedimentary structures, it was also applied to analyse what information is carried by certain ranges of amplitude within the datasets presented in this project.

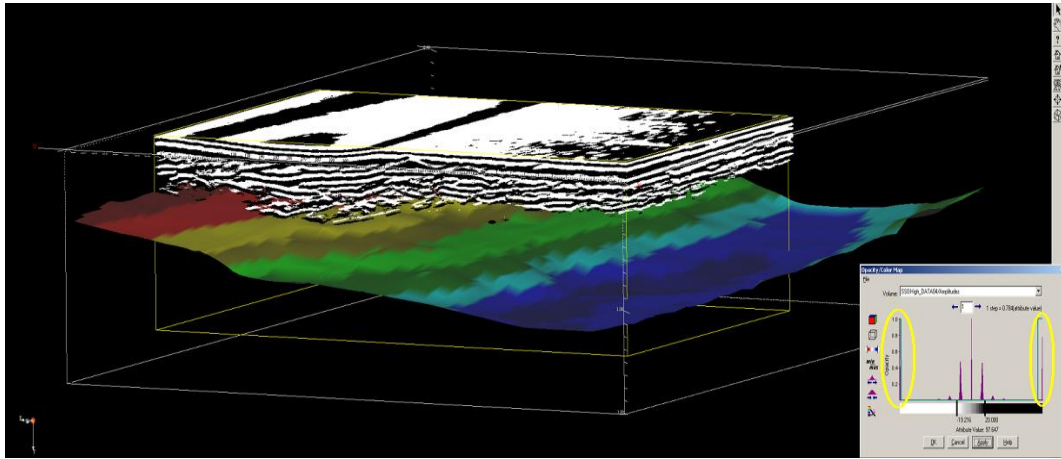


Fig. 3.2.4A The South Saskatchewan River 120 x 40 m dataset: transparency applied to the low and moderate signal amplitudes, *i.e.* only high amplitude signal displayed (indicated with yellow circles in the diagram), resulted in the near-surface structures being imaged with reasonable resolution and lower part of the volume being transparent.

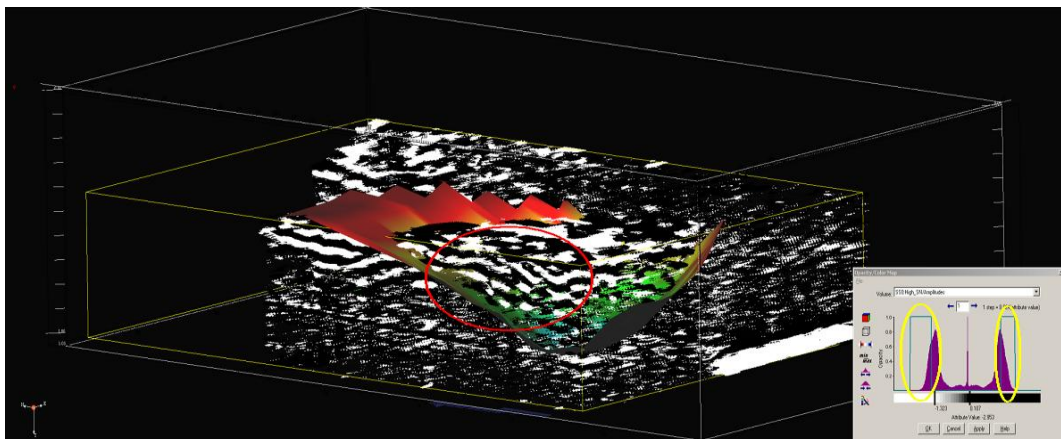


Fig. 3.2.4B The Macclesfield dataset: transparency applied to low and lower-moderate signal amplitudes, *i.e.* only high amplitude signal is displayed (indicated with yellow circles in the diagram). Slightly deeper structures within the recirculation zone are shown.

The histograms show that relatively moderate amplitude samples dominate the GPR data volumes while samples of the lowest amplitude are less frequent. Such proportions may be a result of the different shape of electromagnetic wavelets when compared to the acoustic signal. Figure 3.2.4a presents the volume which consists of the dominant moderate amplitude samples. The samples represent mainly noise within the upper part of the volume, although sedimentary structures are well-resolved within the middle part of the volume. Transparency proved to be useful for displaying complex sedimentary structures such as those deposited by reverse currents on the Macclesfield site (shown in Figure 3.2.4b). Together with adjustment of the colour scale, it is possible to display only the relevant reflections.

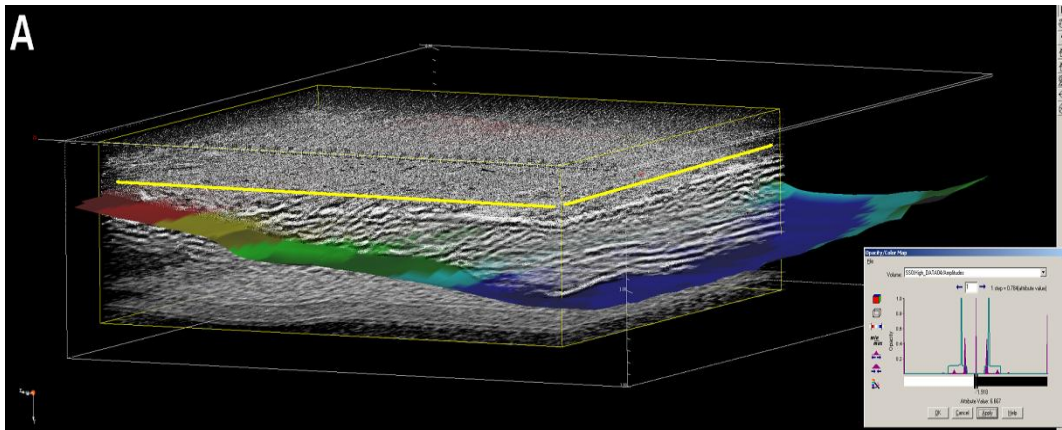


Fig. 3.2.5A The South Saskatchewan River 120 x 40 m dataset: transparency applied to low and high signal values. Moderate amplitude volume reveals well the sedimentary structures within the middle part between the yellow line and the radar surface (colours indicate relative TWTT). Repetitive noise which obscures the dipping reflection lines is shown in this part of the volume. Vertical extent of the volume is 160 ns.

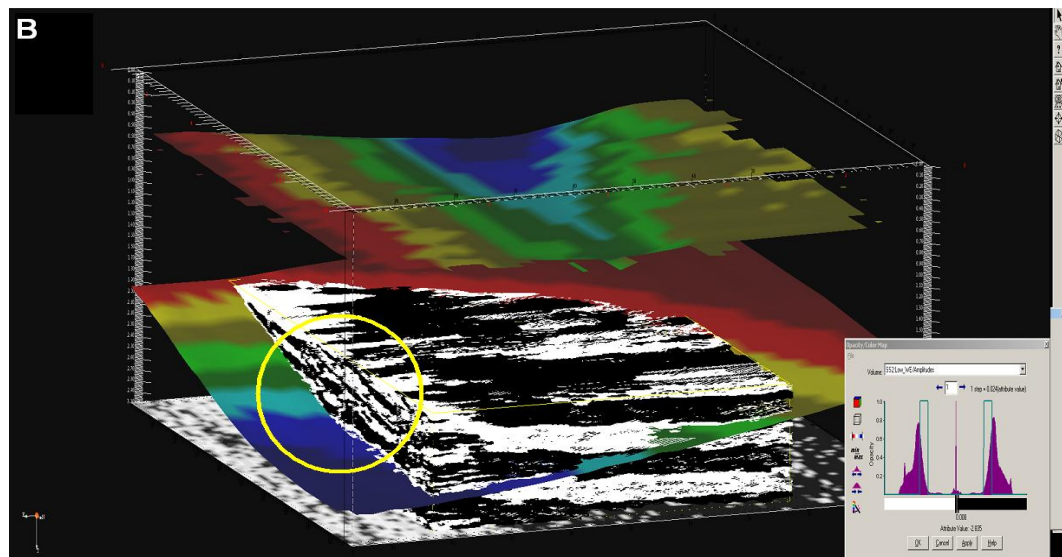


Fig. 3.2.5B The South Saskatchewan River 10 x 10 m dataset: transparency applied to low and high signal values. Moderate amplitude volume reveals dipping reflection lines indicated by the yellow circle and the surface. Repetitive noise is weaker although the structures are located in the bottom part of the volume. Bottom of the displayed volume is at 270 ns.

The images would suggest that similarly as with seismic data information related to fluvial sedimentary structures is carried by the dominant, moderate amplitude signal (Figures 3.2.5A and B).

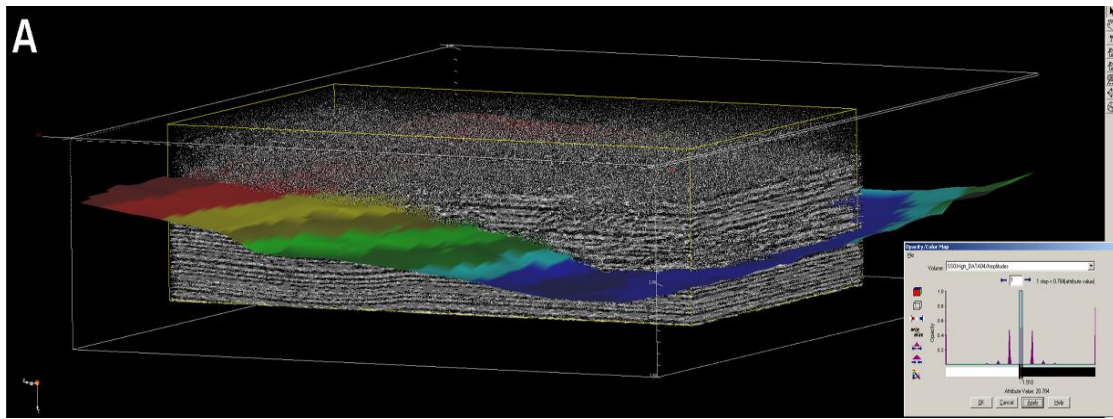


Fig. 3.2.6A Transparency applied to high and moderate amplitudes in the South Saskatchewan River 120 x 40 m volume. The lowest amplitude samples carry only noise. Vertical extent of the volume is 160 ns.

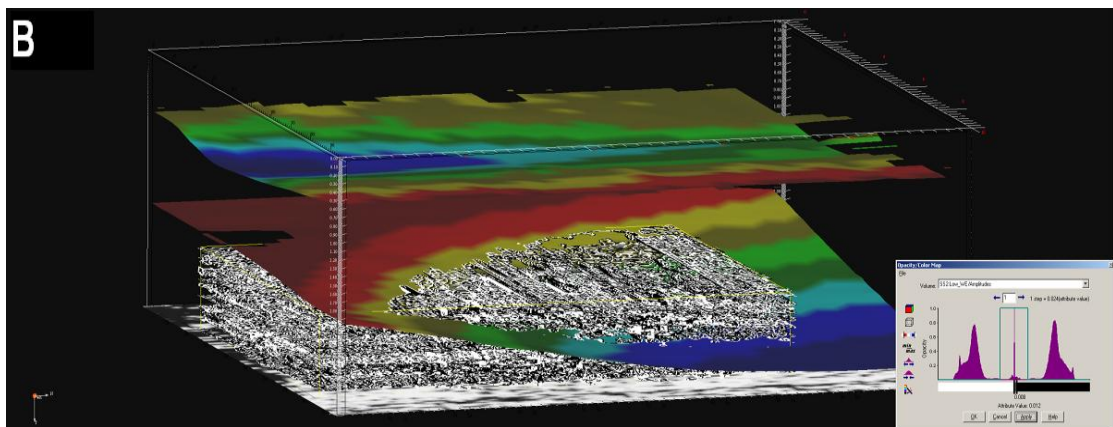


Fig. 3.2.6B Transparency applied to high and moderate amplitudes in the South Saskatchewan River 10 x 10 m volume which also are associated with the noise recorded at greater depths. Bottom of the displayed volume is 270 ns.

Lower parts of radar data volumes are dominated by random and repetitive noise, *i.e.* multiple reflections, represented by the lowest amplitudes (shown in Figures 3.2.6A and B). Only a very limited amount of information related to sedimentary surfaces can be recognised in these images.

As shown above, moderate amplitude signal associated with sedimentary architecture is dominant in the GPR datasets. Signal associated with noise is easy to identify and remove. This makes the volume visualisation of GPR data a very useful tool for investigation of fluvial sedimentary structures. Other techniques, such as high-frequency inversion (described in Section 3.2.5), may also be applied together with it.

### 3.2.3 Horizon tracing

Horizon tracing helps to investigate and visualise in 3-D any features across adjacent lines. An example of such a 3-D display is shown in Figure 3.2.7. Steps required to produce such surfaces are summarised below. Such surfaces use a colour scale to display various associated properties such as the relative depth, frequency, phase or amplitude. Wave properties are useful when automatic picking is used. In seismic data interpretation, horizon tracing is done by various auto-picking techniques. The software searches across adjacent traces for respective peaks, troughs or zero-crossing values (Brown 2004). Displaying various wave properties leads to creation of horizon slices which are frequently used in seismic volumes to identify morphological features such as river channels. An example of the application of horizon slices is presented in Figure 3.2.7 which shows a network of channels highlighted by various attributes (Chopra and Marfurt 2007).

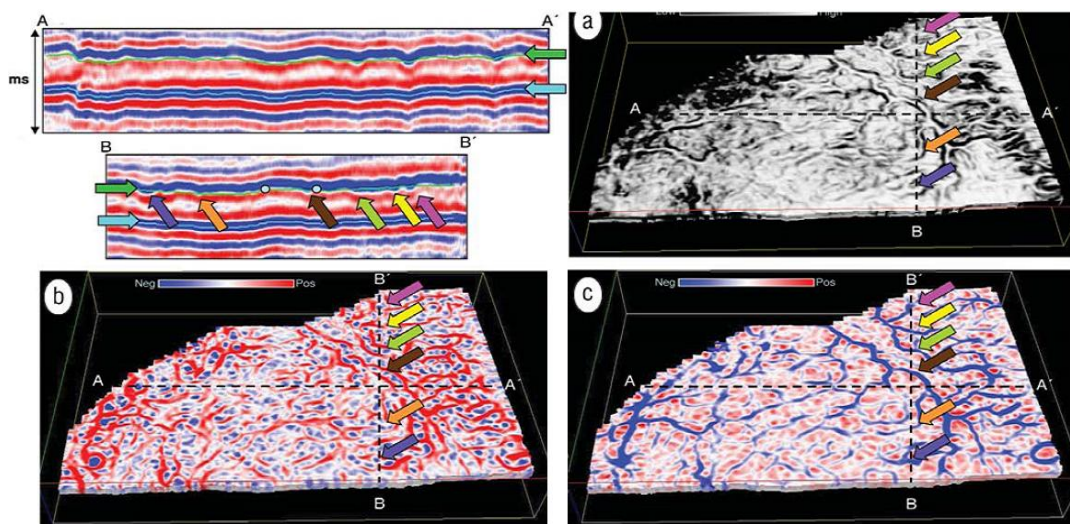


Fig. 3.2.7 Example of applying horizon slices to display geomorphological features, *i.e.* network of river channels, presented by Chopra and Marfurt (2007). The depth of the displayed horizon slices are indicated by the green arrow on the 2-D profiles presented in the top left corner. The horizon slices display semblance (see Glossary) (A), most positive (B) and most negative curvature (C) wave attributes.

Auto-picking techniques require relative similarity between wavelets in adjacent traces, and with GPR data manual picking was required. Low similarity between adjacent wavelets may have been related to the much higher frequency and shorter wavelength of GPR signal when

compared to seismic data. Traced surfaces, *e.g.* erosional surfaces associated with the recirculation pool in the River Dene, were picked manually both on the ‘in-lines’ and ‘cross-lines’. Both the ‘in-line’ and ‘cross-line’ profiles were also used for horizon tracing when the amplitude volumes provided poor information due to strong signal attenuation. As horizon tracing was done manually, points were placed in random sections of the wavelets and also random wave properties were displayed on the traced surfaces. Automatic picking places the picking points in set parts of wavelets and enables the display of various wave attributes on the radar surface such as phase, velocity (Figure 3.2.8), frequency and average energy (Figure 3.2.11). Thus only the colour scale displayed on the radar surfaces represents TWTT.

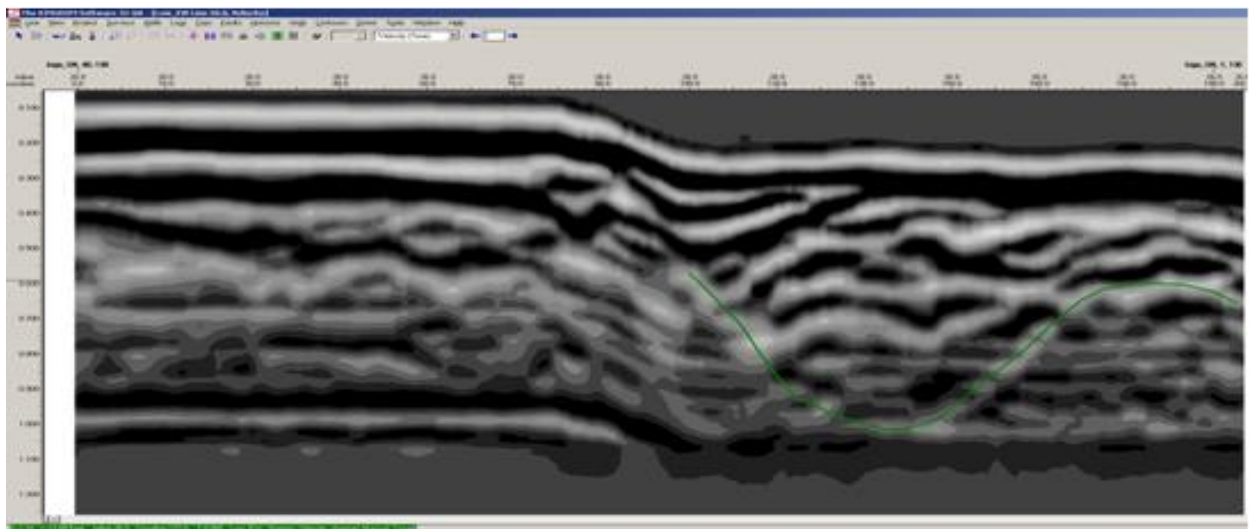


Fig. 3.2.8 Manual tracing of the erosional surface scoured by a recirculation pool was completed on an inverted velocity profile. The velocity attribute was found to better image structures at greater depths.

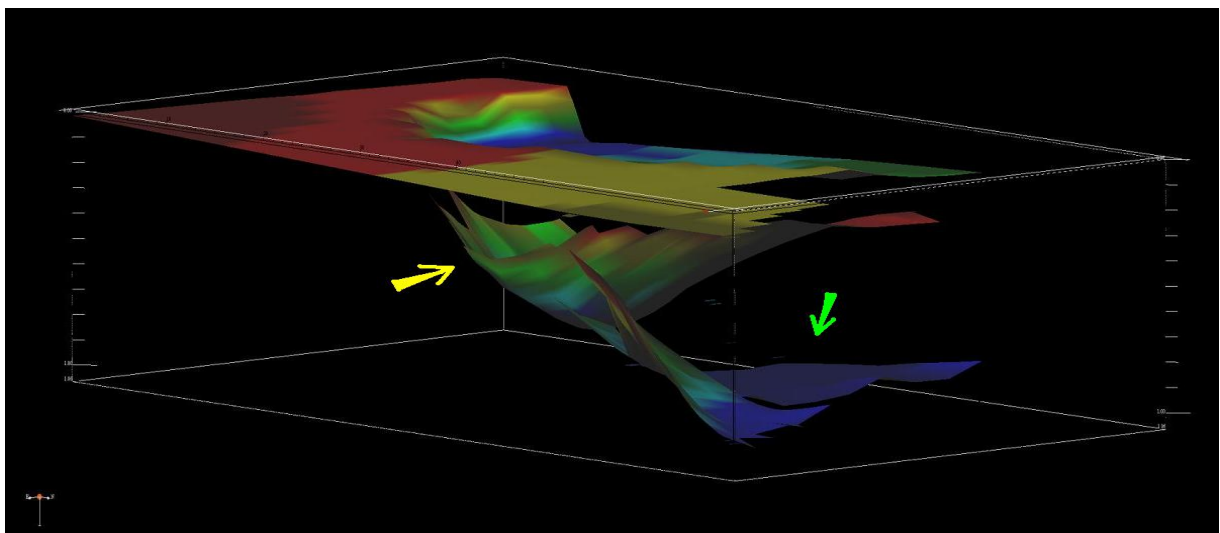


Fig. 3.2.9 The final result of horizon tracing: erosional surfaces of recirculation zone (indicated by yellow arrow) and older channel (indicated by green arrow) with the ground surface above.

### 3.2.4 Time slices

Time slices are used to trace events across adjacent lines and can be very useful when applied to fluvial sedimentary structures. Time slices display amplitude at a certain two-way travel time (TWTT) below the ground surface. An example of the application of a time slice is presented in Figure 3.2.10.

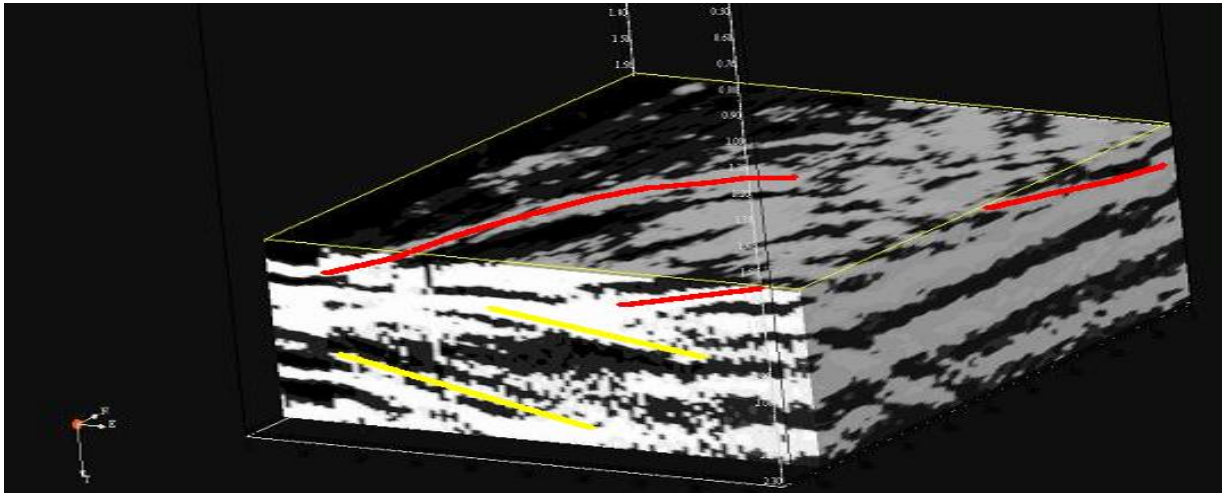


Fig. 3.2.10 The South Saskatchewan River 10 x 10 m grid volume with time slice at 163.2 ns reveals a series of curved lines which could be identified in all the time slices (*e.g.* indicated by red line), slowly moving with depth to the south east and changing orientation with depth (yellow lines). The reflection lines inclined to the south east are also visible on the in-lines and cross-lines. Horizon tracing later led to interpretation as a deep scour with cross-bedded structures within it.

The time slice in the South Saskatchewan River 10 x 10 m dataset showed curved shapes (Figure 3.2.10). This led to an investigation of the reflection lines on vertical profiles and their correlation was possible due to application of horizon tracing. These reflection lines were investigated in 2-D (see Section 4.2); however, only their display in 3-D enabled their interpretation as a deep scour filled with inclined strata parallel to the scour surface (see Section 5.2).

### 3.2.5 Data inversion

The data inversion technique converts profiles which display reflection surfaces, *i.e.*

interfaces between layers of different properties, into sections which directly display zones characterised by wavelet attributes (*e.g.* average velocity) related to properties of the subsurface, *i.e.* electric permittivity (Bacon *et al.* 2003). As a result, profiles display representations of lithological units, such as mud drapes or high porosity layers, instead of boundaries between these lithological units. In the case of seismic datasets inversion converts wave amplitude data volumes, *i.e.* impulses reflected from the interfaces, into acoustic impedance volume. In the case of GPR data, the new volume presents changes in dielectric properties which are related to the lithology. The displayed datasets imitate volumes which would consist of closely spaced geological cross-sections. Such data are easier to interpret in terms of sedimentary architecture.

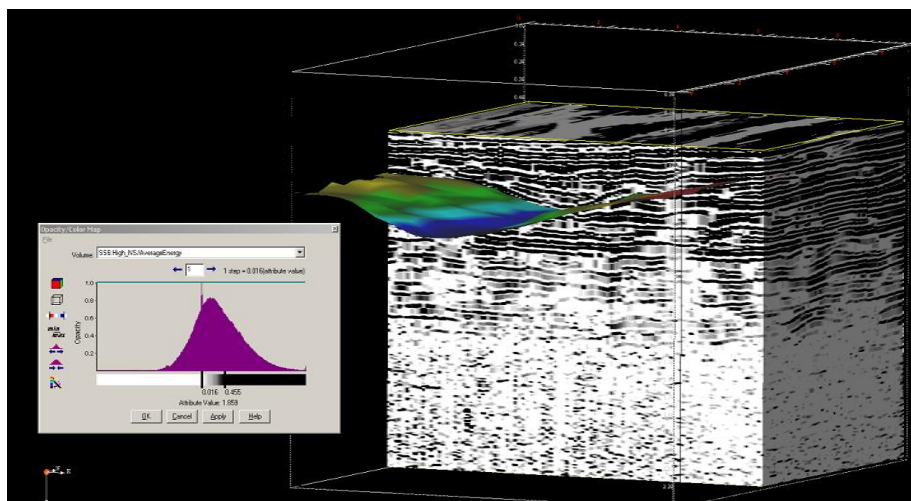


Fig. 3.2.11 Fragment of the South Saskatchewan River 10 x 10 m grid volume. Average energy volume displayed with high contrast together with upper channel horizon. The surface which indicates the boundary between sedimentary units is no longer cutting the middle of the reflection lines but runs along the boundary between the ‘black and white’ lines which should be interpreted as lithological layers. Vertical extent of the volume is 270 ns.

This is shown in Figure 3.2.11, where layers have a specific average energy range. In inverted data, black and white lines, instead of representing interfaces between lithological units as is the case with normal GPR profiles, represent the lithological units themselves.

### 3.2.6 Application of opacity/transparency

Opacity/transparency techniques are useful in such applications as the detection and tracing of plumes of contaminants or general objects of characteristic amplitude or frequency (Annan 1999). Opacity is less important in applications such as investigation of fluvial sedimentary architecture. However, by making a certain range of signal transparent, it is possible to investigate specific sections of the subsurface and view sedimentary structures in greater detail. To illustrate this, the Macclesfield data is used. Figure 3.2.12 shows examples of complex sedimentary structures.

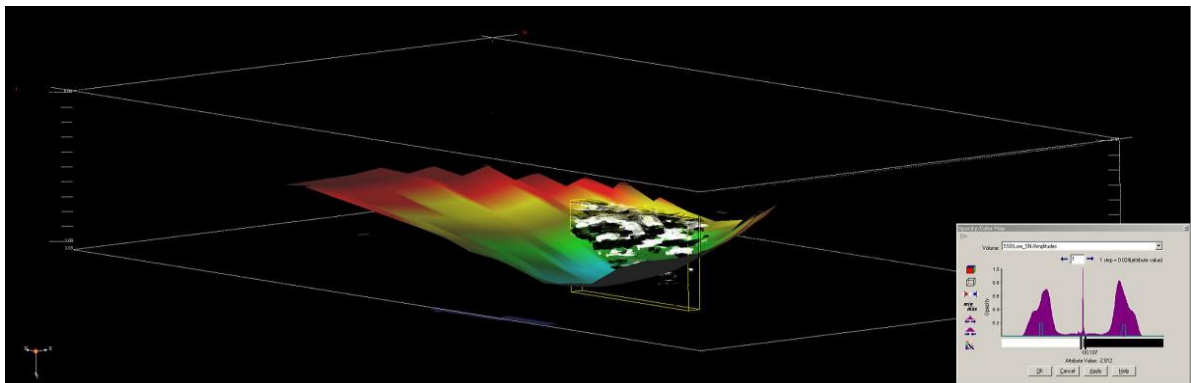


Fig. 3.2.12 Section of volume representing the recirculation zone on Macclesfield site is used to investigate details of sedimentary structures. Opaque amplitude values are shown on the histogram in the bottom right corner.

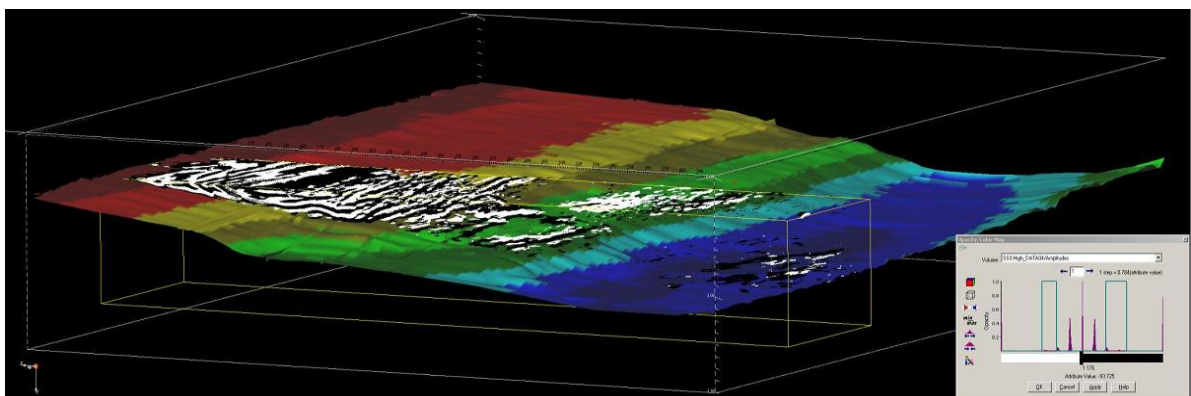


Fig. 3.2.13 Application of opacity/transparency technique to display in detail the sedimentary structures within the South Saskatchewan River 120 x 40 m grid dataset.

In a similar way the opacity/transparency technique was applied to certain ranges of amplitude in the South Saskatchewan River 120 x 40 m data (Figure 3.2.13) to resolve details of cross-bedding and trace reflection surfaces characterised by the strongest amplitude values.

### 3.2.7 Summary

As has been shown in this section, seismic interpretation techniques developed for hydrocarbon exploration can also be applied to grids of closely spaced 2-D GPR profiles and can be used to investigate sedimentary architecture of fluvial deposits. Some of these techniques have already been used for hydrogeological studies (see Section 2.0); however, their application in fluvial sedimentology is less common even though they could be a useful tool for the investigation of spatial relations between sedimentary structures. Further examples of the 3-D display of GPR data is presented using animations in Appendix 3.

## CHAPTER 4

### 4.0 TWO-DIMENSIONAL INTERPRETATION OF GPR PROFILES

This section presents the methodology, with examples, that has been used to interpret individual 2-D GPR lines. Analysis of the sedimentological meaning of single trace events is briefly explained, followed by an explanation of established 2-D interpretation procedures. Examples of 2-D interpretation are presented in Sections 4.1 to 4.3. The methodology for interpretation of 3-D datasets follows in Chapter 5.

#### 4.0.1 Interpretation of single trace events

Different GPR users and geophysical instrument manufacturers use different approaches to the interpretation of recorded reflection events (Yelf 2003). This thesis follows the methodology published by Sensors & Software (2007). The approach was chosen because of the equipment used to collect the presented data, and because the company has published a considerable number of papers on interpretation of GPR data, including its application in sedimentary studies.

The first positive phase peak, marked in black in greyscale profiles, bounded by two slightly weaker negative phase peaks, marked in white, is identified as the direct air-wave. The second recorded wavelet, a negative phase peak bounded by weaker positive peaks, is recognised as the ground-wave. The signal reflected directly from an underground interface may be either negative or positive depending on the Fresnel reflection coefficient  $R$ . As effect of electric conductivity and relative magnetic permittivity is negligible, Neal (2004) expressed  $R$  as the function of contrast in relative electric permittivity  $\varepsilon_r$  between two zones:

$$R = \frac{\sqrt{\varepsilon_1} - \sqrt{\varepsilon_2}}{\sqrt{\varepsilon_1} + \sqrt{\varepsilon_2}}$$

As described in Section 3.0, this depends on the contrast in electric permittivity between two sedimentary units at the interface (shown in Figure 4.0.1). The groundwater table, similarly as the ground surface (air/soil interface), is characterised by an increase in electric permittivity and therefore is indicated on the profile by a white negative phase peak. However, the standard approach developed at the start of the 1990s (Saarenketo 2009) for engineering purposes, mainly to assess the quality of road subgrade, describes reflection from an interface where the lower layer is characterised by a higher electric permittivity and is marked in grey scale in white as ‘positive’.

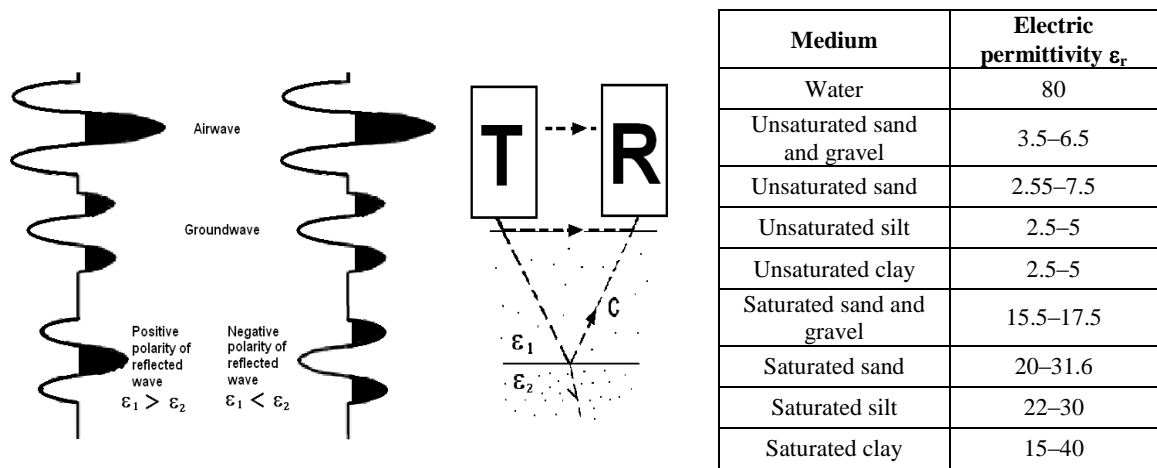


Fig. 4.0.1 Description followed in this work regarding the polarity of recorded wavelets. Direct first arrival (air-wave) is displayed as a positive phase peak usually marked in black, whilst the ground-wave is expressed as a negative phase peak marked in white. The phase of the wave reflected by underground features depends on the relative electric permittivity of the layers at the interface. Image modified from Sensors & Software (2007). Positive phase peak is associated with decrease in electric permittivity. Examples of relative electric permittivity of sediments (right) are taken from Neal (2004).

#### 4.0.2 Classification of reflection patterns on 2-D profiles

Classification of reflection patterns on GPR profiles is based on the concepts of radar stratigraphy which were first introduced at the beginning of the 1990s. Following the principles of seismic stratigraphy, reflection lines are considered to be isochronous, while their termination and truncation surfaces are associated with periods of lack of sedimentation (Neal 2004; Bristow 2009).

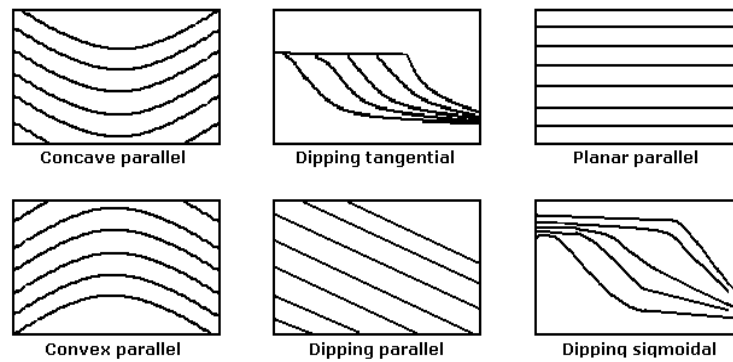


Fig. 4.0.2 Examples of radar facies described in terms of shape, configuration and relations between reflection lines modified from Neal (2004).

When the terminology used in seismic stratigraphy for the interpretation of reflection patterns was adopted for the specific requirements of radar data, it led to the introduction of the concepts of *radar surfaces*, *radar packages* and *radar facies* (Neal 2002, 2004). *Radar packages* refer mainly to 3-D geometries of depositional forms and will be further used in Chapter 5 which describes 3-D data. The term *radar facies* was first used by Jol and Smith (1992) and later defined by Huggenberger (1993, p. 166) as a “mappable, three-dimensional sedimentary unit composed of reflections whose characteristics differ from adjacent units”. Identification of *radar facies*, therefore, requires a description of the configuration of reflection lines: their shape, dip, continuity and relations between reflections (Figure 4.0.2), and their properties such as amplitude and frequency. As is shown in the following sections, although *radar facies* are identifiable from 2-D profiles, they should still be considered in reference to the 3-D character of sedimentary facies. The term *radar surface* refers to the boundaries of *radar facies*.

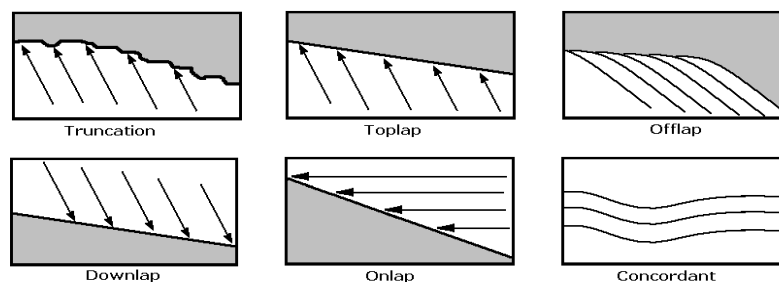


Fig. 4.0.3 Examples of the main types of termination of reflection lines (indicated with arrows) determining classification of reflection surfaces, modified from Neal (2004) and Catuneanu (2002).

Classification of the surfaces is based on the character of termination of reflection lines along their boundaries (Figure 4.0.3), *e.g.* erosional truncation, toplap, onlap, downlap, offlap. Based on these definitions, correct identification of radar facies and radar surfaces really require the application of 3-D datasets.

The terms *radar sequence* and *radar sequence boundary* were introduced by Gawthorpe *et al.* (1993) as an analogue of seismic interpretation. Following the definition given by Mitchum (1977, cited in Catuneanu 2002, p. 5), a sequence is “*a relatively conformable succession of generically related strata bounded by unconformities or their correlative conformities*”. Neal (2004) argued that these terms are related to bodies of different scales and should not be used in radar stratigraphy which deals with features of much smaller scale. Skelly *et al.* (2003), however, presented radar sequence boundaries in the Niobrara River (Figure 2.3.7). These boundaries represented erosional surfaces and surfaces separating components of different types of deposition which included cross-channel accretion, upstream accretion and high-angle downstream deposits. Similarly, Bristow (2009) applied the principles of sequence stratigraphy and identified bodies within a sand dune which were separated by erosional surfaces (Figures 4.0.4a and b) and demonstrated that they comply with the above definition of *sequence boundaries*. Similarly, the resolution and the range of penetration of GPR equipment may dictate that the hierarchy of radar bounding surfaces are generally below the five orders defined by Embry (1995) which are associated with major climatic and tectonically driven base level changes. Thus, the majority of *bounding surfaces* and *depositional sequences* imaged by GPR surveys are related to changes in sediment supply and available accommodation related to periodical, high frequency seasonal events such as floods, or fluvial processes such as unit bar migration. An exception from this in the GPR literature is surfaces such as those separating a meandering style of sedimentation from a braided one,

perhaps resulting from climatic change at the end of the last glaciation (e.g. Asprion and Aigner 1999).

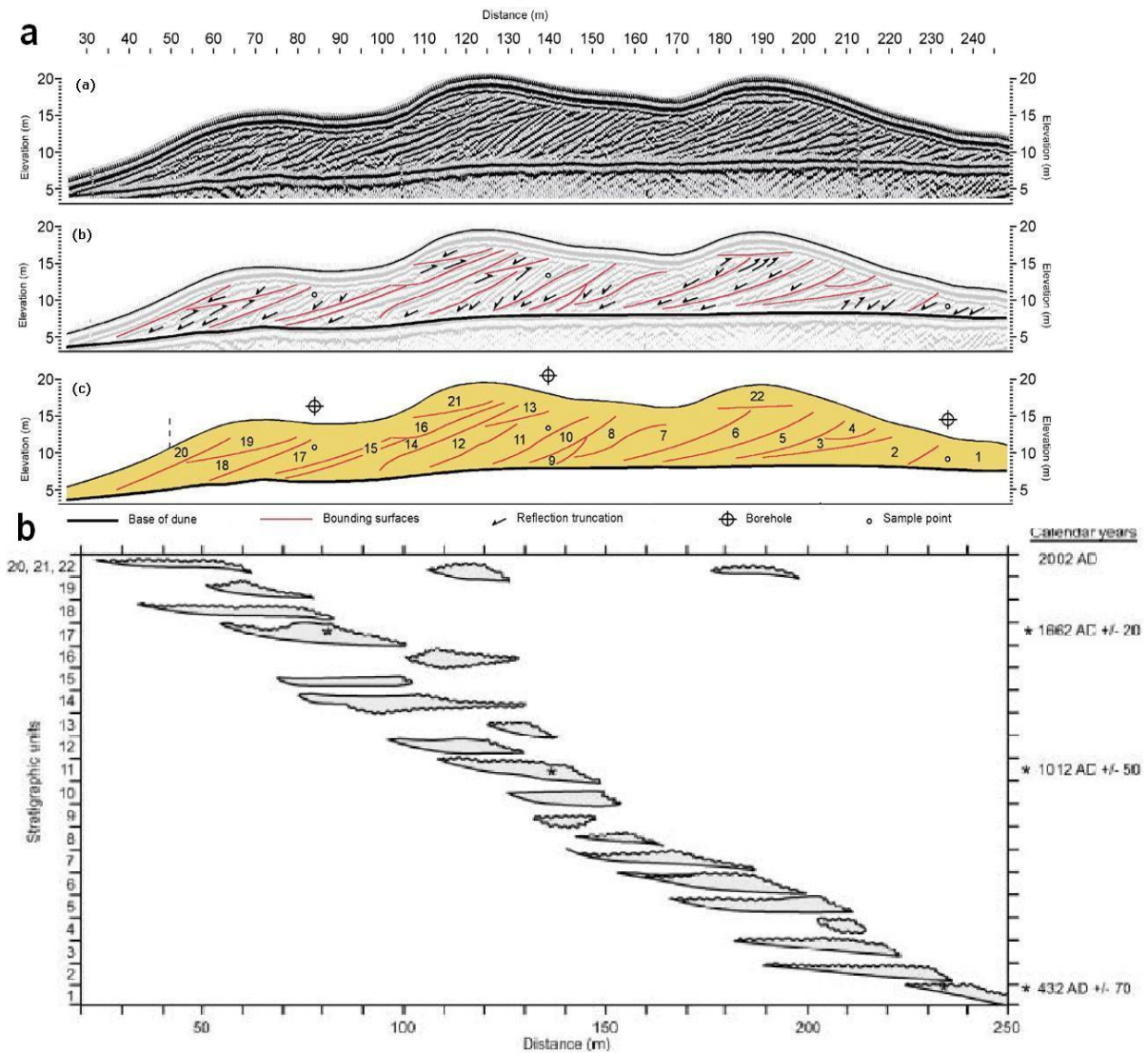


Fig. 4.0.4a Distribution of radar sequences within aeolian dune by Bristow (2009). Fig. 4.0.4b Chronostratigraphic chart (see Glossary) based on radar sequences recognised in GPR profiles. The vertical scale represents time of the origin of radar sequence, *i.e.* older deposits at the bottom of the chart (bottom line represents 432 AD, top line represents 2002 AD). The horizontal scale represents its location (total distance of 250 m).

*Radar facies* identified within the three datasets analysed in this thesis are therefore based on the geometrical relations of reflection lines, their character, location and bounding *radar surfaces*. Additional descriptions such as semi-parallel or semi-concordant, to describe close to parallel or concordant lines, were also introduced. Images shown in this section were created during the post-fieldwork processing described in Section 3.0.

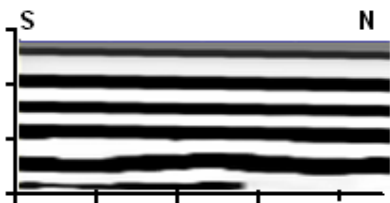
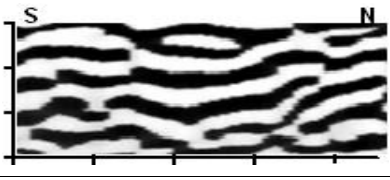
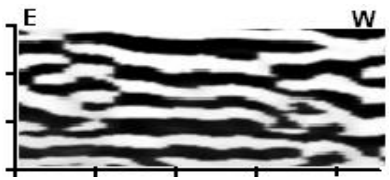
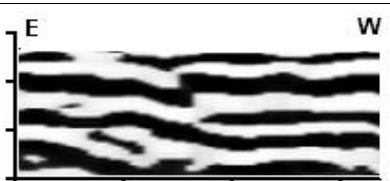
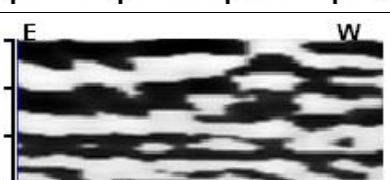
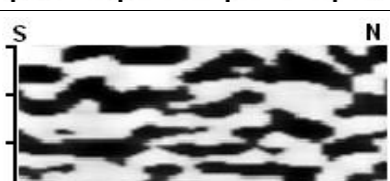
#### 4.1 CLASSIFICATION AND INTERPRETATION OF RADAR FACIES REVEALED BY 2-D MACCLESFIELD DATA

This section describes and classifies radar reflection patterns revealed by 2-D radar profiles collected from the Macclesfield site. An analysis of spatial relations between these radar facies is also presented. Photographs of the site are shown in Figure 4.1.1 and a topographical map is included as Figure 4.1.2.

Identifying radar facies was difficult due to only two main patterns dominating the profiles: (A) low-angle planar parallel pattern and (B) curved concave upwards or undulating reflections.

The first pattern was classified as radar facies (1). The latter pattern, based on its appearance on orthogonally oriented profiles, could be subdivided into the following four radar facies: (2) curved concave upwards or undulating, often concordant, reflections; (3) stronger-amplitude, concave upwards on S-N oriented profiles, parallel horizontal and slightly inclined on E-W oriented lines; (4) discontinuous concave upwards and undulating non-concordant reflections; (5) discontinuous undulating chaotic reflections with hyperbolic diffractions. Quantitative evaluation of radar facies occurrence followed the methodology applied by Sambrook Smith *et al.* (2006b) to the GPR profiles collected in the South Saskatchewan River who applied sampling every 10 m. Here due to the smaller scale of the dataset, vertical lines were drawn every 4 m to the bottom of each profile. The evaluation involved measuring the proportion of radar facies along each vertical sampling line. This led to estimation of proportions of sedimentary facies along each survey line.

Table 4.1 Summary of five identified radar facies with their variability on orthogonally oriented profiles. Vertical scale is in tens of ns, while horizontal scale in m.

	<b>Description</b>	<b>Representation</b>	<b>Sedimentary interpretation</b>
<b>Radar facies (1)</b>	continuous low-angle planar parallel		topsoil and over-bank vertical accretion deposit
<b>Radar facies (2)</b>	curved concave upwards or undulating, often concordant, reflections on S-N oriented profiles		recirculation pool deposits
	curved concave upwards or undulating, often concordant, reflections on E-W oriented profiles		
<b>Radar facies (3)</b>	stronger-amplitude concave upwards and half-concave upwards reflections on S-N oriented profiles		recent point bar deposits
	stronger-amplitude horizontal and slightly inclined semi-parallel reflections on E-W oriented profiles		
<b>Radar facies (4)</b>	discontinuous concave upwards and undulating non-concordant reflections on S-N oriented profiles		older channel deposits
	discontinuous undulating non-concordant reflections on E-W oriented profiles		
<b>Radar facies (5)</b>	discontinuous undulating chaotic reflections with hyperbolic diffractions		deposits surrounding the older channel

Identification of the radar facies which is based on geometrical relations on 2-D profiles would not be possible without taking into account their appearance on perpendicular lines. A

summary of the radar facies identified at the Macclesfield site with an appreciation of their 3-D character, which is represented by differences between patterns on E-W and S-N oriented profiles, is presented in Table 4.1.

#### 4.1.1 Radar facies (1): continuous low-angle planar parallel reflections

Continuous horizontal parallel reflections extend laterally beyond the site boundaries. The amplitude of these reflections is relatively high with vertical TWTT between positive amplitude peaks on higher resolution profiles of up to 5 ns. The value corresponds to a vertical distance of about 0.25 m, which is close to the maximum vertical resolution and therefore may be affected by the tuning effect, *i.e.* interference between signal reflected from adjacent interfaces.

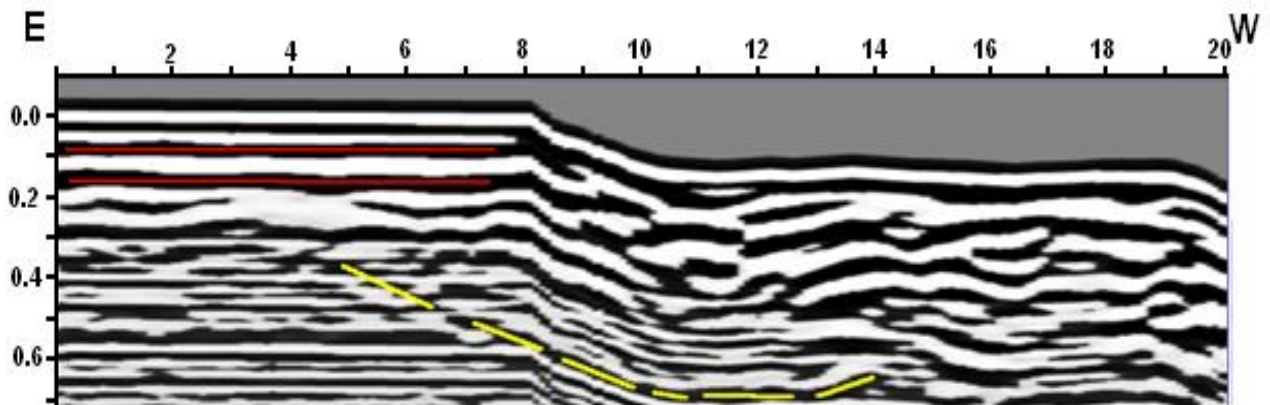


Fig. 4.1.1 Lower resolution line 24 EW (west to the right) from the Macclesfield site. Horizontal parallel reflections extend over the whole area of the site but are more distinct outside the former channel (vertical scale in hundreds of ns). As the lines associated with the direct arrival were removed from the image, the first visible white line (negative phase peak) is considered as the ground surface. Horizontal parallel lines at the bottom of the profiles are related to the repetitive noise. The yellow dashed line indicates a potential 'slip surface' related to instability of the former river bank (vertical TWTT scale in hundreds of ns with 10 ns = 0.40 m).

At least two layers of strong amplitude reflections underlie the area surrounding the pool, and sometimes also extend over the pool area, although sometimes with a more undulating or sub-horizontal character. The total thickness of this group of reflections is up to 1.00 m. This pattern accounts for 25% of all profiles and generally dominates their top parts (Figure 4.1.1).

#### 4.1.2 Radar facies (2): curved concave upwards or undulating, often concordant, reflections

Concave upwards and undulating concordant and semi-concordant reflections extend laterally by up to 10.0 m with depths of single concave upwards reflections not exceeding 0.50 m and the total thickness of the radar facies up to about 1.20 m. The amplitude of these reflections is moderate to strong. The radar facies (2) are indicated by red lines in Figures 4.1.2 to 4.1.4.

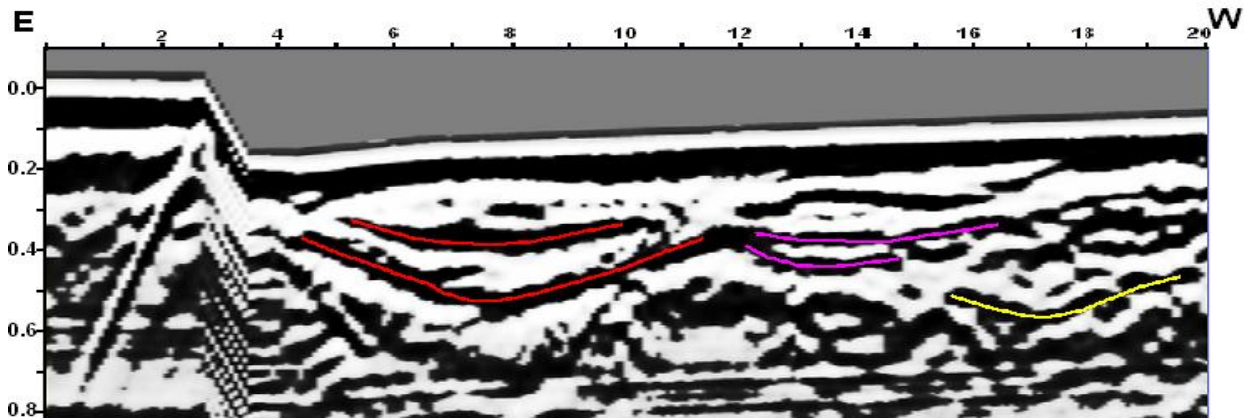


Fig. 4.1.2 Lower resolution line 02 SN (north to the right) is immediately adjacent to the east of the river bank. The profile shows concave upwards reflections, indicated by red lines. The bottom reflection, indicated by a positive phase peak (black line), is related to a decrease in electric permittivity (possibly vertical change from deposits of higher to lower porosity or lower to higher compaction). Such a feature may be interpreted as an erosional surface. The estimated maximum depth of the feature is approximately 1.00 m below ground level. Pink lines indicate reflections of uncertain classification but which may form part of the recirculation zone. Yellow lines indicate concave upwards reflections described as radar facies (4) (see Section 4.1.4) (vertical TWTT scale in hundreds of ns with 10 ns = 0.40 m).

The vertical TWTT between peaks of positive amplitude is between 5 and 20 ns which should correspond to a vertical distance of 0.20 to 0.50 m. This pattern forms approximately 15% of all profiles. These patterns are mainly restricted to the recirculation pool. Convex reflections which join adjacent concave upwards lines may also be present in the central part of the recirculation zone on some of the W-E oriented profiles.

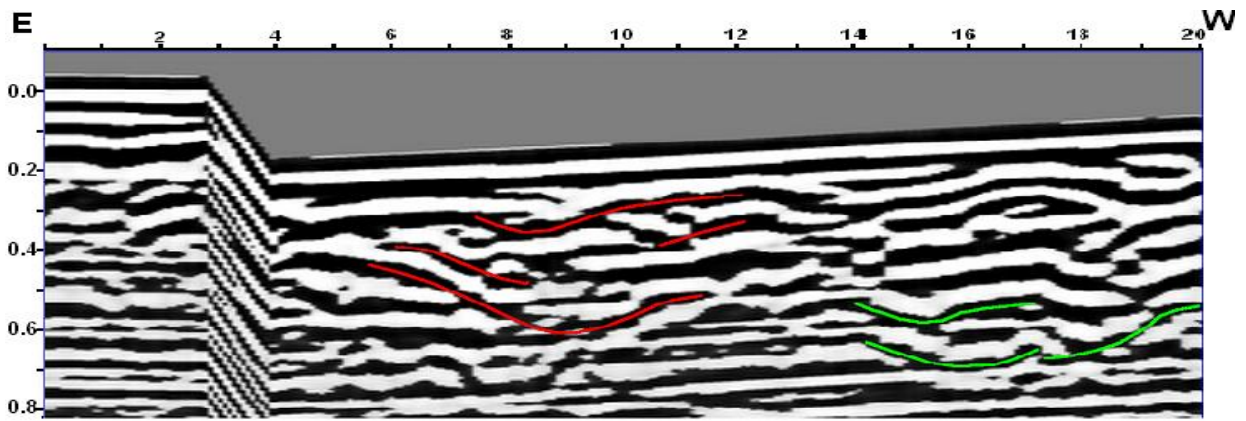


Fig. 4.1.3 Higher resolution line 06 SN (north to the right). The image shows the concave upwards reflections of radar facies (2) marked in red. Green lines indicate radar facies (3) described in Section 4.1.3. The characters of both facies appear to be similar on the S-N oriented profile; however, the shapes have different characters on the E-W oriented lines (vertical TWTT scale in hundreds of ns with 10 ns = 0.40 m).

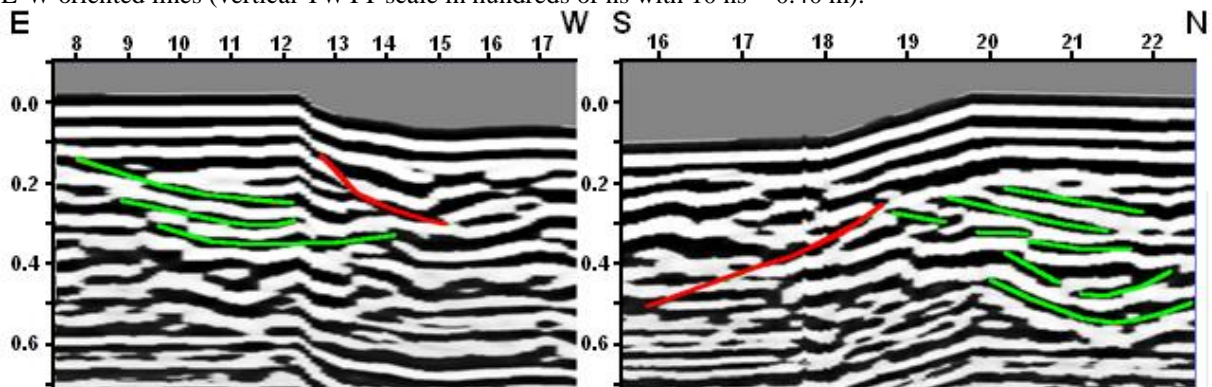


Fig. 4.1.4a (left) Fragment of higher resolution line 43 EW (west to the right). Located along the northern site boundary, concave upwards reflections (shown in red) are truncated by those with a similar pattern (green) located within the eddy pool. Fig. 4.1.4b (right) Fragment of higher resolution line 19 SN (north to the right). The image shows the concave upwards reflections to the north of the recently filled pool area (marked in green) and the eddy pool deposits marked in red (vertical TWTT scale in hundreds of ns with 10 ns = 0.40 m).

It is uncertain, however, without correlation of the profiles with lithology from boreholes or excavations, if these reflections form part of the fill of the recirculation zone or underlie the erosional surface of the pool and represent older deposits (see Section 4.1.4).

#### 4.1.3 Radar facies (3): stronger-amplitude, concave upwards on S-N oriented profiles reflections, parallel horizontal and slightly inclined on E-W oriented lines

Concave upwards concordant and nearly concordant reflections of relatively strong amplitude reflections are visible on S-N oriented lines while on E-W oriented images they are characterised by a low-angle, slightly inclined to the west. Correlation of the adjacent profiles revealed that the axis of the group of concave upwards reflections is most likely to be oriented

along an E-W trending line. The reflections are marked with green lines in Figure 4.1.5.

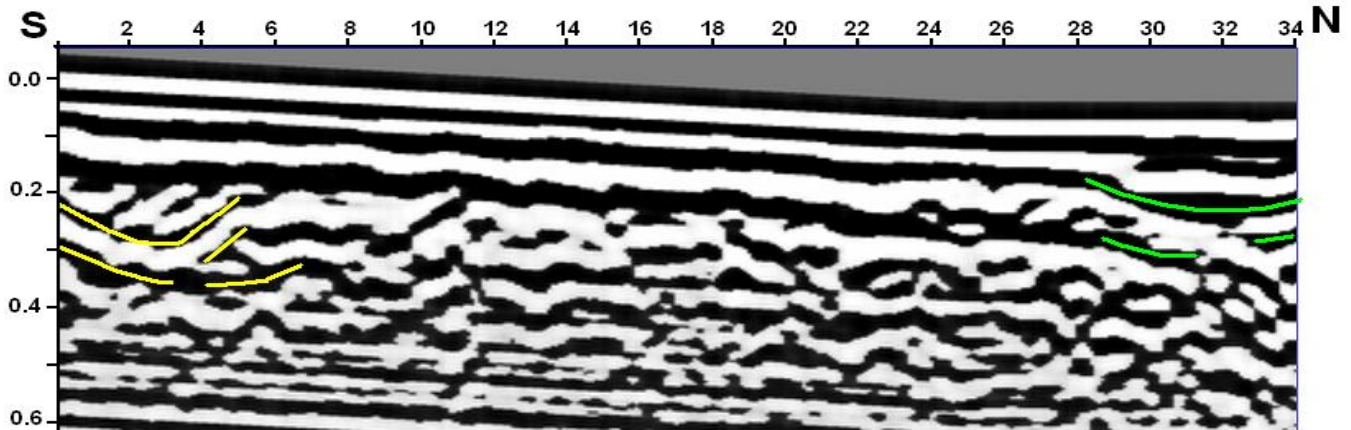


Fig. 4.1.5 Higher resolution line 37 SN (north to the right) shows examples of concave upwards shapes located to the north of the recirculation pool area. A possible 'bow-tie' effect is noticeable at the bottom of the lower line. Green concave upwards lines are located adjacent to the river bank (vertical TWTT scale in hundreds of ns with 10 ns = 0.40 m). Yellow lines indicate radar facies (4) (see Section 4.1.4).

The frequency of occurrence of the pattern across all profiles is approximately 10%. The S-N oriented survey lines terminated at the river bank and the bottom part of the half-concave upwards pattern may further continue to the north below the river bed. This radar facies dominates the northern edge of the site, immediately to the south of the river bank.

#### 4.1.4 Radar facies (4): discontinuous concave upwards non-concordant reflections

A discontinuous concave upwards pattern of reflections of variable scale and relatively weaker amplitude is classified as radar facies (4). These structures are indicated by the yellow line in Figure 4.1.8. The concave upwards reflections seem less concordant, more randomly distributed and often overlap or truncate each other. The vertical extent of radar facies (4) is 55 ns which should correspond to a depth of about 2.50 m.

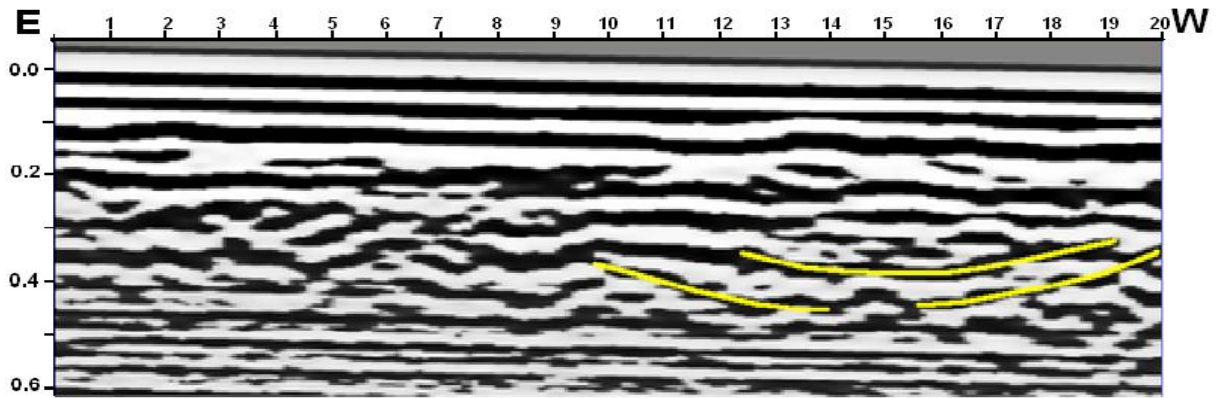


Fig. 4.1.6 Lower resolution line 03 EW (west to the right). Yellow lines indicate radar facies (4) located to the south of the recirculation pool. A possible ‘bow-tie’ effect at the bottom of the lower line (vertical TWTT scale in hundreds of ns with 10 ns = 0.40 m).

The V-shaped reflections (marked with yellow lines in Figure 4.1.7), which appear to dip at an angle of approximately 5 to 15 degrees, may be related to the vertical decrease in signal velocity, *i.e.* in reality the shape may be much smoother. Occasionally, the bottom part of the concave upwards reflection is also slightly elevated and may have a slightly convex character, shown with an orange line in Figure 4.1.7, which is related to the ‘bow-tie’ effect (see Section 3.1). Radar facies (4) form 35% of all profiles and can be found at the bottom part of the profiles within the area surrounding the pool, particularly to the south and east of it.

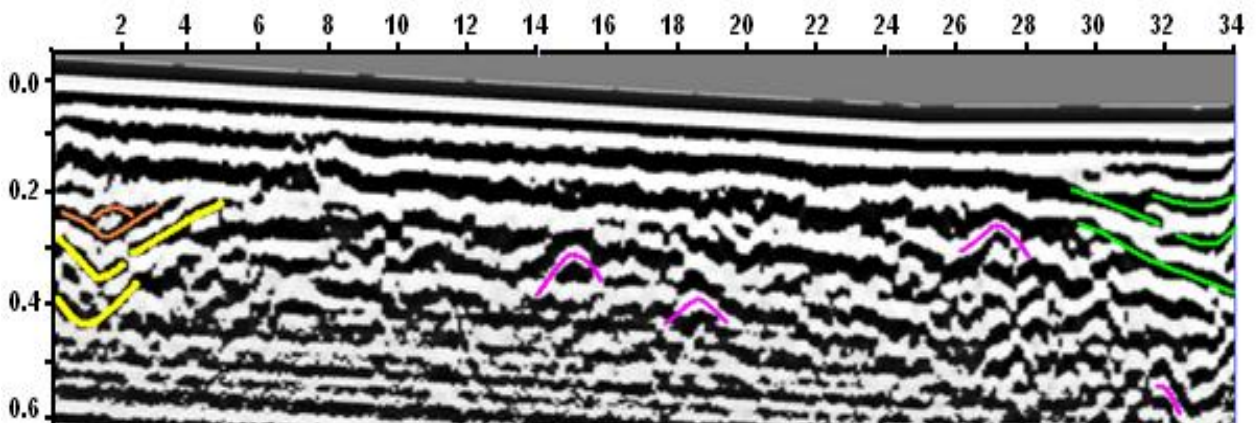


Fig. 4.1.7 Lower resolution line 39 SN (north to the right). Chaotic and parabolic reflections (in the middle of the profile underlying the horizontal lines) of radar facies (5) are truncated by concave upwards green lines on the northern edge. Yellow lines refer to radar facies (4) (see Section 4.1.7). The parabolic pattern is indicated by pink lines. Orange lines indicate a possible ‘bow-tie’ effect (vertical TWTT scale in hundreds of ns with 10 ns = 0.40 m).

This pattern was occasionally also found below the previously described concave upwards reflections within the filled recirculation pool and is shown with yellow lines in Figure 4.1.8.

However, as explained further in Section 4.1.7, these reflections could also be classified as the group of half-concave upwards reflections of radar facies (3).

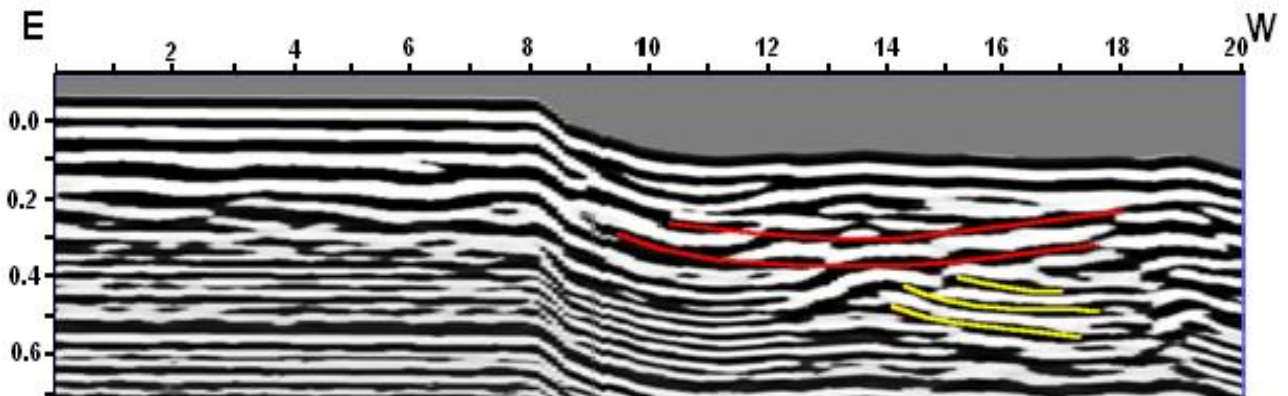


Fig. 4.1.8 Lower resolution line 23 EW (west to the right). The concave upwards, slightly inclined reflections marked in yellow and located below the concave upwards pattern of radar facies (2) (marked in red) are interpreted as radar facies (3) or (4) due to their character. The interpretation is not certain without excavating trenches or application of 3-D datasets (vertical TWTT scale in hundreds of ns with 10 ns = 0.40 m).

Individual half-concave upwards reflections, which are marked by yellow dashed lines in Figure 4.1.9, can be found at greater depths on E-W oriented images below the edge of the recirculation zone and seem not to be directly related to sedimentary structures. Instead, they may be related to instability of the river banks prior to deposition of sediments within the recirculation pool.

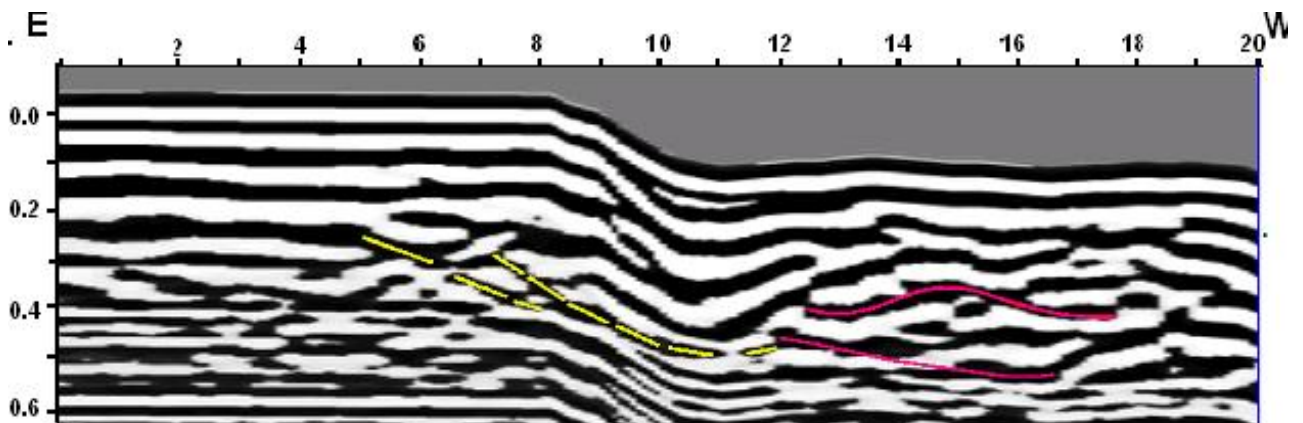


Fig. 4.1.9 Lower resolution line 26 WE (west to the right) shows convex pattern (marked in pink) which separates two concave upwards zones within the recirculation pool. It is difficult to assess if this pattern is part of the recirculation fill or older deposits. Concave upwards reflections cut the edge of the recirculation pool area within the older deposits. Yellow concave upwards lines indicate potential 'slip surfaces'. The angle of the surfaces is difficult to assess based on 2-D lines as the lines may not run parallel to the feature (vertical TWTT scale in hundreds of ns with 10 ns = 0.40 m).

Due to their occurrence within the area that surrounds the pool and below depths of about 0.30 to 0.50 ns, the pattern is classified together with the concave upwards reflections,

described above, as radar facies (4). Both of the patterns are overlain by radar facies (1) and also underlie the concave upwards reflections of radar facies (2) in the recirculation pool.

#### 4.1.5 Radar facies (5): discontinuous undulating chaotic reflections

Discontinuous undulating reflections of a chaotic character form about 30% of all profiles. These reflections were identified in the eastern part of the site area between the recirculation pool, radar facies (3) and radar facies (4). Distinct hyperbolic reflections are indicated by pink lines in Figure 4.1.10.

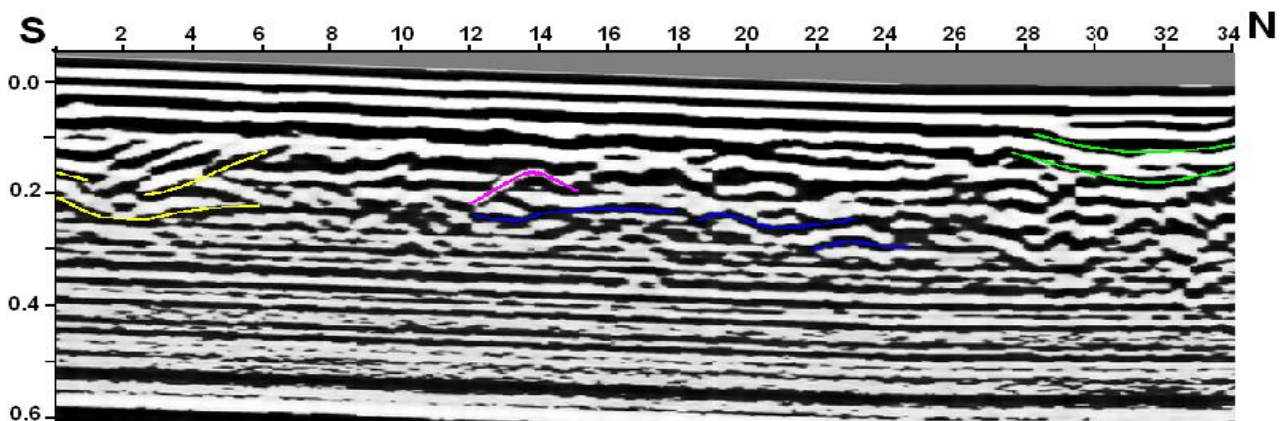


Fig. 4.1.10 Lower resolution line 37 SN (north to the right) shows hyperbolic reflection (marked in pink) with discontinuous undulating reflections of radar facies (5). Yellow lines indicate concave upwards patterns of radar facies (4) and green lines indicate radar facies (3). Blue lines indicate discontinuous undular reflections (vertical TWT scale in hundreds of ns with 10 ns = 0.40 m).

#### 4.1.6 Correlation of GPR data with cut-bank exposure

Ground-truth control provides a basis for interpretation of reflection patterns on GPR profiles. It correlates the reflection patterns on geophysical profiles with information about the subsurface, such as the lithology, texture and structure of the investigated deposits, and is therefore an important step when GPR data is applied in sedimentary studies. Collection of the information is typically done by excavation of trenches or coring along survey lines, although observations carried out in cut-banks may also be used as ground-truth (Woodward *et al.* 2003).

Observations of the lithology were carried out in the cut-banks of the River Dene and these were correlated with GPR lines collected half a metre behind its edge. This survey was carried out immediately downstream from the recirculation pool. Observations were also carried out further upstream, *i.e.* adjacent to the north of the survey area. A photo, which shows the location of the cut-bank and the GPR line in relation to the rest of the site, is shown in Figure 4.1.11.



Fig. 4.1.11 Image of the Macclesfield site with the location of the ground-truth control GPR profile (presented in Figure 4.1.14), indicated by the tape measure, collected and correlated with the cut-bank of the River Dene (river flow direction indicated by blue arrow). Red line marks the location of the GPR grid and yellow line shows the edges of the recently filled eddy pool. Black arrow in the top left corner indicates the north (photo taken in August 2008).

The GPR profile shown in Figure 4.1.12 displays a concave upwards, strong-amplitude reflection which extends laterally by approximately 4.50 m and to an approximate depth of 0.90 m. Observations which were carried out in the cut-bank revealed a channel (orange line in Figure 4.1.12). Its upper part was filled with structureless silty sand underlain by approximately 0.10 to 0.15 m of sandy fine to medium gravel (indicated by green lines in Figure 4.1.12) which in turn was underlain by gravelly sand which dominated the bottom of the channel. The identified channel probably corresponds to concave upwards reflections classified above as radar facies (4).

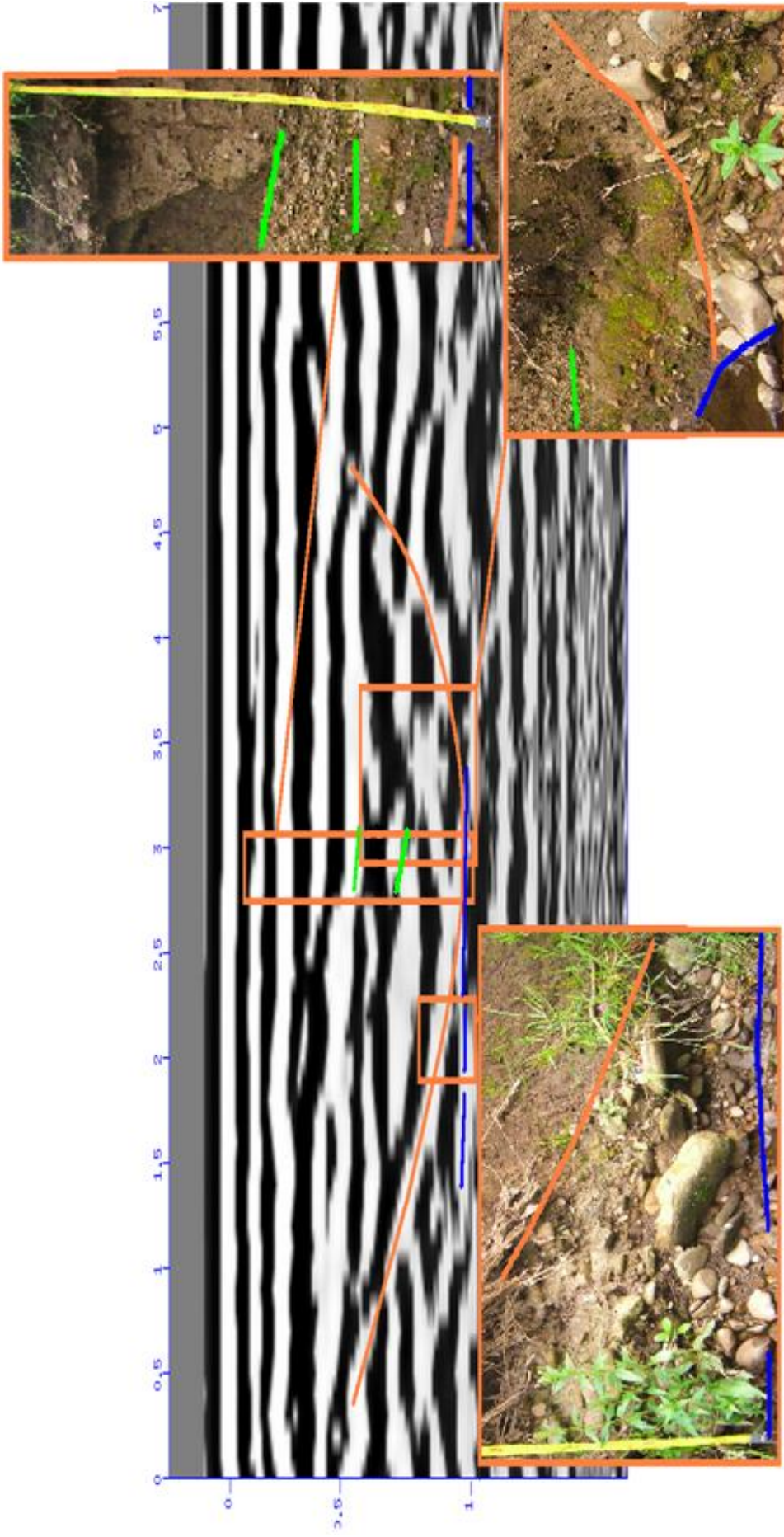


Fig. 4.1.12 Section of the ground-truth control profile (total length of 10.0 m) collected with 200 MHz antenna and correlated with cut-bank observations. Blue line indicates probable groundwater table. Vertical scale in metres. Location of the GPR line and the cut-bank is shown in Figure 4.1.13.

Horizontal, slightly undulating reflections overlie the concave upwards reflection. Short horizontal reflections are also confined within the concave upwards one. A horizontal, continuous reflection, which is marked by a blue line in Figure 4.1.12, and a much stronger attenuation of the signal, can be seen immediately below the concave upwards reflection. Sandy gravel with occasional cobbles forms the deposits surrounding the channel. Gravel and cobbles are tabular, angular to subrounded, and horizontally oriented. An approximately 50 mm thick layer of slightly gravelly sand was recorded within the coarse-grained deposits (below yellow lines in Figure 4.1.12).

Lithological boundaries were correlated with the GPR reflection patterns. The correlation confirmed that the reflection events are related to major changes in lithology, *i.e.* grain size which characterises the sediments. The scale of the sedimentary forms which are resolvable with the GPR data corresponds to boundaries of microforms such as the gravel bed found within the channel, or the thick laminae of gravelly sand within the gravel deposits. Although smaller-scale structures were not identified in the cut-bank, they would probably not be resolved on the GPR profile.

#### 4.1.7 Sedimentary interpretation of radar facies

Due to the complexity of the sedimentary architecture at the Macclesfield site, direct interpretation of the GPR profiles can be very difficult. The identified radar facies revealed the main bounding radar surfaces indicated by the thick red lines in Figure 4.1.13. This systematic approach helped to classify the reflection patterns and interpret them as sedimentary facies which in turn provides a rational basis for suggesting the evolution of the site.

Radar facies (4) and the chaotic and parabolic reflections, which underlie radar facies (4) and are truncated by radar facies (2) and (3), are considered the oldest. The location of this radar facies in relation to other facies is indicated in Figure 4.1.13. As shown in Section 4.1.6, the lithology related to these patterns varies from silty sand, encountered within the channels, to sandy cobbly, angular to subrounded, poorly sorted gravels. The bottom bounding surface of these deposits has not been reached. The diffraction hyperbolas, although not directly related to sedimentary structures, confirm the cut-bank observations of the lithology as they are most likely the effect of reflection from single-point objects such as cobbles. Elongated objects, such as land-drains or tree trunks, could, however, also produce similar patterns.

The vertical extent of radar facies (3) is over 1.20 m below the current river bed. Cut-bank observations suggest that this pattern is associated with silty sand. This facies has been interpreted as recent point bar deposits of the River Dene. The thickness of the stratum, however, raises a question about the recent origin of the bottom part of the radar facies. This is further investigated in 3-D in Section 5.1. Facies (3) is truncated by the concave upwards reflectors found within the recently filled recirculation pool which is described below in relation to radar facies (2).

Radar facies (2), a concave upwards concordant pattern, is restricted to the area of the recirculation pool. Based on surface observations during the fieldwork, the deposits related to this facies are most likely to comprise silty sand. This pattern is indicated by thin red lines in Figure 4.1.13. According to the local farmer, these sediments were deposited during the flood in November 2007. As noted in Section 4.1.6, sedimentary structures associated with microforms, such as small-scale cross-stratification, could not be resolved by the GPR data. In the absence of trenches or other ground-truth information, it is difficult to identify the exact depositional mechanisms responsible for the character of the deposits within the recirculation

pool.

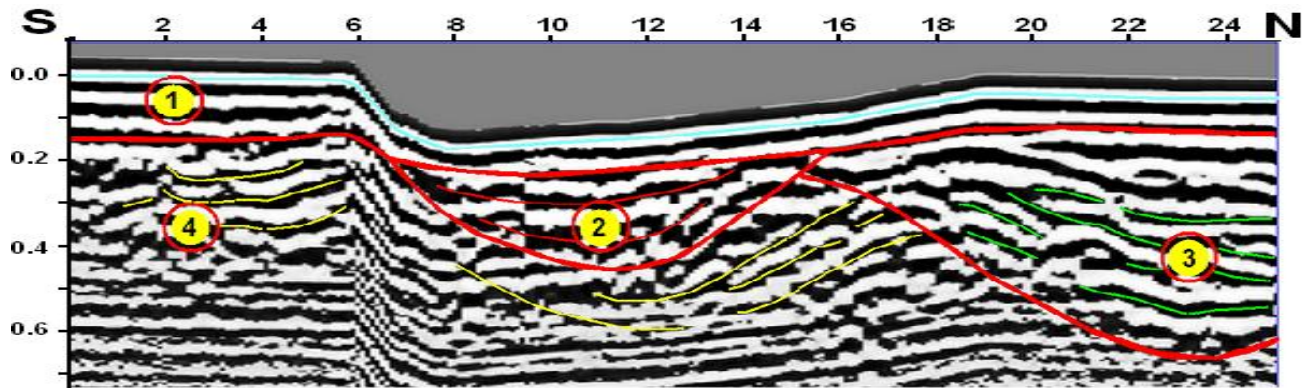


Fig. 4.1.13 Lower resolution line 20 SN (north to the right) which is located approximately 10.0 m from the river bank and cuts the eastern edge of the recirculation pool. The image shows spatial relations between the four main radar facies identified. Blue line indicates the ground surface. Radar facies (4) underlies the other facies and therefore should be considered the oldest. Radar facies (3), which is located between the recirculation pool and the river bank, is considered to be older than radar facies (2) which is restricted to the recirculation zone. Radar facies (1) overlies the other facies. The principle of superposition indicates the relative age of each of the units. Note that radar facies (2) appears to be concordant with the underlying radar facies (4), *i.e.* the recirculation pool might have developed within an older channel.

The concave upwards radar facies pattern was also identified immediately below the concave upwards reflections of radar facies (2). The pattern is associated with stronger signal attenuation than the pool deposits, which may have resulted from a higher clay or moisture content below the erosional surface. The pattern is indicated in yellow in Figure 4.1.13 and appears to be concordant with radar facies (2), although it is also truncated by radar facies (3). Its classification is difficult on 2-D profiles, although the pattern was interpreted to be associated with radar facies (4). However, its classification as radar facies (3) is also possible. The concordant character of these reflections with radar facies (2) could indicate that the recirculation pool developed due to erosion of fine-grained deposits within an older age channel.

Radar facies (2) to (4) are overlain by horizontal parallel reflections classified as radar facies (1), which forms a toplap radar surface with them. Radar facies (1) is generally equally distributed outside the recirculation pool. These deposits could be related to vertical accretion associated with over-bank deposition during flooding periods. The bottom boundary of the

topsoil layer should, however, also be included in this group of reflections. Also, one of the white (negative phase) bottom reflections may be associated with the groundwater table. Reflections associated with the groundwater table may not, however, be clear if deposits have high clay mineral content. Instead, the moisture content would gradually change with depth.

#### 4.2 CLASSIFICATION AND INTERPRETATION OF RADAR FACIES REVEALED BY 2-D SOUTH SASKATCHEWAN RIVER 120 X 40 M GRID DATA

This section describes and classifies reflection patterns revealed by 2-D radar images from the South Saskatchewan River site collected as a 120 x 40 m pseudo 3-D grid. This dataset and the dataset described in Section 4.2 were collected as part of a large-scale investigation of sedimentary architecture of unit and compound bars in the South Saskatchewan River presented by Sambrook Smith *et al.* (2005, 2006) and Parker *et al.* (2008) which comprised collection of 2-D GPR data, vibro-coring, excavation of trenches and review of aerial photographs.

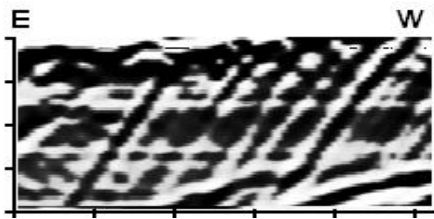
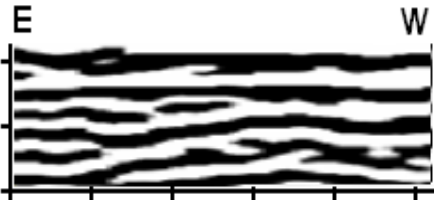
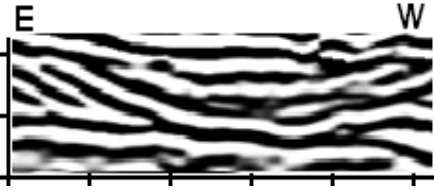
The following four main radar facies were identified on the profiles: (1) high-angle inclined planar and sigmoidal reflections, (2) discontinuous undular and trough-shaped reflections, (3) continuous strong-amplitude large-scale concave upwards and undular reflections, (4) smaller-scale concave upwards, often concordant, reflections. These radar facies are described in Sections 4.2.1 to 4.2.4, and are interpreted in terms of sedimentary architecture in Section 4.2.5.

Quantitative evaluation of radar facies occurrence followed the methodology applied by Sambrook Smith *et al.* (2006b) to the GPR profiles collected in the South Saskatchewan River who applied sampling every 10 m. Here due to smaller scale of the dataset, vertical lines were drawn every 1 m to the bottom of each profile. The evaluation involved measuring proportion

of radar facies along each vertical sampling line. This led to estimation of proportions of sedimentary facies within the dataset.

A summary of the radar facies identified in the 120 x 40 m South Saskatchewan River dataset is presented in Table 4.2. The classification of the radar facies attempted to follow the classification of radar facies in the South Saskatchewan River applied by Sambrook Smith *et al.* (2006b).

Table 4.2 Summary of three identified radar facies with their variability on orthogonally oriented profiles. The classification follows descriptions given by Sambrook Smith *et al.* (2006b) for radar facies identified in the South Saskatchewan River. Vertical scale is in tens of ns, while horizontal scale in m.

	Description	Representation	Sedimentary interpretation
<b>Radar facies (1)</b>	high-angle inclined planar and sigmoidal reflections		downstream accretion on margin slip-faces of unit and compound bars
<b>Radar facies (2)</b>	discontinuous undular and trough-shaped reflections		sinuous-crested dunes
<b>Radar facies (4)</b>	smaller-scale concave upwards, often concordant, reflections		cross-bar channels with fill

#### 4.2.1 Radar facies (1): high-angle inclined planar and sigmoidal reflections

The high-angle inclined planar and sigmoidal pattern is classified here as radar facies (1). The reflections dip at an angle of between 15 and 25 degrees. The facies, shown in Figures 4.2.1 to 4.2.4, stretches laterally over 30 m and continues to the west beyond the boundaries of the grid with a maximum height estimated at 1.2 m. The thickness and the horizontal extent of the

facies gradually decrease on profiles collected further to the south (compare Figures 4.2.1 and 4.2.3). This facies forms about 45% of all GPR profiles and terminates in the eastern part of the grid. The pattern can be found in the central and western part of the profile between 40 and 110 ns (indicated by dashed red lines in Figures 4.2.1 to 4.2.3) but is also present below about 80 ns in the eastern and central parts of the site (indicated by dashed yellow lines in Figures 4.2.2 and 4.2.3).

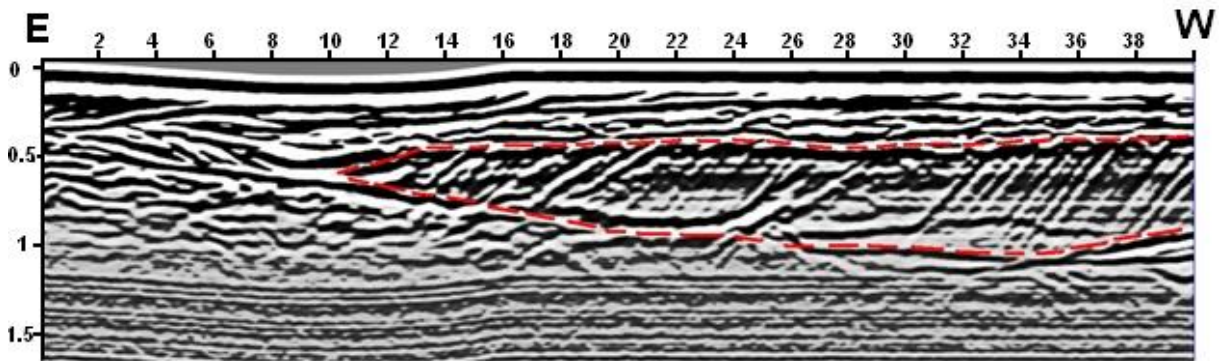


Fig. 4.2.1 Lower resolution line 12. Radar facies (1) shown between red dashed lines. Vertical TWTT in 100 ns (100 ns = approximately 2.55 m).

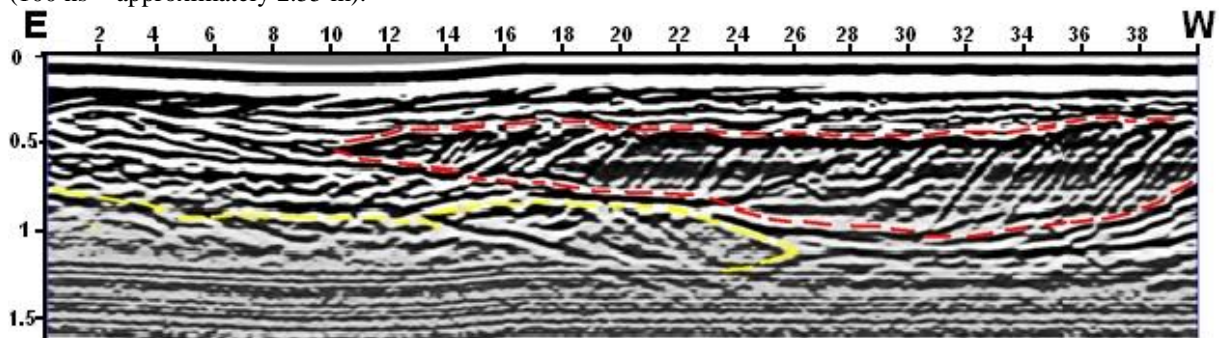


Fig. 4.2.2 Lower resolution line 39. Radar facies (1) shown between red dashed lines and below yellow dashed line. Vertical TWTT in 100 ns (100 ns = approximately 2.55 m).

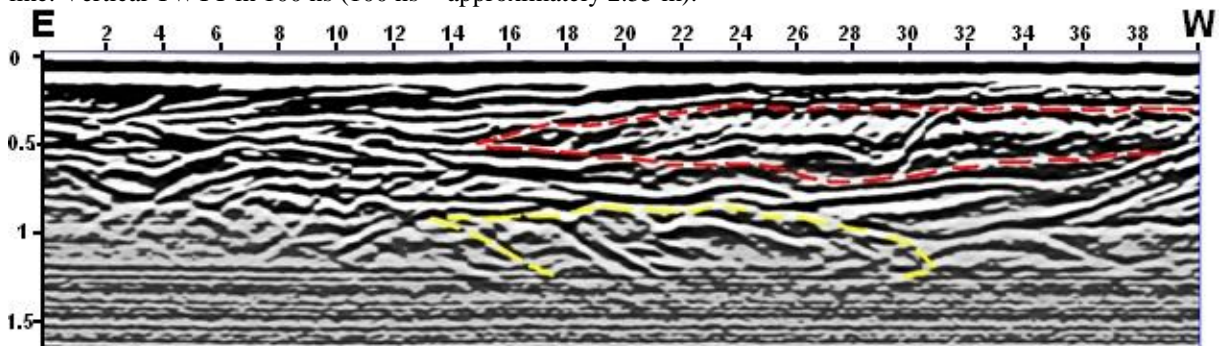


Fig. 4.2.3 Lower resolution line 100 (west to the right). Occurrence of radar facies (1) shown between red dashed lines and below yellow dashed line. Vertical TWTT in 100 ns (100 ns = approximately 2.55 m).

Hyperbolic reflections were also recorded within radar facies (1). These patterns are shown by pink lines in Figure 4.2.4 and could be associated with unknown point objects such as

cobbles, tree trunks, etc. Parabolic shapes sometimes visible in the top part of profiles may therefore be produced by the upper breaks of foresets.

#### 4.2.2 Radar facies (2): Discontinuous undular and trough-shaped reflections

Discontinuous undulating and trough-shaped reflections which are often gently inclined towards the east are recognised as radar facies (2). The lateral extent of individual reflections is between 0.50 to 15.0 m. This radar facies forms approximately 40% of all profiles. The radar facies rarely reaches the total thickness of 40 ns, *i.e.* about 1.0 m. It dominates the upper parts of the profiles, particularly their western and central sections, with its boundaries marked by yellow lines in Figures 4.2.4 and 4.2.5.

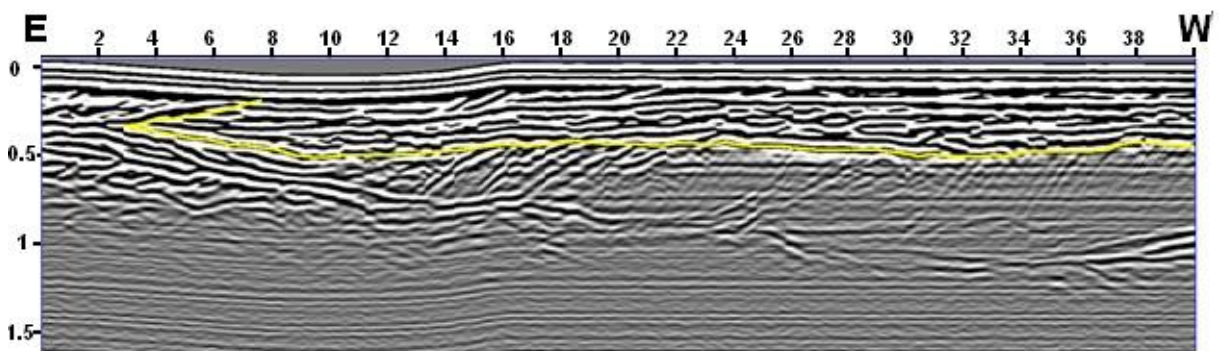


Fig. 4.2.4 Higher resolution line 20. Yellow line indicates bottom boundary of radar facies (2). Vertical TWTT in 100 ns (100 ns = approximately 2.55 m). Also notice radar facies (1) across the whole profile immediately below the yellow line. Hyperbolic diffractions are indicated by pink lines.

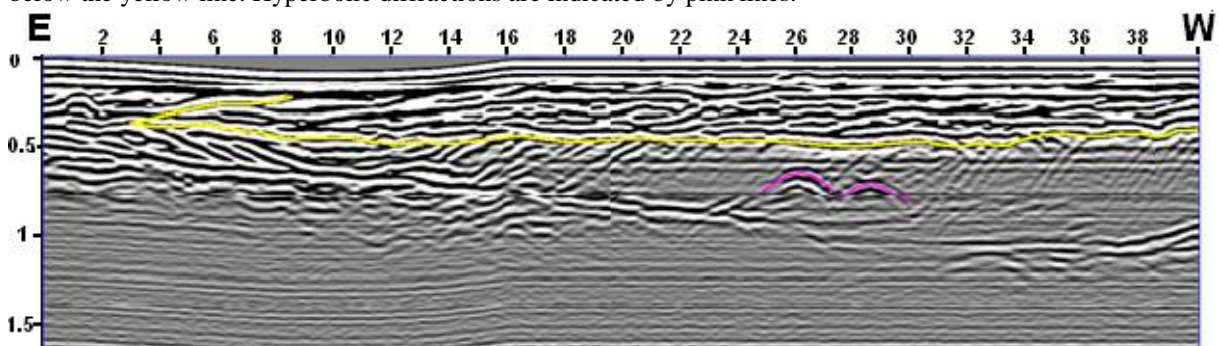


Fig. 4.2.5 Higher resolution line 09. Yellow line indicates bottom boundary of facies (2). Vertical TWTT in 100 ns (100 ns = approximately 2.55 m).

The discontinuous undular and trough-shaped reflections can also be found in the western part of the profiles between 50 and 100 ns, *i.e.* between depths of about 1.2 and 2.5 m, which is marked with green dashed lines in Figures 4.2.6 and 4.2.7. This group of radar facies (2) is

characterised by a slightly steeper inclination and are more undulating when compared with the upper group.

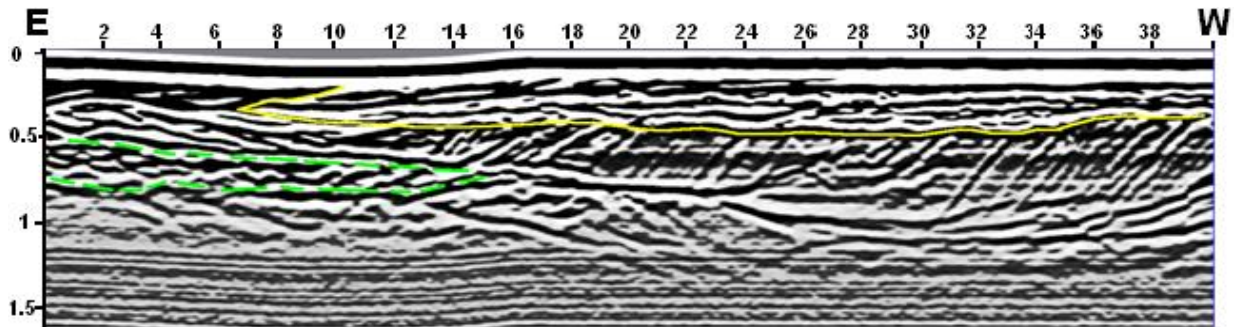


Fig. 4.2.6 Lower resolution line 39 (west to the right). Lower group of radar facies (2) shown between green dashed lines. Vertical TWTT in 100 ns (100 ns = approximately 2.55 m).

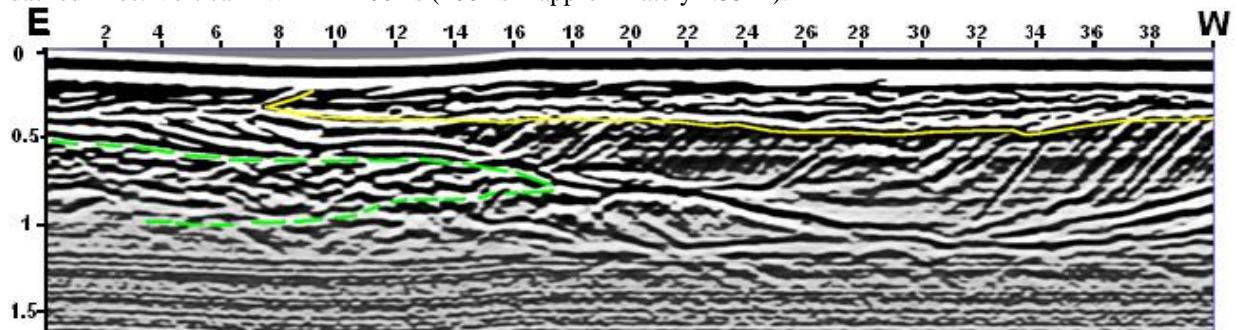


Fig. 4.2.7 Lower resolution line 47 (west to the right). Lower group of radar facies (2) shown between green dashed lines. Vertical TWTT in 100 ns (100 ns = approximately 2.55 m).

#### 4.2.3 Radar facies (4): small-scale concave upwards, often concordant, reflections

Individual smaller-scale concave upwards reflections spread vertically by approximately 10 ns, *i.e.* about 0.50 m, and extend laterally by about 5.0 to 7.0 m. This radar facies typically comprises up to three reflections which are often concordant. These patterns dominate the top eastern part of the profiles and form 10% of all profiles. The radar facies is typically underlain by a radar surface (explained below in Section 4.2.4) and may be overlain by facies (2) further to the west (see Figures 4.2.8 to 4.2.10).

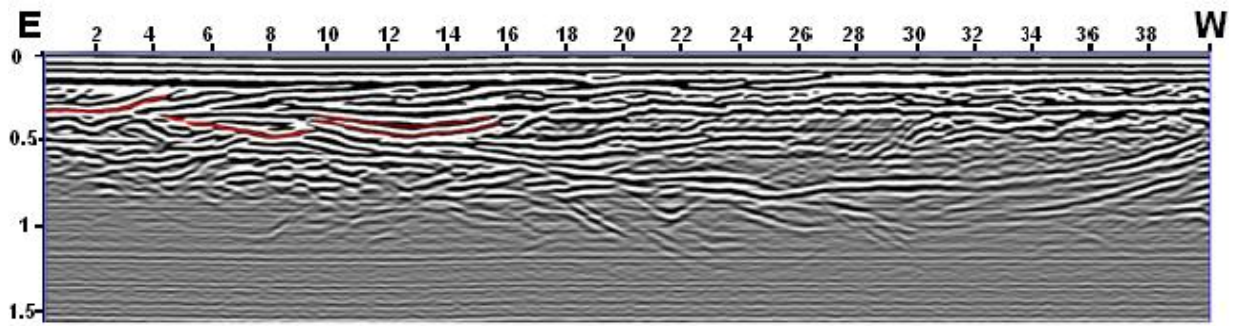


Fig. 4.2.8 Lower resolution line 69 (west to the right). Examples of reflections classified as radar facies (4) shown by red lines (vertical TWTT in hundreds of ns, 100 ns = approximately 2.55 m).

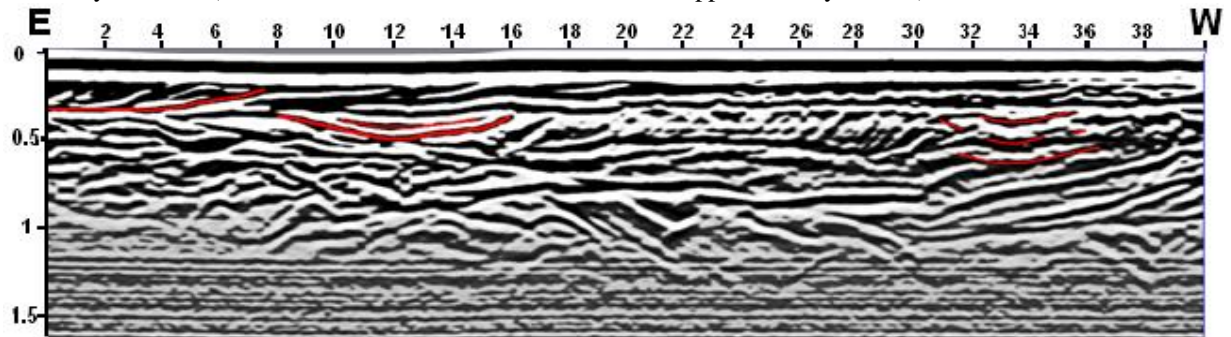


Fig. 4.2.9 Higher resolution line 95 (west to the right). Examples of reflections classified as radar facies (4) shown above red lines (vertical TWTT in hundreds of ns, 100 ns = approximately 2.55 m).

Radar facies (4) was sometimes also identified in the top western part of some profiles of the grid (shown in Figure 4.2.10). This group appears to truncate inclined reflections of radar facies (1).

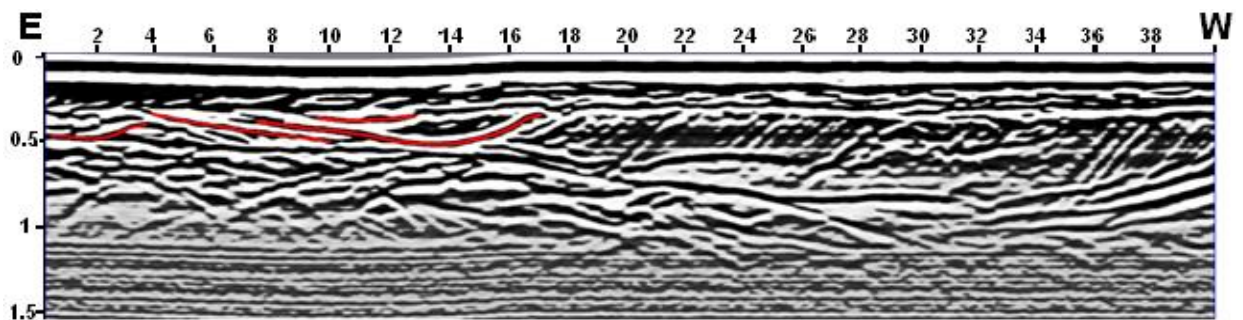


Fig. 4.2.10 Lower resolution line 93 (west to the right). Reflections classified as radar facies (4) are shown by thick red lines. Radar facies (4) was also occasionally identified in the top western part of some profiles and is indicated by thin red lines above the group of radar facies (3) (vertical TWTT in hundreds of ns, 100 ns = approximately 2.55 m).

#### 4.2.4 Continuous strong-amplitude radar surface

Continuous strong-amplitude reflection lines have both concave upwards and sigmoidal shapes. These lines were distinguished as a radar surface, *i.e.* they separate radar facies. The lines can be found across the whole stratum between 50 and 150 ns, *i.e.* depths of about 1.30

to 3.50 m. In the western and central parts of the site they underlie radar facies (1); in the eastern part they separate radar facies (2) from radar facies (4). These reflections form a small fraction of all profiles (Figures 4.2.12 and 4.2.13) although a group of reflections of greater thickness, often truncating each other, has been recorded by the southernmost lines (see Figure 4.2.11 which presents line 100). Thus the radar surface has an erosional character and can be treated as a sequence boundary. Its interpretation is included in the following section.

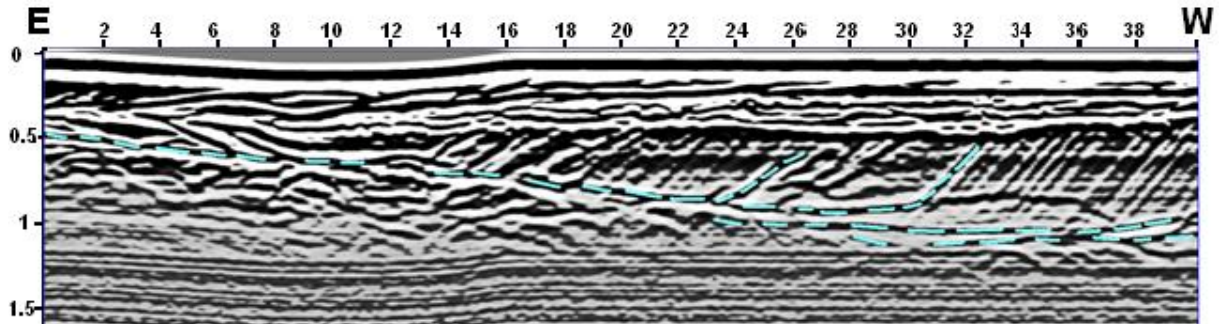


Fig. 4.2.11 Lower resolution line 05 (west to the right). Reflections classified as a radar surface, which separates facies (4) and (2) in the eastern part of the profile, are shown by blue dashed lines. Vertical TWTT in 100 ns (100 ns = approximately 2.55 m).

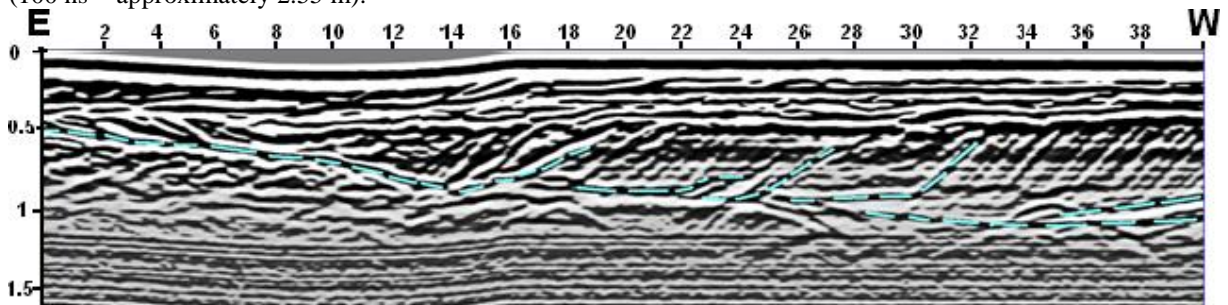


Fig. 4.2.12 Lower resolution line 18 (west to the right). Reflections classified as a radar surface, shown by blue dashed lines, reveal a series of erosional surfaces related to breaks in sedimentation on slip-faces of the unit bar margin. Vertical TWTT in 100 ns (100 ns = approximately 2.55 m).

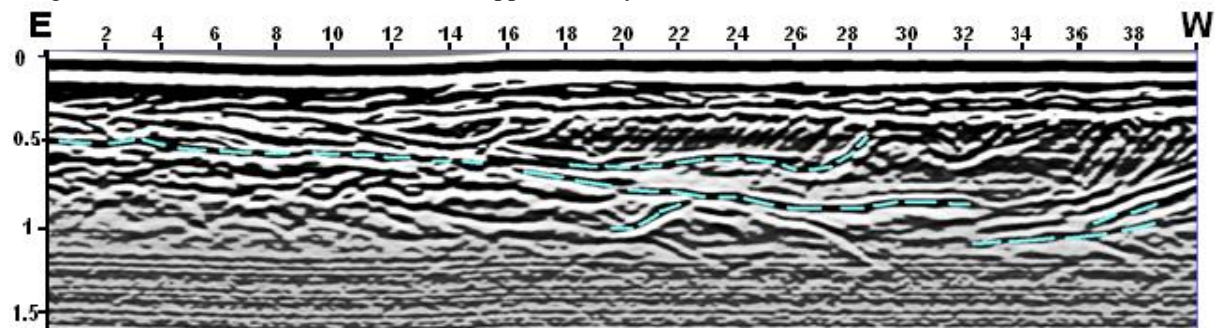


Fig. 4.2.13 Lower resolution line 73 (west to the right). Reflections classified as a radar surface shown below by dashed lines. Vertical TWTT in 100 ns (100 ns = approximately 2.55 m).

#### 4.2.5 Ground-truth control and sedimentary interpretation

Based on the four radar facies identified above, further interpretation of sedimentary facies was carried out and was supported by ground-truth control for the South Saskatchewan River data presented by Woodward *et al.* (2003). The ground-truthing was based on comparison of GPR profiles with observations carried out on the cut-faces. This correlation revealed that the reflection events are related to changes in grain size of the sandy deposits as well as to the presence of mud drapes. The mud drapes are probably present within the dataset presented here and may be related to the strong reflection surface described above; however, this is difficult to establish without direct observations.

Radar facies (1), also identified by Sambrook Smith *et al.* (2006b), are interpreted to represent deposition on the slip-faces of migrating unit or compound bars. Stronger-amplitude inclined reflections sometimes found between high-angle reflections of radar facies (1) are interpreted as lower hierarchy radar surfaces (see below). These radar surfaces are associated with reactivation surfaces, possibly related to fine-grained drapes deposited during low water stages. Radar facies (1) is typically overlain by radar facies (2), associated with smaller-scale forms deposited on top of unit bars such as sinuous-crested dunes.

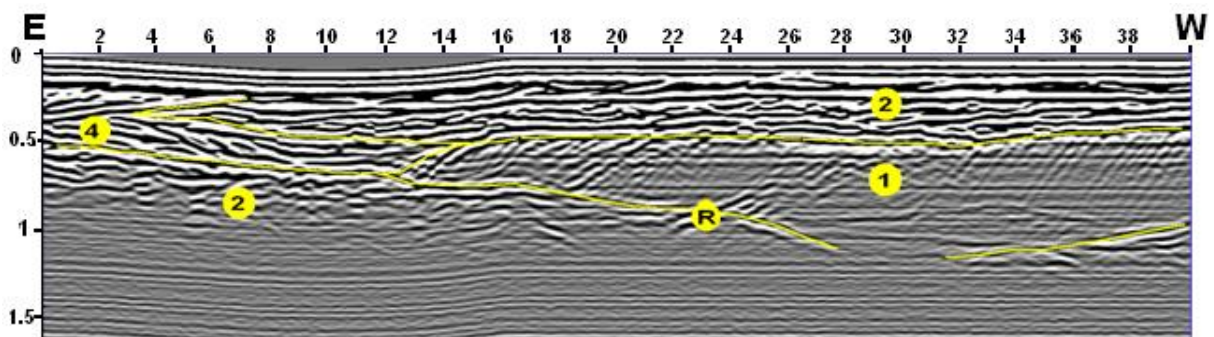


Fig. 4.2.14 Higher resolution line 14 (west to the right) shows distribution of the radar facies (1), (2) and (4). 'R' indicates the main radar surface associated with a scour. Vertical TWTT in 100 ns (100 ns = approximately 2.55 m).

Radar facies (2) of slightly more undular character, when compared with the upper group, can

be found below the reflection classified as a radar surface and indicated in Figure 4.2.14 as 'R'. This reflection is considered as an erosional surface which separates the deposits of two different unit bars and forms a scour in the bottom of the western part of the profile.

Radar facies (4) represents a small-scale channel which developed on top of the eastern unit bar, adjacent to the edge of the western unit bar. It is unknown if the concave upwards reflections are produced only by changes in sediment grain size or also by the presence of mud drapes. The profiles are interpreted as migration of the western unit bar (right) onto the eastern bar, the top of which is indicated by the radar surface. Radar facies (1), which was also identified below radar facies (2) shown by yellow dashed lines in Figure 4.2.2 and 4.2.3, is a result of migration of the eastern bar towards the west. These patterns were identified on 2-D profiles and some of the sedimentary structures may be obliquely oriented to the direction of the GPR lines.

Based on the above, two depositional sequences can be distinguished, separated by the identified radar surface. Each of the sequences comprises radar facies (1) at the bottom, overlain by radar facies (4) and (2). Lateral changes between the facies are also imaged by this dataset. Further investigation and interpretation is carried out in 3-D in Section 5.2.

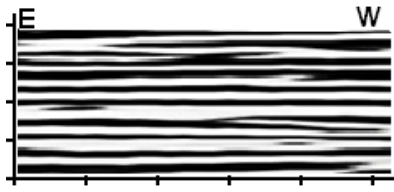
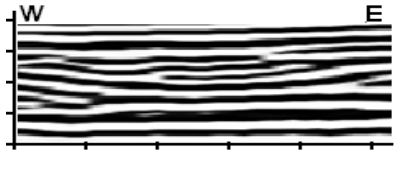
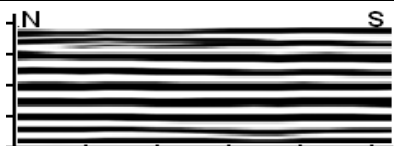
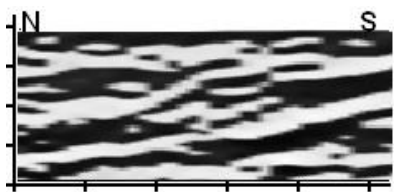
#### 4.3 CLASSIFICATION AND INTERPRETATION OF RADAR FACIES REVEALED BY 2-D SOUTH SASKATCHEWAN RIVER 10 X 10 M GRID DATA

This section contains a description and classification of the reflection patterns revealed by 2-D radar profiles collected in the South Saskatchewan River as a 10 x 10 m grid which is located in a different section of the South Saskatchewan River than the 120 x 40 m grid. The grid was collected with 0.10 m distances between survey points and adjacent lines, while the

dataset in the previous section was collected with 0.10 m distance between survey points and 0.50 m between adjacent lines. The radar facies are described in Sections 4.3.1 to 4.3.5 and interpreted in terms of sedimentary architecture in Section 4.3.6.

This dataset and the dataset described in Section 4.2 were collected as part of a large-scale investigation of sedimentary architecture of unit and compound bars in the South Saskatchewan River presented by Sambrook Smith *et al.* (2005, 2006b) and Parker *et al.* (2008).

Table 4.3 Summary of four identified radar facies with their variability on orthogonally oriented profiles. The classification follows descriptions given by Sambrook Smith *et al.* (2006b) for radar facies identified in the South Saskatchewan River. Vertical scale is in tens of ns, while horizontal scale in m.

	<b>Description</b>	<b>Representation</b>	<b>Sedimentary interpretation</b>
<b>Radar facies (3)</b>	continuous low-angle, often parallel, slightly undulating reflections		low-amplitude dunes and ripples
<b>Radar facies (4)</b>	small-scale concave upwards, often concordant, reflections on W-E oriented profiles		cross-bar channel with fill
	continuous low-angle, often parallel, slightly undulating reflections on N-S oriented profiles		
<b>Radar facies (5)</b>	horizontal reflections enclosed by continuous strong-amplitude negative-phase reflection inclined to the west on W-E oriented profiles		fragment of a large-scale erosional surface with scour fill
	variable dip reflections enclosed by continuous strong-amplitude negative-phase reflection inclined to the south on N-S oriented profiles		
<b>Radar facies (6)</b>	discontinuous low-angle parallel reflections		possible older alluvial deposit, glacial till or bedrock

The following four radar facies were identified within the dataset: (3) continuous low-angle, often parallel, reflections; (4) small-scale concave upwards, often concordant, reflections on W-E oriented lines, which in N-S profiles appear as continuous low-angle parallel reflections; (5) reflections of variable dip enclosed by a strong-amplitude continuous negative-phase reflection inclined to the west on W-E oriented profiles, on N-S oriented profiles appearing as horizontal reflections enclosed by a continuous strong-amplitude negative-phase reflection inclined to the south; (6) discontinuous low-angle parallel reflections.

Quantitative evaluation of radar facies occurrence followed the methodology applied by Sambrook Smith *et al.* (2006b) to the GPR profiles collected in the South Saskatchewan River who applied sampling every 10 m. Here due to smaller scale of the dataset, vertical lines were drawn every 1 m to the bottom of each profile. The evaluation involved measuring proportion of radar facies along each vertical sampling line. This led to estimation of proportions of sedimentary facies within the dataset. A summary of the radar facies with an appreciation of their 3-D character, represented by differences between patterns on E-W and S-N oriented profiles, identified in the 10 x 10 m South Saskatchewan River dataset is presented in Table 4.3.

#### 4.3.1 Radar facies (3): continuous low-angle, often parallel, reflections

The upper parts of the profiles are dominated by continuous low-angle, often parallel, reflections forming approximately 55% of all profiles. The reflection lines extend laterally beyond the boundaries of the grid. The TWTT distance between negative-phase events is about 10 ns, which would correspond to a distance of about 0.30 m. This radar facies is shown to dominate the upper parts of the profiles and is shown in Figures 4.3.1 and 4.3.2 to overlie the shallow concave upwards reflection which is described in the following section.

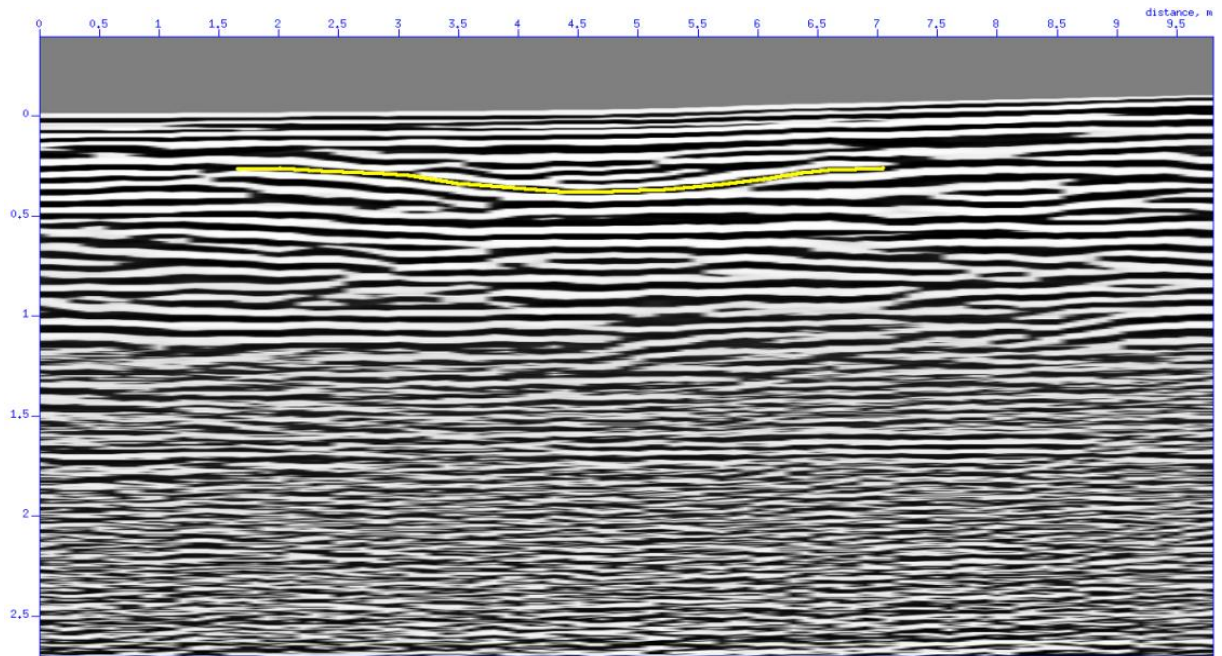


Fig. 4.3.1a The upper part of higher resolution line 45 WE (east to the right). The concave upwards reflection is shown by a yellow line and truncates the underlying parallel horizontal reflections. Overlying continuous low-angle lines form a toplap radar surface. Vertical TWTT in 100 ns (100 ns = approximately 2.55 m).

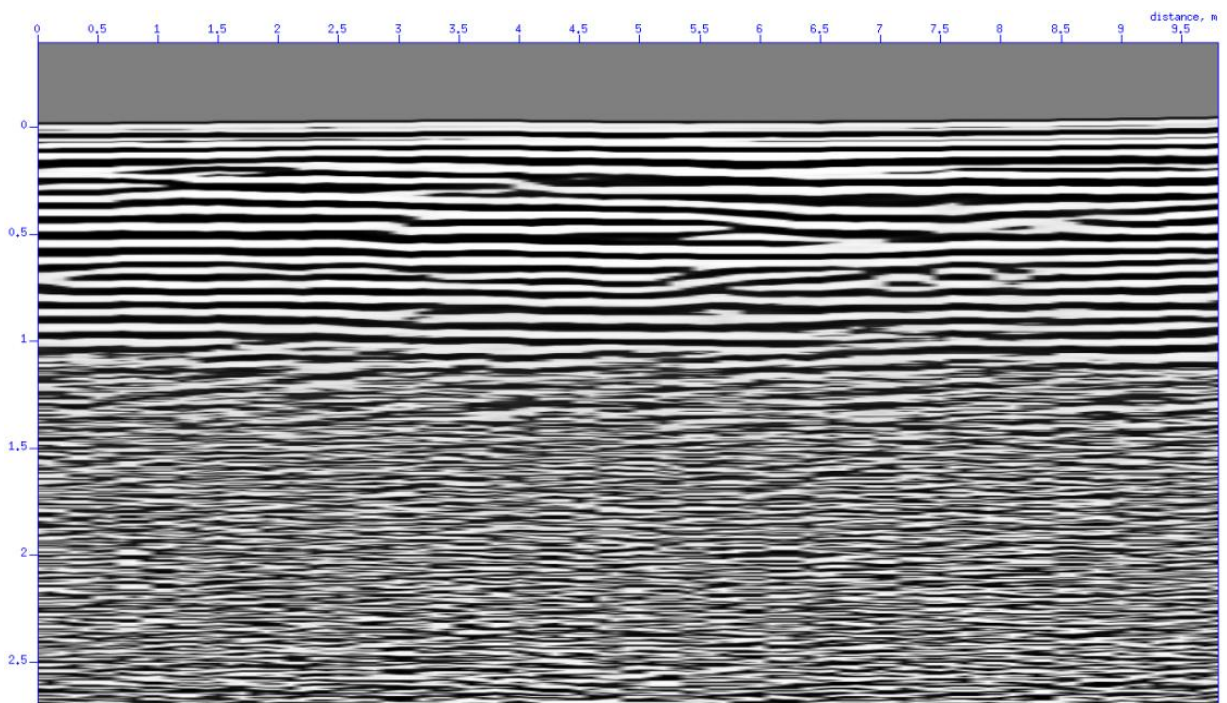


Fig. 4.3.1b The upper part of higher resolution line 45 NS (north to the right). The radar facies (4) appear as low-angle parallel reflections. Vertical TWTT in 100 ns (100 ns = approximately 2.55 m).

#### 4.3.2 Radar facies (4): small-scale concave upwards, often concordant reflections

The shallow small-scale concave upwards reflections that truncate continuous low-angle reflections and are often concordant can be found on W-E oriented profiles. This facies, however, appears as low-angle parallel reflections on N-S oriented profiles and are not

distinguishable from the reflections of radar facies (3). The events are marked by yellow lines in Figures 4.3.1a/b and 4.3.2.

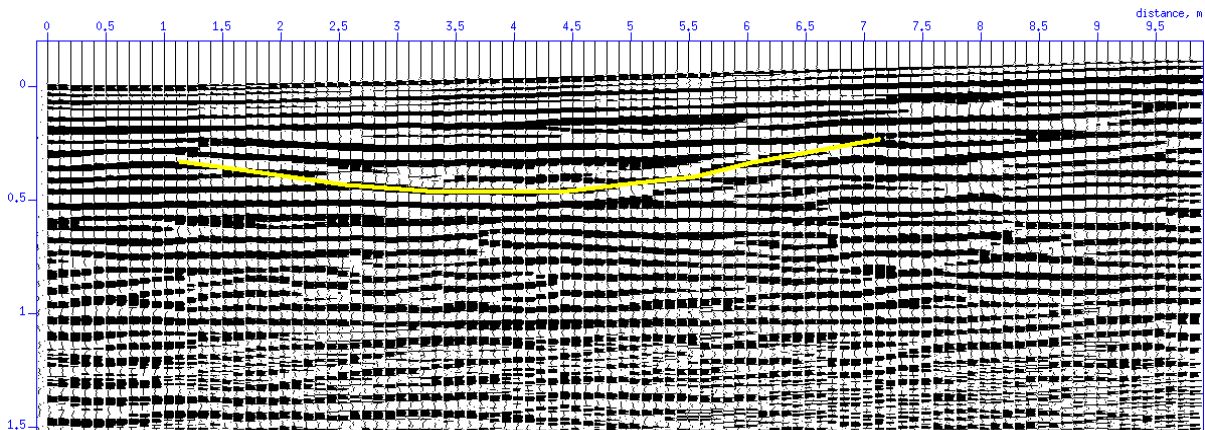


Fig. 4.3.2 The upper part of higher resolution line 10 WE (east to the right). The concave upwards reflection truncates the underlying lines and is overlain by low-angle parallel events. Vertical TWTT in 100 ns (100 ns = approximately 2.55 m).

In the northern part of the grid the feature has a depth of up to 25 ns, *i.e.* a depth of about 0.60 m, and is much shallower in the southern part. The individual concave upwards lines have a lateral extent of about 6.0 to 7.0 m and are located at between 0.25 and 0.50 ns. The radar facies (4) forms approximately 5% of all profiles. The overlying low-angle parallel reflections, classified above as radar facies (3), form a toplap boundary with the concave upwards pattern. A similar pattern, although of slightly smaller scale, can also be noted at greater depths on some of the profiles, *e.g.* between 90 and 95 ns in Figure 4.3.7.

The negative-phase inclined reflection is present both on the W-E and N-S oriented profiles but is only traceable in the lower resolution images. The reflection is indicated by red lines in Figures 4.3.3 to 4.3.5. The feature is dipping to the north on N-S profiles and to the east on W-E oriented ones. It stretches between 140 and 250 ns, *i.e.* depths of about 3.50 and 6.50 m. This estimate would indicate an inclination of between 5 and 30 degrees. The estimate of the angle is based on patterns shown on N-S and W-E oriented 2-D profiles which may be obliquely oriented to the structure and therefore its values may be misleading. This pattern

accounts for 20% of all profiles.

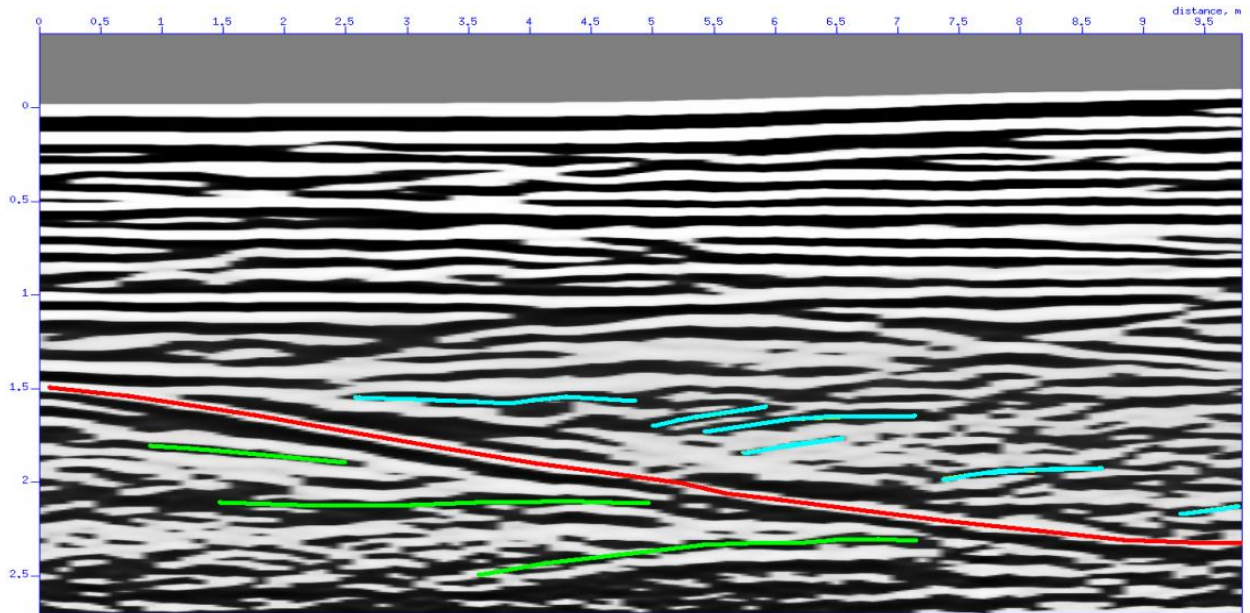


Fig. 4.3.3 Lower resolution line 79 WE (east to the right). Strong negative-phase inclined reflection (red line) truncates underlying reflections of radar facies (4) marked in green and is overlain by discontinuous reflections shown by blue lines (note difference in inclination in Figure 4.3.5). Vertical TWTT in 100 ns (100 ns = approximately 2.55 m).

Between the inclined negative-phase reflection and radar facies (3), which have been distinguished in the upper parts of the profiles, there is a zone dominated by radar facies (5): discontinuous reflections which on N-S oriented profiles have various orientations, although inclination to the south is most often identified (indicated in blue in Figure 4.3.3).

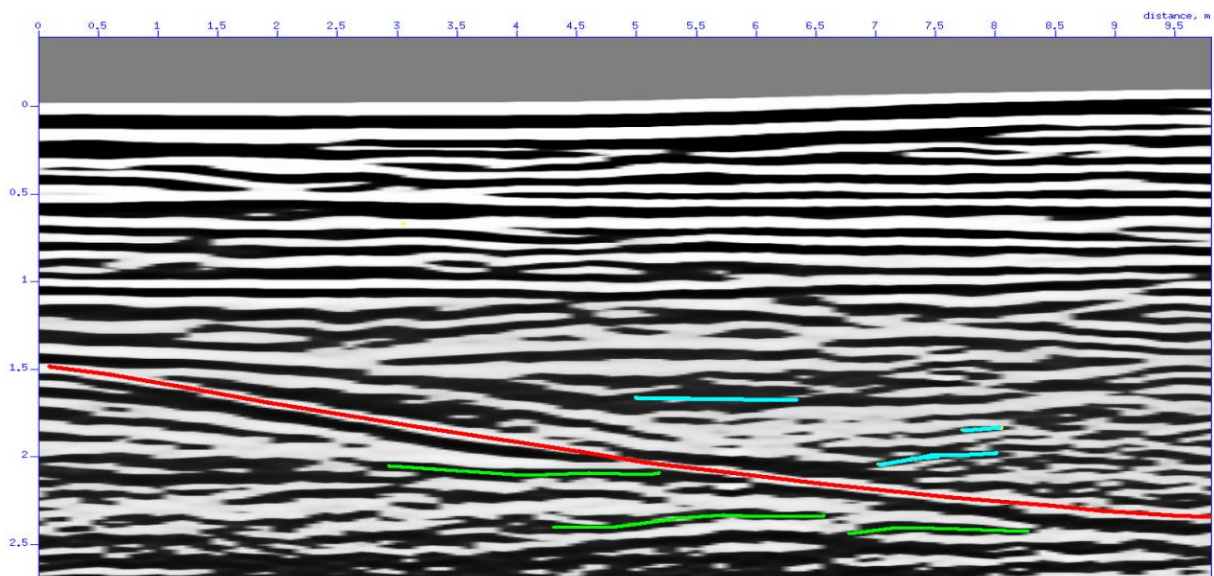


Fig. 4.3.4 Lower resolution line 60 NS (north to the right). Strong negative-phase inclined line (marked in red), which truncates underlying horizontal layers (indicated in green) described in the following section, is overlain by short dipping reflection lines (blue). Vertical TWTT in 100 ns (100 ns = approximately 2.55 m).

The reflections are mostly horizontal on W-E oriented profiles and are shown in blue in Figure 4.3.4. It is difficult to assess the influence of the repetitive noise in this zone; however, the inclination of the pattern varies and in some profiles is parallel to the continuous inclined negative-phase reflection.

#### 4.3.4 Radar facies (6): discontinuous low-angle parallel reflections

Radar facies (6) consists of discontinuous low-angle planar and undulating events which are indicated in green in Figure 4.3.5. The pattern underlies radar facies (5) and constitutes approximately 20% of the profiles. These reflections are truncated by the continuous strong-amplitude negative-phase reflection indicated in red in Figure 4.3.5. As is the case with radar facies (5), it is again difficult to assess the influence of the repetitive noise in this zone.

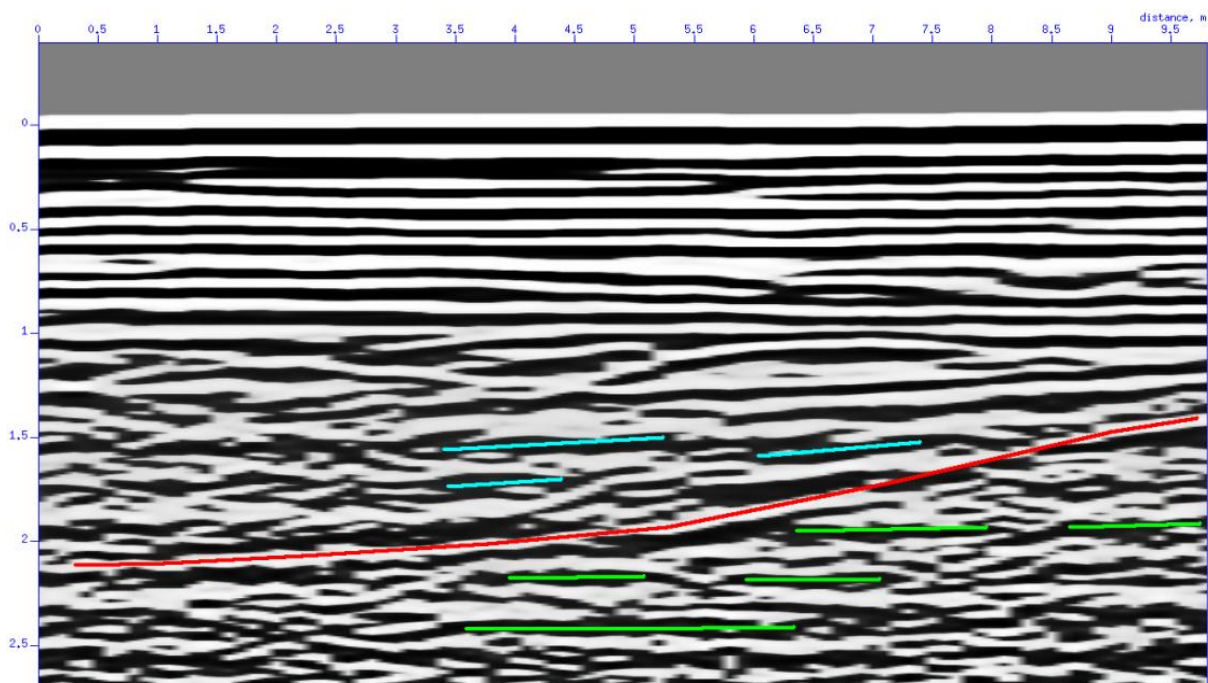


Fig. 4.3.5 Lower resolution line 83 WE (west to the right). Strong negative-phase dipping line, which is marked in red and represents radar surface between radar facies (5) and (6), truncates the underlying horizontal pattern (indicated in green). Vertical TWTT in 100 ns (100 ns = approximately 2.55 m).

Hyperbolic reflections were recorded below 100 ns and an example is marked by a green line in Figure 4.3.6. The pattern is considered to be an effect of reflection from single limited-size objects.

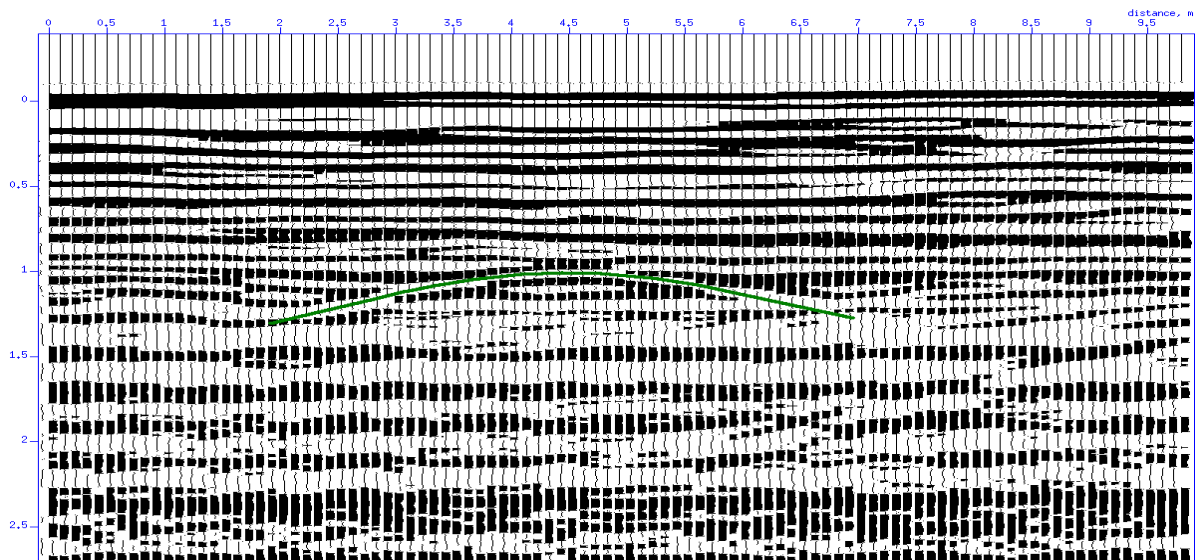


Fig. 4.3.6 Lower resolution line 93 NS (north to the right) shows hyperbolic reflections underlying the zone of the horizontal lines. Vertical TWTT in 100 ns (100 ns = approximately 2.55 m).

#### 4.3.5 Ground-truth control and sedimentary interpretation

Based on the four radar facies identified above and the ground-truth mentioned in Section 4.2.5, the main sedimentary facies were interpreted. Radar facies (3) characterised by continuous low-angle, often parallel, reflections, which dominate the upper part of the profiles, could be traced across all lines oriented in both directions. A similar pattern was classified on GPR profiles collected in the South Saskatchewan River by Sambrook Smith *et al.* (2006b) and interpreted as bounding surfaces of trough cross-strata related to migration of small sinuous-crested dunes and ripples. The radar facies are shown with numbers in Figure 4.3.7. The small-scale cross-stratification is not resolvable by GPR, but the geophysical data was correlated with observations carried out in excavated trenches after the collection of GPR profiles. Small-scale concave upwards reflections, classified as radar facies (4) in this thesis, were also identified by Sambrook Smith *et al.* (2006b) and interpreted as sedimentary structures associated with cross-bar channels or bartop hollows. The concave upwards reflections in the dataset presented here can be traced across all W-E oriented profiles and appear to form an elongated N-S oriented channel. The individual continuous strong-

amplitude inclined reflection, identified here as radar surface 'R', was encountered in the bottom part of the datasets, and is interpreted as a large-scale deep erosional surface, or a scour.

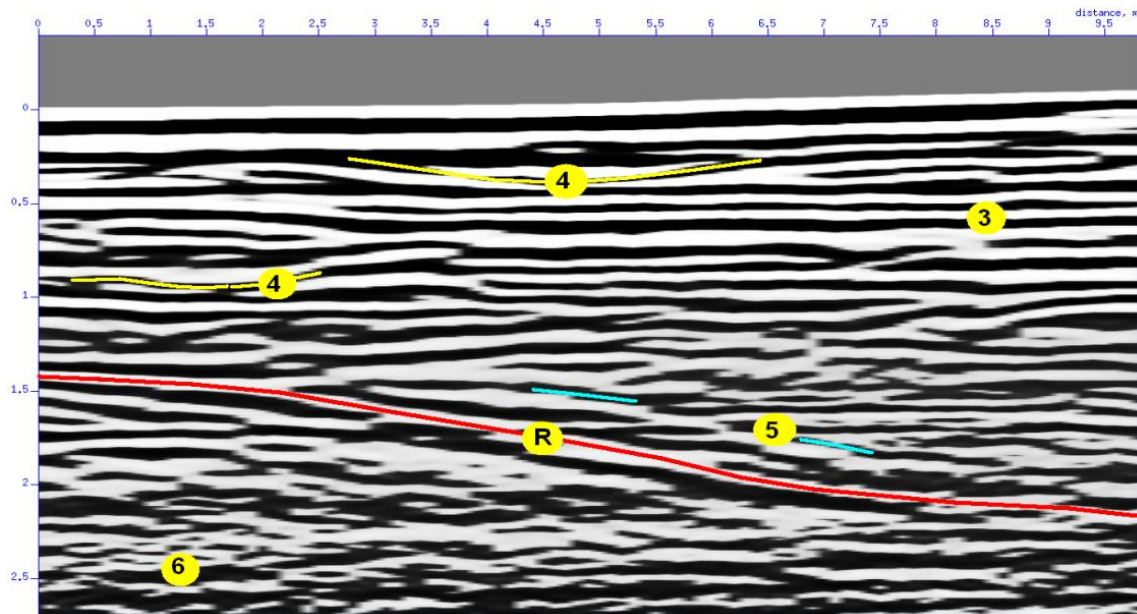


Fig. 4.3.7 Lower resolution line 45 WE (west to the right) showing main radar facies. Radar facies (3) is interpreted as migration of sinuous-crested dunes with radar facies (4) interpreted as cross-bar channels. Radar facies (5) represents a deep scour with fill (blue) above it and truncating a bedrock, possibly older fluvial or glacial deposits (note the proximity of the river bank shown in Figure 4.3.1), which is represented on the profiles as radar surface 'R'. Vertical TWTT in 100 ns (100 ns = approximately 2.55 m).

The overlying pattern is inclined in various directions and its bottom boundary forms a mixed onlap/downlap radar surface. The downlap reflection pattern (marked by blue lines in Figure 4.3.4) may have been distorted by interference of the reflected signal with the repetitive noise. As explained in Section 4.0, negative polarity peaks (shown as white lines on greyscale profiles) indicate an interface associated with an increase in dielectric permittivity. This could be related to the porosity and water content of sediments which increase with depth. Such a situation would exist at an interface between saturated sand and saturated clay, *e.g.* fluvial deposits underlain by glacial deposits, or when saturated gravel is underlain by saturated sand of lower porosity, *i.e.* gravel lag at the base of large scour underlain by sandy fluvial deposits. The line also truncates underlying reflection patterns, *i.e.* radar facies (6), which may be associated with older fluvial or glacial deposits.

## CHAPTER 5

### 5.0 INTERPRETATION OF 3-D DATASETS

Identification of the main reflection patterns on 2-D profiles, in Sections 4.1 and 4.3, both on W-E and N-S oriented profiles, enabled investigation of the sedimentary architecture of the deposits and revealed the evolution of these study sites. Despite the advantages provided by the demonstrated methodology of interpreting radar profiles, the true spatial character of the radar facies could not be fully explored in 2-D. Some of the patterns and dimensions presented above may also be misleading if the profiles are not oriented parallel and perpendicularly to the investigated sedimentary structures. It is difficult to determine the precise orientation of inclined strata with only one set of orthogonal GPR profiles. Additionally, difficulties in correlating adjacent lines led to some uncertainties in classification and interpretation of the radar facies. These problems may be addressed by investigating the sedimentary architecture within 3-D datasets. This chapter presents sedimentary architecture imaged by 3-D datasets.

Interpretation of 3-D data follows the same principles of radar stratigraphy as interpretation of 2-D data in terms of *radar facies* and *radar surfaces* that bound them. Specific to the 3-D approach is the use of *radar packages*. Identification of radar facies is facilitated by horizon tracing, and recognition of unique patterns on time slices as demonstrated by Beres *et al.* (1999). Patterns on time slices can be described in a similar way as geometrical relations on cross-lines, *i.e.* shape, orientation, relations between lines and their continuity.

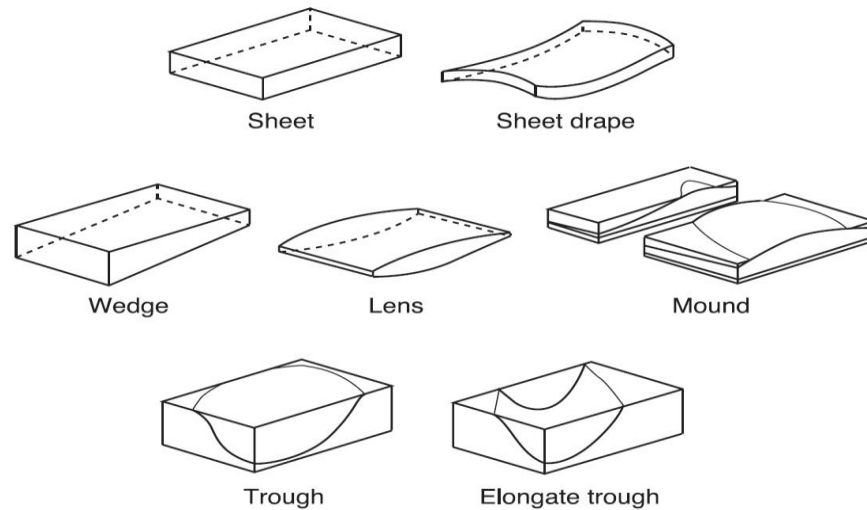


Figure 5.0.1 Radar packages used in radar stratigraphy identified for general use in sedimentology proposed by Neal (2004).

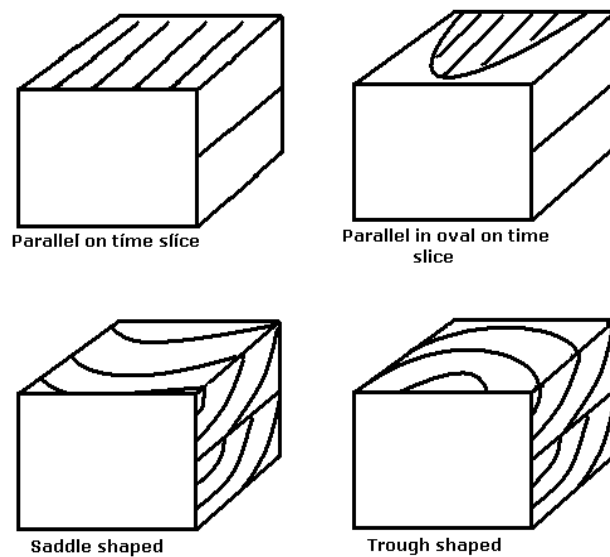


Figure 5.0.2 Examples of description of geometries of radar facies in 3-D. Top two are modified from Beres *et al.* (1999), bottom two modified from Neal (2004). The example described as ‘parallel on time slice’ with horizontal parallel reflections on the in-line could indicate a number of sedimentary structures depending on the geometrical pattern shown on the cross-line.

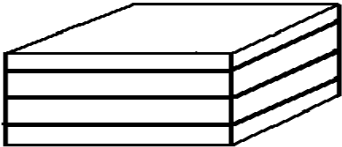
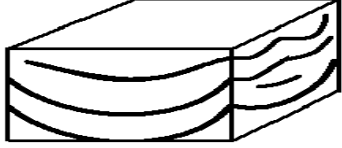
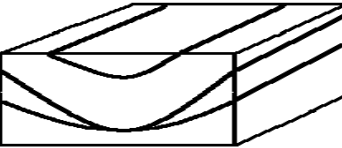
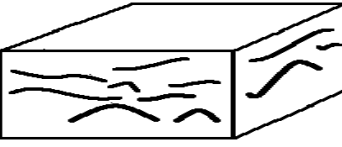
Radar facies are most often identified in 3-D data on vertical sections with time slices described independently, *e.g.* Beres *et al.* (1999). However, 3-D geometry of reflection patterns can also be described as they appear in 3-D space, such as examples given by Neal (2004) and shown in Figure 5.0.2. As presented in the following sections, reflection patterns identified on time slices are included as part of the radar facies description and help to better image their 3-D character. Images of 3-D data volumes not only present much more

information by including orthogonal profiles combined with time slices, but are also more realistic representations of the spatial arrangement of sedimentary facies.

### 5.1 CLASSIFICATION AND INTERPRETATION OF THE MACCLESFIELD RADAR FACIES BASED ON 3-D VISUALISATION

The following five main radar facies have already been identified on 2-D profiles: (1) continuous horizontal and sub-horizontal, (2) curved concave or undulating, often concordant reflections; (3) stronger-amplitude concave reflections on S-N oriented profiles, parallel horizontal and slightly inclined on E-W oriented lines; (4) discontinuous concave and undulating non-concordant reflections; (5) discontinuous undulating chaotic reflections with hyperbolic diffractions. These radar facies are reviewed below based on the geometry revealed by lower and higher resolution 3-D radar volumes.

Table 5.1 Summary of five 3-D radar facies identified in Macclesfield site (some patterns idealised).

	<b>Description</b>	<b>Representation</b>	<b>Sedimentary interpretation</b>
<b>Radar facies (1)</b>	continuous low-angle planar parallel		topsoil and over-bank vertical accretion deposit
<b>Radar facies (2)</b>	curved concave or undulating, often concordant		recirculation pool deposits
<b>Radar facies (3)</b>	upper part concordant, less concordant in lower part, half trough-shaped		recent point bar deposits
<b>Radar facies (4)</b>	mainly non-concordant elongated trough-shaped		older channel deposits
<b>Radar facies (5)</b>	irregular elongated discontinuous with hyperbolic diffractions		deposits with cobbles surrounding the older channel

A summary of the radar facies that incorporates their 3-D character as identified in the Macclesfield site is presented in Table 5.1. Some of the boundaries of radar facies have been traced across adjacent profiles.

As shown in this section, volume visualisation of the pseudo 3-D Macclesfield dataset together with visualisation techniques, such as time slicing, horizon tracing and transparency, revealed the internal organisation of the radar facies as well as spatial relations between the radar facies previously not identifiable with just 2-D profiles. Radar facies displayed in 3-D volumes are representations of the spatial character and distribution of sedimentary facies which makes the interpretation much easier and more certain.

Manual picking led to a random display of wave attributes and therefore TWTT could only be displayed on horizons which represent a radar surface. Horizon tracing led to the identification of four main horizons: a 'bowl-shaped' horizon bounding concave reflections of radar facies (2); lower and upper elongated trough-shaped horizons bounding concave and half-concave reflections to the north of the recirculation pool; and an elongated trough-shaped horizon bounding concave reflections surrounding the recirculation pool from the south and east. Geometrical relations, and particularly the application of principles of superposition and cross-cutting relations between surfaces, were used to interpret the relative age of the individual sedimentary facies. These radar surfaces are presented below in chronological order from the oldest to the newest.

#### 5.1.1 Elongated trough-shaped horizon which bounds radar facies (4)

A complex set of discontinuous concave non-concordant reflections were traced to create an elongated trough-shaped horizon which is shown in Figures 5.1.1 and 5.1.2. The horizon

bounds the group of concave-shaped reflections of radar facies (4), which truncate each other and are generally non-concordant, from the more chaotic undulating reflection pattern which has also been classified as radar facies (5).

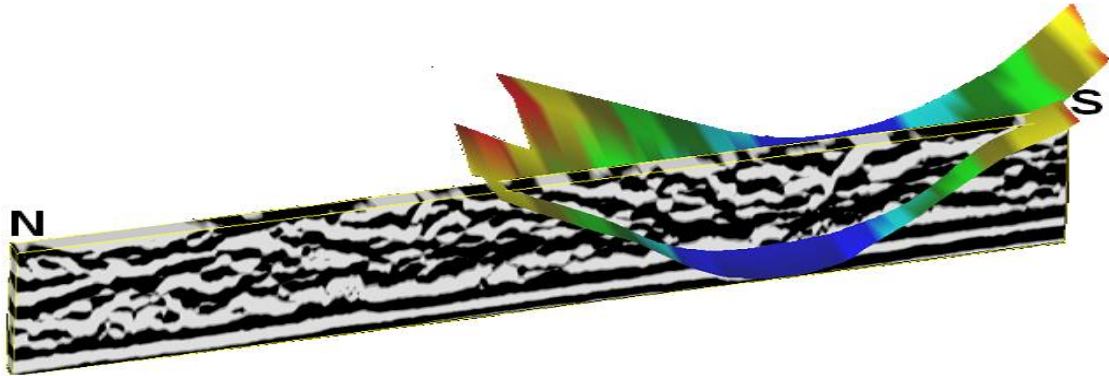


Fig. 5.1.1 Section of the lower resolution S-N amplitude volume (line 30 NS at the front) with the elongated trough-shaped horizon bounding concave reflections of radar facies (4). The axis of the horizon is oriented along the SEE-NWW direction. Note also more concave reflections immediately to the left (north) of the horizon.

Due to loss of signal below 100 ns, the bottom part of the horizon on some of the profiles is based on interpolation. The axis of the feature is oriented SEE-NWW, has a depth of approximately 4.0 m and stretches laterally up to about 20.0 m. The horizon is located in the south eastern part of the site and is shown in Figure 5.1.2. The pattern could be identified on the time slices to be irregular, elongated and oriented along the SEE-NWW direction. This pattern is also shown in Figure 5.1.3.

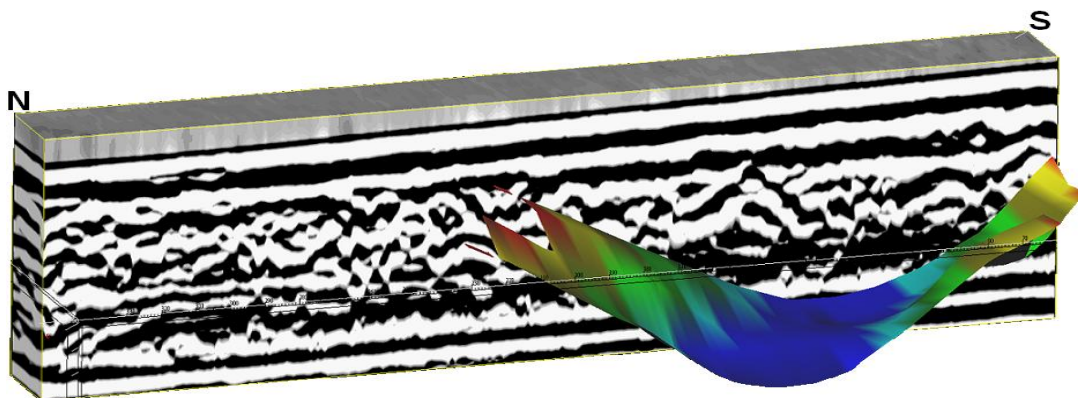


Fig. 5.1.2 Eastern section of the lower resolution 3-D Macclesfield amplitude volume (the S-N length of the volume is 34.0 m).

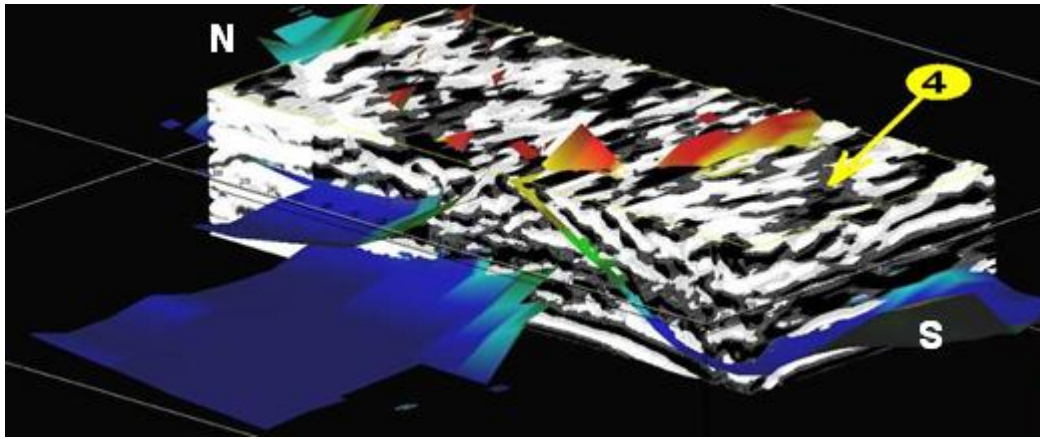


Fig. 5.1.3 Section of the lower resolution S-N volume inverted to velocity seen from the south west also showing radar facies (4) within the elongated half trough-shaped horizon. The lateral dimensions of the volume are approximately 25 x 10 m.

### 5.1.2 Elongated half trough-shaped horizons bounding radar facies (3)

Continuous concave and half-concave reflections have been identified in Section 4.1 as radar facies (3) and interpreted as recent point-bar deposits. This radar facies is located along the northern edge of the site. The interpretation is, however, problematic due to the thickness of the radar facies, which was far greater than expected when compared with the depth of the current river bed. However, when investigated in 3-D this facies appeared slightly different in the upper and lower parts. As a result of this, the facies classification needed to be reviewed and two separate reflection patterns are now distinguished.

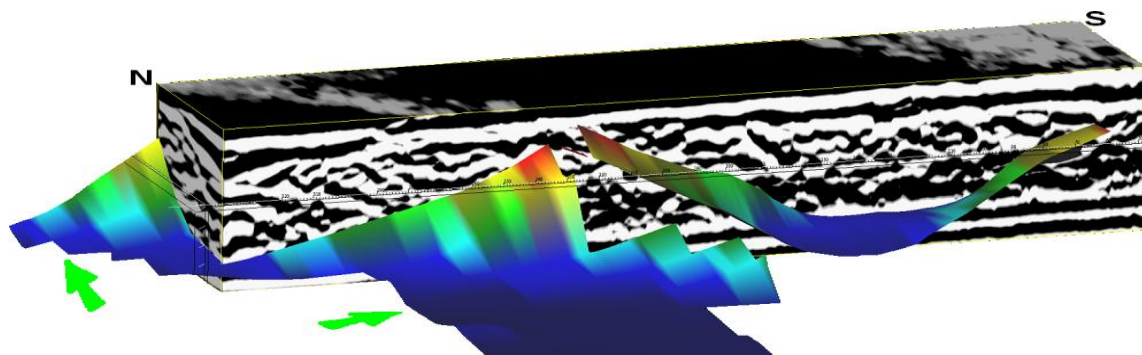


Fig. 5.1.4 Section of the lower resolution S-N amplitude volume shows the elongated half trough-shaped horizon (indicated by green arrows), which bounds radar facies (3). Note a number of concave reflections within the horizon. The axis of the horizon is oriented along the SE-NW direction. The lateral dimensions of the volume are approximately 25 x 5 m.

The bottom radar surface encloses similar reflection patterns to the one described in Section 5.1.1 which was classified as radar facies (4). These reflections comprise multiple concave

shapes of discontinuous irregular and non-concordant character. Some of the concave reflections appear to be truncated by others. Figure 5.1.4 shows the bottom elongated half-trough horizon, indicated by green arrows, which bounds a group of deeper concave reflections. The figure also shows that this horizon and elongated trough-shaped horizon, described in Section 5.1.1, may form a confluence if extended further west. However, this could not be confirmed due to the presence of radar facies (2) in this area (see Section 5.1.3).

The upper half-concave reflections have a more continuous concordant character and can be distinguished from underlying concave reflections. The base of the upper continuous concave concordant pattern, located at a depth of approximately 1.20 m, was traced across the volume. This resulted in the creation of the upper elongated half-trough horizon (3) shown in Figures 5.1.5 to 5.1.7. The lower and upper half-trough horizons are concordant and have a similar orientation and only differ by their depth and width.

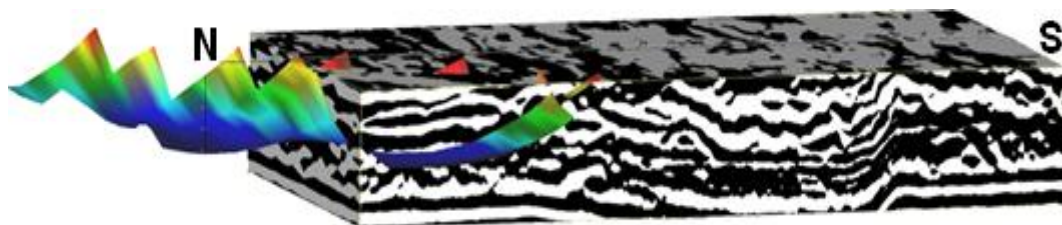


Fig. 5.1.5 Upper elongated half-trough horizon which forms a boundary of the continuous concave concordant reflections. Note boundary of the horizon also distinguishable on the time slice. The lateral dimensions of the volume are approximately 20 x 8 m.

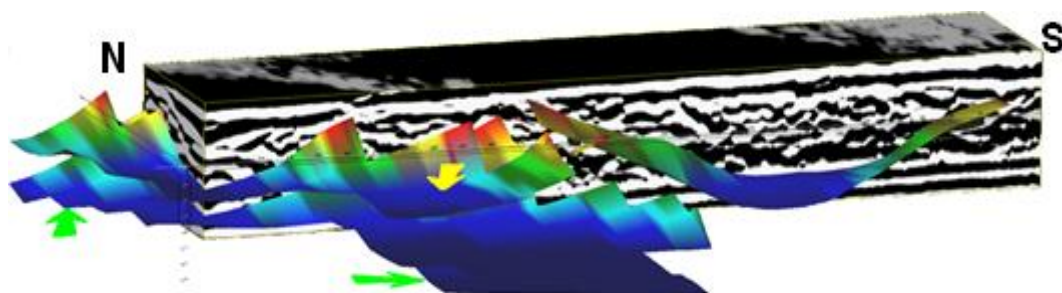


Fig. 5.1.6 Upper (yellow arrow) and lower (green arrow) half-trough horizons. The NE-SW orientation of the edge of the structure is also visible on the time slice. Field observations indicate silty sand deposits. The lateral dimensions of the volume are approximately 25 x 5 m.

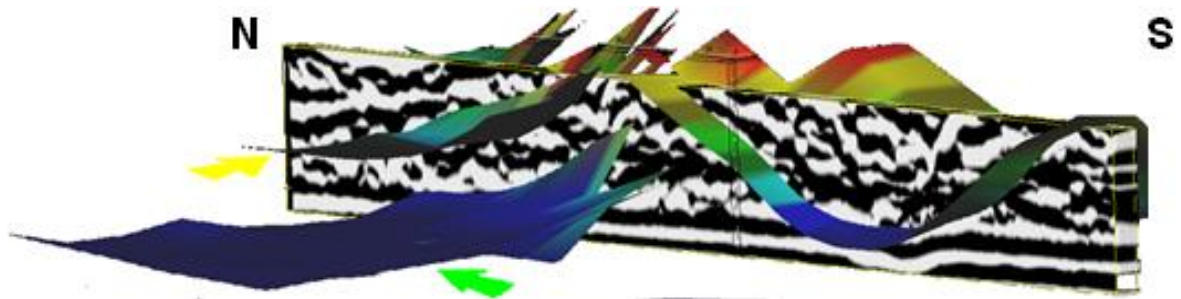


Fig. 5.1.7 Upper (yellow arrow) and lower (green arrow) half-trough horizons. Inclined reflections suggest point-bar deposits. The lateral dimensions of the volume are approximately 30 x 2 m.

### 5.1.3 Bowl-shaped horizon bounding concordant concave reflections of radar facies (2)

The boundary of the concave reflections restricted to the recirculation pool is shown in Figures 5.1.8 and 5.1.9. Volume visualisation of the data enabled the establishment of the boundaries of radar facies (2) with greater certainty. Kingdom Suite also enabled the creation of sections perpendicular to adjacent lines, described as cross-lines, in order to help investigate the radar facies boundaries. Tracing of the horizon on cross-lines led to a more robust interpretation of the architecture of the recirculation pool.

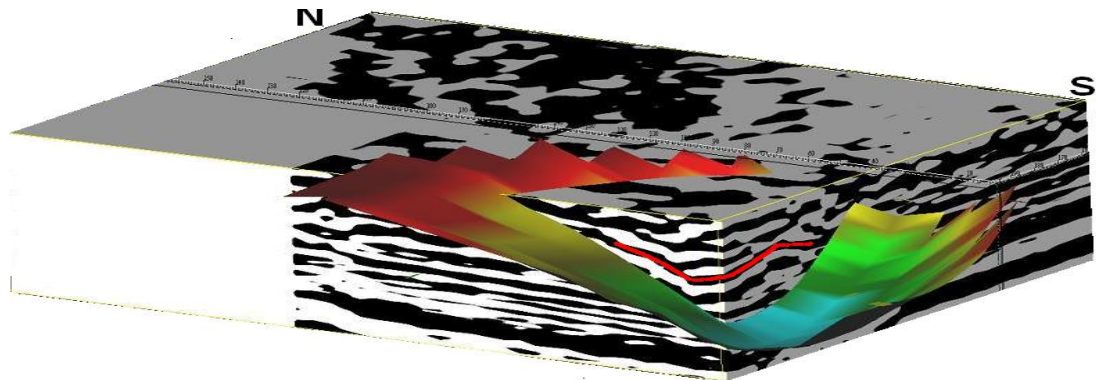


Fig. 5.1.8 The recirculation pool horizon with concave reflection surfaces which dominate the N-S oriented profiles and edges of the pool on the E-W profiles. Convex reflections are mostly recognisable on the E-W oriented profiles. The lateral dimensions of the volume are approximately 25 x 17 m.

The 3-D display revealed that the bottom part of the pool is dominated by concave reflections, and is bowl-shaped in 3-D.

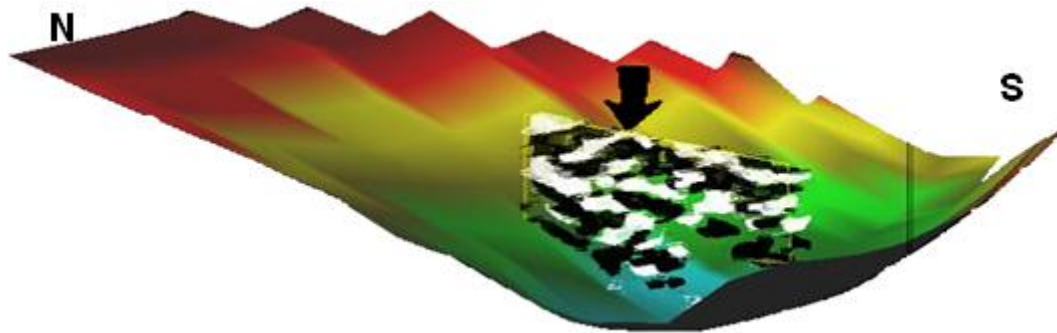


Fig. 5.1.9 The recirculation pool horizon with a small section of the lower resolution amplitude volume. The transparency technique was applied to investigate the internal architecture of the pool fill and revealed the convex shape of reflections in the upper central part of the pool (indicated by the arrow).

A slightly convex and undulating pattern, which in 3-D would create a mound shape, was also identified in the east-central part of the pool. This pattern is mainly recognisable on E-W oriented lines and is represented by a red line on higher resolution amplitude volumes in Figures 5.1.8 and 5.1.10. It is also indicated by an arrow on the N-S oriented section presented in Figure 5.1.9.

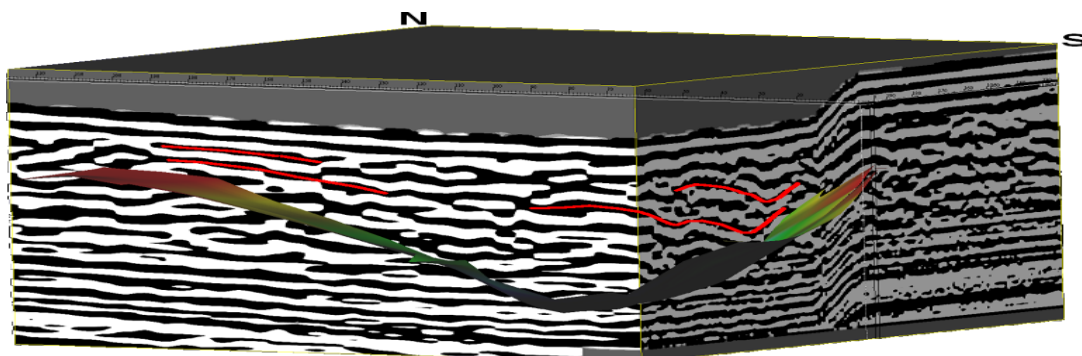


Fig. 5.1.10 Part of the higher resolution amplitude volume and the horizon which represents the erosional surface associated with the recirculation pool. The concave shape lines, which in the upper central parts of the pool are slightly undulating, may indicate potential depositional mechanisms within the recirculation pool. The lateral dimensions of the volume are approximately 20 x 17 m.

#### 5.1.4 Sedimentary interpretation and evolution of the Macclesfield site

The recent point-bar deposits, *i.e.* associated with the upper elongated half-trough reflection pattern, described in Section 5.1.2, are likely to be related to lateral channel migration. The lower group of half-concave reflections, however, has a different character from the upper ones. The lower elongated half-trough horizon, also described in Section 5.1.2, appears to comprise a series of trough reflections which may represent channels. Together with radar

facies (4) they may represent the multi-channel style of deposition. A greater vertical extent of radar facies (4) and a less concordant character of reflections in comparison with the upper part of radar facies (3) could be a record of abandoned channels. Their character, vertical and lateral extent would indicate a different depositional environment from the more recent one, *i.e.* different discharge, sediment supply and climatic conditions.

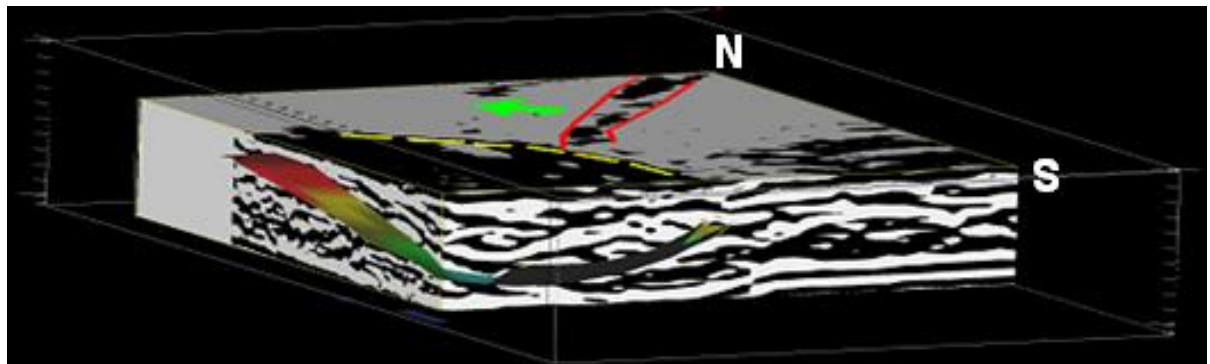


Fig. 5.1.11 The Macclesfield volume with time slice at 30.2 ns reveals shape of recirculation pool (indicated by yellow line) and the edge of point bar (indicated by red line). Green line indicates the direction of the river bank migration prior to erosion and creation of the pool. The lateral dimensions of the volume are approximately 20 x 18 m.

The lower and upper horizons associated with radar facies (3) follow the same course. Similarly, the location of the recirculation zone, shown in Figure 5.1.9, coincides with the extension of the channel marked by the elongated trough-shaped horizon presented in Section 5.1.1. The image in Figure 5.1.11 shows the relation between point-bar deposits and the recently filled recirculation pool in the River Dene. The erosional surface of the pool (indicated with a yellow line) cuts the elongated edge of the point-bar deposits (marked in red). This reveals the sequence of the river bank evolution, *i.e.* the recirculation pool is of later origin in relation to the point bar. The river bank must have moved further north (direction of bank migration indicated by green arrow).

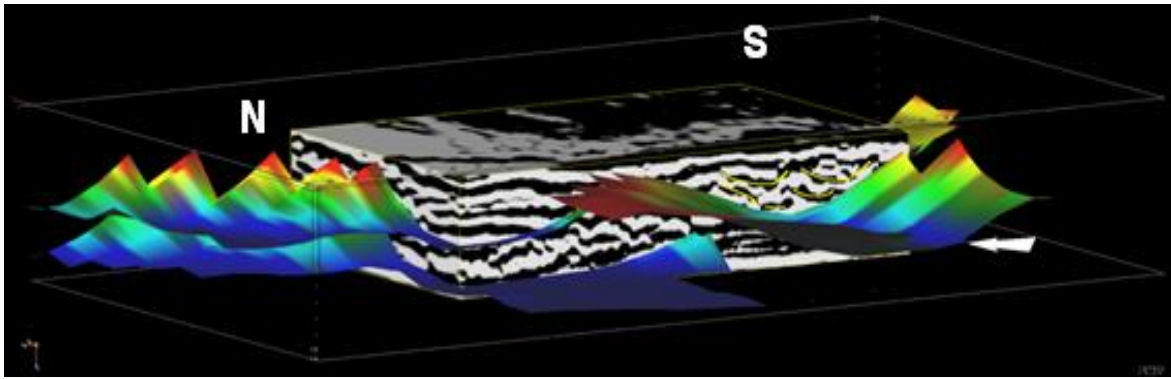


Fig. 5.1.12 Lower resolution amplitude volume (looking from the north west) with all four distinguished horizons. The recirculation pool, the horizon indicated by a white arrow, could have been developed through erosion of deposits associated with radar facies (4), indicated by yellow lines, which are bound by the elongated trough-shaped horizon described in Section 5.1.1. The lateral dimensions of the volume are approximately 10 x 24 m.

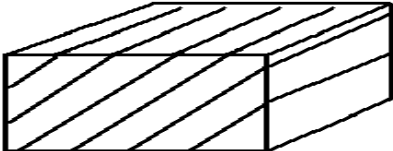
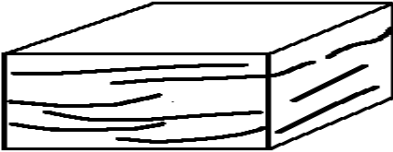
As already stated in Section 5.1, it is difficult to assess without excavation of trenches if the fill material within the channel associated with the horizon presented in Section 5.1.1 could be more easily eroded. The reflection pattern within the recirculation zone would indicate circular movement of the water during deposition of the fill material.

The pattern shown in Figure 5.1.10 indicates that the deepest parts of the pool are located along its edges with an elevated part in the central-east area of the pool. The central part of the pool acted as a place of deposition for the transported material. The 3-D display of the Macclesfield GPR dataset enabled a more in-depth analysis of the depositional architecture and better interpretation of the evolution of this section of the River Dene valley. It revealed changes in the channel course as well as possible changes in the character of the depositional environment. The hypothesis of different climatic conditions can be supported by the character of the deposits, which was identified in the cut-banks of the river. The heterogeneity of the deposits and presence of the cobble fraction could indicate fluvial transport characterised by a relatively higher energy environment to the current one. However, a more detailed analysis including trench excavation, sampling, grain size analysis and sedimentological classification would be required to establish its origin with greater certainty.

## 5.2 CLASSIFICATION AND INTERPRETATION OF RADAR FACIES REVEALED BY 3-D SOUTH SASKATCHEWAN RIVER 120 X 40 M GRID DATA

A summary of the radar facies identified on profiles and time slices of the South Saskatchewan River 140 x 70 m dataset is presented in Table 5.2.

Table 5.2 Summary of radar facies identified in the South Saskatchewan River 120 x 40 m pseudo 3-D grid. The classification follows descriptions given by Sambrook Smith *et al.* (2006b) for radar facies also identified in the South Saskatchewan River.

	<b>Description</b>	<b>Representation</b>	<b>Sedimentary interpretation</b>
<b>Radar facies (1)</b>	high-angle inclined planar and sigmoidal reflections, parallel on time slices		downstream accretion on margin slip-faces of unit and compound bars
<b>Radar facies (2)</b>	discontinuous undular and non-concordant trough-shaped reflections		sinuous-crested dunes
<b>Radar facies (4)</b>	concordant elongated trough-shaped reflections		cross-bar channels with fill

### 5.3.1 Description of radar facies based on 3-D datasets

The horizon shown in Figure 5.2.1 represents reflections classified in 2-D as a radar surface, which was interpreted as the main erosional surface separating the deposits of two unit bars. Distribution of the other radar facies is also presented in this figure and can be traced on the time slice across the whole dataset. As mentioned in Section 4.3, 2-D profiles are slightly oblique to the investigated depositional forms.

The volume is dominated by high-angle inclined reflections classified as radar facies (1) which, as identified in Section 4.3, forms 45% of all profiles. Two groups of radar facies (1) were identified. Time slices enabled correlation and identification of the distribution of facies as well as investigation of their character across the whole dataset.

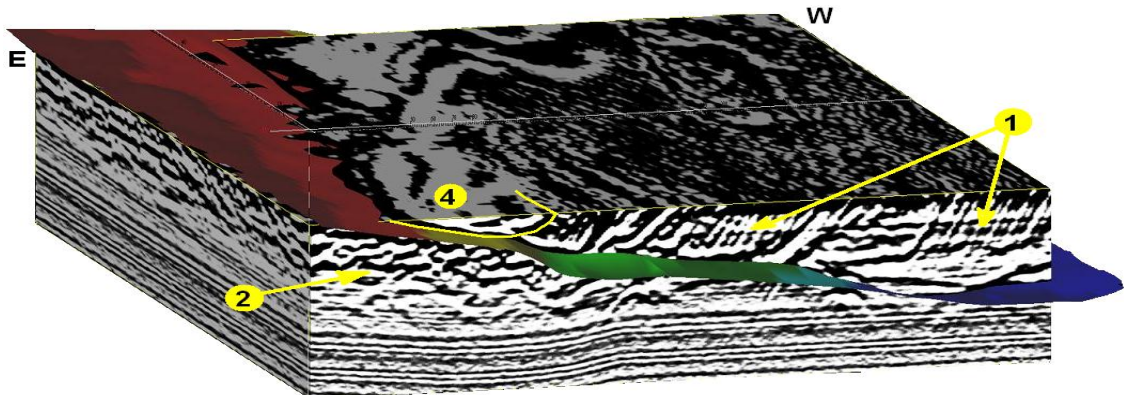


Fig. 5.2.1 Lower resolution amplitude volume showing 62.0 ns time slice. The volume shows, above the horizon, reflections of radar facies (1) inclined to the east and radar facies (4), *i.e.* small-scale concave reflections, located along the eastern edge of the volume. The lateral extent of these two facies as well as their directions can be traced on the time slice. Note the potential change of direction of bar migration indicated by crests of the inclined reflections which have NWN-SES orientation in the central section of the volume, while crests of the westernmost foresets are oriented along the N-S running line. The radar surface indicates full volume dimensions.

The upper group of radar facies (1) is located immediately above the horizon (labelled '1' in Figure 5.2.1). This radar facies is overlain by radar facies (2), but radar facies (4) can also be found along the eastern edge of radar facies (1).

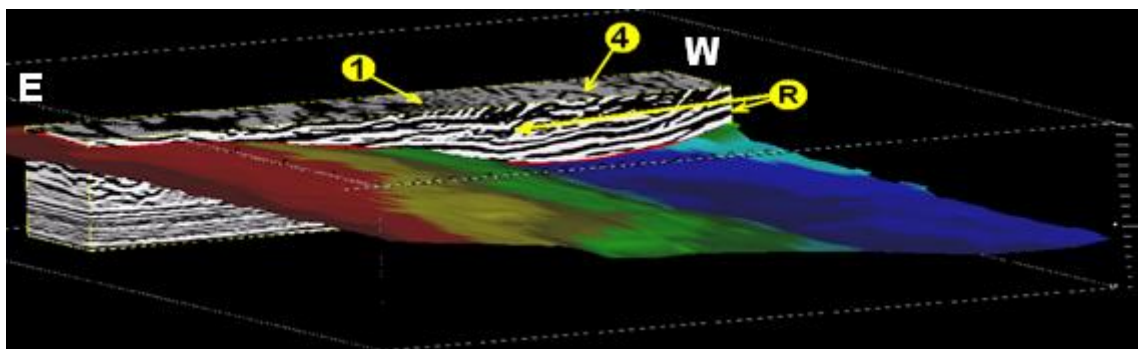


Fig. 5.2.2 Southern section of lower resolution amplitude volume showing 62.0 ns time slice. Radar facies (1) is represented only by a limited thickness of steeply inclined reflections. Radar surface, marked as 'R', is represented by a number of strong-amplitude reflections. Radar facies (4), represented by an oval shape on the time slice, is possibly related to a 'bartop hollow' described by Best *et al.* (2006). The radar surface indicates full volume dimensions.

Radar facies (4) rests on top of radar facies (1) in the south western part of the volume,

labelled '3' in Figure 5.2.3. The crests of the inclined reflections of radar facies (1) are oriented along the NWN-SES direction in the central part of the volume; further along the western edge of the volume, the inclination is oriented perpendicular to the W-E oriented profiles. This facies was identified to be associated with deposition on downstream bar margins.

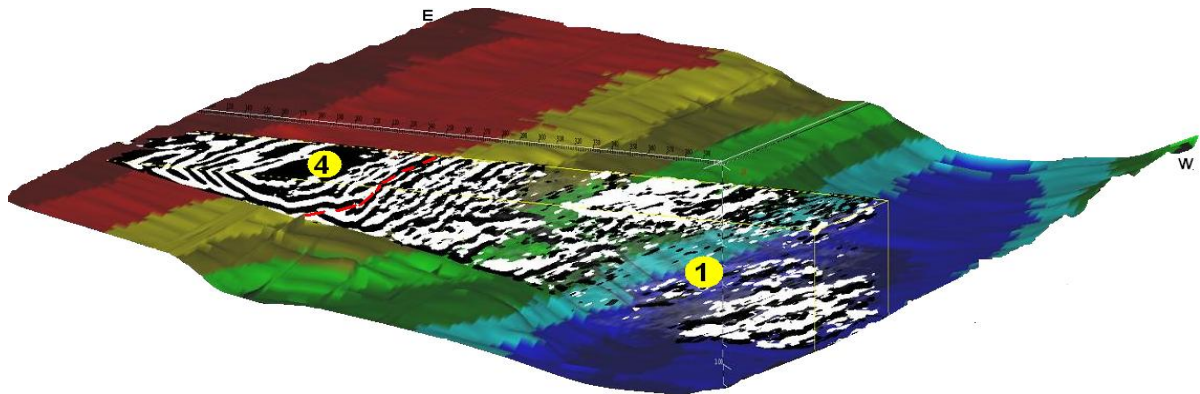


Fig. 5.2.3 Section of lower resolution amplitude volume with transparency technique applied which revealed the upper group of radar facies (1) and (4). The boundary between these facies is marked by a red line. The radar surface indicates full volume dimensions and the colours refer to the relative TWTT.

The direction of the bar migration can now be estimated based on information from time slices (see Figure 5.2.4). An assessment of the orientation of foresets on 2-D would be very difficult. However, the time slices revealed the orientations across the whole dataset. The time slice in Figure 5.2.4 shows that the orientation of the foresets changes from dipping towards NE (indicated by red line) to dipping towards the E and SE further west (indicated by green lines). Such information would not be available if interpretation were based only on 2-D profiles.

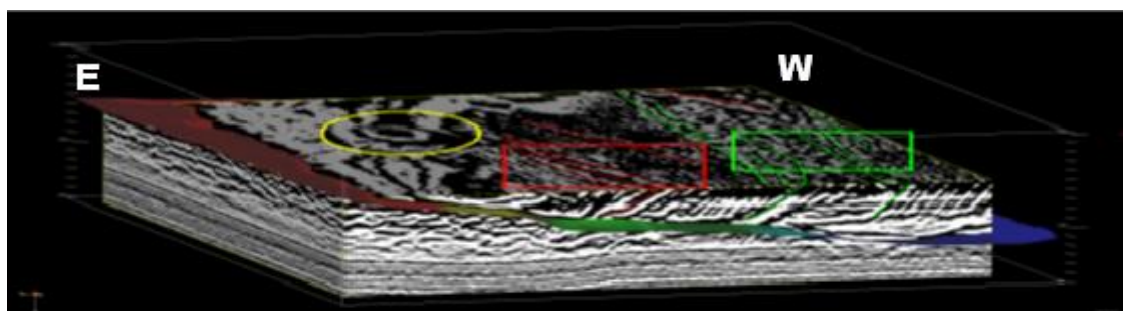


Fig. 5.2.4 The South Saskatchewan River 120 x 40 m grid volume with time slice at 57.5 ns reveals the orientation of foresets (red and green rectangles). The time slice showed that the orientation changes significantly across the dataset. The yellow circle indicates a scour located between two unit bars. The radar surface indicates full volume dimensions and the colours refer to the relative TWTT.

As already identified in Section 4.3, the lower group of radar facies (1) is located at the bottom of the central parts of the profiles and immediately below the horizon. In the eastern parts of profiles this radar facies is overlain by a layer of radar facies (2) up to 1.50 m thick. The eastern part of the volume is occupied by elongated trough-shaped reflections which together resemble a channel. Two ‘bartop hollows’ (Best *et al.* 2006) were identified on time slices (indicated by a yellow circle in Figure 5.2.4). Their identification in 2-D sections would not be possible due to poor correlation between adjacent 2-D lines.

### 5.2.2 Sedimentary interpretation and evolution of the site

The 3-D data visualisation enabled a detailed investigation of the distribution of sedimentary facies within the upper, *i.e.* western, unit bar. The presented horizon, which marks a radar surface, represents a boundary between two unit bars, each of which comprises radar facies (1) overlain by radar facies (2), *i.e.* deposits formed by downstream accretion on bar margins overlain by dune deposits classified as vertical accretion.

The thickness of inclined sets of radar facies (1) increases downstream (to the north) with increasing depth of the channel. Sinuous and trough-shaped reflections of the lower group of radar facies (2) appear to be of a larger scale than those of the upper group of radar facies (2). This can also be explained by the greater depth of the channel associated with their origin.

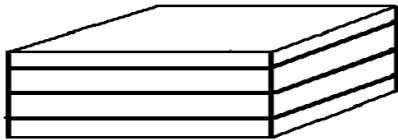
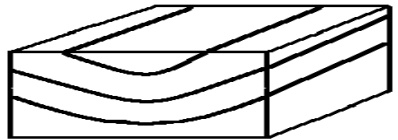
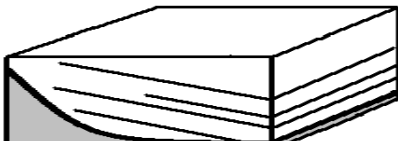
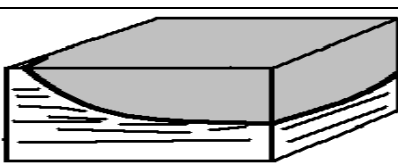
The demonstrated sequence documents the cross-channel migration of the western unit bar towards the south west and onto the eastern bar. The time slices would indicate the direction of migration of the bar towards the ENE. The small-scale elongated trough of radar facies (4) located in the eastern part of the volume and on the margin of the western unit bar is interpreted as fill deposited in the cross-bar channel which developed as a result of the

migration of the western bar onto the eastern one. The sedimentary architecture of the fill within the cross-bar channel would suggest a general direction of the flow towards the north. Animations of the 3-D volumes are included in Appendix 3.

### 5.3 CLASSIFICATION AND INTERPRETATION OF RADAR FACIES REVEALED BY 3-D SOUTH SASKATCHEWAN RIVER 10 X 10 M GRID DATA

A summary of the radar facies with an appreciation of their 3-D character, represented by differences between patterns on E-W and S-N oriented profiles, identified in the South Saskatchewan River 10 x 10 m dataset is presented in Table 5.3.

Table 5.3 Summary of identified radar facies in the South Saskatchewan River 10 x 10 m true 3-D volume.

	Description	Representation	Sedimentary interpretation
<b>Radar facies (3)</b>	continuous low-angle, often parallel, slightly undulating reflections		low-amplitude dunes
<b>Radar facies (4)</b>	concordant elongated trough-shaped reflections		cross-bar channels with fill
<b>Radar facies (5)</b>	inclined reflections within continuous, inclined to the west, strong-amplitude negative-phase reflection		fragment of a large-scale erosional surface with scour fill
<b>Radar facies (6)</b>	discontinuous low-angle parallel reflections		older alluvial deposit, possibly glacial till or bedrock

#### 5.3.1 Large-scale inclined horizon

A continuous inclined high-amplitude negative-phase reflection overlain by variable dip reflections and truncating radar facies (4) was traced across adjacent lines and led to the creation of a large-scale inclined horizon which extends between depths of about 3.50 and

6.50 m. The horizon is indicated by a red arrow in Figure 5.3.1. Volume display, time slicing and application of the transparency technique enabled investigation of the inclination of reflections within the scour. The scour fill is shown as a section of the amplitude volume in Figures 5.3.1 to 5.3.3 and contain an upstream-inclined set of reflections of a vertical extent of approximately 90 ns, *i.e.* a thickness of about 2.50 m, and inclination of up to 15 degrees.

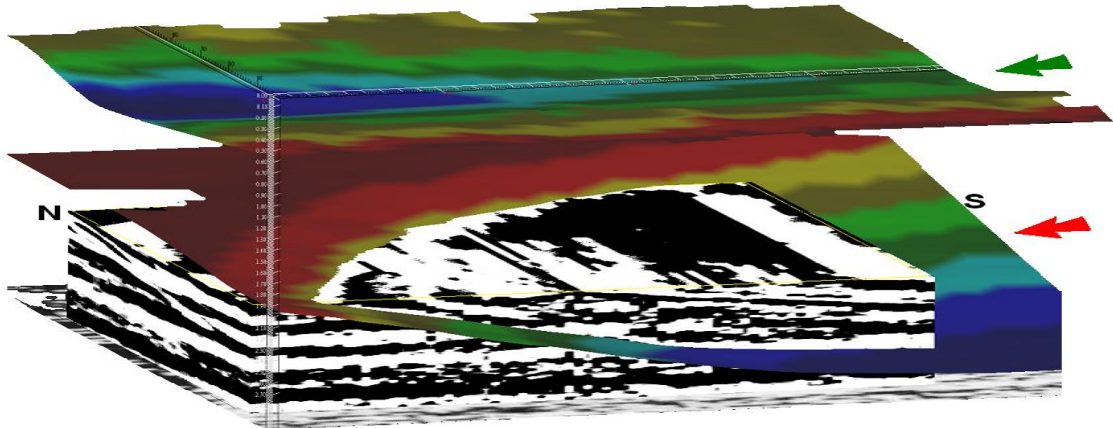


Fig. 5.3.1 Lower resolution volume (looking from the north east) which shows the large-scale inclined horizon (indicated by a red arrow) interpreted as fragment of a deep scour between depths of 3.50 and 6.50 m and marked by negative-phase amplitude. Time slice at 216 ns and fragment of the amplitude volume show series of reflections interpreted as upstream-inclined bedding of the scour fill. The green arrow indicates the small-scale elongated trough-shaped reflection (described in Section 5.3.2) and the approximate direction of the river flow.

The inclined reflections, indicated by blue lines in Figure 5.3.2, have a planar character. These reflections terminate by forming onlap onto the inclined horizon. The pattern is interpreted as a result of upstream accretion associated with the migration of a large bedform such as a large dune or unit bar.

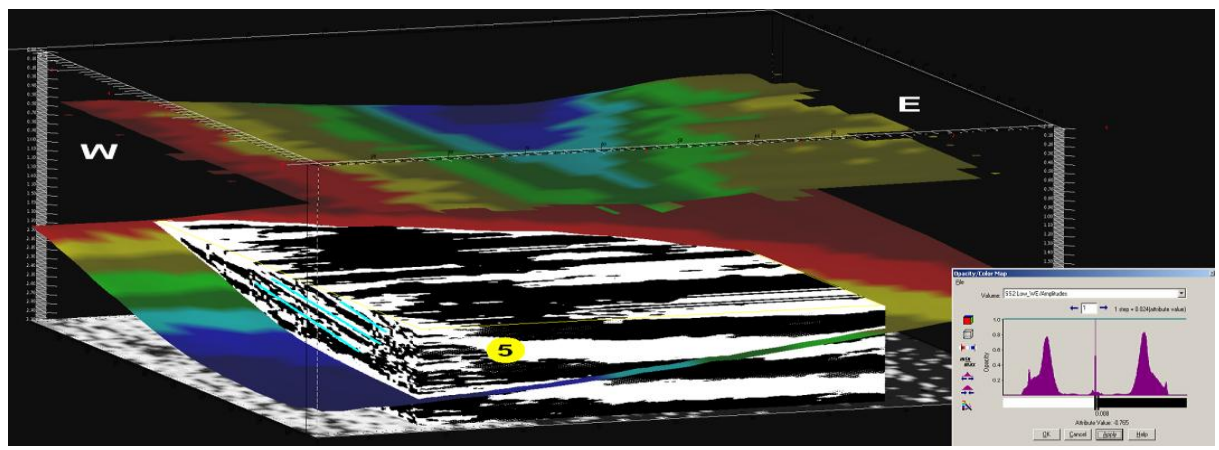


Fig. 5.3.2 Low resolution volume (looking approximately from the south) with time slice at 216 ns and which shows both of the horizons and radar facies (5). Inclined reflections of the scour fill are indicated by blue lines.

Detailed investigation which involved time slices of the zone immediately above sets of reflections inclined to the south (upstream) revealed depositional features previously not recognisable on 2-D profiles. The time slice included in Figure 5.3.3 shows a curved shape with small-scale reflections, shown by red lines, which are inclined towards the north on the N-S oriented sections and to the east on E-W oriented profiles. The feature can be found between 150 to 180 ns, *i.e.* between depths of about 3.80 and 4.30 m. This pattern was previously interpreted on 2-D profiles as hyperbolic diffraction from a point object. These inclined reflections marked by red lines may be interpreted as lateral or downstream accretion. Their height would indicate depositional features larger than the dunes, which in the South Saskatchewan River range between 0.15 and 0.49 m with typically a third of each dune preserved (Parker *et al.* 2008).

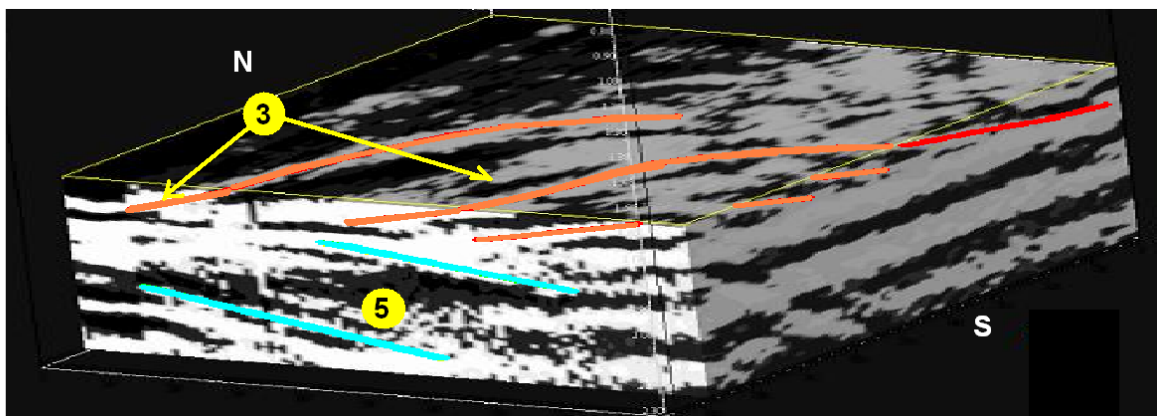


Fig. 5.3.3 Section of the amplitude volume with time slice at 163 ns, front section oriented N-S (north to the left). The volume reveals a pattern previously not recognisable above the large-scale inclined horizon. Blue lines represent upstream-inclined reflections within the scour fill. Red lines indicate a group of slightly inclined reflections which on the time slice create a circular shape resembling a point bar or a unit bar with downstream (N-S oriented section) and lateral accretion (W-E oriented section). Radar facies indicated by numbers.

### 5.3.2 Small-scale elongated trough-shaped horizon

A concave reflection was traced across the E-W oriented lines and this led to the creation of a small-scale elongated trough-shaped horizon which is shown in Figures 5.3.4 to 5.3.6. The horizon presents detailed morphology of the cross-bar channel previously not recognisable based on 2-D profiles.

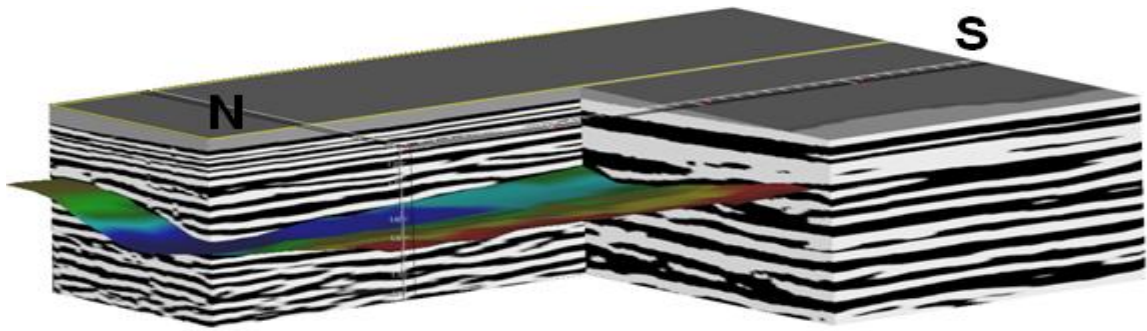


Fig. 5.3.4 Comparison of sections of the higher (left) with lower resolution (right) South Saskatchewan River 10 x 10 m volume which show N-S oriented elongated trough-shaped horizon and 3-D sedimentary architecture of deposits within it.

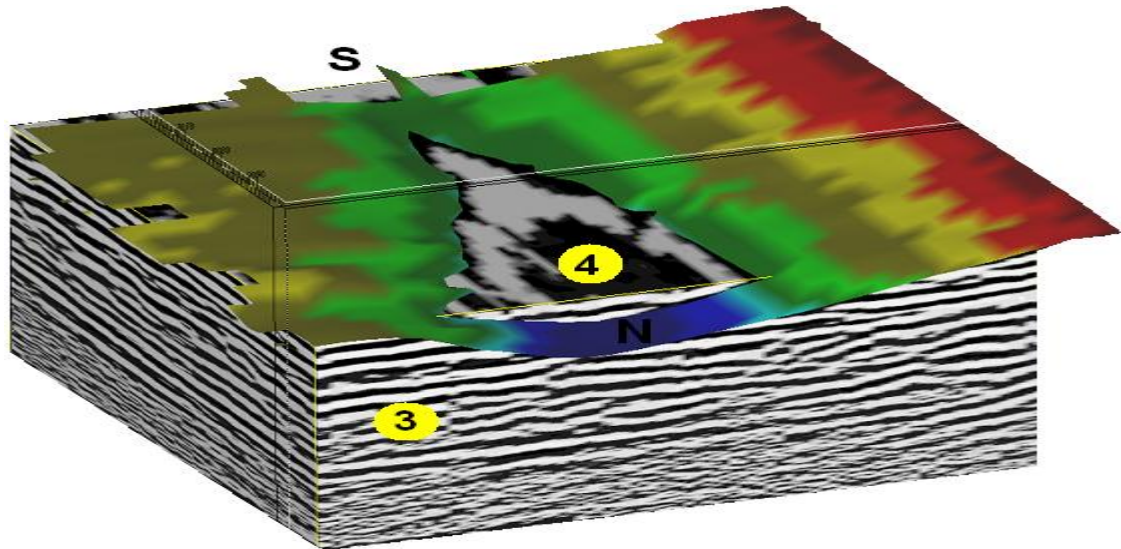


Fig. 5.3.5 Upper part of the high resolution South Saskatchewan River 10 x 10 m amplitude volume with small-scale elongated trough-shaped horizon with its axis oriented along the N-S direction (view from the north). The time slice at 73 ns revealed the morphology of the buried channel. Note the slightly concave shape of the reflection within the channel.

The time slice presented in Figure 5.3.5 revealed also more details about the internal structure of the fill material. The horizon both truncates and is overlain by the low-angle continuous lines which have been correlated with small-scale cross-stratification and are interpreted as dune deposits. Investigation of radar facies (2) also utilised time slices. As was established in Section 4.2, the continuous low-angle, often parallel, reflections represent boundaries of sets of small-scale cross-stratification related to migration of low-amplitude dunes and bars (Sambrook Smith *et al.* 2006b). The time slice shown in Figure 5.3.6 revealed the direction of inclination of these low-angle reflection interfaces. Such inclination may be related to gently climbing dunes and the linear pattern of N-S orientation could indicate the direction of the dune migration.

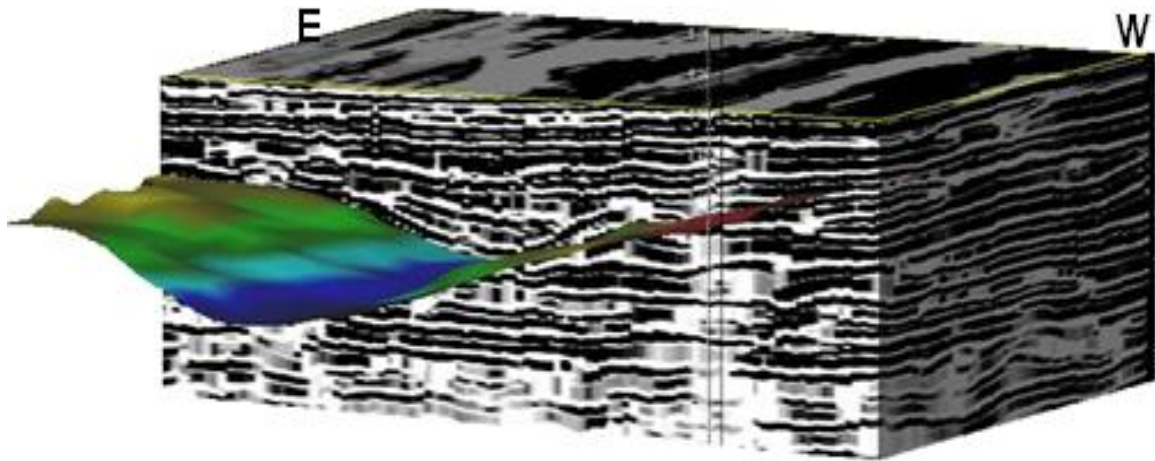


Fig. 5.3.6 Part of the volume inverted to velocity created from the South Saskatchewan River true 3-D dataset with the elongated trough-shaped horizon (view from the north). As a result of the inversion process, the black and white layers directly represent lithological units instead of the boundaries between them. Note the pattern visible on the time slice. The pattern may indicate the linearity of lithological units which are interpreted as sets of small-scale cross sets. The linearity may indicate the direction of migration of these forms. The lateral dimensions of the displayed volume are approximately 5 x 10 m and the total depth of ~3 m.

### 5.3.3 Sedimentary interpretation and evolution of the site

Based on the identified radar facies and their spatial distribution, it has been established that the radar surface, described in Section 4.3.1, represents a deep scour with upstream sedimentation. Upstream accretion deposits are immediately overlain by an approximately 0.50 m thick layer of deposits which possibly resulted from lateral accretion. A change in style of deposition from upstream to lateral and possibly downstream accretion is indicated by low-angle reflection lines between the blue and red lines in Figure 5.3.3 and may be a result of sedimentation during a period of lower water discharge (Best *et al.* 2003). These deposits are in turn overlain by radar facies (5), presented in Section 5.3.2, which represents a change in depositional character to vertical accretion related to the migration of dunes of various scales.

The low-angle reflections represent boundaries between sets of small-scale cross-stratification which itself is not resolvable by GPR data (Sambrook Smith 2006). The elongated trough-shaped horizon (Figure 5.3.7) is most likely to be related to the cross-bar channel. The 10 x 10

m dataset represents a vertical sequence of deposits which record a continuous change between upstream, lateral and vertical accretion related to changing flow conditions.

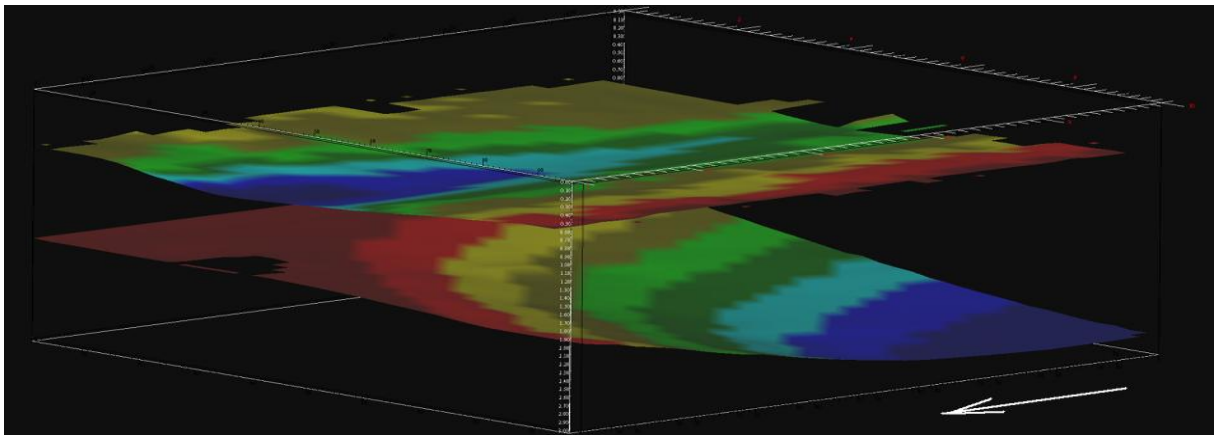


Fig. 5.3.7 Both of the identified horizons which helped in interpreting the 3-D volume. The bottom horizon represents the fragment of a deep scour, while the upper one represents the cross-bar channel. The arrow indicates the north and an approximate flow direction (towards the north).

Interpretation of the lower horizon as a deep scour was confirmed by a 2-D S-N oriented GPR profile which runs through the middle point of the 10 x 10 m grid analysed here. Part of the profile is shown in Figure 5.3.8 with vertical white lines indicating the boundaries of the 10 x 10 m volume and the red line indicating the scour-related reflection. The zone of lateral and possibly downstream accretion on the unit bar was identified between depths of about 3.50 and 4.80 m, and is overlain by the vertical accretion. Animations of the 3-D volumes are included in Appendix 3.

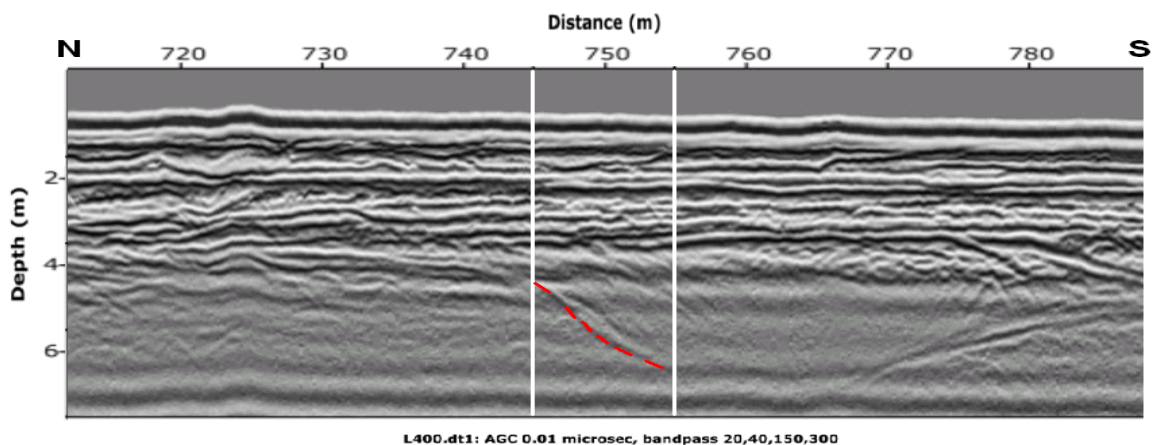


Fig. 5.3.8 Part of a 2-D GPR profile collected in the South Saskatchewan River and which runs through the centre of the 10 x 10 m GPR grid. The white lines indicate the horizontal extent of the 3-D GPR grid. The above 10 x 10 m volume presents part of a large scour (marked in red). The location of the profile is indicated in Figure 4.2.1. Note upstream (flow to the north) inclined reflections between the vertical white lines within the scour and frequent diffraction hyperbolas below the scour surface.

## CHAPTER 6 DISCUSSION

The previous chapters dealt with the methodology of collecting, displaying and interpreting GPR data in fluvial sedimentology. This section tries to establish best practice for using GPR in fluvial sedimentology and summarise the benefits and constraints of using 3-D display generated from grids of GPR profiles in contrast with using 2-D data without 3-D visualisation. Thus, this section discusses such subjects as choosing the most suitable survey mode, optimal distances between survey stations, scope of processing, displaying data and using interpreted data to construct sedimentary models.

**Survey mode:** To choose the most effective survey mode it is beneficial to have a preliminary knowledge of the subsurface. When studying contemporary fluvial deposits some information can be inferred from the surface features based on existing sedimentary models. However, a trial GPR survey could also help to assess the complexity of the architecture. Both 2-D and 3-D survey modes have their advantages and limits. Despite the efficiency and resolution of using individual 2-D profiles, interpreting sedimentary architecture from such profiles may be difficult and misleading. The orientation of the profiles to the direction of the paleocurrent may still remain uncertain due to the dynamic and alternating character of the river flow. Another difficulty is associated with the necessity of inferring their 3-D appearance from individual 2-D profiles and interpolating radar facies and surfaces between GPR lines.

When structures are viewed on individual 2-D profiles, some patterns associated with sedimentary forms of a very contrasting depositional nature may appear similar. Similarities between sedimentary forms in meandering and braided rivers have been presented by many

authors (e.g. Bristow and Best 1993), and they can be misleading when interpreting ancient depositional records.

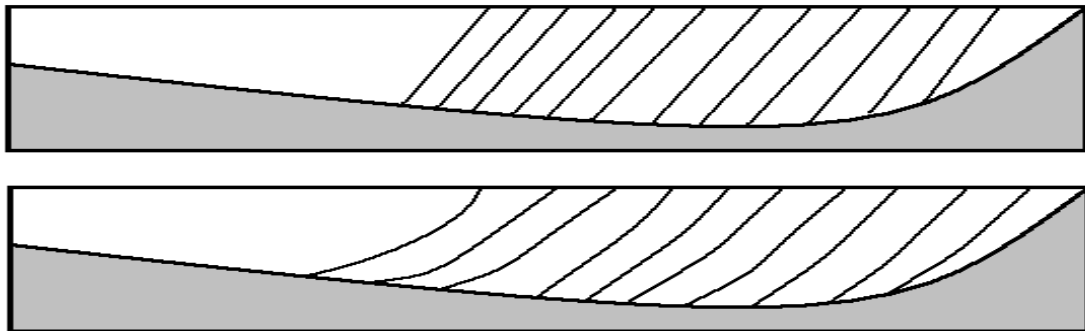


Fig. 6.1 Comparison of 2-D profiles of inclined bedding related to the downstream accretion on the margin of a braid bar (above) and of lateral accretion of point bar deposits in a meandering river (below). Correct interpretation would require knowledge of the paleocurrent directions or at least orthogonally oriented profiles.

Figure 6.1 illustrates the similarity between high-angle inclined bedding produced by downstream accretion on slip faces of a braid bar and inclined bedding in a point bar as a result of lateral accretion in a meandering river. Displaying grids of closely spaced profiles with seismic interpretation software in 3-D provides a solution to this. A comparison of the scope and quality of information available from 2-D and 3-D data is shown in Figure 6.2.

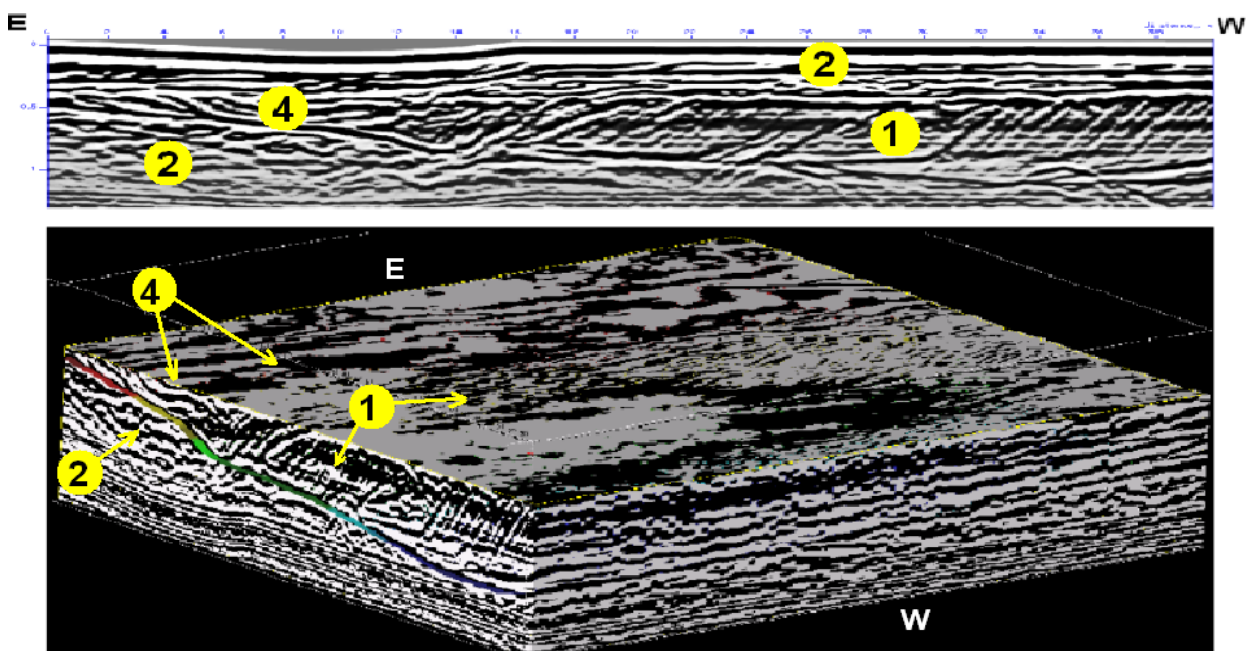


Fig. 6.2 Comparison of 2-D profile (line 02) from the South Saskatchewan River 120 x 40 m grid with a section of 3-D volume (line 02 and time slice at 47 ns). Note that the N-S oriented profile in the 3-D volume presents all of the radar facies as parallel horizontal lines. The 3-D GPR data volume displays the information as 2-D enriched by the time slice and 3-D display of the radar surface. Better demonstration of the method is presented as the 3-D animation in Appendix 3.

The 2-D profile shown in Figure 6.2 is almost parallel to the river current direction during the high flow period which resulted in deposition associated with radar facies (1). The 2-D profile is however, nearly perpendicular to the flow during the low water level period responsible for the character of radar facies (2). The paleoflow directions changed by nearly 90 degrees. Thus orientation of the survey line resulted in the profile displaying relatively good information about the sedimentary architecture. However, if the lines were collected in a N-S orientation, both the radar facies (1), (2), (4) and the radar surfaces would appear as a series of horizontal lines, as demonstrated by looking at the N-S running profile in the 3-D volume in Figure 6.2. Interpretation of such a profile would thus lead to misleading conclusions. Both examples demonstrate that even if a 2-D survey mode is used, collection of a widely spaced grid of orthogonally oriented lines is a minimum requirement. The analysis and interpretation of sedimentary architecture therefore should not be limited to individual 2-D exposures or single 2-D geophysical profiles.

Figure 6.2 also demonstrates that when data is viewed in 3-D, precise orientations of accretion deposits, changes in the flow direction and facies relationships become apparent, thus allowing unequivocal interpretation of the origin of deposits. The 3-D display also shows the spatial extent of facies which cannot be judged from individual 2-D profiles, or even wide spaced grids of data. Without knowledge of their pattern in 3-D, radar facies viewed on individual profiles can be readily mis-interpreted. For example bar-top hollows (see Glossary) can be interpreted as cross-bar channels when only viewed on 2-D profiles. This is illustrated in Figure 6.3 which shows radar facies (4) viewed on the 2-D profile. Radar facies (4) was found both in the western and eastern part. When viewed in 3-D volume, their oval plan form shape in the western part (marked with green circle) becomes apparent, hence, the interpretation as a bar-top hollow.

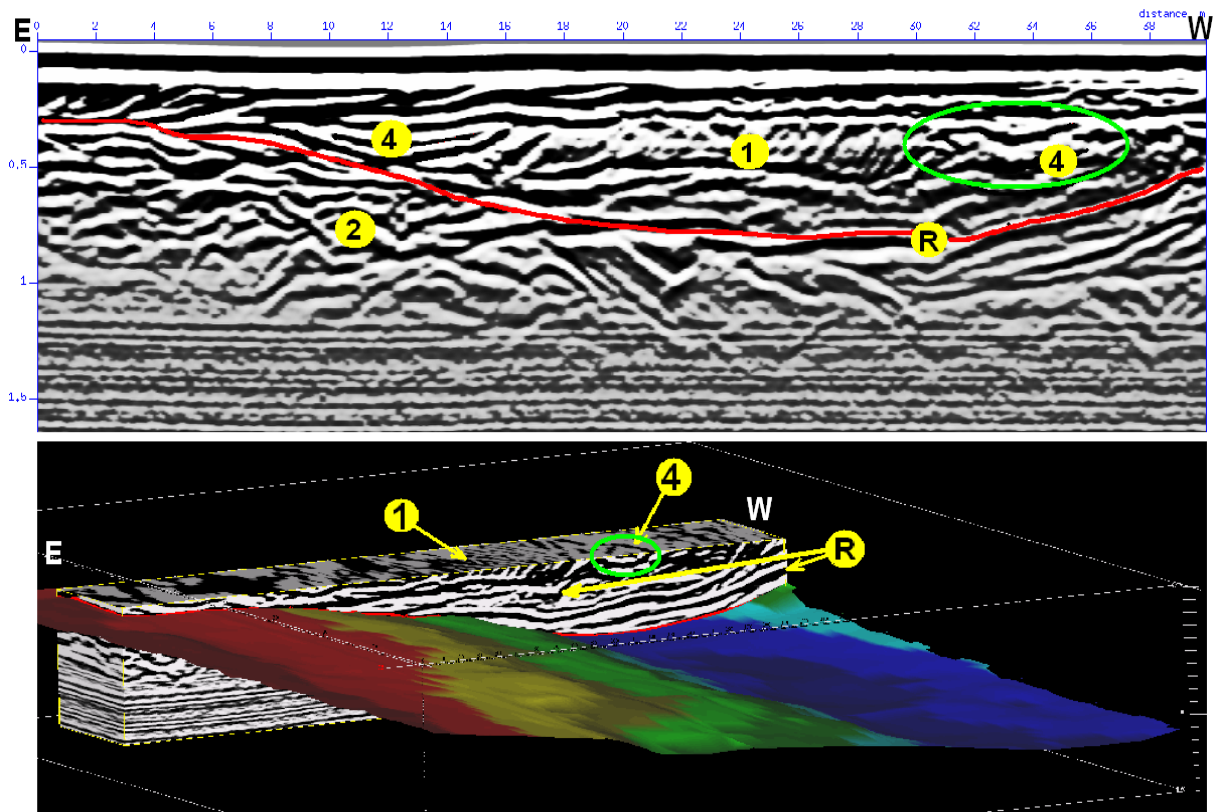


Fig. 6.3 The South Saskatchewan River 120 x 40 m dataset comparing the appearance of radar facies (4). The 3-D volume display revealed that this facies is associated both with crossbar channels and bar-top hollows (indicated by the green circle).

Although the interpretation stage is done more efficiently, collecting such GPR grids particularly with equal distances between lines and stations may be time-consuming when compared to individual 2-D profiles, as is the compilation of 3-D datasets. This could be one of the reasons why 3-D surveys have been so rarely used in fluvial sedimentary studies. Outside sedimentology, pseudo 3-D GPR surveys are conventionally performed as part of archaeological investigations (Novo *et al.* 2008, Boniger and Tronicke 2010). They are also not uncommon as part of geotechnical ground studies, *e.g.* mapping the topography of peat/bedrock interface for wind farm development (Carpenter *et al.* 2006), although true 3-D GPR surveys are very rare and considered impractical. As a compromise, if large lateral coverage is required it can be beneficial to use a grid of GPR profiles with wider line spacing satisfying the required lateral resolution. Another alternative is to collect a laterally extensive grid of widely spaced profiles combined with smaller grids of densely spaced survey lines

taken in areas where the architecture is more complex or of greater interest.

In order to highlight the factors which determine the most appropriate GPR survey method, a decision flow chart is presented in Figure 6.4.

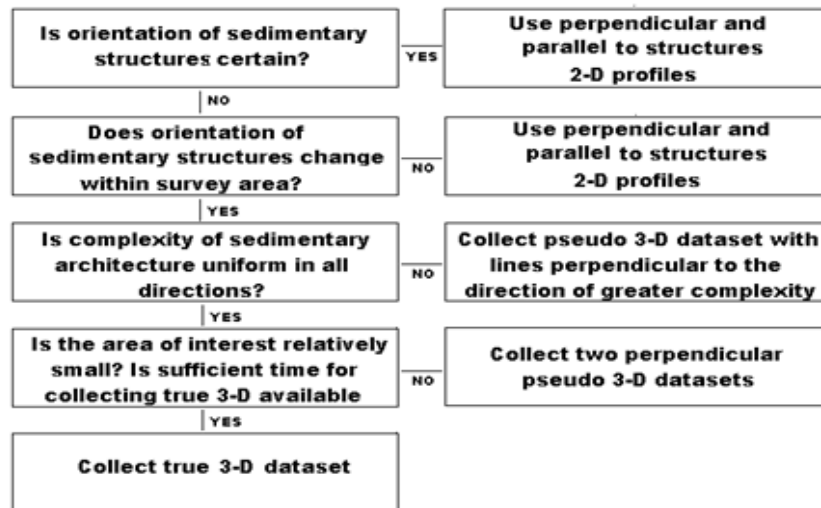


Fig. 6.4 Simplified decision flow chart for choosing optimal GPR survey method.

The following aspect can also be taken into account when considering the survey mode: (1) how important is the lateral extent of the targeted depositional elements in relation to their vertical character, (2) changes of the paleoflow direction in time and space, (3) the scale of targeted sedimentary structures in relation to the distances between 2-D GPR profiles. If the architecture is complex and interpretation requires patterns to be displayed on time slices, 3-D methods may be necessary. Likewise, if frequent changes of flow direction in space and time within the dataset are expected, 3-D display may be more appropriate. The next paragraph discusses the subject of choosing appropriate distances between survey points.

**Distances between survey points:** When the method of survey is established, the optimum distance between survey points should also be determined based on knowledge of the subsurface. Generally, with higher frequency antenna smaller distances between adjacent survey points are recommended. Woodward *et al.* (2003) reported that at least 10 adjacent

traces on a 2-D profile were necessary to be located above a sedimentary structure. The experiment presented in Section 3.2, where traces were removed from datasets, highlighted the relation between the dimensions of structures and the maximum distance between adjacent survey points able to resolve them. The relation identified during this experiment is shown in Figure 6.5.

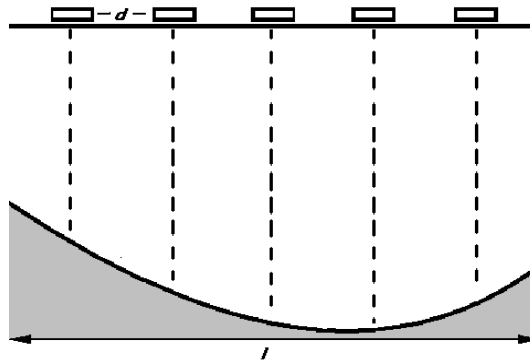


Fig 6.5 Required maximum distance between survey points (stations and lines) in relation to dimensions of structures.

The example from the Macclesfield site shows near surface structures at a depth of ~1.0 m and with dimensions of ~1.5 x 2.0 m were resolvable although oversimplified with distances of 0.50 m between lines and traces. This situation would suggest the following empirical relationship:

$$d < 0.2 l$$

where  $d$  is the mean distance between adjacent lines and survey stations and  $l$  is the lateral extent of sedimentary forms. This is an approximate relation as the lateral resolution is affected by many other factors such as the antenna used, dielectric properties of the subsurface, complexity of the sedimentary architecture, attenuation of materials in the subsurface and most importantly depth of investigated bodies. At the South Saskatchewan River 10 x 10 m site, however, large-scale inclined strata within a deep scour that extended laterally ~6 m were resolved with 0.30 m between traces but could not be recognised with 0.50 m distance between traces. This would suggest the requirement for a distance three times

closer between survey points when compared with the Macclesfield site. The structure was identified at a depth of between 4 and 6 m. A similar problem of losing resolution with depth was also identified by Heinz (2001) who mentioned that very similar structures when imaged at greater depth were resolved with lower resolution.

With the seismic reflection method the problem of lateral resolution is expressed by the Fresnel zone concept (see Glossary). The Fresnel zone is the area where waves interfere with each other constructively (the theory of signal reflection was explained in Section 3.0). The lateral resolution is defined by the Fresnel zone radius  $r$  expressed by the Pythagorean theorem (Sheriff 1977)

$$r = \sqrt{\left(D + \frac{\lambda}{4}\right)^2 - D^2}$$

where  $\lambda$  is the wavelength and  $D$  is the depth of the surface of reflection. The equation indicates that the zone expands with depth due to geometrical spreading of the wave front thus the lateral resolution should decrease. The wavelength  $\lambda$  is a ratio of mean velocity  $v_s$  to depth of the investigated structure, and peak frequency  $f$  (explained in Section 3.1). The zone at the ground surface has a radius of a quarter of the wavelength, which for the South Saskatchewan River site is approximately 0.16 m, however, at 1.0 m depth the radius would be approximately 0.35 m. For structures at 4.0 m depth the radius of the Fresnel zone is approximately 1.3 m, while for the structures at a depth of 6.0 m it is ~1.4 m. For the Macclesfield site, the radius of the Fresnel zone at 1.0 m depth is ~0.9 m. The ratio of the radius at shallow depth and the depth of the structure investigated would describe the loss of resolution due to geometrical spreading.

Thus to address the geometrical spreading of the wave front it is proposed to use a correction

factor  $F$  which would address changes of resolution between the ground surface and the depth of structures investigated,  $D_s$ .  $F$  is therefore expressed as a ratio between the radius of the Fresnel zone near the ground surface and at the depth of the structure:

$$F = \frac{r_0}{r_s} = \sqrt{\frac{\left(D_s + \frac{v_s}{4f}\right)^2 - D_s^2}{\left(1 + \frac{v_1}{4f}\right)^2 - 1}}$$

Where  $v_1$  is signal velocity at 1.0 m depth. The ratio between the radiuses from the Macclesfield site at 1.0 m depth and the South Saskatchewan River at 6.0 m depth is approximately 2.5 times which generally confirms the earlier observations. The empirical relation between the size of the imaged feature and distances between survey points is expressed as

$$d < 0.2 \frac{l}{F}$$

Thus the above equation suggests for structures at 4.0 – 6.0 m depth from the South Saskatchewan River the maximum distance between stations should be < 0.5 - 0.6 m. This confirms the observations from Section 3.2. As the antenna has a dipolar character, the Fresnel zone of the GPR signal will have an ellipsoidal plan shape, and the resolution may be affected by the electric permittivity (Neal 2004). Thus more work is required to empirically confirm the accuracy of the above formulas.

**Processing:** The methodology for GPR data processing was highlighted in Section 3.1. Initially, the standard scope of processing, *i.e.* AGC, ‘dewow’ and band-pass filtering, was used, and then compared with an alternative method suited to the particular requirements of the datasets presented here. This analysis confirmed the commonly expressed view (*e.g.* Cassidy 2009) that over-processing of GPR data leads to poorer results when compared to a very limited scope of processing which aims to accurately address the character of a particular

dataset. Some of the processing steps which were tried as part of the processing stage (see Section 3.1) degraded the images. ‘Dewow’ and predictive filtering (deconvolution) are examples of the algorithms which tended to remove significant amounts of energy and change the character of the recorded signal. Time-variable filtering was found to be particularly suitable for cases when the GPR signal dramatically changed with penetration depth. Instead of using one set of filter values with the pass region set up around the peak frequency, separate lower and higher frequency datasets were also created by using two sets of filters. Lower frequency profiles recovered information that would otherwise be lost from deeper parts of the profiles, adding 40% to the interpretable parts of profiles, while higher frequency data improved the resolution of the upper parts of the profiles and revealed ~30–40% more interfaces in comparison with the lower resolution profiles. Comparisons of both datasets helped to assess the influence of the frequency range used on the reflection pattern and therefore added objectivity to the interpretation. Replacing the typically used AGC with the time power exponential gain function also slightly improved the penetration of the interpretable part of profiles by approximately 10%. Excessive strength of the signal at the bottom of the profiles was, however, restricted by the application of the Gaussian power function. A decision flow chart summarising the above is presented below in Figure 6.6.

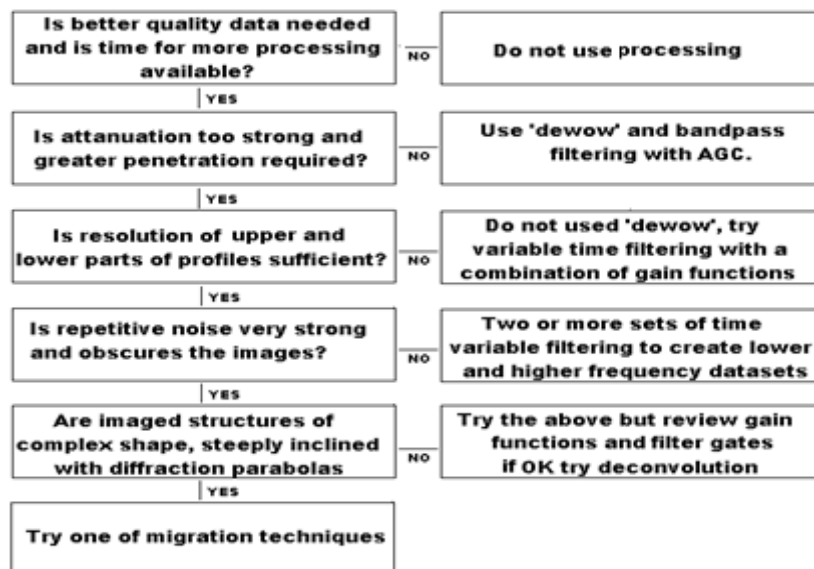


Fig. 6.6 Decision flow chart for basic data processing.

**Interpretation:** Three datasets were presented in Chapters 4 and 5 to compare interpretation based on individual 2-D profiles and as 3-D volumes. Closely spaced (0.10 and 0.50 m) 2-D GPR lines presented in Sections 4.1 to 4.3 provided high resolution images of the sedimentary architecture of the subsurface, which enabled a quantitative evaluation of the radar facies occurrence. The 3-D display of these datasets, however, led to a more in-depth investigation of the depositional features as it enabled more emphasis to be put on the spatial distribution and relations between radar facies.

The improvements in quality of interpretation achievable by using 3-D volumes over 2-D profiles are further illustrated with reference to Figure 6.7 of the South Saskatchewan 10 x 10 m grid. The profiles from the South Saskatchewan River 10 x 10 m grid could not be used to identify upstream accretion deposits within the deep scour due to the low resolution of the data. 3-D display helped to resolve the planar upstream inclined bedding within the scour. Immediately above the scour fill, the lower part of the radar facies (3), which on 2-D profiles was interpreted as vertical accretion deposits associated with migration of low amplitude dunes, was also identified in 3-D as lateral accretion deposits (Figure 6.7). Thus structures which required the lateral extent or pattern to be known could be more easily identified in 3-D volume.

Even when the architecture is relatively simple and can be imaged with 2-D profiles, 3-D display offers information which can be directly interpreted as depositional forms. 2-D interpretation of the Macclesfield data did not reveal the oblique orientation of the point bar deposits in relation to the W-E and S-N oriented profiles, for example. Similarly, individual profiles from the South Saskatchewan River 120 x 40 m grid did not identify the patterns associated with the bartop hollows. Finally, the 3D volumes allow the full range of

palaeoflow directions to be quantified. Interpretation of 2-D profiles enables differences of palaeoflow orientation greater than ~ 20 degrees to be identified. However, subtle features associated with small changes in orientation of less than 20 degrees (e.g. changes in direction of migrating bar fronts), required display of datasets as time slices.

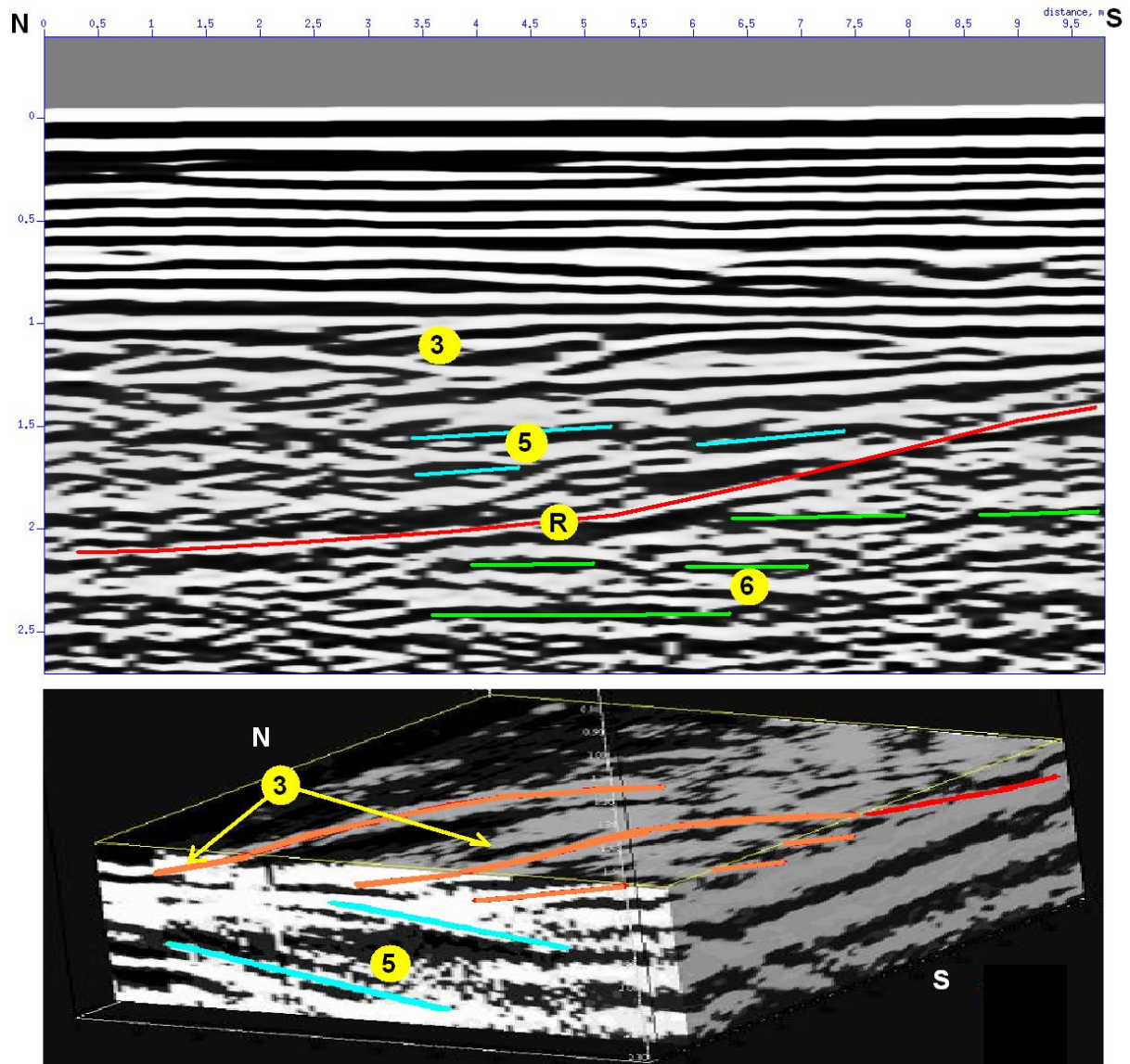


Fig. 6.7 Comparison of interpretation of 2-D profile with a section of the low resolution 3-D volume of the South Saskatchewan 10 x 10 m grid. Both images present radar facies (3) which according to information from 2-D profiles were interpreted to be associated with vertical accretion on bar top. The 3-D volume revealed that the lower part of radar facies 3 had a curved shape on the time slice (at 163 ns) and can be associated with lateral accretion.

To compare interpretations between 2-D and 3-D data sedimentary facies for both types of data were quantified in a similar way as was described in Chapter 4. This was assessed based on representative profiles which were selected every 2.5 m for the Macclesfield grid, every

1.0 m for the South Saskatchewan River 10 x 10 m grid, and every 10 m for the South Saskatchewan River 120 x 40 m grid. The facies were sampled every 5, 2 and 5 m along each survey line respectively. Approximately 8% of the radar facies from the Macclesfield site were interpreted differently. This number was associated with radar facies (4) located immediately below the point bar deposits, *i.e.* below radar facies (3). Based on 2-D display this facies was previously classified as part of radar facies (3). The difference in interpreting the sedimentary facies from the South Saskatchewan River 10 x 10 m grid was nearly 24%. This was mainly associated with recognition of the upstream accretion deposits from the deep scour, *i.e.* radar facies (5), which on 2-D profiles could not be resolved, while in 3-D the upstream planar inclination became apparent. Also, the lower part of the radar facies (3) located immediately above the scour fill described in 2-D as vertical accretion, in 3-D was described as lateral accretion deposits. Less than 1% of the South Saskatchewan River 120 x 40 m grid radar facies were classified differently in 2-D and 3-D. This difference was related to the radar facies (4) which in 3-D was recognised as bartop hollows. Here, the quantification does not include the changes of orientation of high-angle inclined strata, *i.e.* radar facies (1), which could not be assessed based on 2-D profiles. This would indicate that the interpretation based on 2-D display was between 76% to over 99.9% accuracy. The last value does not take into account recognition of changes of orientation of high-angle inclined strata on downstream bar margin. 2-D interpretation presented in this thesis was, however, based on densely spaced 2-D profiles (0.5 or 0.1 m distances between lines). Thus 2-D interpretation was more accurate than typical 2-D interpretation based on widely spaced lines (typically tens of m). The accuracy of 2-D interpretation of widely spaced lines should therefore be even lower when compared with 3-D interpretation.

**Sedimentology:** The three datasets presented in this thesis represent three slightly different

scales not only in terms of the size of surveys but also in a depositional context. The Macclesfield dataset presents the evolution of a meandering river. It revealed former river channels distributed across the site, more recent point-bar deposits and recirculation pool sediments which were deposited in autumn 2007. A model of the recirculation zone formed within a scour at the edge of the meandering River Dene is presented in Figure 6.8 with the river flow direction indicated by the red and black arrows. The reverse flow within the recirculation pool resulted in vertical and lateral (at the centre of the pool) accretion.

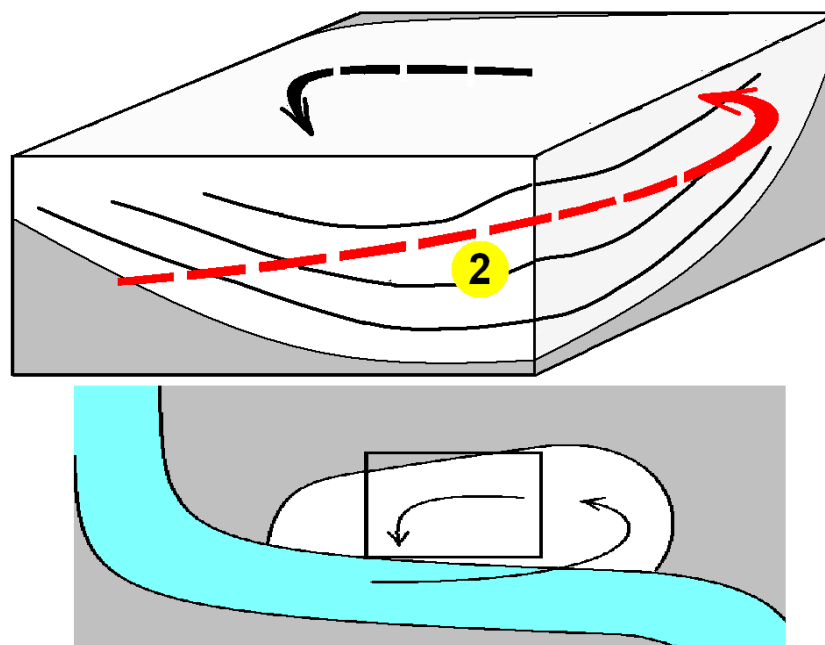


Fig. 6.8 Model of the recirculation pool deposits, represented as '2' at the Macclesfield site. The red arrow represents the location of the river current diverted into the recirculation pool (at the entrance to the recirculation pool). The black arrow represents flow direction within the recirculation zone and the exit from the recirculation pool. The depth of the scour surface is about 1.2 m and the lateral extent of the image is about 5 m. Plan view presenting the location of the model in relation to the river banks is shown in image below.

The architecture of these deposits, when viewed in relation to the main river flow, appear as upstream at the entrance to the pool (marked with the red arrow). Conversely, at the exit from the pool (marked with a black arrow) the orientation of the deposits indicates downstream accretion.

A model of point bar deposits based on the 3-D Macclesfield dataset is presented in Figure 6.9A. The inclined bedding has a slightly concave character, and thus varies somewhat from

the expected inclined sets (Figure 6.9B) described by Allen (1963). His model assumes only lateral accretion on a point bar, while the architecture of the point bar from the Macclesfield site would indicate that a considerable amount of sediments were deposited within the thalweg (see Glossary), suggesting continued deposition within the channel and on the point bar in contrast to two separate depositional units.

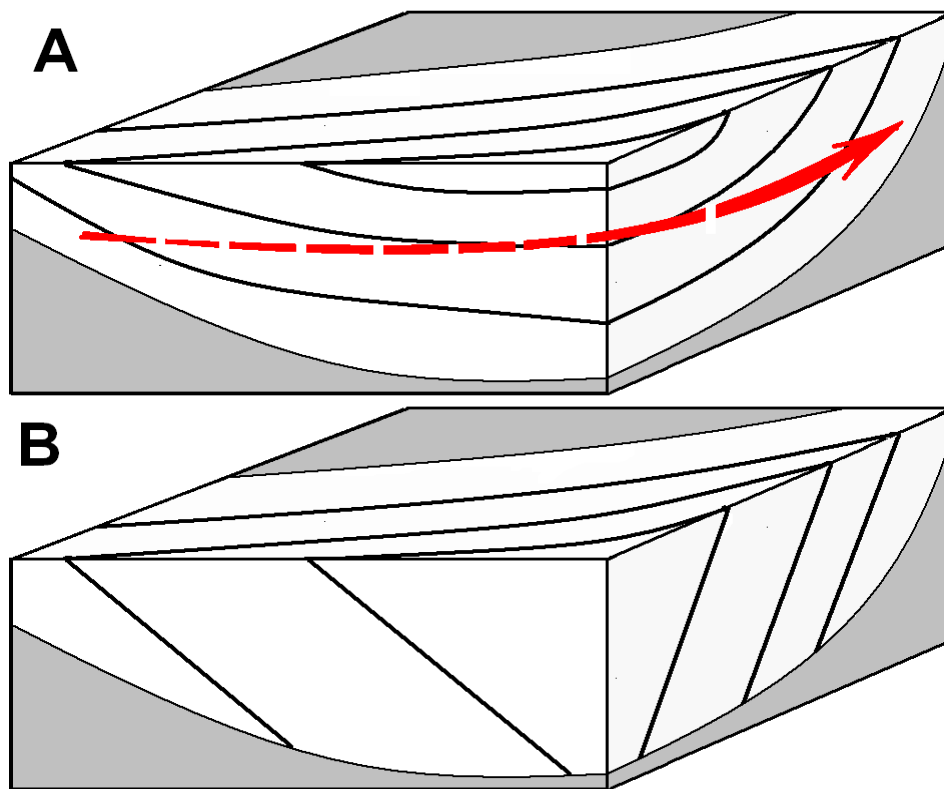


Fig. 6.9A Model of point bar deposits based on the 3-D data from the Macclesfield site. Note the slightly concave character of the inclined bedding. The red arrow indicates the flow direction. The lateral extent of the figure is approximately 3 m and the maximum depth is about 1.2 m. B Expected model of the point bar deposits as described in classic examples such as Allen (1963).

The South Saskatchewan River 10 x 10 m data illustrates upstream deposition within the downstream part of the scour. In the upper sections of the deposits lateral accretion is more prevalent with vertical accretion on a unit bar at the top of the succession.

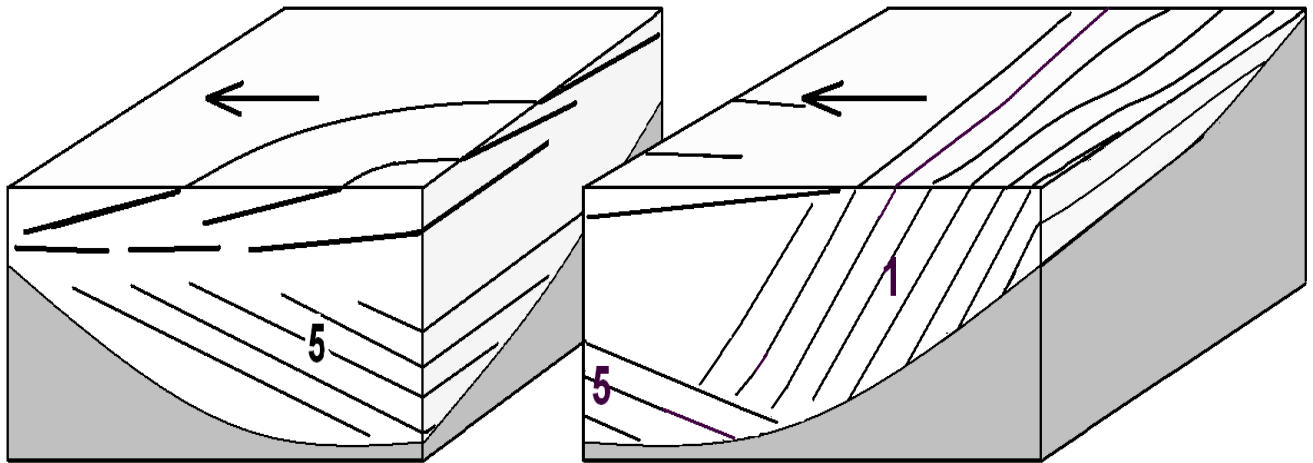


Fig. 6.10 Model of scour fill deposits based on the South Saskatchewan River 10 x 10 m grid. Number '5' indicates radar facies (5) associated with upstream accretion within the scour. Number '1' indicates deposits representing radar facies (1) which are associated with downstream accretion on slip faces. Lines above the scour indicate lateral accretion. The arrows indicate the general flow direction. The depth of the scour surface is ~3.5 and 6.5 m with total length of the scour ~50 m and total width ~20 m. The upstream part of the scour architecture (right) is based on Figure 5.3.8.

These images can be used to construct a model representing the distribution of sedimentary facies associated with a scour fill (Figure 6.10). The scour fill is formed by upstream accretion deposits marked as '5' within the downstream part of the scour. Figure 5.3.8 suggests downstream accretion at the upstream part of the scour.

Taken together, the data from the scours in these two contrasting rivers suggests that a complex alluvial architecture of upstream and downstream accretion is the norm within such features. The spatially variable structure of the fill within these scours can only be resolved with data displayed in 3-D.

The dataset collected in the South Saskatchewan River 120 x 40 m grid illustrated two sequences of deposits, which were separated by a radar boundary. Both of these sequences again comprised vertical changes; but here they also comprised lateral changes from downstream deposition on bar slip-faces to lateral and vertical accretion on top of the bars. The characteristic sequence of sedimentary facies within both of the South Saskatchewan

River datasets represents a cyclic pattern of deposition, change from downstream/upstream deposition, through lateral to vertical accretion. A model of a unit bar with a cross-bar channel, based on the 3-D datasets presented in this thesis, is shown as Figure 6.11.

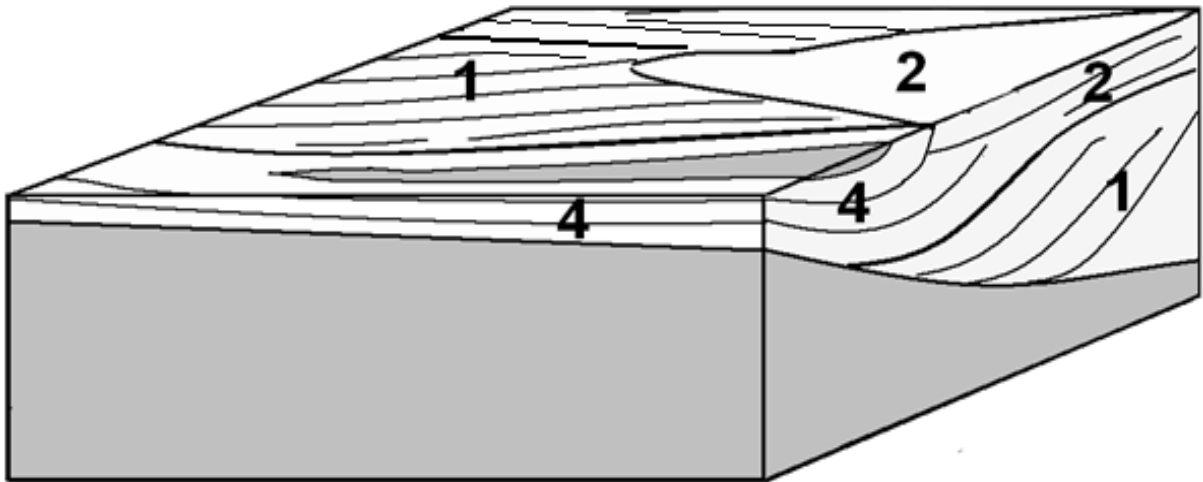


Fig. 6.11 Model of unit bar deposits based on 3-D data from the South Saskatchewan River. Numbers represent radar facies described in the previous chapters. Lateral extent of the figure is approximately 20 m and the maximum depth is about 3 m.

## CHAPTER 7

### CONCLUSION

Based on the review of literature and analysis of the three datasets presented in this thesis the original objectives outlined in the introduction were accomplished. The key conclusions with respect to these objectives are briefly outlined below.

1. The review of the literature on the application of GPR in fluvial sedimentology highlighted that 2-D GPR data was introduced shortly after the demand for more accurate, quantitative information about sedimentary architecture was realised. Although 3-D display of GPR data was adopted in other earth related fields of science and engineering it has not been applied in purely sedimentological works. Several authors collected 2-D GPR data and displayed them in 3-D for characterisation of hydraulic properties of fluvial deposits; however, procedures for collection, display and 3-D interpretation according to the principles of radar stratigraphy, which could be followed by sedimentologists, were not documented.
2. The benefits of 3-D interpretation were illustrated by the sedimentary models which were presented in the Discussion section. Quantitative comparison of interpretations carried out on 2-D profiles and 3-D volumes revealed that the accuracy of 2-D interpretation in relation to the facies recognised in 3-D was 76% accurate for the South Saskatchewan River 10 x 10 m grid, 92% accurate for the Macclesfield data and over 99.9% for the South Saskatchewan River 120 x 40 m grid. However, this relates to just facies identification and does not include accuracy in detecting angular relations between architectural elements such as the orientation of sedimentary structures. Time slices, were useful to identify subtle aspects of sedimentary architecture, such as angular relations below 20 degrees (orientation of the structures or changes in the paleoflow), which cannot be imaged by 2-D profiles.

3. The thesis also presented best practices for acquisition, display and interpretation of GPR data which can be followed by sedimentologist to investigate alluvial architecture. It established the workflow for choosing the most suitable survey mode and presented the formula for assessment of maximum distances between survey stations in relation to the size of the investigated structures and their depth. Collection of the Macclesfield and the South Saskatchewan River 10 x 10 m grids took one day, while the South Saskatchewan River 120 x 40 m grid took two days. The 2-D data processing workflow was also presented, with these processing steps adding up to 40% to the interpretable part of the profiles. For an experienced user, 2-D processing of a grid of data can be done within several hours with the most time consuming step being initial editing of the files with 2-D profiles. Compiling a 3-D dataset of the size of the Macclesfield grid, displaying it in 3-D and interpreting radar facies and surfaces could be done within one day. Thus collecting pseudo 3-D datasets processing it in 2-D and interpreting with seismic package can provide an efficient tool for investigating fluvial sedimentary architecture in 3-D. When the survey has to address architecture of large depositional forms, there is still an option of displaying extensive 2-D GPR profiles together with multiple 3-D volumes, which would be focused on areas of more complex architecture.

## RECOMMENDATIONS FOR FURTHER WORK

The following aspects of using GPR data are recommended for future research:

- Lateral resolution depends on density of sampling and the character of the Fresnel zone. As the Fresnel zone for a GPR signal is more complex than for a seismic wave, further work, which would empirically check the validity of the formula for maximum distances between GPR survey stations and determine the character of the Fresnel

zone for GPR signal, would help to adjust GPR surveys more accurately to the complexity of sedimentary architecture.

- Data processed in 2-D and displayed in 3-D could be compared with full-resolution 3-D processed data, particularly 3-D migrated. This would clarify the uncertain level of distortion of 3-D images built from 2-D processed GPR profiles which results from recording of off-line reflections. Ground truth control, *i.e.* information from excavations, vibro-cores and outcrops, could be used to assess potential distortions of the 3-D image of fluvial deposits.
- The use of seismic software in displaying GPR datasets is not only limited to techniques presented in this thesis but can be extended to various other techniques. Oblique slices, *i.e.* slices which cut data volumes at a given angle, could be used when orthogonal profiles are not parallel and perpendicular to sedimentary structures. Numerous wave attributes such as coherence, which is useful for detecting lithological boundaries or erosional surfaces, could also be utilised. Additionally, it would be beneficial to compare ground truth data with lower and higher resolution datasets to assess the impact of interference between reflections from adjacent interfaces and their vertical resolution.

## REFERENCES

- Alexander, D.E., Fairbridge, R.W., 1999. *Encyclopedia of Environmental Science*. Kluwer Academic Publishers, Netherlands
- Allen, J.R.L., 1963. The classification of cross-stratified units with notes on their origin. *Sedimentology* 2, 93-114.
- Annan, A.P., 1999. Practical processing of GPR data. *Proceedings of the Second Government Workshop on Ground Penetrating Radar*, Columbus, Ohio, 53–58.
- Asprion, U., Aigner, T., 1997. Aquifer architecture analysis using ground-penetrating radar: Triassic and Quaternary examples (S. Germany). *Environmental Geology* 31, 66–75.
- Asprion, U., Aigner, T., 1999. Towards realistic aquifer models: three-dimensional georadar surveys of Quaternary gravel deltas (Singen Basin, SW Germany). *Sedimentary Geology* 129 (3–4), 281–297.
- Aigner, T., Asprion, U., Hornung, J., Junghans, W.D., Kostrewa, R., 1996. Integrated outcrop analogue studies for Triassic alluvial reservoirs: examples from southern Germany. *Journal of Petroleum Geology* 19, 393–406.
- Augustinus, P.C., Nichol, S., 1999. Ground-penetrating radar imaging of Pleistocene sediments, Boco Plain, Western Tasmania. *Australian Journal of Earth Sciences* 46, 275–282.
- Bacon, M., Simm, R., Redshaw, T., 2003. *3-D Seismic Interpretation*. Cambridge University Press.
- Baker, G.S., Jol, H.M., 2007. *Stratigraphic Analyses Using GPR*. Geological Society of America.
- Baker, G.S., Steeples, D.W., Schmeissner, C., Pavlovic, M., Plumb, R., 2001. Near-surface imaging using coincident seismic and GPR data. *Geophysical Research Letters*. 28, 627–630.
- Barrash, W., Reboulet, E.C., 2004. Significance of porosity for stratigraphy and textural composition in subsurface, coarse fluvial deposits: Boise Hydrogeophysical Research Site. *Geological Society of America Bulletin* 116, 1059–1073.
- Barry, K.M., Cavers, D.A., Kneale, C.W. 1975. Recommended standards for digital tape formats. *Geophysics* 40, 344–352
- Beres, M., Haeni, F.P., 1991. Application of ground-penetrating-radar methods in hydrogeologic studies. *Ground Water* 29, 375–386.
- Beres, M., Green, A.G., Huggenberger, P., Horstmeyer, H., 1995. Mapping the architecture of glaciofluvial sediments with three-dimensional georadar. *Geology* 23, 1087–1090.
- Beres, M., Huggenberger, P., Green, A.G., Horstmeyer, H., 1999. Using two- and three-dimensional georadar methods to characterize glaciofluvial architecture. *Sedimentary Geology* 129, 516–530.
- Best, J.L., Ashworth, P.J. 1997. Scour in large braided rivers and the recognition of sequence stratigraphic boundaries. *Nature* 387, 275-277
- Best, J.L., Ashworth, P.J., Bristow, C.S., Roden, J., 2003. Three-dimensional sedimentary architecture of a large, mid-channel sand braid bar, Jamuna River, Bangladesh. *Journal of Sedimentary Research*. 73, 516–530.
- Best, J.L., Woodward, J., Ashworth, P.J., Sambrook Smith, G., Simpson, C., 2006. Bar-top hollows: A new element in the architecture of sandy braided rivers, *Sedimentary Geology* 190, 241-255
- Birkhead, A.L., Heritage, G.L., White, H., van Niekerk, A.W., 1996. Ground-penetrating radar as a tool for mapping the phreatic surface, bedrock profile, and alluvial stratigraphy in the Sabie River, Kruger National Park. *Journal of Soil and Water Conservation*. 51, 234–241.

- Böniger U., Tronicke, J., 2010. Integrated data analysis at an archaeological site: A case study using 3D GPR, magnetic, and high-resolution topographic data. *Geophysics* 75
- Bowling, J.C., Rodriguez, A.B., Harry, D.L., Zheng, C., 2005. Delineating alluvial aquifer heterogeneity using resistivity and GPR data. *Ground Water* 43, 890–903.
- Bradford, J.H., Ramaswami, M., Peddy, C., 1996. Imaging PVC gas pipes using 3-D GPR. *Proceedings of the Symposium on the Application of Geophysics to Engineering and Environmental Problems*, Colorado, USA, 519–524
- Bridge, J. S., Smith, N. D., Trent, F., Gabel, S. L., Bernstein, P., 1986. Sedimentology and morphology of a low-sinuosity river: Calamus River, Nebraska Sand Hills. *Sedimentology* 33, 851–870.
- Bridge, J.S., Alexander, J., Collier, R.E.L.L., Gawthorpe, R.L., Jarvis, J., 1995. Ground-penetrating radar and coring used to study the large-scale structure of point-bar deposits in three dimensions. *Sedimentology* 42, 839–852.
- Bridge, J.S., Collier, R., Alexander, J., 1998. Large-scale structure of Calamus River deposits (Nebraska, USA) revealed using ground-penetrating radar. *Sedimentology* 45, 977–986.
- Bridge, J.S. 2003. Depositional models of braided rivers. In: Sambrook Smith, G.H., Best, J.L., Bristow, C.S., Petts, G.E. (eds.), *Braided Rivers: Process, Deposits, Ecology and Management*, IAS Special Publication 36, Blackwell Publishing, 11–50.
- Bridge, J.S., 2009. Advances in fluvial sedimentology using GPR. In: *Ground Penetrating Radar Theory and Application*, Elsevier.
- Brierley, G.J., 1989. River planform facies models: the sedimentology of braided, wandering and meandering reaches of the Squamish River, British Columbia, *Sedimentary Geology*, 61
- Bristow, C.S., Best, J.L., 1993. Braided rivers: perspective and problems. *Geological Society of London Special Publication* 75, 1–11.
- Bristow, C.S., Skelly, R.L., Etheridge, F.G., 1999. Crevasse splays from the rapidly aggrading, sand-bed, braided Niobrara River, Nebraska: effect of base-level rise. *Sedimentology* 46, 1029–1047.
- Bristow, C.S., Best, J.L., Ashworth, P.J., 2000. The use of GPR in developing a facies model for a large sandy braided river, Brahmaputra River, Bangladesh. *Proceedings of the Eighth International Conference on Ground Penetrating Radar*, Gold Coast, Australia, 95–100.
- Bristow, C.S., Lancaster, N., Duller, G.A.T., 2005. Combining ground penetrating radar surveys and optical dating to determine dune migration in Namibia. *Journal of the Geological Society* 162, 315–321.
- Bristow, C.S., 2009. Ground penetrating radar in Aeolian dune sands. In: Jol, H.M. (ed.), *Ground Penetrating Radar: Theory and Application*, Elsevier Science.
- Brodzikowski, K., van Loon A.J., 1999. *Glacigenic Sediments*. Elsevier Science.
- Brown, A.R., 2004. *Interpretation of Three-dimensional Seismic Data*, Sixth Edition. AAPG and SEG.
- Cant, D.J., Walker, R.G., 1978. Fluvial Processes and Facies Sequences in the Sandy Braided South Saskatchewan River, Canada. *Sedimentology* 25, 625–648.
- Carpenter, D., O’Conor, D., Donnelly, L., 2006. The Farr Windfarm: site investigation for an ecologically sensitive infrastructure project. *10th Congress of the International Association for Engineering Geology and the Environment*, paper 107, Geological Society of London
- Cassidy, N.J., 2009. Ground penetrating radar data processing, modelling and analysis. In: Jol, H.M. (ed.), *Ground Penetrating Radar: Theory and Application*, Elsevier Science.

- Castanie, L., Bosquet, F., Levy, B., 2005. Advances in seismic interpretation using new volume visualization techniques. *First Break* 23, 69–72.
- Catuneanu, O., 2002. Sequence stratigraphy of clastic systems. *Journal of African Earth Sciences*, 35, 12–43.
- Chopra, S., Marfurt, K. J., 2007. Volumetric curvature attributes add value to 3D seismic data interpretation. *The Leading Edge* 26, 856–867.
- Claerbout, J., 2000. *Basic Earth Imaging*. Stanford Exploration Project. [http://sepwww.stanford.edu/sep/prof/bei/toc\\_html](http://sepwww.stanford.edu/sep/prof/bei/toc_html) [last accessed 12 December 2009].
- Clement, W.P., Barrash, W., Knoll, M.D., 2006. Reflectivity modeling of a ground-penetrating-radar profile of a saturated fluvial formation. *Geophysics* 71, K59–K66.
- Corbeanu, R.M., McMechan, G.A., Szerbiak, R.B., Soegaard, K., 2002. Prediction of 3-D fluid permeability and mudstone distributions from ground-penetrating radar (GPR) attributes: examples from the Cretaceous Ferron Sandstone Member, east-central Utah. *Geophysics* 67, 1495–1504.
- Daniels, J.J., Harris, D., Schilling, B., Roberts, R., 1992. GPR measurements for locating underground mine workings at an active open-pit mine. *Special Paper - Geological Survey of Finland*, 16, 237–245
- Daniels, D.J., 1996. *Ground Penetrating Radar*. Institution of Electrical Engineers, London.
- Doolittle J., Nelson, F., 2009. Characterising Relict Cryogenic Macrostructures in Mid-Latitude Areas of the USA with Three-Dimensional Ground-Penetrating Radar. *Permafrost and Periglacial Processes* 20, 257–268
- Fisher, E., McMechan, G.A., Annan, A.P., Cosway, S.W., 1992a. Examples of reverse-time migration of single-channel, ground penetrating radar profiles. *Geophysics* 57, 577–586.
- Fisher, E., McMechan, G.A., Annan, A.P., 1992b. Acquisition and processing of wide-aperture ground-penetrating radar data. *Geophysics* 57, 495–504.
- Fisher S.C., Steward, R.R., Jol, H.M., 1992. Processing ground penetrating radar (GPR) data. *CREWES Research Report* 4.
- Fisher, T.G., Jol, H.M., Smith, D.G., 1996. Ground-penetrating radar used to assess aggregate in catastrophic flood deposits, northeast Alberta, Canada. *Canadian Geotechnical Journal* 32, 871–879.
- Folk, R.L., 1965. *Petrology of sedimentary rocks*, Hemphill, Texas.
- Gawthorpe, R.L., Collier, R.E.L., Alexander, J., Leeder, M., Bridge, J.S., 1993. Ground penetrating radar: application to sand body geometry and heterogeneity studies. *Geological Society of London Special Publication* 73, 421–432.
- Grandjean G., Gourry, J. C.. 1996 GPR data processing for 3D fracture mapping in a marble quarry (Thassos, Greece). *Journal of Applied Geophysics* 36, 19–30.
- Grasmueck, M. 1996. 3-D ground-penetrating radar applied to fracture imaging in gneiss. *Geophysics* 4, 1050 - 1064
- Grasmueck, M., Weger, R., Horstmeyer, H., 2005. Full-resolution 3D GPR imaging. *Geophysics* 70, 12–19.
- Hammon, W.S., Zeng, X., Corbeanu, R.M., McMechan, G.A., 2002. Estimation of the spatial distribution of fluid permeability from surface and tomographic GPR data and core, with a 2-D example from the Ferron Sandstone, Utah. *Geophysics* 67, 1505–1515.
- Heinz, J., Aigner, T., 2003. Three-dimensional GPR analysis of various Quaternary gravel-bed braided river deposits (southwestern Germany). *Geological Society of London Special Publication* 211, 99–110.

- Peter Hoube, 2007. Geomorphological facies reconstruction of Late Quaternary alluvial by the application of fluvial architecture concepts. *Geomorphology* 86, 94–114.
- Huggenberger, P., 1993. Radar facies: recognition of facies patterns and heterogeneities within Pleistocene Rhine gravels, NE Switzerland. *Geological Society of London Special Publication* 75, 163–176.
- Huggenberger, P., Meier, E., Pugin, A., 1994. Ground-probing radar as a tool for heterogeneity estimation in gravel deposits: advances in data-processing and facies analysis. *Journal of Applied Geophysics* 31, 171–184.
- Huisink, M., 2000. Changing river styles in response to Weichselian climate changes in the Vecht Valley, eastern Netherlands. *Sedimentary Geology* 133, 115–134.
- Jackson, R.G., 1975. Hierarchical attributes and a unifying model of bedforms composed of cohesionless material and produced by shearing flow. *Geological Society of America Bulletin*, 1523- 1533
- Jol, H.M., Smith, D.G., 1992. Ground penetrating radar: recent results. *CSEG Recorder* 17, 15–20.
- Kidd, G.D., 1999. Fundamentals of 3-D seismic volume visualization. *The Leading Edge*, 18, 702.
- Leatherman, S.P., 1987. Coastal geomorphological applications of ground-penetrating radar. *Journal of Coastal Research*, 3, 397– 399.
- Leclerc, R.F., Hickin, E.J., 1997. The internal structure of scrolled floodplain deposits based on ground-penetrating radar, North Thompson River, British Columbia. *Geomorphology*, 21, 17–38.
- Leopold, M., Völkel, J., Heine, K., 2006. A ground-penetrating radar survey of late Holocene fluvial sediments in NW Namibian river valleys: characterization and comparison. *Journal of the Geological Society* 163, 923–936.
- Lestari A.A., Yarovoy, A.G., Lighthart, L.P., 2002. Analysis and design of improved antennas for GPR. *Subsurface Sensing Technologies and Applications* 3, 295–326.
- Lunt, I.A., Bridge, J.S., Tye, R.S., 2004. A quantitative, three-dimensional depositional model of gravelly braided rivers. *Sedimentology* 51, 377–414.
- McClymont, A.F., Green, A.G., Kaiser, A. Horstmeyer, H., Langridge, R., 2010. Shallow fault segmentation of the Alpine fault zone, New Zealand revealed from 2- and 3-D GPR surveying. *Journal of Applied Geophysics* 70
- McMechan, G.A., Gaynor, G.C., Szerbiak, R.B., 1997. Use of ground-penetrating radar for 3-D sedimentological characterization of clastic reservoir analogs. *Geophysics* 62, 786–796.
- Miall, A.D., 1977. A review of the braided-river depositional environment. *Earth-Science Review* 13, 1–62 .
- Miall, A.D., 1985. Architectural-element analysis: a new method of facies analysis applied to fluvial deposits. *Earth-Science Review* 22, 261-308.
- Miall, A.D., 1989. Architectural elements and bounding surfaces in channelized clastic deposits: note on comparison between fluvial and turbidite systems. In: Taira, A., Masuda, F. (eds.), *Sedimentary Facies in the Active Plate Margins*, Terra Scientific Publishing Company, Tokyo, 3-15
- Middleton, G.V., 2003. *Encyclopaedia of Sediments and Sedimentary Rocks*. Kluwer Academic Publishers.
- Mellett, J.S., 1995. Ground penetrating radar applications in engineering, environmental management, and geology. *Journal of Applied Geophysics* 33, 157–166.
- Mumpy, A.J., Jol, H.M., Kean, W.F., Isbell, J.L., 2007. Architecture and sedimentology of an active braid bar in the Wisconsin River based on 3-D ground penetrating radar. *Geological Society of America Special Papers* 432, 111–131.

- Munroe, J.S., Doolittle, J.A., Kanevskiy, M.Z., Hinkel, K.M., Nelson, F.E., Jones, B.M., Shur, Y., Kimble, J.M., 2007. Application of Ground-Penetrating Radar Imagery for Three-Dimensional Visualisation of Near-Surface Structures in Ice-Rich Permafrost, Barrow, Alaska. *Permafrost and Periglacial Processes* 18, 309–321
- Naegeli, M.W., Huguenberger, P., Uehlinger, U., 1996. Ground penetrating radar for assessing sediment structures in the hyporheic zone of a prealpine river. *Journal of the North American Benthological Society* 15, 353–366.
- Neal, A., 2004. Ground penetrating radar and its use in sedimentology: principles, problems and progress. *Earth-Science Review* 66, 261–330.
- Nobes, D.C., Ferguson, R.J., Brierley, G.J., 2001. Ground-penetrating radar and sedimentological analysis of Holocene floodplains: insight from the Tuross valley, New South Wales. *Australian Journal of Earth Sciences* 48, 347–355.
- Novo, A. Grasmueck, M., Viggiano, D.A., Lorenzo, H., 2008. 3D GPR in Archeology: What can be gained from dense Data Acquisition and Processing? 12<sup>th</sup> International Conference on Ground Penetrating Radar, Birmingham, *Permafrost and Periglacial Processes* 18, 309–321
- Parsons, D.R., 2002. *Flow separation in meandering bends*. PhD thesis (unpublished), Department of Geography, University of Sheffield.
- Parker, N.O., Sambrook Smith, G.H., Ashworth, P.J., Best, J.L., Bridge, J.S., Lane, S.N., Lunt, I.A. and Simpson, C.J., 2008. Sedimentological impact of a high magnitude, low frequency flood in a braided river revealed from sequential GPR surveys. *Proceedings of the 12th International Conference on Ground Penetrating Radar*, Birmingham, 1–5.
- Peretti, W.R., Knoll, M.D., Clement, W.P., Barrash, W., 1999. 3-D GPR imaging of complex fluvial stratigraphy at the Boise hydrogeophysical research site. *Proceedings of the Symposium on the Application of Geophysics to Engineering and Environmental Problems (SAGEEP99 – Oakland, CA)*, Environmental and Engineering Geophysical Society, Wheat Ridge, 555–564.
- Pipan, M., Forte, E., Finetti, I., 1996. Multi-fold GPR techniques with applications to high-resolution studies: two case histories. *European Journal of Environmental and Engineering Geophysics* 1
- Poole, G.C., Naiman, R.J., Pastor, J., Stanford, J.A., 1997. Uses and limitations of ground penetrating radar in two riparian systems. In: Gibert, J., Mathieu, J., Fournier, F. (eds.), *Groundwater/Surface Water Ecotones: Biological and Hydrological Interactions and Management*, Cambridge Univ. Press, Cambridge, 140–148.
- Pringle, J.K., Westerman, A.R., Clark, J.D., Drinkwater, N.J., Gardiner, A.R., 2004. 3D high-resolution digital models of outcrop analogue study sites to constrain reservoir model uncertainty: an example from Alport Castles, Derbyshire, UK. *Petroleum Geoscience* 10
- Reading, H.G., 2001. Clastic facies models, a personal perspective, *Bulletin of Geological Society of Denmark*, 48, 101–115
- Regli, C., Huguenberger, P., Rauber, M., 2002. Interpretation of drill core and georadar data of coarse gravel deposits. *Journal of Hydrology* 255, 234–252.
- Reynolds, J.M., 1997. *An Introduction to Applied and Environmental Geophysics*. John Wiley & Son Ltd.
- Roberts, M.C., Bravard, J.P., Jol, H.M., 1997. Radar signatures and structure of an avulsed channel, Rhone River, Aoste, France. *Journal of Quaternary Sciences* 12, 35–42.
- Rogers, C.D.F., Chapman, D.N., Entwisle, D., Jones, L., Kessler, H., Metje, N., Mica, L., Morey, M., Pospíšil, P., Price, S., Raclavsky, J., Raines, M., Scott, H., Thomas, A.M., 2009. Predictive mapping of soil. Geophysical properties for GPR utility location surveys. *Fifth International Workshop on Advanced Ground Penetrating Radar*, Granada, Spain, 27–29 June, 60–67.

- Sambrook Smith, G. H., Ashworth, P. J., Best, J. L., Woodward, J., Simpson, C. J., 2005. The morphology and facies of sandy braided rivers: some considerations of spatial and temporal scale invariance. In: *Fluvial Sedimentology*, VII, Blum, M.D., Marriott, S.B., Leclair, S.F. (eds.), IAS Special Publication, 35, Blackwell Publishing, 145–158.
- Sambrook Smith, G.H., Best, J.L., Bristow, C.S., Petts, G.E., 2006a. Braided rivers: where have we come in 10 years? Progress and future needs. In: Sambrook Smith, G.H., Best, J.L., Bristow, C.S., Petts, G.E. (eds.), *Braided Rivers: Process, Deposits, Ecology and Management*, IAS Special Publication 36, Blackwell Publishing, 1–10.
- Sambrook Smith, G.H., Ashworth, P.J., Best, J.L., Woodward, J., Simpson, C.J., 2006b. The sedimentology and alluvial architecture of the sandy braided South Saskatchewan River, Canada. *Sedimentology* 53, 413–434.
- Sambrook Smith, G.H., Ashworth, P.J., Best, J.L., Lunt, I.A., Orfeo, O., Parsons, D.R., 2009. The sedimentology and alluvial architecture of a large braid bar, Río Paraná, Argentina. *Journal of Sedimentary Research* 79, 629–642.
- Saarenketo, T., Hietala, K., Salmi, T. 1992. GPR applications in geotechnical investigations of peat for road survey purposes, *Special Paper of Geological Survey of Finland* 16, 293-305.
- Saarenketo, T. 2009. NDT transportation. In: Jol, H.M. (ed.), *Ground Penetrating Radar: Theory and Application*, Elsevier Science.
- Sensors & Software, 2007. *GPR Technology* 3, April.
- Sheriff, R.E., 1973. *Dictionary of geophysics*. Society of Exploration Geophysicists, Tulsa, Oklahoma.
- Skelly, R.L., Bristow, C.S., Ethridge, F.G., 2003. Architecture of channel-belt deposits in an aggrading shallow sandbed braided river: the lower Niobrara River, northeast Nebraska. *Sediment. Geol.* 158, 249–270.
- Smith, S.W., 1999. *The Scientist and Engineer's Guide to Digital Signal Processing*. California Technical Publishing, California.
- Stephens, M., 1994. Architectural element analysis within the Kayenta Formation (Lower Jurassic) using ground-probing radar and sedimentological profiling, southwestern Colorado. *Sedimentary Geology* 90, 179–211.
- Stockwell, J.W., Cohen, J.K., 2008. *The New SU User's Manual*.  
[ftp://ftp.cwp.mines.edu/pub/cwpcodes/sumanual\\_300dpi\\_a4.pdf](ftp://ftp.cwp.mines.edu/pub/cwpcodes/sumanual_300dpi_a4.pdf) [last accessed August 2009].
- Szerbiak, R.B., McMechan, G.A., Corbeanu, R., Forster, C., Snelgrovel, S.H., 2001. 3-D characterization of a clastic reservoir analog: from 3-D GPR data to a 3-D fluid permeability model. *Geophysics* 66, 1026–1037.
- Tronicke, J., Dietrich, P., Wahlig, U., Appel, E., 2002. Integrated surface georadar and crosshole radar tomography: a validation experiment in braided stream deposits. *Geophysics* 67, 1516–1523.
- Van Dam, R.L., 2001. Causes of ground-penetrating radar reflections in sediment. PhD thesis, Vrije Universiteit, Faculty of Earth Sciences, p. 3.
- Vandenbergh, J., van Overmeeren, R.A., 1999. Ground penetrating radar images of selected fluvial deposits in the Netherlands. *Sedimentary Geology* 128, 245–270.
- Van Heteren, S.V., Fitzgerald, D.M., Mckinlay, P.A., Buynevich, I.V., 1998. Radar facies of paraglacial barrier systems: coastal New England, USA. *Sedimentology*, 45.
- Van Overmeeren, R.A., 1995. Georadar in hydrogeology. *International Journal of Rock Mechanics and Mining Sciences and Geomechanics Abstracts* 32.
- Van Overmeeren, R.A., 1997. Radar facies of unconsolidated sediments in The Netherlands: a radar stratigraphy interpretation method for hydrogeology. *Journal of Applied Geophysics*. 40, 1–18.

- Visher, G.S., 1965. Use of vertical profile in environmental reconstruction. *Bulletin of American Association of Petroleum Geology* 49, 41-61.
- Wheeler, H.E., 1958. Time Stratigraphy, *Bulletin of American Association of Petroleum Geology* 42, 1047-1063
- Whiting, B.M., McFarland, D.P, Hackenberger, S., 2001. Three-dimensional GPR study of a prehistoric site in Barbados, West Indies. *Journal of Applied Geophysics* 47, 217–226
- Woodward, J., Ashworth, P.J., Best, J.L., Sambrook Smith, G.H., Simpson, C.J., 2003. The use and application of GPR in sandy fluvial environments: methodological considerations. *Geological Society of London Special Publication* 211, 127–142.
- Wooldridge, C.L., Hickin, E.J., 2005. Radar architecture and evolution of channel bars in wandering gravel-bed rivers: Fraser and Squamish Rivers, British Columbia, Canada. *Journal of Sedimentary Research* 75, 844–860.
- Wyatt, D.E., Temples, T.J., 1996. Ground-penetrating radar detection of small-scale channels, joints and faults in the unconsolidated sediments of the Atlantic Coastal Plain. *Environmental Geology* 27, 219–225.
- Wen, R., 2005. 3D geologic modelling of channelized reservoirs: applications in seismic attribute facies classification. *First Break* 23.
- Yelf, R., Yelf, D., 2006. Where is true time zero? *Electromagnetic Phenomena* 7, 158–163.

APPENDIX 1  
Glossary of term used in the thesis

**Bar-top hollows** - morphological elements of sandy braided rivers first described by Best *et al.* (2006). Bar-top hollows have an oval plan shape, may extend by 10 to 30 m in the parallel or perpendicular direction to the river flow with a depth of up to 1.70 m. Bar-top hollows are typically filled with foresets inclined up to the angle of repose. Three mechanisms which are responsible for their formation were identified by Best *et al.* (2006): (1) isolation of a depression by deposition on a bar-tail which ‘wraps’ around it; (2) blocking of the upstream end of a cross-bar channel by migrating dunes during high and falling flow stages; (3) migration of a unit bar onto a channel bar and creating a hollow between the newly deposited material and the bar-head.

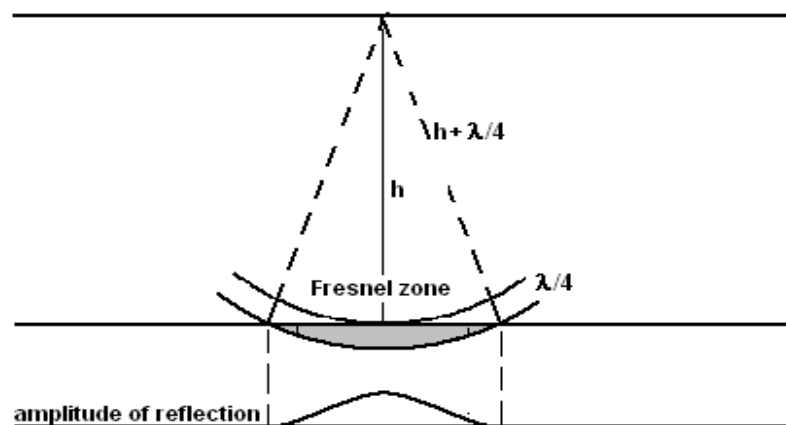
**Braid-bars** - or mid-channel bars, are morphological elements of braided rivers which separate them into multiple channels. Bar length is in the same range as the channel width, while its height is in the same range as the mean depth of the river flow. Compound-bars are formed by stacking individual unit-bars. Main types of unit-bars are longitudinal (diamond shaped), transverse (linguoid or lobate shape) and side bars which resemble point-bars from meandering rivers (Miall 1977).

**Chronostratigraphic chart** - also known as Wheeler diagram named after the geoscientist who first presented it (Wheeler 1958). This is a chart which presents stratigraphic units in the vertical scale of geologic time and the horizontal scale of distance. Such graphical presentation displays both periods of sedimentation, lack of sedimentation and erosion.

**Deconvolution** – one of the seismic processing steps which aims to remove systematic noise such as multiple reflections of ground surfaces. It has the character of an inverse filter. This means that its desired outcome, *i.e.* the undistorted or unconvoluted signal related to the architecture of the subsurface, has to be known before applying it. The recorded signal is assumed to be a result of convolution of a number of functions. Based on the comparison of the recorded signal with the desired unconvoluted signal the character of the noise can be assessed. As the nature of the subsurface is usually unknown, this situation is rarely possible. For this reason deconvolution is used to limit the difference between the expected signal, and the signal recorded in the field known as a ‘least-squares filter’ (Daniels 1996). Thus due to the lack of information regarding the subsurface, which acts as a filter of the emitted signal, it is usually hard to apply deconvolution and it is most often used as a trial-and-error technique. However, prior to application of deconvolution time-lag of repetitive noise is assessed by application of autocorrelation and it is used to remove the systematic noise. Aside from the removal of systematic noise, deconvolution is also applied to remove effects of interference between signals reflected from interfaces which are separated by a distance shorter than half a wavelength. Thus it improves the resolution of the data. It may, however, also introduce random noise and weaken the recorded signal. Stockwell and Cohen (2008) also advise that gains should follow deconvolution to compensate the removed signal.

**Fresnel reflection coefficient** - coefficient which depends on the contrast in electric permittivity between two sedimentary units at the interface and which describes the rate of reflected to transmitted energy together with changes in the phase of the reflected signal.

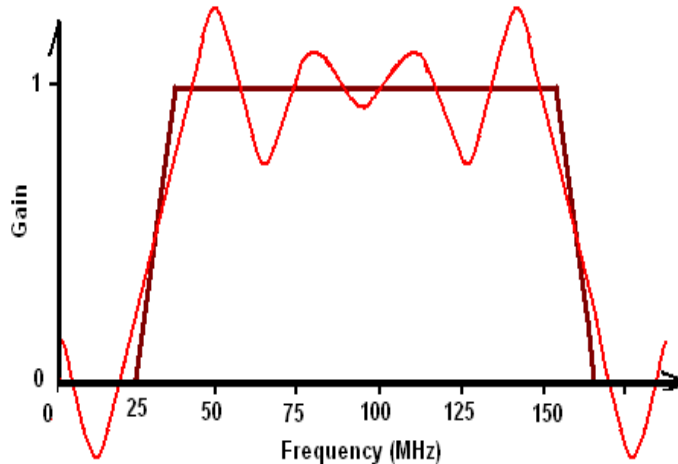
**Fresnel zone** - also referred to as first Fresnel zone is the area on a reflecting interface within which diffracted waves interfere in a constructive way and part of the energy is reflected back to the surface (see Section 3.0). In seismic reflection the wave front has a spherical shape, while in the plan view Fresnel zone has a circular shape (Sheriff 1973). Due to geometrical spreading the Fresnel zone expands with depth, thus resolution decreases with depth. The width of the Fresnel zone depends on the depth of the interface and the peak frequency of wave (illustrated by the image below). The lower the frequency signal the wider is the Fresnel zone. Outside the Fresnel zone, also described as the second Fresnel zone, the signal can interfere both constructively and destructively.



The concept also generally applies to GPR signal. GPR transmitting antennas, however, have a dipolar character and the signal spreads more laterally. Thus, the Fresnel zone has a more elliptical plan shape (Neal 2004). Additionally, the shape of the Fresnel zone may be complicated by complex sedimentary architecture such as inclined bedding surfaces (Annan 2009). Image modified from Sheriff (1973).

**Full-resolution 3-D data processing** - processing and interpretation of datasets which were first compiled into a 3-D volume and then processed to address the distortion of 3-D volumes associated with geometrical spreading, off-line reflections and diffractions from point objects, which in 3-D have a dome shape. Such distortions can be addressed with 3-D migration (Grasmueck *et al.* 2005).

**Gibbs effect** - term used in mathematics and signal processing. In signal processing it denotes ringing of signal in frequency domain as a result of encountering a discontinuity or a sudden change of amplitude (see image). In GPR processing Gibbs effect manifests itself as reverberations created by steep sides of a trapezoidal shaped bandpass filter and results in unclear images of recorded reflections. A graphical illustration of Gibbs phenomenon is shown by the image below. The red line is the signal response to application of a trapezoidal bandpass filter which is shown by the black line. The filter should remove frequencies between 0 and 25 MHz and above 180 MHz. The signal of frequencies between 25 and 40 MHz and between 165 and 180 MHz should gradually be introduced as shown by the inclined sides of the trapezoid. Signal characterised by frequencies between 40 and 165 should be fully represented.



As a result of Gibbs effect, however, signal associated with the frequencies is represented with proportions indicated by the red line. Thus some frequencies are overrepresented while some are removed. Particularly when steep edges of a band pass filter are used, reflection lines on GPR profiles may appear smeared and unfocused.

**Holocene** - term first time used by Gervais in 1867 (Alexander and Fairbridge 1999) for the last epoch which started approximately 10,000 years ago counting from 1950. This date marks the end of glaciation and beginning of agriculture.

**Migration** - one of the processing steps which aims to migrate distorted points in images of the subsurface to their original locations. An assumption that all recorded events were reflected from the points located directly below the place where they were recorded usually also results in image distortion. In reality, transmitted signal propagates in three dimensions and recorded signal, particularly in the case of dipping reflectors, may be reflected from points located anywhere in the subsurface or sometimes even above ground level. In this case the depth and location of the events may be false and may result in the recording of patterns such as diffraction hyperbolas (reflection from point objects) or bow-tie effects (reflection from concave-shaped interfaces). Successful migration requires a good knowledge of the mean velocities and may be difficult when the signal velocity changes significantly with depth. There are a number of algorithms which can be used to migrate reflection events back to their original location, such as Stolt (presented in this thesis), Kirchhoff or finite difference modelling migration, which can be performed both in 2-D and 3-D (Cassidy 2009).

**Point bar** - depositional form of a crescent shape which occurs on the convex river bank and which is a result of vortex-shape water flow on a meander bend. Point bar deposits are typically characterised by cross-strata inclined towards the centre of the channel with upwards and downstream fining grain size (Allen 1963). As shown by Bridge *et al.* (1995), point bars may include unit bars in their lower parts.

**Pseudo 3-D dataset** - as defined by Neal (2004), this is a dataset with distances between adjacent lines greater than distances between survey stations along the line.

**Recirculation zone** - this is a zone of reverse (*i.e.* with an upstream component) circulation within a meandering river channel which originates from the flow separation on sharp meander bends. It may erode river banks and create a scour pool on the side of the river channel.

**Scour in river bed** - an elongated bowl-shaped erosional form which may form in river confluences, bar confluences, as a result of spiral vortices, and which also include smaller scale features such as bar-top hollows. The size of the scour varies. Bartop hollow scours in the South Saskatchewan River are up to 1.7 m deep (Bridge *et al.* 2006). Best and Ashworth (1997) reported that confluence scour depth of five times the mean channel depth and, in some rivers, may have a depth of over 40 m.

**SEG-Y format** - introduced in 1975 by the Society of Exploration Geophysicists (SEG), this is the standard format for

recording 2-D seismic data which replaced SEG Exchange Tape Format (or SEG Ex)..

**Semblance** - one of the seismic wave attributes, which can be used on time slices or horizon slices to show similarity between wavelets (such as wavelength, phase, velocity) on adjacent traces. Semblance is widely used to search for sudden changes of wavelet character which are associated with boundaries between depositional forms, faults or erosional surfaces.

**Step** - is the distance between adjacent survey stations.

**Survey line** - is a line along which the GPR is moved and collects individual traces. When lines are oriented into a 3-D grid, survey lines are sometimes referred to as 'in-lines', while the lines which are oriented perpendicularly to the survey lines and are formed by traces that are referred to as 'cross-lines'.

**Survey station** - is a point along the GPR line where signal is sent and recorded. In common-offset survey mode it is assumed as a point halfway between the transmitting and receiving antenna. Step is a distance along the survey line between adjacent survey stations.

**Thalweg** - is the line which joins the deepest points in a river channel.

**Trace** – is a plot of amplitude in time or depth domain recorded at a survey station. A set of individual traces recorded along a survey line forms geophysical profile.

**True 3-D dataset** - defined by Neal (2004) as a dataset with equal distances between adjacent lines and stations.

APPENDIX 2A  
SEISMIC UNIX SCRIPTS FOR DATA PROCESSING

```
#!/bin/bash

file=/home/tomasz/GPR/DATA/LINE04
rm junk.su
#rm $file.su
# Input parameters in metres and nanoseconds
ntr=400
npts=900
t0=176
twin=360
startlocx=0
startlocy=0
deltax=0.1
deltay=0.1
vmigr=4.0

dt=`bc <<END0
    scale=3
    $twin/$npts*10000
END0`
delrt=`bc <<END1
    $t0 * $dt /1000
END1`
dx=`bc <<END2
    100 * $deltax
END2`
x0=`bc <<END3
    100 * $startlocx
END3`
y0=`bc <<END4
    100 * $startlocy
END4`
dy=`bc <<END5
    100 * $deltay
END5`
xax=`bc <<END6
    scale=3
    $ntr / 125
END6`
yax=`bc <<END7
    scale=3
    ($twin-($delrt/10)) / 100
END7`
echo "dt, t0, x0, dx, y0, dy, xax, yax"
echo $dt, $delrt, $startlocx, $dx, $startlocy, $dy, $xax, $yax
dt1tosu <$file.DT1 ns=$npts dt=$dt swap=0 |

#Set header values common to all traces
sushw key=dt,offset a=$dt,10 |

#Set sx, sy, cdp and tstat
sushw key=sx,sy,cdp a=$x0,$y0,1 b=$dx,$dy,1 >junk.su

#sufliip < junk.su flip=2 > junka.su
a2b < ${file}staticx10.txt n1=1 > ${file}staticx10.binary
sushw < junk.su infile=${file}staticx10.binary key=tstat |
```

```

#AMPLITUDE SPECTRUM IN FREQUENCY DOMAIN (uncheck to display)
#suspecfx | suxwignb &

# FILTERS
# No filter

#sufilter f=0,10.0,40.0,100.0 amps=1.,1.,1.,1. |

# Dewow
#sufilter f=0,1,4,10 amps=0.,0.,1.,1. |

# Bandpass Filter
#sufilter f=2,4,10,50 amps=0,1,1,0 |

# Time Variable Filter
sutvband tf=1.2,3.5 f=1,5,20,40 f=.1,5,15,30 |

# Autocorrection (to display time lag for Wiener predictive filtering)
#suacor | suxwignb |

# Wiener predictive error filtering
#supef maxlag=0.012 |

# Dip Move Out (DMO)
sudmotx cdpmin=0 cdpmax=$ntr dxcdp=0.1 noffmix=1 vrms=$vmig |

# GAIN FUNCTION
# Set Function
sugain tpow=1.2 gpow=0.2 |

# Automatic Gain Control (AGC)
#sugain gagc=1 wagc=0.5 qbal=1 |

# ZERO THE RINGING DUE TO BANDPASS
suzero itmax=$t0 |

# SET STATIC CORRECTION
sustatic hdrs=1 |

# STOLT MIGRATION
#sustolt cdpmin=1 cdpmax=400 dxcdp=0.1 vmig=$vmigr noffmix=10 |

# CUT OFF DATA PRIOR TO tZERO
suwind dt=0.1 itmin=$t0 | sushw key=f1,d1 a=-0.05, 0.01 > $file.su

# INTERPOLATE TRACES
#suinterp ninterp=1 > $file.su

# DISPLAY FINAL GPR PROFILE
#suxwignb < $file.su f2=$startlocx d2=$deltax mpicks=${file}.a.picks |
title="$file.DT1: Gains tpow=3 gpow=0.1; Time variable bandpass f1=40,120,600,1000 f2=20,40,400,600" |
titlesize=12 labelsz=6 xbox=200 ybox=100 wbox=1200 hbox=700 perc=90| label1='depth, m' label2='distance, m'
#supswignb < $file.su f2=$startlocx d2=$deltax |
title="$file.DT1: Gains tpow=3 gpow=0.1; Time variable bandpass f1=40,120,600,1000 f2=20,40,400,600" |
titlesize=4 labelsz=6 width=$x3x height=$yax | label1='depth, m' label2='distance, m' > $file.ps

suximage < $file.su f2=$startlocx d2=$deltax |
title="$file.DT1: Gains tpow=3 gpow=0.1; Time variable bandpass f1=40,120,600,1000 f2=20,40,400,600" |
titlesize=12 labelsz=6 xbox=400 ybox=100 wbox=1200 hbox=700 perc=90| label1='depth, m' label2='distance,

```

m'

```
supsimage < $file.su f2=$startlocx d2=$deltax | title="$file.DT1: Gains tpow=3 gpow=0.1; Time variable  
bandpass f1=40,120,600,1000 f2=20,40,400,600" | titlesize=4 labelsiz=6 width=$x3x height=$yax |  
label1='depth, m' label2='distance, m' > $file.ps
```

```
# create SEG Y file  
segyhdrs < $file.su  
segywrite < $file.su endian=0 tape=$file.sgy
```

APPENDIX 2B  
SEISMIC UNIX SCRIPTS FOR COMPILATION OF 3-D DATA

```

#!/bin/csh
touch spam
unalias rm
rm cube.su

set sy=0
set line=0
while ($line <= 99)
if ($line <= 9) then
set line=0${line}
else
endif

#Include below the number of lines to be compiled
echo "Line is $line / 99"
segypread tape=./DATA04/LINE${line}.sgy endian=0 conv=1 | segyclean >! DATA04.tmp
sushw <DATA04.tmp key=sy a=$sy >! DATA04.tmp2
suchw <DATA04.tmp2 key1=gx key2=sx | suchw key1=gy key2=sy >! DATA04.tmp3
set nocdp=`sugethw <DATA04.tmp3 key=cdp output=geom | awk 'END {print NR}'`

#Script for checking number of traces in each line. Empty traces are added if the number is lower from the set
number
echo "Number of CDP is $nocdp"
if ($nocdp == 400) then
echo "Full number of traces"
else
echo "Not a full number of traces"
set nonulls=`echo "400-{$nocdp}" | bc -l`
echo "Number of null traces being created is $nonulls"

set dt=`suwind <DATA04.tmp3 count=1 | sugethw key=dt output=geom | awk '{print $1/1000000}'`
set nt=`suwind <DATA04.tmp3 count=1 | sugethw key=DATA04 output=geom`
set tracl=`suwind <DATA04.tmp3 count=1 | sugethw key=tracl output=geom`
set offset=`suwind <DATA04.tmp3 count=1 | sugethw key=offset output=geom`
set tstat=`suwind <DATA04.tmp3 count=1 | sugethw key=offset output=geom`
sugethw <DATA04.tmp3 key=sx output=geom >! sxs
set notraces=`awk 'END {print NR}' sxs`
set sxorigin=`awk '{if (NR == "{$notraces}") {print $1+10}}' sxs`
sunull ntr=$nonulls dt=$dt nt=$nt | sushw key=delrt a=230 | sushw key=offset a=$offset | sushw key=trid a=1 |
sushw key=tracl a=$tracl | sushw key=sy a=$sy | sushw key=sx a={$sxorigin} b=10 | suchw key1=gx key2=sx |
suchw key1=gy key2=sy | sushw key=tstat a=$tstat >! nulls
cat DATA04.tmp3 nulls >! tmp
sushw <tmp key=cdp a=1 b=1 | sushw key=tracr a=1 b=1 >! DATA04.tmp3
endif

#suximage <DATA04.tmp3 perc=99 title="Line $line"

cat DATA04.tmp3 >>! cube.su
set sy=`echo "$sy+99" | bc -l`
@ line ++
end
sushw <cube.su key=cdp,tracl,flidr,tracl,ep a=1,1,1,1,1 b=1,1,1,1,1 >! cube2_High_DATA04.su
echo "Converting to Seg-Y"
segyphdrs <cube2_High_DATA04.su | segypwrite tape=High_DATA04.sgy conv=1 endian=0
sugethw <cube2_High_DATA04.su key=sy,sx output=geom >! shots
set count=`awk 'END {print NR}' shots`
a2b <shots n1=2 | xgraph n=$count linewidth=0 mark=5 marksize=5 &

```

APPENDIX 3  
ANIMATIONS

(See CD.)